Neuroscience Bulletin

The Official Journal of The Chinese Neuroscience Society
神经科学通报

Volume 36
Number 4
April 2020

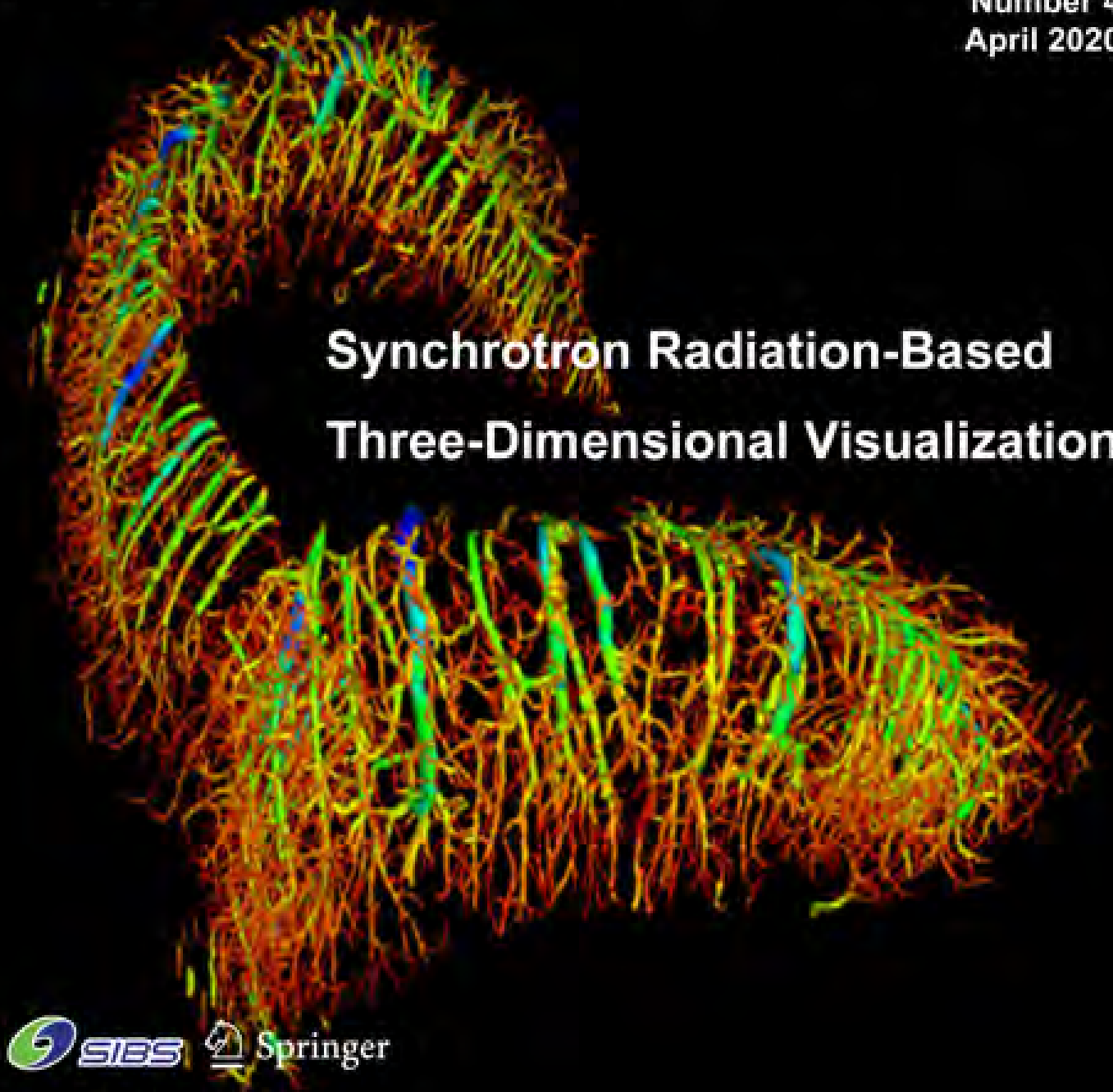

Synchrotron Radiation-Based Three-Dimensional Visualization

SIBS Springer
www.neurosci.cn

CONTENTS

Neuroscience Bulletin

About the Cover

The morphological alterations of microvessels under both normal and seizure conditions might be essential for investigating the pathogenesis and development of epilepsy. Xiao and Zhang *et al.*, by firstly applying synchrotron radiation-based X-ray in-line phase-contrast imaging and quantitative 3-D characterization without any contrast-enhancing agents to discover 3-D hippocampal microvascular remodeling alongside the progression of epilepsy, found that the number of microvessels was markedly increased on days 1 and 14, but decreased on day 60 after seizures. The surface area, diameter distribution, mean tortuosity, and number of bifurcations and network segments also showed similar trends. The cover image indicates the 3-D angioarchitecture of the hippocampus. Continuous pseudo-color changes are used to depict the distribution spectrum of vessel diameters, ranging from 10 μm to 100 μm. See pages 333–345. (Cover image provided by Prof. Bo Xiao and Mengqi Zhang).

Volume 36 Number 4
April 2020

Editorial

Original Articles

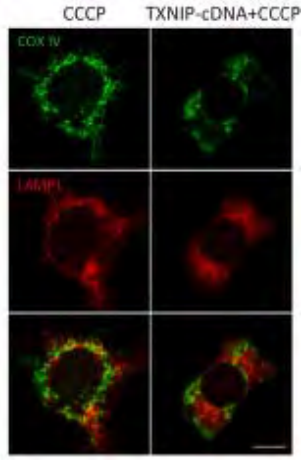

p 355

www.neurosci.cn

CONTENTS

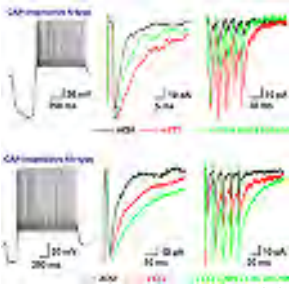

p 403

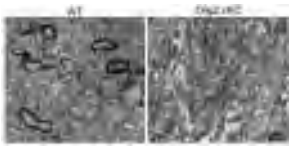

p 422

CONTENTS

Neuroscience Bulletin

Letter to the Editor

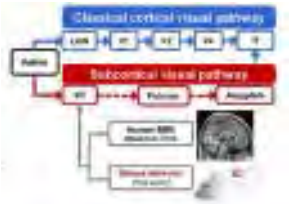

p 430

Review

Research Highlight

Neurosci. Bull. April, 2020, 36(4):331–332
https://doi.org/10.1007/s12264-020-00491-w

www.neurosci.cn
www.springer.com/12264

EDITORIAL

Imaging Three-Dimensional Microvascular Networks of Brain with Synchrotron Radiation Microangiography

Ming Song[1,2,3]

Received: 19 February 2020 / Accepted: 13 March 2020 / Published online: 2 April 2020

The adult human brain represents about 2% of the body weight, yet consumes about 20% of the body's total energy. A key constituent in meeting this high energy demand is a complex cerebral vascular system. A detailed knowledge of this system is important for understanding the basic principles of cerebral blood flow and its coupling to neural processing and neuropathological alterations in brain diseases. In this issue, Gu and collaborators utilized synchrotron radiation (SR) microangiography to acquire high-resolution (about 5 μm), high-contrast images of the brain tissue of rats under both normal and epileptic seizure conditions without the use of any contrast agent or labeling marker [1]. This study demonstrates that SR microangiography can provide systematic and detailed views of cerebrovascular anatomy at the micron level.

The diameters of cortical vessels range from several hundreds of microns (arteries/veins) to a few microns (capillaries). Although the detection of cortical vessels at the macro-level (> 500 μm) has been successful using current techniques such as digital subtraction angiography, magnetic resonance angiography, and computed tomography angiography, methods to detect microvascular networks (< 100 μm) are still scarce. In order to estimate the diameters of capillaries, submicron spatial resolution is required. Classical studies of microvascular networks are based on a combination of tissue staining (*e.g.* filling with Indian ink) or immunohistochemistry with microscopic imaging techniques. However, most of these studies did not make direct images of the whole brain in a three-dimensional fashion, rather than isolated slices of brain tissue after tissue removal and manipulation with aggressive fixatives, various chemical detergents, and geometric distortions [2].

Recently, some new technologies have opened promising avenues for imaging the detailed three-dimensional vascular network topology of the brain, although these methods can only be applied to small animals at present. One of these novel technologies is based on microscopic optical imaging. For example, researchers have developed the all-optical histology technique [3], whereby two-photon microscopy is used to image fluorescently-labeled vasculature. Although this method has the ability to measure vascular diameters *in vivo*, the field of view is normally limited to a few hundred microns, without covering the entire brain of a mammal. With the advent of tissue clearing methods, selective plane illumination microscopy or ultramicroscopy is becoming an increasingly powerful approach to acquire and reconstruct these fluorescently-labeled vessels [4–6]. Unfortunately, tissue clearing technology can only be used in specimens. Another possible approach is the use of SR microangiography, where a high photon flux is exploited to acquire detailed high-resolution images of microvessels even down to a diameter of 1 μm or even higher resolution. In a specimen, SR microangiography can quickly characterize the three-dimensional morphology without sectioning. In particular, a recent study reported that the total volume of a mouse brain specimen can be acquired with micron resolution in about 15 min [7]. In fact, SR microangiography has the potential

✉ Ming Song
msong@nlpr.ia.ac.cn

[1] National Laboratory of Pattern Recognition, Institute of Automation, Chinese Academy of Sciences, Beijing 100190, China

[2] Brainnetome Center, Institute of Automation, Chinese Academy of Sciences, Beijing 100190, China

[3] University of the Chinese Academy of Sciences, Beijing 100049, China

to generate images of the cerebral vascular networks in large animals *in vivo* [8], which is impossible with the methods based on tissue-clearing technology. In addition, one major advantage of SR microangiography is its ability to differentiate vessels without the use of any contrast agent or labeling marker. Therefore, when combined with tomography algorithms, SR microangiography can permit very detailed analysis of the whole brain vasculature.

In summary, the cerebrovascular system plays an important role in brain function, both in health and disease. Novel cerebrovascular imaging approaches are needed, especially for detecting micro-vascular anatomy and physiology at the micron level. The study of Gu and collaborators [1] suggests that SR microangiography could be one of the most promising approaches to addressing relevant questions regarding the involvement of microvascular network alterations in brain diseases.

Acknowledgements This editorial was supported by the National Natural Science Foundation of China (31870984).

References

1. Gu P, Xu ZH, Cao YZ, Liao SH, Deng QF, Yin XZ, *et al*. Synchrotron radiation-based three-dimensional visualization of angioarchitectural remodeling in hippocampus of epileptic rats. Neurosci Bull 2020, 36: 333–345. https://doi.org/10.1007/s12264-019-00450-0.
2. Zhu X, Xia Y, Wang X, Si K, Gong W. Optical brain imaging: a powerful tool for neuroscience. Neurosci Bull 2017, 33: 95–102.
3. Tsai PS, Friedman B, Ifarraguerri AI, Thompson BD, Lev-Ram V, Schaffer CB, *et al*. All-optical histology using ultrashort laser pulses. Neuron 2003, 39: 27–41.
4. Ertuerk A, Becker K, Jaehrling N, Mauch CP, Hojer CD, Egen JG, *et al*. Three-dimensional imaging of solvent-cleared organs using 3DISCO. Nature Protocols 2012, 7: 1983–1995.
5. Susaki EA, Tainaka K, Perrin D, Yukinaga H, Kuno A, Ueda HR. Advanced CUBIC protocols for whole-brain and whole-body clearing and imaging. Nat Protocols 2015, 10: 1709–1727.
6. Rocha MD, Duering DN, Bethge P, Voigt FF, Hildebrand S, Helmchen F, *et al*. Tissue clearing and light sheet microscopy: imaging the unsectioned adult zebra finch brain at cellular resolution. Front Neuroanat 2019, 13, 13.
7. Massimi L, Bukreeva I, Santamaria G, Fratini M, Corbelli A, Brun F, *et al*. Exploring Alzheimer's disease mouse brain through X-ray phase contrast tomography: From the cell to the organ. Neuroimage 2019, 184: 490–495.
8. Schueltke E, Kelly ME, Nemoz C, Fiedler S, Ogieglo L, Crawford P, *et al*. Dual energy CT at the synchrotron: A piglet model for neurovascular research. Eur J Radiol 2011, 79: 323–327.

Neurosci. Bull. April, 2020, 36(4):333–345
https://doi.org/10.1007/s12264-019-00450-0

www.neurosci.cn
www.springer.com/12264

ORIGINAL ARTICLE

Synchrotron Radiation-Based Three-Dimensional Visualization of Angioarchitectural Remodeling in Hippocampus of Epileptic Rats

Pan Gu[1] · Zi-Hao Xu[1] · Yu-Ze Cao[1] · Sheng-Hui Liao[2] · Qian-Fang Deng[1] · Xian-Zhen Yin[3] · Zhuo-Lu Wang[4] · Zhuo-Hui Chen[1] · Xin-Hang Hu[1] · Hui Wang[1] · Li-Zhi Li[1] · Shi-Xin Liu[1] · Hui Ding[1] · Shu-Peng Shi[1] · Hong-Lei Li[1] · Ti-Qiao Xiao[5] · Bo Xiao[1] · Meng-Qi Zhang[1]

Received: 12 June 2019 / Accepted: 11 September 2019 / Published online: 10 December 2019

Abstract Characterizing the three-dimensional (3D) morphological alterations of microvessels under both normal and seizure conditions is crucial for a better understanding of epilepsy. However, conventional imaging techniques cannot detect microvessels on micron/sub-micron scales without angiography. In this study, synchrotron radiation (SR)-based X-ray in-line phase-contrast imaging (ILPCI) and quantitative 3D characterization were used to acquire high-resolution, high-contrast images of rat brain tissue under both normal and seizure conditions. The number of blood microvessels was markedly increased on days 1 and 14, but decreased on day 60 after seizures. The surface area, diameter distribution, mean tortuosity, and number of bifurcations and network segments also showed similar trends. These pathological changes were confirmed by histological tests. Thus, SR-based ILPCI provides systematic and detailed views of cerebrovascular anatomy at the micron level without using contrast-enhancing agents. This holds considerable promise for better diagnosis and understanding of the pathogenesis and development of epilepsy.

Keywords Epilepsy · Synchrotron radiation · 3D · Angioarchitecture · Blood vessel · Remodeling

Introduction

Epilepsy is an extremely common neurological disorder, impacting ~ 50 million people worldwide [1]. The term "epilepsy" encompasses a large number of syndromes, ranging from diseases with various etiopathogeneses to recurring spontaneous seizures. The seizures occur due to aberrant neuronal networks, resulting in transient excessive or hyper-synchronous discharges involving several cortical neurons [2, 3]. The exact pathogenesis of epilepsy, however, remains largely unknown. Temporal lobe epilepsy (TLE), for instance, is a focal form that is usually associated with hippocampal atrophy, sclerosis, axonal sprouting, neuronal loss, and various genetic factors [4–7]. Previous studies have mostly dealt with the neuropathological and neurophysiological aspects of epilepsy. Experimental and clinical research over the past decade suggests that systemic hypertension and cerebral small vessel disease amplify the risk of epilepsy, even in the absence of a clinically-detected stroke [8, 9]. Alterations in the neurovasculature have been shown to be of vital importance as well [10, 11]. Neurovascular units in particular play a significant role in the regulation of nutrient supply,

Pan Gu, Zi-Hao Xu and Yu-Ze Cao have contributed equally to this work.

✉ Bo Xiao
csuxiaobo123456@163.com

✉ Meng-Qi Zhang
zhangmengqi8912@163.com

[1] Department of Neurology, Xiangya Hospital, Central South University, Changsha 410008, China

[2] School of Information Science and Engineering, Central South University, Changsha 410008, China

[3] State Key Laboratory of Drug Research, CAS Key Laboratory of Receptor Research, Shanghai Institute of Materia Medica, Chinese Academy of Sciences, Shanghai 201203, China

[4] Department of Breast Surgery, Hunan Provincial Maternal and Child Health Care Hospital, Changsha 410008, China

[5] Shanghai Synchrotron Radiation Facility, Shanghai Advanced Research Institute, Chinese Academy of Sciences, Shanghai 201800, China

vascular growth, hemodynamics, toxin elimination, and brain protection, thus emphasizing the function of neurons, glia, and vascular endothelium as a whole unit [12]. This link between blood vessels and the blood–brain barrier (BBB) provides a novel perspective from which to explore the possible pathogenesis of epilepsy.

The BBB in the neurovascular unit is a dynamic barrier with a variety of physiological functions, such as regulation of cerebral blood flow, nutrient metabolism, transport, and immunization. The BBB can respond to different pathophysiological signals and induce microvascular remodeling as well as angiogenesis in lesioned areas [13–15]. Following observations of pericytosis during seizures, pericytes have now been reported to introduce a pericyte–microglia-mediated mechanism underlying BBB dysfunction in epilepsy patients [16, 17]. Current research suggests that the induction of microvascular neovascularization and remodeling in the hippocampus seen in TLE may be associated with its chronic progression [18]. Microvascular neovascularization has been reported in the hippocampus of patients with previous TLE and chronic refractory periods. The hippocampus consists of four regions, cornu ammonis 1 (CA1), CA2, CA3, and CA4. In TLE patients, neovascularization has been found in the CA1 and CA3 regions, where metabolism is the most exuberant and, therefore, any changes in vascularization are likely to affect the function and metabolism of these regions [19]. Ndode *et al*. reported that the total length of hippocampal blood vessels is decreased two days after status epilepticus (SE) is induced in adult rats, but they did not find any change in hippocampal blood volume or blood flow. In addition, the proliferation of endothelial cells and angiogenesis in CA3 have been found at four days and two weeks after SE, respectively [20]. And several highly-expressed angiogenic factors have been detected in the brain tissue of epileptic rats 24 h after seizures [21–23]. Ruba *et al*. administered sunitinib to block angiogenesis in rats suffering from TLE and found that this resulted in atrophy of the hippocampus and control of seizures [24]. The existing body of research suggests a complex relationship between BBB damage and seizures [20, 25].

Following from all these studies, it can be inferred that the local angioarchitecture undergoes some remodeling after a lesion. However, the relationship between epilepsy and neovascularization is not well characterized, probably due to difficulties in accurately visualizing changes in hippocampal angioarchitecture during seizures. Admittedly, conventional vascular visualization techniques such as histological sections [26, 27], immunostaining [12], and digital subtraction angiography (DSA) have high resolution and can resolve data at the micron level. However, they can only display two-dimensional section structure and are unable to reveal the complex spatial networks of blood vessels. DSA also requires contrast-enhancing agents, which may lead to anaphylaxis and neural poisoning [28]. More recently, high-resolution MRI for the non-destructive microscopic analysis of tissue specimens has been proposed [29, 30]. The brain structure of both normal and CNS disease models (such as intracranial artery dissection [31] and spinal cord injury [32]) visualized using diffusion MRI exhibits excellent contrast between grey and white matter. Despite these advantages, high-field and small-bore MRI remains relatively expensive and difficult to set up and maintain. This technique also has a limitation in terms of unavoidable homogeneity-induced image distortions. Moreover, patients with metal implants are unsuitable for MRI scanning, which limits its general applicability.

Fortunately, the development of synchrotron radiation (SR) has pioneered a new method in the field of biomedical imaging. SR is characterized by high monochromatic photon flux and a wide energy spectrum, emitted with energies ranging from infrared light to hard x-rays [33–35]. Unlike conventional attenuation-contrast imaging, which is based on tissue density variations, state-of-the-art SR is based on the phase-contrast imaging (PCI) model [36, 37]. X-ray PCI exploits differences in the refractive index of different materials to differentiate structures [38], allowing it to clearly define biological soft tissues with weak X-ray absorption capacities without having to resort to contrast-enhancing agents [39]. In recent years, several PCI modalities have been developed, such as interferometry [40], diffraction-enhanced imaging [41, 42], grating-based phase-contrast X-ray imaging [43], and in-line phase contrast imaging (ILPCI) [44].

The simplest X-ray PCI-based method, ILPCI, was the main technique used in the present study [45]. Although it is the simplest method, the principle of ILPCI rests on a complicated phase-retrieval step. The constraints placed on SR source size guarantee good spatial coherence and enhancement of edge signals, enabling the visualization of biological tissue microstructures for preclinical evaluation [46]. This technique has been used to visualize a range of biological structures and phenomena, such as renal arteries [47], morphological changes in intervertebral discs and endplates [48], brain microvasculature [49, 50], neovascularization of hepatocellular carcinoma [51], and the internal microstructure of vessels and nerve fibers in the rat spinal cord [52, 53]. In addition to these, it has also recently been used as a promising tool for epilepsy treatment [54, 55] and breast cancer diagnosis [56, 57]. In the current study, we applied SR imaging to visualize the structural remodeling of cerebral vessels under pathological conditions in a dynamic, non-destructive manner.

Methods and Materials

Experimental Animals

The Animal Ethics Committee of Central South University, Changsha, China, approved the experimental protocols, which were in compliance with experimental animal use and ethical requirements per the Ministry of Health of China.

We used 48 male Sprague-Dawley rats (weighing 230–250 g on average) from the Animal Centre of Central South University, Changsha, China. The rats were randomly divided into four groups (12 rats per group): the first was a normal control group, the second was analyzed one day after seizures, the third was analyzed 14 days after seizures, and the fourth was analyzed 60 days after seizures.

Induction of Seizures

Seizures were induced in the experimental groups by intraperitoneal (i.p.) injection of an aqueous solution of lithium chloride (125 mg/kg; Sigma, St. Louis, MO), followed after 18–24 h by scopolamine (1 mg/kg, i.p.; Minsheng Pharma, China) to overcome the peripheral cholinergic antagonism induced by pilocarpine (PILO), and finally, treatment with PILO (30 mg/kg, i.p.; Sigma) 30 min after scopolamine administration [58, 59]. Animals in the control group were given saline in the same volume as the drugs administered to the experimental groups. After PILO injection, the animals were observed for a sequence of behavioral alterations following the Racine's standard criteria [60]; rats classified as stage 4 or 5 were considered to have developed SE. SE was then terminated by i.p. injection of diazepam (7.5 mg/kg) 2 h after its onset to stop or limit the behavioral seizures; the same dose of diazepam was also given to control animals. Additional diazepam (5 mg/kg) was administered if seizures were not reduced efficiently or if they recurred within 1 h of the first diazepam injection [61, 62]. The experimental animals were housed in acrylic cages with free access to food and water, under a 12:12 h light:dark cycle at constant temperature (25°C) and humidity (50% ± 10%).

Sample Preparation

Before transcardiac perfusion, animals were deeply anesthetized with 10% chloral hydrate (0.4 mL/kg, i.p.). We then perfused paraformaldehyde (4%) in 0.1 mol/L phosphate buffer (pH 7.4) at different time points. The rat brains were dissected and fixed in 4% paraformaldehyde at 4°C for 24 h, and then separated for different experiments. Three brains per group were prepared for SR-ILPCI and the remaining three for histological observation. The rinsed brain specimens were fully dehydrated for ILPCI using an ascending ethanol gradient.

Image Acquisition and Post-processing

We performed all experiments with the biomedical application beamline (BL13W1) of the Shanghai Synchrotron Radiation Facility (SSRF), which is a third-generation synchrotron source [50]. Its average beam current is 180 mA and storage energy is 3.5 GeV. The BL13W1 beamline offers tunable photon energy from 8 to 72.5 keV, with a maximal target size of $\sim$ 5 mm (vertical) $\times$ 45 mm (horizontal) at 20 keV. The distance between the downstream detector and sample can be changed from 0 to 8 m. Our samples were fixed on a rotating stage, allowing the detector-to-sample distance to be adjusted by moving the detector along a rail vertical to the axis. High-contrast images were captured by a camera with a charge-coupled device (CCD). A schematic of the equipment used for SR imaging at BL13W1 is shown in Fig. 1A.

The effective pixel size of the CCD detector was 5.2 μm. To acquire clear, high-contrast images of the vasculature, we set the scanning energy to 20.0 keV and the detector-to-sample distance to 0.5 m. By continuously rotating the samples from 0° to 180° and setting the exposure time to 1.5 s, a total of 900 projection images were acquired. We also recorded flat-field and dark-field images for subtracting background signals, filtering noise, and eliminating small intensity discrepancies. To improve the quality of reconstructed slices, we performed propagation-based phase-contrast extraction with PITRE software (Phase-sensitive X-ray Image processing and Tomography REconstruction – supplied by BL13W1) [63]. According to the principles of phase contrast imaging, the phase and amplitude of X-rays are influenced by interactions with matter, and the forward diffraction can be described by the complex refractive index "n" of the medium ($n = 1 - \delta + i\beta$), where δ is the refractive index decrement in relation to the phase shift, and β is the linear absorption coefficient. Based on preliminary experiments, the parameter δ/β was adjusted to 100 during phase extraction. After phase retrieval and reconstruction, intensity scales were reduced and rescaled to a grey value ranging from 0 to 255. The reformatted digital slice images were acquired using fast slice reconstruction software, based on fast Fourier transformation (supplied in PITRE). We then used VG Studio Max 3D reconstruction software v. 3.0 (Volume Graphics GmbH, Heidelberg, Germany), Image Pro Analyzer 3D v. 7.0 (Media Cybernetics Inc., USA) and Amira v. 6.4 (Thermo Fisher Scientific, Waltham, MA) to render

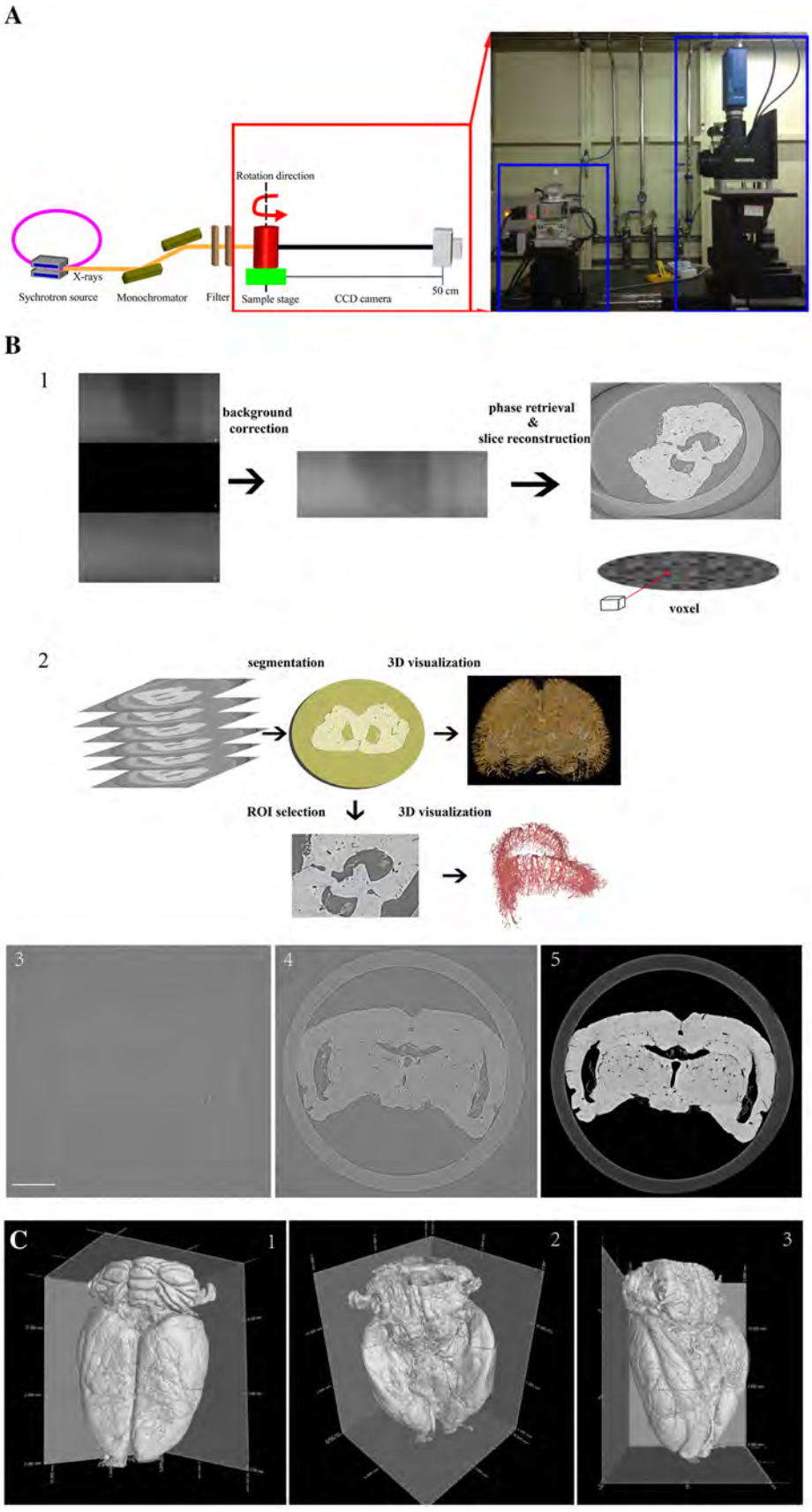

Fig. 1 Reconstruction procedure and overview of the 3D surface morphology of rat brain. **A** Schema of the Shanghai Synchrotron Radiation Facility. **B** Reconstruction procedure, consisting of acquiring CT images, reconstruction of a series of CT slices, and in-depth processing (scale bar, 2 mm). **C** Overview of the 3D surface morphology of rat brain from dorsal, ventral, and lateral views.

sequential CT slices into 3D microtomography and performed in-depth 3D analysis. A schematic for obtaining CT images and performing final 3D reconstruction is shown in Fig. 1B1. Through these operations, the 3D images of gross cerebral angioarchitecture and hippocampal regional vasculature were reconstructed (Fig. 1B2). Figure 1B3–B5 shows the step-by-step optimized image processing for slice reconstruction; Fig. 1B3 shows the original image used for slice reconstruction; Fig. 1B4 shows background subtraction; and Fig. 1B5 shows phase retrieval before slice reconstruction. Vascular information was further enhanced through filtered de-noising. Thus, the surface microvasculature of normal rat brain was completely exposed to identify multi-level branches of blood vessels on the pia mater (Fig. 1C).

As described previously, the network analysis mainly incorporated segmentation, skeletonization, and vectorization [49, 64]. We used color codes to define vasculature of different diameters. Using the geometric information of blood vessels and vascular corrosion algorithms, the centerline of the blood vessel (a line connecting points equidistant from both edges of the vessel) was extracted from the 3D images [65]. The vessel centerline provided detailed 3D topological data for subsequent complex morphometric analysis. The distance from the edge of the vessel to the centerline varied with diameter, so we constructed intuitive 3D images to determine the cerebral vascular diameter distribution, by which tortuosity can be measured.

Lastly, we used vascular analysis modules to calculate a series of parameters such as vascular surface area, vessel diameter, the number of vascular bifurcations, and the number of vascular segments for further analysis.

Immunohistochemistry

Animals were perfused with paraformaldehyde, as described earlier, at the time of euthanasia. The samples were cryoprotected overnight in 30% sucrose in PBS, embedded in optimal cutting temperature compound (Sakura Finetek, Torrance, CA) and then cut into 10-μm sections. We collected coronal sections and washed them three times with PBS. CD31 antigen unmasking was done by treatment with PBS containing 1 μg/mL proteinase K for 15 min at room temperature. The sections were blocked with PBS containing 0.25% Triton and 20% normal horse serum for 90 min at room temperature. The sections were incubated overnight at 4°C with primary antibody against CD31 (1:100; Abcam, Cambridge, UK). The sections were washed thrice in PBS and incubated with horseradish peroxidase-conjugated secondary antibody (1:200; Santa Cruz Biotechnology, Santa Cruz, CA) for 1 h at room temperature. Following the manufacturer's instructions, we first stained the sections using a diaminobenzidine kit (Maixin, Fuzhou, China) and then counterstained them with Harris hematoxylin. All samples were imaged using an Olympus BX51 microscope (Olympus America, Center Valley, PA) and compared with the vascular images obtained using SR imaging. For quantitative analysis, microvessel densities (MVDs) in hippocampal areas were calculated on a 2D plane of the images using Image Pro Plus 6.0. The MVD was defined as the number of microvessels divided by the total area analyzed.

Data Analysis

Statistical analysis was conducted using SPSS 20.0 (IBM, Armonk, NY). The data were analyzed by one-way analysis of variance followed by Tukey's *post hoc* test for changes in morphological parameters after seizures. $P < 0.05$ denoted a statistically significant difference. Differences in blood vessel surface area, number of vascular segments, and number of vascular bifurcations were assessed using nonparametric tests, first by the Kruskal-Wallis test and then by the Mann-Whitney U-test. Data are presented as the mean ± SEM.

Results

3D Morphology of Cerebral and Hippocampal Angioarchitecture

A high-throughput, high-brilliance, quasi-coherent, and high-purity synchrotron radiation source was used to display the spatial and temporal characteristics of rat hippocampal microvessels, including microvascular morphologies, shapes, branches, and nodes. Continuous pseudocolor changes depicted the distribution of vessel diameters, which ranged from 10 μm to 100 μm (Fig. 2). Using this information, the 3D microvascular network of the whole hippocampus was successfully reconstructed (Fig. 2D). Once this was done, the detailed 3D network of only the right hippocampus was extracted from the whole brain by SR-based ILPCI reconstruction. The spatial distribution of this section (the right hippocampus) was accurately outlined (Fig. 2A, B) and hippocampal vessel diameters were rendered to identify vessels with different diameters (Fig. 2C).

3D Visualization and Vascular Remodeling of Hippocampus after Epileptic Seizures

The 3D reconstructions of the experimental groups (days 1, 14, and 60) were compared with those of the control group. The reconstructions were performed using ILPCI to

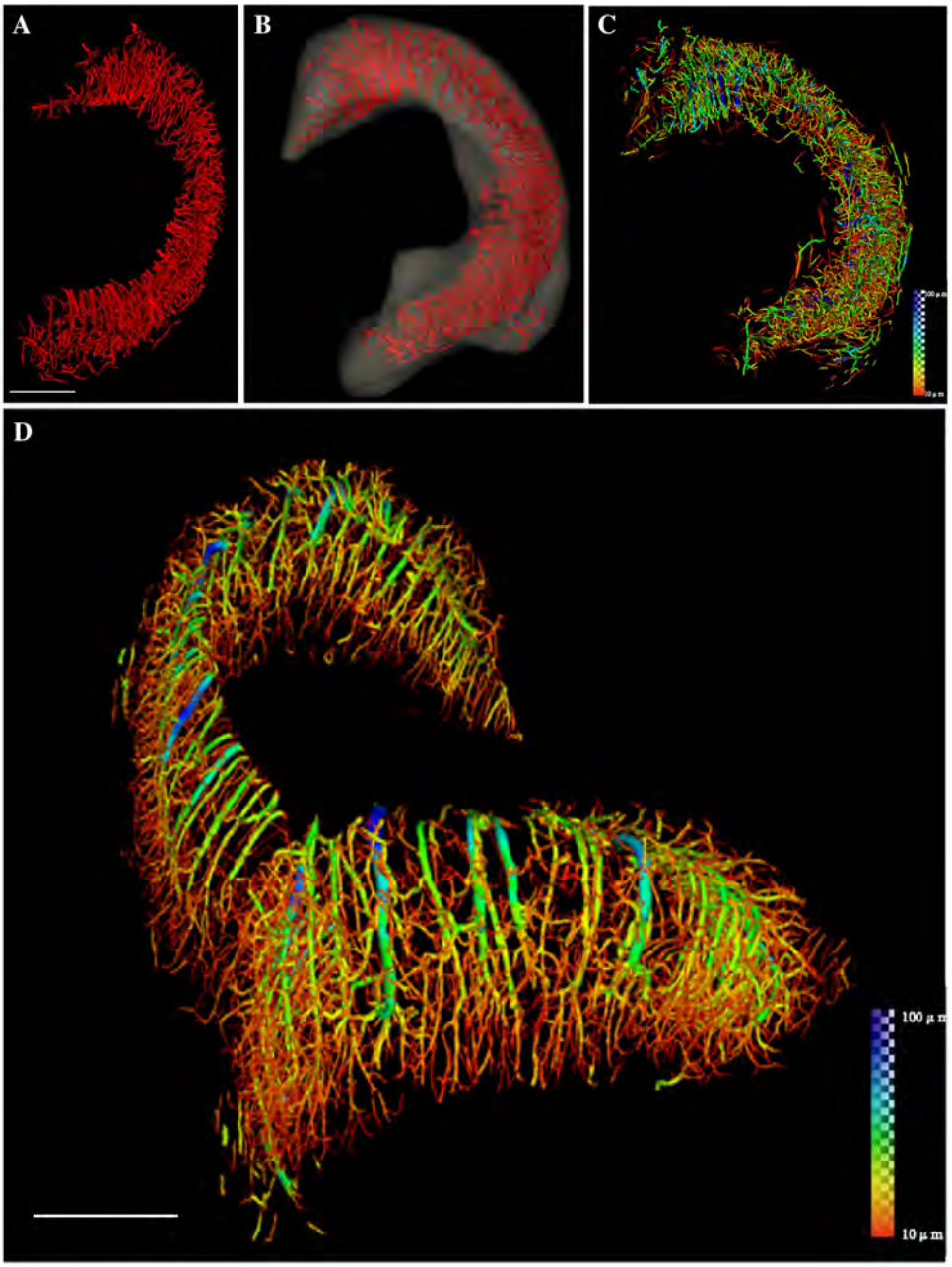

Fig. 2 Reconstruction of the 3D angioarchitecture of the hippocampus in normal rat brain. **A**, **B** By SR-ILPCI reconstruction, the spatial structure distribution of the right hippocampal three-dimensional network was extracted from the whole brain (**A**) and accurately outlined (**B**) (scale bar, 600 μm). **C** Hippocampal vessel diameter rendering identifies the distribution of vessels with different diameters. **D** The original distribution of intracerebral vessels within the hippocampus with continuous pseudocolor changes depicting the distribution spectrum of vessel diameters, ranging from 10 μm to 100 μm (dark blue) (scale bar, 700 μm).

dynamically track angioarchitectural remodeling at different time points after the occurrence of epileptic seizures (Fig. 3). Compared to controls, the hippocampal angioarchitecture of the experimental groups showed remodeling in a dendritic pattern and increased density on day 1 after seizures. On day 14, the number of fine blood vessels with a twisted shape was significantly higher. On day 60, the total number of blood vessels decreased, and their distribution was loose and disordered, unlike the control group that had tightly-packed and well-organized blood vessels. On day 60, however, the diameters of the vessels varied widely and distinct differences were found (Fig. 4).

Quantitative Analysis of Hippocampal Angioarchitecture Following Policarpine-Induced Status Epilepticus

In order to objectively evaluate specific changes in the microvascular network after seizures, we analyzed the reconstructed hippocampal microvasculature based on the vascular tree module. For this, the surface area, blood vessel segments, mean tortuosity, vascular bifurcations, and diameter distribution were calculated and compared (Fig. 5).

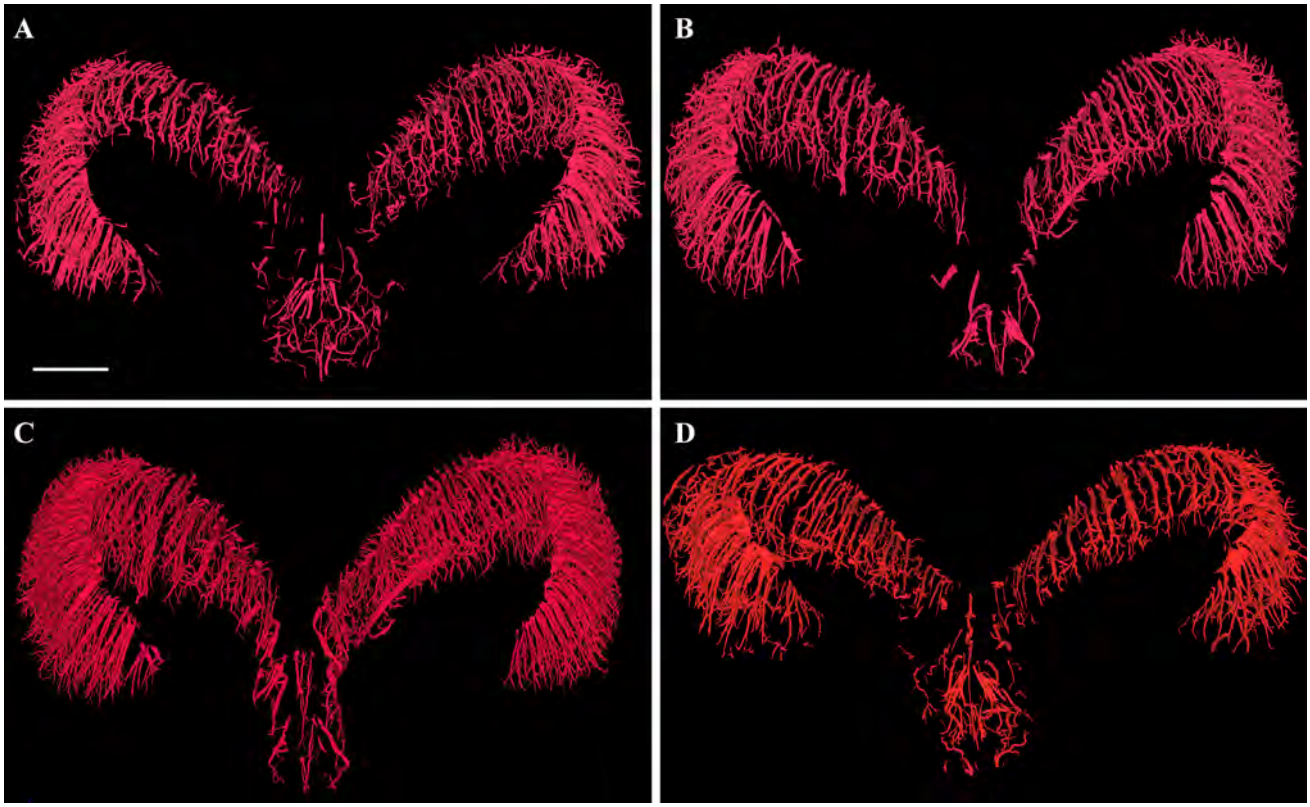

Fig. 3 Representative images of 3D microvasculature of hippocampus at different time points. **A** 3D image of vascular trees in rat hippocampus extracted from the whole brain in the control group (scale bar, 500 μm). **B–D** Images from day 1 (**B**), day 14 (**C**), and day 60 (**D**) after seizures.

The blood vessel surface area, number of vascular segments, and number of vascular bifurcations were measured in the control and experimental groups (days 1, 14, and 60). As the disease progressed, the surface area of blood vessels increased at days 1 and 14, while mice at day 60 showed a slight decline when compared to the control group ($P < 0.05$). The hippocampal microvascular segments and the number of bifurcations of hippocampal microvessels showed a similar trend, in that the days 1 and 14 groups had more and the day 60 group had fewer segments and bifurcations than the control group ($P < 0.05$).

To further examine the changes in microvasculature, we calculated the frequency distribution of blood vessels with different diameters. The changes at different time points occurred mainly in small blood vessels 10 μm and 20 μm in diameter, which showed an increasing trend over time compared to the control group ($P < 0.05$) (Fig. 5E). The changes that manifested on day 14 seemed more prominent than those on other days. There were no significant differences among the blood vessels of larger diameters.

In addition to changes in vascular surface area and diameter, vascular lesions can also affect vascular tortuosity in spatial changes. The mean tortuosity of a blood vessel was calculated based on the virtual vascular centerline. The value of this indicator increased with time, and the mean tortuosity in all three experimental groups was higher than that of the control group (Fig. 5C).

Overall, the number of vascular segments and mean tortuosity were higher on days 1 and 14 ($P < 0.05$), indicating an expansion of the hippocampal microvascular network. On the contrary, the number of segments and bifurcations was lower on day 60 ($P < 0.05$), suggesting a contraction of the hippocampal microvascular network. The surface area showed an increase on days 1 and 14, and a decline on day 60, which may account for the vessel constriction. Parallel quantifications using immunohistochemistry showed that the blood vessels displayed increased CD31 staining on day 1 and a significant decrease on day 60, consistent with the SR-ILPCI data (Fig. 6).

Discussion

The hippocampus is highly sensitive to ischemia, which is intimately associated with epilepsy. For instance, mesial TLE with hippocampal sclerosis is a common and well-documented phenomenon [4, 5, 66]. Recent research has shown that hippocampal vascularization changes that occur after seizures might be closely associated with the

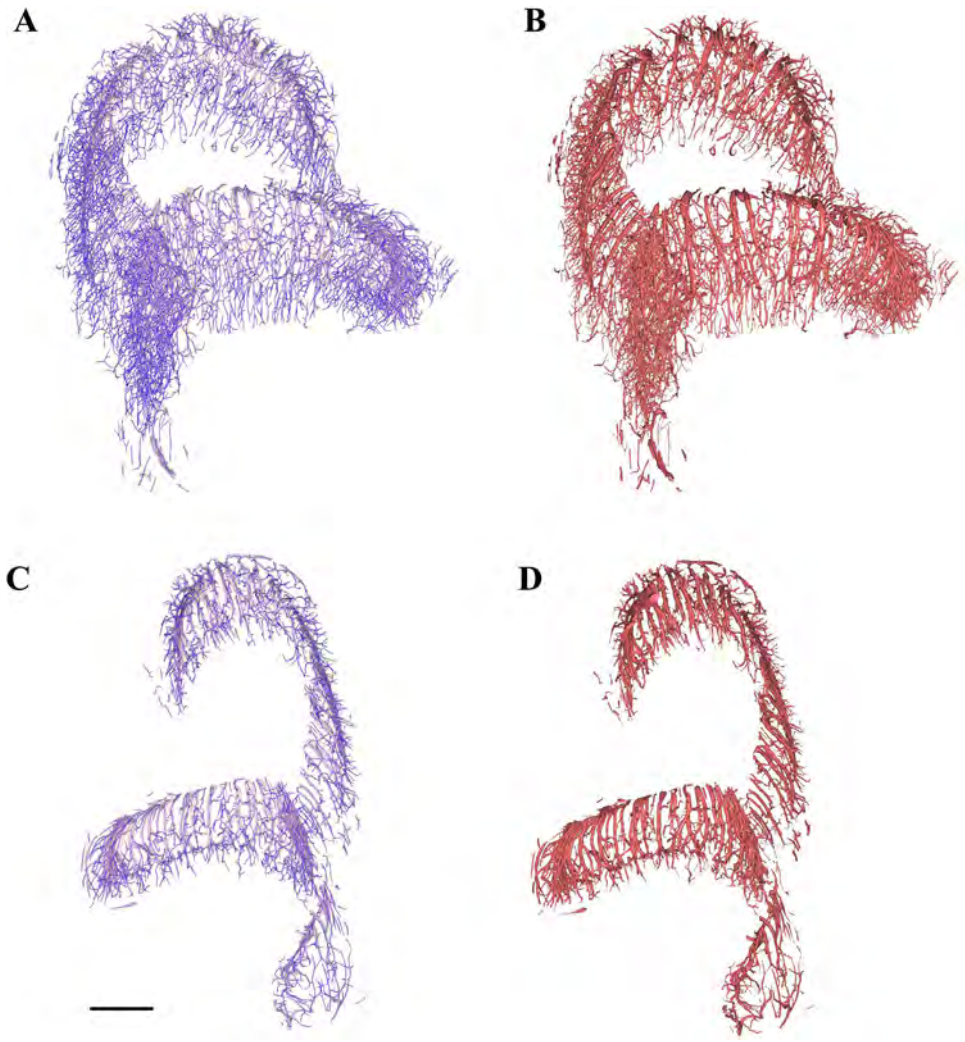

Fig. 4 Reconstructed 3D angioarchitecture on days 1 and 60 after epileptic seizures. **A** Day 1 hippocampal vascular centerlines (blue lines). **B** Day 1 reconstruction of hippocampal blood vessels. **C** Day 60 hippocampal vascular centerlines (blue lines). **D** Day 60 reconstruction of hippocampal blood vessels. Scale bar, 600 μm.

development of epilepsy [16, 18, 21, 22, 67]. To further investigate the role of hippocampal vascularization in the occurrence and progression of epilepsy, a more detailed understanding of angioarchitectural remodeling under normal physiological and pathological conditions is needed. Previous studies have confirmed that visualization techniques like histology and immunostaining have unavoidable limitations due to their invasiveness or lack of information on the spatial configuration of microvessels.

Other more modern technologies such as magnetic resonance angiography (MRA) [68] and CT angiography (CTA), including micro-CT, have their own shortcomings and cannot provide sufficiently detailed images of the microvasculature [69]. MRA requires long acquisition times and is not able to detect acute vascular changes [70], while CTA lacks the resolution to identify microvessels on a micron/submicron scale. Even though contrast-enhancing agents aid in delineating the 3D vasculature of whole brains, they may negatively affect the images [71]. MRI is advantageous for soft tissue visualization, but like CTA, is not sensitive enough to detect microvessels at micron/submicron levels [50]. These restrictions pose rather large limitations if one wishes to study the relationship between hippocampal vascularization and epilepsy.

SR-based ILPCI provides direct and straightforward visualization of microvascular networks in the brain. SR X-rays are different from traditional X-rays as the electrons come from the curvilinear motion of the sample in a magnetic field and the change of direction can often approach the speed of light. The magnetic field in a storage ring can therefore control the direction of electrons, giving SR X-rays high directivity, small divergence, and variable polarization. Such features confer upon SR X-rays the capability of providing more detailed information about microvessel shape and spatial organization, helping us better understand the changes in microvascular networks during epilepsy [72]. In this study, we used ILPCI and the SSRF BL13W1 beamline with a pixel size of 5.2 μm to

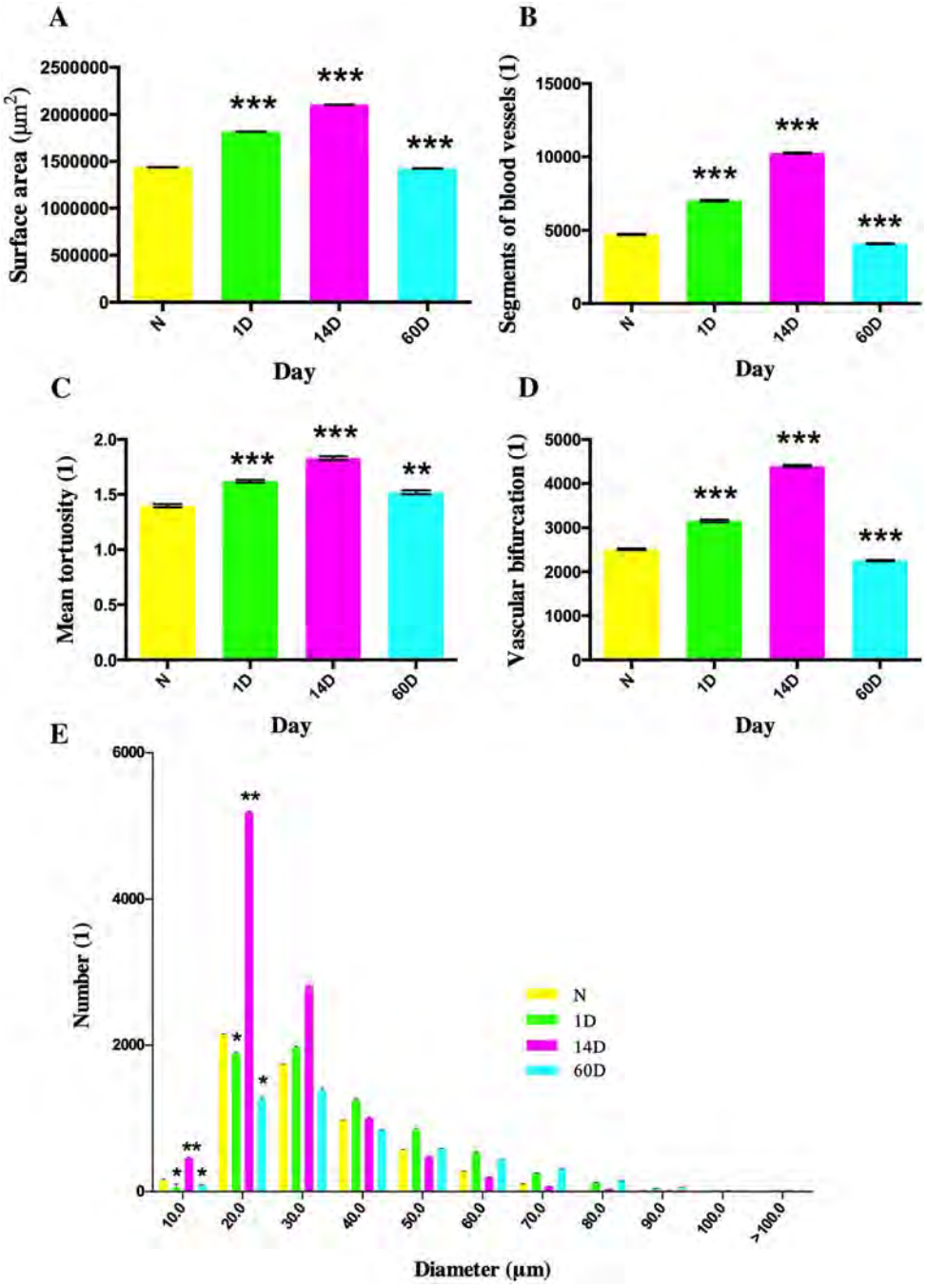

Fig. 5 Analysis of vascular changes in hippocampus following PILO-induced SE. **A–D** The change of hippocampal microvessels in surface area (**A**), number of hippocampal microvascular segments (**B**), mean tortuosity (**C**), and number of bifurcations (**D**) with the course of disease. **E** The frequency distribution of blood vessels of different diameters. $^{*}P < 0.05$, $^{**}P < 0.01$, $^{***}P < 0.001$ *vs* control group (N) at each time point; one-way analysis of variance followed by Tukey's *post-hoc* test.

obtain high-resolution images of rat brain vasculature and hippocampal microvasculature. No contrast-enhancing agents were added at any point in the process and therefore this method provides reliable depictions of microvessel configuration through a boundary-enhancement effect.

The 3D angioarchitecture reconstructed in this study demonstrated hippocampal microvascular remodeling alongside the progression of epilepsy. Such high resolution, 3D visualization facilitated further exploration of hippocampal microvascular angiogenesis, including the analysis of microvascular surface area, vascular tortuosity, and diameter distribution. The hippocampal microvasculature in rats suffering from lithium-PILO-induced epilepsy showed dramatic changes in overall organization. There is now a growing body of evidence that the density of blood vessels is increased in the sclerotic hippocampal regions of patients with TLE [23, 73]. Aside from this, it has been suggested that collagen-IV [23] and X-box binding protein 1 splicing [74] positively regulate cell proliferation and angiogenesis, pointing to possible molecular mechanisms

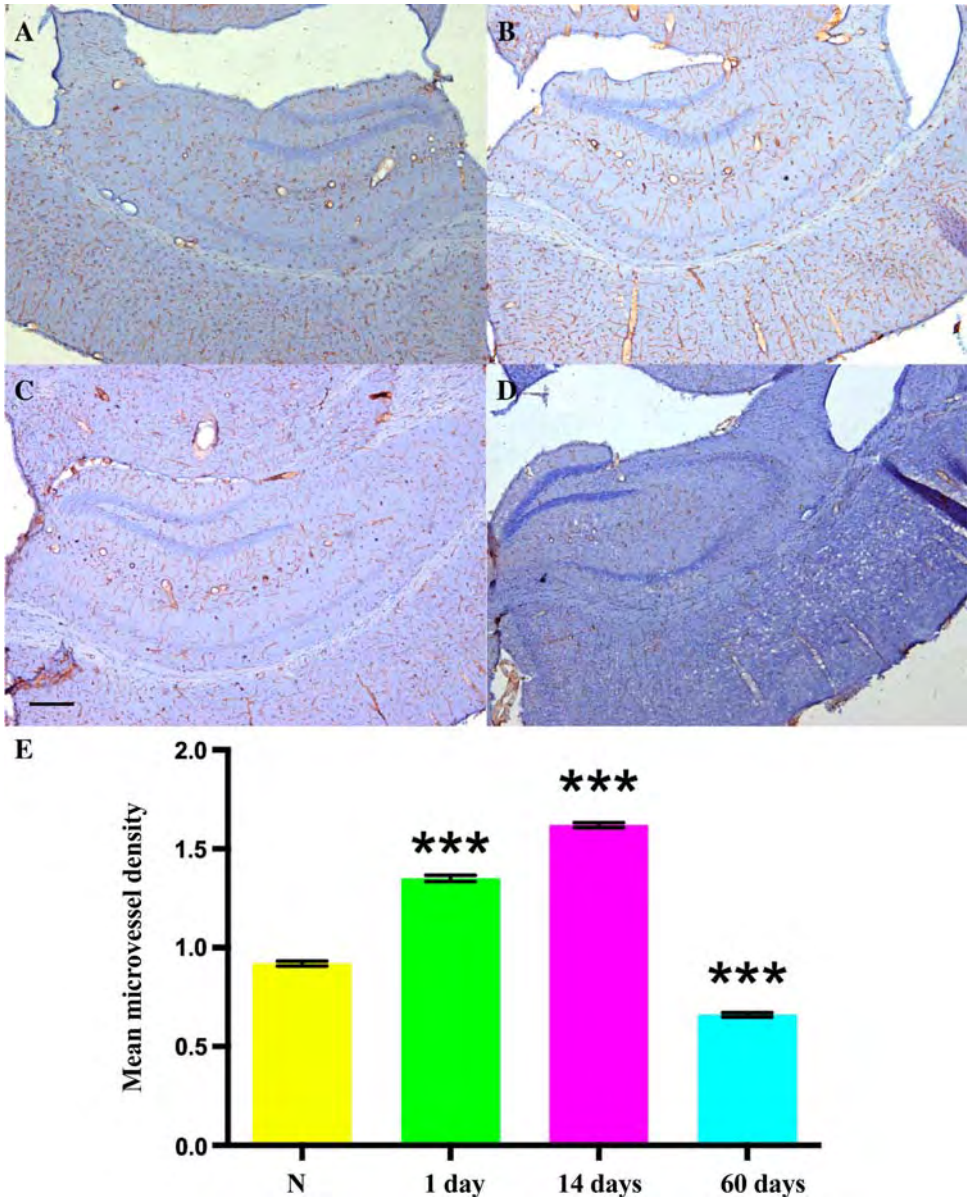

Fig. 6 Immunohistochemical staining of CD31 and quantitative analysis. **A**–**D** Representative images showing 5-fold magnification of histological staining for CD31 in the right hippocampus in the control (**A**), day 1 (**B**), day 14 (**C**), and day 60 (**D**) groups, revealing that the distribution of blood vessels in the hippocampus is not as rich as in cortex (scale bar, 200 μm). **E** Microvessel density in the hippocampal area (***$P < 0.001$ *vs* control (N)).

underlying hippocampal angiogenesis during epilepsy. In our study, the 3D images generated showed that the surface area of blood vessels, number of hippocampal microvascular segments, and number of bifurcations of hippocampal microvessels were higher in SE-induced rats on days 1 and 14. Research by Alonso-Nanclares *et al*. showed that these new blood vessels are actually atrophic vascular structures with reduced or even absent lumens, often filled with the processes of reactive astrocytes [55]. Furthermore, one study has shown that angiogenesis and microglial activation are linked to epilepsy-induced neuronal death in the cerebral cortex [75]. It has been suggested that the newly-formed microvasculature is soon filled with reactive astrocytes and atrophy sets at a later stage. The atrophy might in fact be triggered by the act of being filled with astrocytes.

Our results showed that, during the development of epilepsy, the angioarchitecture of the hippocampus undergoes some remodeling, and eventually, vessel constriction. Hippocampal vascularization and angiogenesis in SE may be facilitated by bone marrow-derived cells, which can penetrate through parenchyma and help to build new cerebral vasculature in a time-dependent manner [68].

Some studies have proposed that angiogenesis increases the permeability of the BBB, which may directly induce epilepsy [76, 77]. In such scenarios, hippocampal angiogenesis may be the result of an unfortunate positive feedback loop, providing a potential intervention point and

a treatment strategy for epilepsy. It has been reported that drugs targeting specific vascular endothelial growth factor (VEGF) receptor 2 pathways help to reduce epileptogenicity [77]. The progression of epilepsy can also be accelerated by inflammatory factors and neurotoxic amino-acids that pass through the injured BBB [78]. Therefore, a combination of drugs targeting angiogenesis, which also aid in clearing toxic cellular by-products, along with traditional anti-epileptic drugs may offer a new strategy for the treatment of epilepsy. Our findings provide visual evidence that can be used to test these hypotheses and also set in place methods to further study vascular changes in the brain.

The SR-ILPCI technique is a novel and reliable method for direct visualization of hippocampal microvascular networks during the progression of epilepsy. Despite its many advantages, there are still some limitations to the clinical application of this method. On the one hand, synchrotron radiation devices are excessively large, making the development of small-scale diagnostic instruments a challenge. On the other hand, SR-based ILPCI technology can currently only image small-volume samples due to the narrow light spot and high-resolution detectors, which also require small fields of view. Consequently, expanding the visual fields is an obstacle that needs to be overcome. Moreover, the radiation required for high-resolution imaging may damage biological tissues, even though efforts have been made to reduce the exposure time and radiation dose. Finally, the complete dehydration requirement for samples can potentially introduce small deformations, which is a common problem faced by any *ex vivo* 3D visualization of brain vasculature. The acceptable extent of deformation and feasibility of existing methods have been discussed in detail in our previous work [49]. In spite of these constraints, our data demonstrated that original morphological features are retained better using this method than with other invasive processes. In general, the method we used broadens the scope of study of cerebrovascular microstructural changes, and it does so better than existing technologies. While we still need to develop more accurate and efficient imaging technology in the future, we believe that SR-based techniques will provide a valuable platform to explore microvascular plasticity during epilepsy. This will ultimately help us understand the underlying pathogenic mechanisms of epilepsy in depth.

Conclusions

The 3D configuration of microvascular networks in the rat hippocampus under normal and seizure conditions was reconstructed using SR-based ILPCI and without any contrast-enhancing agents. This allowed microvessels to be distinguished at ultra-high resolution. Remodeling of focal brain microvasculature plays a vital role in the pathogenesis and development of epilepsy, and therefore SR-based ILPCI opens new avenues for the 3D imaging of brain vasculature and facilitates quantitative analysis of vascular networks in diverse pathologies. SR-based PCI holds considerable promise for the visualization of subtle structural details in microvessels, without the use of contrast-enhancing agents. Coupled with the further advancements in microtomography, future investigations using SR imaging will provide auxiliary diagnoses in neurovascular disorders and efficient evaluation of therapeutic strategies.

Acknowledgements This work was completed at the BL13W1 beamline of the Shanghai Synchrotron Radiation Facility (SSRF) in China and was supported by Key Research Project of the Ministry of Science and Technology of China (2016YFC0904400), the National Natural Science Foundation of China (81501025 & 81671299), the Natural Science Foundation of Hunan Province (2016JJ3174), and the Science and Technology Department Funds of Hunan Province Key Project (2016JC2057). We would like to thank Prof. Tiqiao Xiao and other staff at the BL13W1 station of SSRF for their kind assistance during the experiments.

References

1. Aronica E, Muhlebner A. Neuropathology of epilepsy. Handb Clin Neurol 2017, 145: 193–216.
2. Fisher RS, van Emde Boas W, Blume W, Elger C, Genton P, Lee P, *et al.* Epileptic seizures and epilepsy: definitions proposed by the International League Against Epilepsy (ILAE) and the International Bureau for Epilepsy (IBE). Epilepsia 2005, 46: 470–472.
3. Truccolo W, Donoghue JA, Hochberg LR, Eskandar EN, Madsen JR, Anderson WS, *et al.* Single-neuron dynamics in human focal epilepsy. Nat Neurosci 2011, 14: 635–641.
4. Schuele SU, Luders HO. Intractable epilepsy: management and therapeutic alternatives. Lancet Neurol 2008, 7: 514–524.
5. Semah F, Picot MC, Adam C, Broglin D, Arzimanoglou A, Bazin B, *et al.* Is the underlying cause of epilepsy a major prognostic factor for recurrence? Neurology 1998, 51: 1256–1262.
6. Xu XX, Luo JH. Mutations of N-methyl-D-aspartate receptor subunits in epilepsy. Neurosci Bull 2018, 34: 549–565.
7. Wei F, Yan LM, Su T, He N, Lin ZJ, Wang J, *et al.* Ion channel genes and epilepsy: functional alteration, pathogenic potential, and mechanism of epilepsy. Neurosci Bull 2017, 33: 455–477.
8. De Reuck J, Nagy E, Van Maele G. Seizures and epilepsy in patients with lacunar strokes. J Neurol Sci 2007, 263: 75–78.
9. Maxwell H, Hanby M, Parkes LM, Gibson LM, Coutinho C, Emsley HC. Prevalence and subtypes of radiological cerebrovascular disease in late-onset isolated seizures and epilepsy. Clin Neurol Neurosurg 2013, 115: 591–596.
10. Naik P, Cucullo L. *In vitro* blood-brain barrier models: current and perspective technologies. J Pharm Sci 2012, 101: 1337–1354.
11. Camidge DR, Pao W, Sequist LV. Acquired resistance to TKIs in solid tumours: learning from lung cancer. Nat Rev Clin Oncol 2014, 11: 473–481.
12. Morin-Brureau M, De Bock F, Lerner-Natoli M. Organotypic brain slices: a model to study the neurovascular unit microenvironment in epilepsies. Fluids Barriers CNS 2013, 10: 11.

13. Fischer S, Wobben M, Marti HH, Renz D, Schaper W. Hypoxia-induced hyperpermeability in brain microvessel endothelial cells involves VEGF-mediated changes in the expression of zonula occludens-1. Microvasc Res 2002, 63: 70–80.
14. Rochfort KD, Cummins PM. Cytokine-mediated dysregulation of zonula occludens-1 properties in human brain microvascular endothelium. Microvasc Res 2015, 100: 48–53.
15. Marchi N, Lerner-Natoli M. Cerebrovascular remodeling and epilepsy. Neuroscientist 2013, 19: 304–312.
16. Milesi S, Boussadia B, Plaud C, Catteau M, Rousset MC, De Bock F, *et al.* Redistribution of PDGFRbeta cells and NG2DsRed pericytes at the cerebrovasculature after status epilepticus. Neurobiol Dis 2014, 71: 151–158.
17. Klement W, Garbelli R, Zub E, Rossini L, Tassi L, Girard B, *et al.* Seizure progression and inflammatory mediators promote pericytosis and pericyte-microglia clustering at the cerebrovasculature. Neurobiol Dis 2018, 113: 70–81.
18. Gales JM, Prayson RA. Chronic inflammation in refractory hippocampal sclerosis-related temporal lobe epilepsy. Ann Diagn Pathol 2017, 30: 12–16.
19. Li Z, You Z, Li M, Pang L, Cheng J, Wang L. Protective effect of resveratrol on the brain in a rat model of epilepsy. Neurosci Bull 2017, 33: 273–280.
20. Ndode-Ekane XE, Hayward N, Grohn O, Pitkanen A. Vascular changes in epilepsy: functional consequences and association with network plasticity in pilocarpine-induced experimental epilepsy. Neuroscience 2010, 166: 312–332.
21. Nicoletti JN, Shah SK, McCloskey DP, Goodman JH, Elkady A, Atassi H, *et al.* Vascular endothelial growth factor is up-regulated after status epilepticus and protects against seizure-induced neuronal loss in hippocampus. Neuroscience 2008, 151: 232–241.
22. Xu Y, Zhang Y, Guo Z, Yin H, Zeng K, Wang L, *et al.* Increased placental growth factor in cerebrospinal fluid of patients with epilepsy. Neurochem Res 2012, 37: 665–670.
23. Rigau V, Morin M, Rousset MC, de Bock F, Lebrun A, Coubes P, *et al.* Angiogenesis is associated with blood-brain barrier permeability in temporal lobe epilepsy. Brain 2007, 130: 1942–1956.
24. Benini R, Roth R, Khoja Z, Avoli M, Wintermark P. Does angiogenesis play a role in the establishment of mesial temporal lobe epilepsy? Int J Dev Neurosci 2016, 49: 31–36.
25. van Vliet EA, Otte WM, Wadman WJ, Aronica E, Kooij G, de Vries HE, *et al.* Blood-brain barrier leakage after status epilepticus in rapamycin-treated rats II: Potential mechanisms. Epilepsia 2016, 57: 70–78.
26. Barnett A, Audrain S, McAndrews MP. Applications of resting-state functional MR imaging to epilepsy. Neuroimaging Clin N Am 2017, 27: 697–708.
27. Russo E, Leo A, Scicchitano F, Donato A, Ferlazzo E, Gasparini S, *et al.* Cerebral small vessel disease predisposes to temporal lobe epilepsy in spontaneously hypertensive rats. Brain Res Bull 2017, 130: 245–250.
28. Zhao W, Zhang J, Song Y, Sun L, Zheng M, Yin H, *et al.* Irreversible fatal contrast-induced encephalopathy: a case report. BMC Neurol 2019, 19: 46.
29. Sengupta S, Fritz FJ, Harms RL, Hildebrand S, Tse DHY, Poser BA, *et al.* High resolution anatomical and quantitative MRI of the entire human occipital lobe *ex vivo* at 9.4T. Neuroimage 2018, 168: 162–171.
30. Federau C, Gallichan D. Motion-correction enabled ultra-high resolution *in-vivo* 7T-MRI of the brain. PLoS One 2016, 11: e0154974.
31. Jung SC, Kim HS, Choi CG, Kim SJ, Lee DH, Suh DC, *et al.* Quantitative analysis using high-resolution 3T MRI in acute intracranial artery dissection. J Neuroimaging 2016, 26: 612–617.
32. Li P, Yu X, Griffin J, Levine JM, Jim J. High-resolution MRI of spinal cords by compressive sensing parallel imaging. Conf Proc IEEE Eng Med Biol Soc 2015, 2015: 4266–4269.
33. Zhang M, Peng G, Sun D, Xie Y, Xia J, Long H, *et al.* Synchrotron radiation imaging is a powerful tool to image brain microvasculature. Med Phys 2014, 41: 031907.
34. Schulz G, Weitkamp T, Zanette I, Pfeiffer F, Beckmann F, David C, *et al.* High-resolution tomographic imaging of a human cerebellum: comparison of absorption and grating-based phase contrast. J R Soc Interface 2010, 7: 1665–1676.
35. Lewis R. Medical applications of synchrotron radiation X-rays. Phys Med Biol 1997, 42: 1213–1243.
36. Eggl E, Schleede S, Bech M, Achterhold K, Loewen R, Ruth RD, *et al.* X-ray phase-contrast tomography with a compact laser-driven synchrotron source. Proc Natl Acad Sci U S A 2015, 112: 5567–5572.
37. Hoshino M, Uesugi K, Tsukube T, Yagi N. Quantitative and dynamic measurements of biological fresh samples with X-ray phase contrast tomography. J Synchrotron Radiat 2014, 21: 1347–1357.
38. Zhou SA, Brahme A. Development of phase-contrast X-ray imaging techniques and potential medical applications. Phys Med 2008, 24: 129–148.
39. Endrizzi M. X-ray phase-contrast imaging. Nucl Inst Methods Phys Res A 2018, 878: 88–98.
40. Snigirev A, Snigireva I, Lyubomirskiy M, Kohn V, Yunkin V, Kuznetsov S. X-ray multilens interferometer based on Si refractive lenses. Opt Express 2014, 22: 25842–25852.
41. Chapman D, Thomlinson W, Johnston RE, Washburn D, Pisano E, Gmur N, *et al.* Diffraction enhanced x-ray imaging. Phys Med Biol 1997, 42: 2015–2025.
42. Zhang X, Yang XR, Chen Y, Li HQ, Li RM, Yuan QX, *et al.* Visualising liver fibrosis by phase-contrast X-ray imaging in common bile duct ligated mice. Eur Radiol 2013, 23: 417–423.
43. Sztrokay A, Herzen J, Auweter SD, Liebhardt S, Mayr D, Willner M, *et al.* Assessment of grating-based X-ray phase-contrast CT for differentiation of invasive ductal carcinoma and ductal carcinoma *in situ* in an experimental *ex vivo* set-up. Eur Radiol 2013, 23: 381–387.
44. Lundstrom U, Larsson DH, Burvall A, Scott L, Westermark UK, Wilhelm M, *et al.* X-ray phase-contrast CO(2) angiography for sub-10 mum vessel imaging. Phys Med Biol 2012, 57: 7431–7441.
45. Bravin A, Coan P, Suortti P. X-ray phase-contrast imaging: from pre-clinical applications towards clinics. Phys Med Biol 2013, 58: R1–35.
46. Mayo SC, Stevenson AW, Wilkins SW. In-line phase-contrast X-ray imaging and tomography for materials science. Materials (Basel) 2012, 5: 937–965.
47. Debatin JF, Spritzer CE, Grist TM, Beam C, Svetkey LP, Newman GE, *et al.* Imaging of the renal arteries: value of MR angiography. AJR Am J Roentgenol 1991, 157: 981–990.
48. Cao Y, Liao S, Zeng H, Ni S, Tintani F, Hao Y, *et al.* 3D characterization of morphological changes in the intervertebral disc and endplate during aging: A propagation phase contrast synchrotron micro-tomography study. Sci Rep 2017, 7: 43094.
49. Zhang MQ, Zhou L, Deng QF, Xie YY, Xiao TQ, Cao YZ, *et al.* Ultra-high-resolution 3D digitalized imaging of the cerebral angioarchitecture in rats using synchrotron radiation. Sci Rep 2015, 5: 14982.
50. Zhang MQ, Sun DN, Xie YY, Peng GY, Xia J, Long HY, *et al.* Three-dimensional visualization of rat brain microvasculature following permanent focal ischaemia by synchrotron radiation. Br J Radiol 2014, 87: 20130670.
51. Li B, Zhang Y, Wu W, Du G, Cai L, Shi H, *et al.* Neovascularization of hepatocellular carcinoma in a nude mouse orthotopic

liver cancer model: a morphological study using X-ray in-line phase-contrast imaging. BMC Cancer 2017, 17: 73.
52. Hu J, Li P, Yin X, Wu T, Cao Y, Yang Z, *et al.* Nondestructive imaging of the internal microstructure of vessels and nerve fibers in rat spinal cord using phase-contrast synchrotron radiation microtomography. J Synchrotron Radiat 2017, 24: 482–489.
53. Fratini M, Bukreeva I, Campi G, Brun F, Tromba G, Modregger P, *et al.* Simultaneous submicrometric 3D imaging of the micro-vascular network and the neuronal system in a mouse spinal cord. Sci Rep 2015, 5: 8514.
54. Studer F, Serduc R, Pouyatos B, Chabrol T, Brauer-Krisch E, Donzelli M, *et al.* Synchrotron X-ray microbeams: A promising tool for drug-resistant epilepsy treatment. Phys Med 2015, 31: 607–614.
55. Pouyatos B, Nemoz C, Chabrol T, Potez M, Brauer E, Renaud L, *et al.* Synchrotron X-ray microtransections: a non invasive approach for epileptic seizures arising from eloquent cortical areas. Sci Rep 2016, 6: 27250.
56. Pacile S, Baran P, Dullin C, Dimmock M, Lockie D, Missbach-Guntner J, *et al.* Advantages of breast cancer visualization and characterization using synchrotron radiation phase-contrast tomography. J Synchrotron Radiat 2018, 25(Pt 5): 1460–1466.
57. Tavakoli Taba S, Baran P, Lewis S, Heard R, Pacile S, Nesterets YI, *et al.* Toward improving breast cancer imaging: radiological assessment of propagation-based phase-contrast CT technology. Acad Radiol 2019, 26: e79–e89.
58. Honchar MP, Olney JW, Sherman WR. Systemic cholinergic agents induce seizures and brain damage in lithium-treated rats. Science 1983, 220: 323–325.
59. Eslami SM, Ghasemi M, Bahremand T, Momeny M, Gholami M, Sharifzadeh M, *et al.* Involvement of nitrergic system in anticonvulsant effect of zolpidem in lithium-pilocarpine induced status epilepticus: Evaluation of iNOS and COX-2 genes expression. Eur J Pharmacol 2017, 815: 454–461.
60. Racine RJ. Modification of seizure activity by electrical stimulation. II. Motor seizure. Electroencephalogr Clin Neurophysiol 1972, 32: 281–294.
61. Wu T, Ido K, Osada Y, Kotani S, Tamaoka A, Hanada T. The neuroprotective effect of perampanel in lithium-pilocarpine rat seizure model. Epilepsy Res 2017, 137: 152–158.
62. Wu Q, Li Y, Shu Y, Feng L, Zhou L, Yue ZW, *et al.* NDEL1 was decreased in the CA3 region but increased in the hippocampal blood vessel network during the spontaneous seizure period after pilocarpine-induced status epilepticus. Neuroscience 2014, 268: 276–283.
63. Chen RC, Dreossi D, Mancini L, Menk R, Rigon L, Xiao TQ, *et al.* PITRE: software for phase-sensitive X-ray image processing and tomography reconstruction. J Synchrotron Radiat 2012, 19: 836–845.
64. Luo Y, Yin X, Shi S, Ren X, Zhang H, Wang Z, *et al.* Non-destructive 3D microtomography of cerebral angioarchitecture changes following ischemic stroke in rats using synchrotron radiation. Front Neuroanat 2019, 13: 5.
65. Yang G, Kitslaar P, Frenay M, Broersen A, Boogers MJ, Bax JJ, *et al.* Automatic centerline extraction of coronary arteries in coronary computed tomographic angiography. Int J Cardiovasc Imaging 2012, 28: 921–933.
66. Chatzikonstantinou A. Epilepsy and the hippocampus. Front Neurol Neurosci 2014, 34: 121–142.
67. Romariz SA, Garcia Kde O, Paiva Dde S, Bittencourt S, Covolan L, Mello LE, *et al.* Participation of bone marrow-derived cells in hippocampal vascularization after status epilepticus. Seizure 2014, 23: 386–389.
68. Yamamoto H, Iku S, Adachi Y, Imsumran A, Taniguchi H, Nosho K, *et al.* Association of trypsin expression with tumour progression and matrilysin expression in human colorectal cancer. J Pathol 2003, 199: 176–184.
69. Hu JZ, Wu TD, Zeng L, Liu HQ, He Y, Du GH, *et al.* Visualization of microvasculature by x-ray in-line phase contrast imaging in rat spinal cord. Phys Med Biol 2012, 57: N55–63.
70. Figueiredo G, Brockmann C, Boll H, Heilmann M, Schambach SJ, Fiebig T, *et al.* Comparison of digital subtraction angiography, micro-computed tomography angiography and magnetic resonance angiography in the assessment of the cerebrovascular system in live mice. Clin Neuroradiol 2012, 22: 21–28.
71. Liu X, Zhao J, Sun J, Gu X, Xiao T, Liu P, *et al.* Lung cancer and angiogenesis imaging using synchrotron radiation. Phys Med Biol 2010, 55: 2399–2409.
72. Margaritondo G, Meuli R. Synchrotron radiation in radiology: novel X-ray sources. Eur Radiol 2003, 13: 2633–2641.
73. Alonso-Nanclares L, DeFelipe J. Alterations of the microvascular network in the sclerotic hippocampus of patients with temporal lobe epilepsy. Epilepsy Behav 2014, 38: 48–52.
74. Shi S, Tang M, Li H, Ding H, Lu Y, Gao L, *et al.* X-box binding protein 1 splicing attenuates brain microvascular endothelial cell damage induced by oxygen-glucose deprivation through the activation of phosphoinositide 3-kinase/protein kinase B, extracellular signal-regulated kinases, and hypoxia-inducible factor-1alpha/vascular endothelial growth factor signaling pathways. J Cell Physiol 2019, 234: 9316–9327.
75. Sakurai M, Morita T, Takeuchi T, Shimada A. Relationship of angiogenesis and microglial activation to seizure-induced neuronal death in the cerebral cortex of Shetland Sheepdogs with familial epilepsy. Am J Vet Res 2013, 74: 763–770.
76. Myczek K, Yeung ST, Castello N, Baglietto-Vargas D, LaFerla FM. Hippocampal adaptive response following extensive neuronal loss in an inducible transgenic mouse model. PLoS One 2014, 9: e106009.
77. Morin-Brureau M, Rigau V, Lerner-Natoli M. Why and how to target angiogenesis in focal epilepsies. Epilepsia 2012, 53 Suppl 6: 64–68.
78. Winkler EA, Bell RD, Zlokovic BV. Central nervous system pericytes in health and disease. Nat Neurosci 2011, 14: 1398–1405.

Neurosci. Bull. April, 2020, 36(4):346–358
https://doi.org/10.1007/s12264-019-00459-5

www.neurosci.cn
www.springer.com/12264

ORIGINAL ARTICLE

Thioredoxin-Interacting Protein (TXNIP) Regulates Parkin/PINK1-mediated Mitophagy in Dopaminergic Neurons Under High-glucose Conditions: Implications for Molecular Links Between Parkinson's Disease and Diabetes

Cun-Jin Su[1,2] · Zhu Shen[1] · Ru-Xiao Cui[2] · Ya Huang[2] · De-Lai Xu[1] · Feng-Lun Zhao[1] · Jie Pan[1] · Ai-Ming Shi[1] · Tong Liu[2] · Yun-Li Yu[3]

Received: 28 March 2019 / Accepted: 6 December 2019 / Published online: 14 January 2020

Abstract Patients with diabetes mellitus have a higher risk of developing Parkinson's disease (PD). However, the molecular links between PD and diabetes remain unclear. In this study, we investigated the roles of thioredoxin-interacting protein (TXNIP) in Parkin/PINK1-mediated mitophagy in dopaminergic (DA) cells under high-glucose (HG) conditions. In streptozotocin-induced diabetic mice, TXNIP was upregulated and autophagy was inhibited in the midbrain, while the loss of DA neurons was accelerated by hyperglycemia. In cultured PC12 cells under HG, TXNIP expression was upregulated and the intracellular reactive oxygen species (ROS) levels increased, leading to cell death. Autophagic flux was further blocked and PINK1 expression was decreased under HG conditions. Parkin expression in the mitochondrial fraction and carbonyl cyanide 3-chlorophenylhydrazone (CCCP)-induced co-localization of COX IV (marker for mitochondria) and LAMP1 (marker for lysosomes) were also significantly decreased by HG. Overexpression of TXNIP was sufficient to decrease the expression of both PINK1 and Parkin in PC12 cells, while knockdown of the expression of TXNIP by siRNA decreased intracellular ROS and attenuated cellular injury under HG. Moreover, inhibition of TXNIP improved the CCCP-induced co-localization of COX IV and LAMP1 in PC12 cells under HG. Together, these results suggest that TXNIP regulates Parkin/PINK1-mediated mitophagy under HG conditions, and targeting TXNIP may be a promising therapeutic strategy for reducing the risk of PD under hyperglycemic conditions.

Keywords Diabetes mellitus · Parkinson's disease · High glucose · TXNIP · Mitophagy · PC12 cells

Introduction

Diabetes mellitus is primarily characterized by hyperglycemia, which leads to secondary pathological changes in multiple organs, especially the central nervous system [1, 2]. Patients with type-2 diabetes mellitus have a higher risk of developing Parkinson's disease (PD) [3]. Hyperglycemia induces the overproduction of reactive oxygen species (ROS) [4] and the resulting oxidative stress is a core mechanism in diabetic complications [5]. However, the mechanism underlying the neuronal injury induced by hyperglycemia is not clear.

Thioredoxin-interacting protein (TXNIP) is the endogenous inhibitor protein for ROS elimination. Overexpression of TXNIP causes oxidative stress and promotes apoptosis [6]. TXNIP is upregulated under high-glucose (HG) conditions in several cell-types, such as endothelial and renal tubular cells [7, 8], and the overexpression of TXNIP results in the loss of dopaminergic (DA) neurons [9]. However, the effect of HG conditions on TXNIP in neurons has rarely been reported.

Cun-Jin Su and Zhu Shen have contributed equally to this work.

✉ Tong Liu
liutong80@suda.edu.cn

✉ Yun-Li Yu
haoyyl0902@163.com

[1] Department of Pharmacy, The Second Affiliated Hospital of Soochow University, Suzhou 215004, China

[2] Institute of Neuroscience, Soochow University, Suzhou 215004, China

[3] Department of Clinical Pharmacology, The Second Affiliated Hospital of Soochow University, Suzhou 215004, China

Mitochondrial dysfunction, which disturbs energy metabolism and depletes ATP, has been implicated in the pathogenesis of PD [10, 11]. Normally, the damage to mitochondria caused by exposure to mitochondrial toxins, environmental pesticides, or other forms of mitochondrial stress associated with the pathogenesis of PD, is mainly removed *via* the macroautophagy pathway (mitophagy) [12, 13]. Mitophagy is important for maintaining mitochondrial quality by coordinating mitochondrial dynamics, biogenesis, fission, and fusion. In mammals, there are both Parkin-dependent and Parkin-independent pathways of mitophagy [14, 15]. Here, we focused on Parkin-dependent mitophagy. A decrease in mitochondrial membrane potential caused by damage leads to the stabilization of PTEN-induced kinase 1 (PINK1) on the outer mitochondrial membrane. Then PINK1 phosphorylates ubiquitin, activating Parkin's E3 ubiquitin ligase, leading to the recruitment of Parkin to the impaired mitochondria. Subsequently, activated Parkin polyubiquitinates mitochondrial outer membrane proteins, leading to their association with the ubiquitin-binding domains of autophagy receptors and the formation of autophagosomes. Next, the autophagosomes fuse with lysosomes to form autolysosomes, leading to degradation of the damaged mitochondria [16, 17]. Dysfunctional mitophagy is closely linked to PD. Mutations of Parkin and PINK1 lead to an autosomal recessive form of PD [18, 19]. Mitophagy is disturbed in diabetic nephropathy under hyperglycemic conditions [20]. However, the effect of HG on mitophagy in neurons has rarely been reported. This study was designed to investigate the relationship between TXNIP and mitophagy in DA neurons under HG conditions.

Materials and Methods

Reagents and Antibodies

The reagents/antibodies used were: Dulbecco's modified Eagle's medium (DMEM; Hyclone, Logan, UT), fetal bovine serum (FBS, BI, Israel), 6-OHDA (6-hydroxydopamine) and glucose (Aladdin, Shanghai, China), Parkin, LC3, and p62 antibodies (Cell Signaling Technology, Danvers, MA), tyrosine hydroxylase (TH; Millipore, Waltham, MA), PINK1 and TXNIP (Abcam, Cambridge, MA), GAPDH, goat anti-rabbit, and goat anti-mouse IgG horseradish peroxidase (HRP)-conjugated secondary antibodies (Santa Cruz, Dallas, TX), and dihydroethidium (DHE, Sigma, St Louis, MO).

Induction of Experimental Diabetes and PD models

C57BL/6 mice (23 g–25 g) were purchased from SLAC Laboratory Animal Co., Ltd. (Shanghai, China). All procedures involving animals were approved by the Committee on Animal Care of Soochow University and were conducted in accordance with the Guidelines for Animal Use and Care of the National Institutes of Health. The mice were fasted for 12 h before streptozotocin (STZ) injection. A single intraperitoneal injection of STZ (100 mg/kg; Sigma) dissolved in citrate buffer (0.1 mol/L, pH 4.2) was administered. Control animals were injected with vehicle only. The development of diabetes was confirmed by measuring the fasting plasma glucose concentration (>16.7 mmol/L). Seven days later, the mice were randomly assigned into saline-treated, STZ-treated, MPTP (1-methyl-4-phenyl-1,2,3,6-tetrahydropyridine)-treated, and MPTP + STZ-treated groups. The mice in the latter two groups received 20 mg/kg MPTP and 250 mg/kg probenecid daily for 5 days to generate the PD model.

Behavioral Test

The mice performed the "pole test" to assess motor coordination 1 day prior to MPTP injection and on days 1, 3, 5 and 12 after injection. Mice were trained for 3 days before MPTP injection. The pole test consisted of a gauze-taped pole (50 cm high, 1 cm diameter) with a small cork ball at the top. Mice were placed with their head facing upwards immediately below the ball. The time to turn (T-turn) and the time to the floor (T-total) were recorded. The test was performed 3 times at 10-min intervals, and the average time was recorded.

Detection of ROS *In Vivo*

Based on a previous publication [21], we used DHE to investigate the *in situ* production of ROS. DHE (200 μg in 200 μL saline) was injected *via* tail vein in anesthetized mice. Three hours after DHE injection, the mice were transcardially perfused with fixative (4% paraformaldehyde, 0.1% glutaraldehyde, and 15% picric acid in PBS). Brains were removed and postfixed overnight in 4% paraformaldehyde. To observe ROS in SNc dopaminergic cells, sections were incubated overnight with TH antibody (1:800; Millipore). Sections were incubated with the fluorescent secondary antibody (anti-rabbit IgG Alexa fluor 488, 1:500; Cell Signaling Technology) to visualize TH-positive cells. The images of DHE and TH fluorescence were recorded by fluorescence 275 microscopy (Axio Scope A1, Zeiss, Jena, Germany).

Immunohistochemistry

After fixation, brain samples were postfixed in 4% paraformaldehyde at 4°C overnight and then transferred to 15% and 30% sucrose in PBS for 2 days. The samples were sectioned at 30 μm. Briefly, the sections were permeabilized in PBST (PBS containing 0.3% Triton X-100) for 1 h and blocked with 5% BSA in PBS for 1 h at room temperature. Then, they were incubated with primary antibody (anti-TH, 1:800; Millipore) at 4°C overnight and the appropriate anti-rabbit secondary antibody for 1 h at room temperature. Immunostaining was visualized by immersion in DAB (3,3′-diaminobenzidine) solution for 10 min. For quantification in *in vivo* studies, the numbers of TH-positive cells in the substantia nigra pars compacta (SNc) were assessed using an optical fractionator (Stereo Investigator 7, MBF Bioscience, Williston, VT). This method has been described in a previous publication [22]. Briefly, the region of the SNc in midbrain sections was outlined at low magnification (40×). The counting frame size was 50 μm × 50 μm and the sampling grid size was 100 μm × 100 μm. All stereological analyses were performed at 200× magnification under an Olympus BX52 microscope (Olympus America Inc., Melville, NY).

Dopamine and DOPAC Determination in the Striatum

Dopamine and its metabolite dihydroxyphenylacetic acid (DOPAC) in mouse striatum were determined using liquid chromatography with tandem mass spectrometry (LC-MS/MS). Dissected striatal tissue was homogenized in ice-cold 70% acetonitrile (10 μL/mg tissue) and centrifuged at 20,000 rpm for 25 min. Then, the supernatant was injected into the LC-MS/MS. Sample separations were carried out at 25°C on a C18 column (Hypersil GOLD C18, 100×2.1 mm, 3 μm, Thermo Scientific, Waltham, MA). The mobile phase was a mixture of 5 mmol/L ammonium formate in MilliQ water (30%) and 0.1% formic acid in acetonitrile (70%). The flow rate was 0.3 mL/min. The MS detection system consisted of Q-Exactive (Thermo Savant, Waltham, MA) with electrospray ionization (ESI) in positive ion mode for dopamine, and negative ion mode for DOPAC.

Cell Culture

PC12 cells were cultured in DMEM supplemented with 10% FBS. Cells were cultured as a monolayer under 5% CO_2 in a humidified incubator at 37°C.

Assay of MTT Conversion

The PC12 cells were seeded into 96-well plates at 10^4 cells/well in 200 μL culture medium. PC12 cells were exposed to 50 mmol/L glucose for 24 h followed by 100 mmol/L 6-OHDA for another 24 h. After treatment, the medium was replaced with 200 μL DMEM containing 0.5 mg/mL MTT and incubated at 37°C for 4 h. Afterwards, the supernatant was aspirated and the cells were lysed in 200 μL dimethylsulfoxide for 20 min at 37°C. The optical density values were measured at 490 nm using a plate reader. The values are presented as fold of the control group.

Quantitative Real-time Polymerase Chain Reaction (PCR)

Total RNA was extracted using TRIzol reagent (Invitrogen, Carlsbad, CA) according to the protocol supplied by the manufacturer. Reverse transcription of 0.5 μg total RNA for synthesizing cDNA was performed using the RevertAid First Strand cDNA Synthesis Kit (Thermo Fisher Scientific, Waltham, MA). Real-time PCR was conducted using SYBR Green PCR Master Mix (Selleck, Shanghai, China) on an Opticon real-time PCR Detection System (7500; Applied Biosystems, Grand Island, NY). Relative fold differences in expression were calculated using the 2(-Delta Delta C(t)) method after normalization to GAPDH expression. The following primers for mouse were synthesized by Genewiz (Suzhou, China): GAPDH forward: 5′-CAAGTTCAACGGCACAGTCA-3′; reverse: 5′-CACCC-CATTTGATGTTAGCG-3′; PINK1 forward: 5′-GGTGT CAGGCTGGGGCAA-3′; reverse: 5′-TGGCTTCATACA-CAGCGGC-3′.

Plasmids and Transfection

The plasmids expressing TXNIP and TXNIP siRNA were from Gene Pharma (Suzhou, China). PC12 cells were cultured in 6-well plates (5×10^5 cells/well). PC12 cells at 70%–80% confluence were transfected with TXNIP cDNA (2 μg) using Lipofectamine 3000 for 48 h. To inhibit TXNIP expression, TXNIP siRNA (5′-CAU CCU UCG AGU UGA AUA UTT-3′) or negative control siRNA (120 pmol per 6-well plate) was transfected using Lipofectamine 3000. The cells were transfected with siRNAs for 48 h.

Mitochondrial Fraction

Cells cultured in 10-cm dishes were suspended in 5 mL cytosol buffer, and lysed by passage through a 25-gauge needle 20 times. Then, the buffer was centrifuged at 13,000 rpm for 10 min at 4°C. Then, the supernatant was

centrifuged at 80,000 rpm for 15 min at 4°C. The pellet, corresponding to the mitochondrial fraction, was lysed in ice-cold NP-40 lysis buffer on ice for 30 min, then centrifuged at 13,000×g for 20 min. Formulation of cytosol buffer (in mmol/L): 20 HEPES, 10 KCl, 1.5 $MgCl_2$, 1 EDTA, 1 EGTA, and 1 dithiothreitol. Formulation of NP-40 lysis buffer: 50 mmol/L Tris-HCl (pH 7.5), 150 mmol/L NaCl, 1% Nonidet P-40, 0.5% sodium deoxycholate, 0.1% sodium dodecyl sulfate, and 1 mmol/L dithiothreitol. Finally, protease inhibitor reagent (Selleck, China) was added to each buffer before use.

Western Blot Analysis

The cells were washed thrice with ice-cold PBS and lysed in RIPA containing phenylmethylsulfonyl fluoride on ice for 30 min. Meanwhile, brain tissues were homogenized in RIPA (10 μL/mg tissue) by a homogenizer for 30 s, and lysed on ice for 30 min. The samples were centrifuged for 25 min at 12,000 rpm at 4°C, and the supernatants were collected. The protein (60 μg for each extract) was resolved by 10% SDS-PAGE, electroblotted to PVDF membrane, and blocked in 5% non-fat milk at room temperature. The membranes were incubated with primary antibodies overnight at 4°C, then washed with TBST and probed with HRP-conjugated anti-rabbit or anti-goat IgG.

Measurement of Intracellular ROS

The intracellular ROS were measured using the fluorescent marker 2,7-dichlorodihydrofluorescein diacetate (H2DCFDA) (Sigma-Aldrich, St Louis, MO) according to the manufacturer's instructions. The medium was replaced with 1 mL H2DCFDA (25 μmol/L) and the cells were incubated at 37°C for 30 min. Then, the cells were washed thrice with cold PBS and suspended in 500 μL PBS for flow cytometry (FC500; Beckman Coulter, Brea, CA).

Immunofluorescence

Cells were fixed in ice-cold methanol for 15 min at –20°C, followed by 3×5 min washes in PBS. Then, they were fixed in 4% paraformaldehyde for 15 min at room temperature (RT) and permeabilized in 0.3% Triton-X for 30 min at RT. Blocking was carried out for 1 h at RT in 5% BSA-PBST. The cells were incubated in goat anti-mouse cytochrome c oxidase IV (COX IV, 1:200; Cell Signaling Technology) and goat anti-rabbit LAMP1 (1:400; Abcam) for 18 h at 4°C. Secondary antibodies were incubated for 1 h at RT. The images were recorded by fluorescence microscopy (Axio Scope A1, Zeiss, Jena, Germany).

Statistical Analysis

Data are presented as the mean ± SEM. Statistical comparisons were conducted using one-way ANOVA and Student's *t* test in SPSS 16.0 (SPSS Inc., Chicago, IL). $P < 0.05$ was considered to be statistically significant.

Results

TXNIP is Increased in the Brains of Diabetic Mice

Seven days after STZ injection, blood glucose was determined after fasting overnight and was significantly higher in the STZ-treated mice than in the control mice (22.9 ± 1.8 mmol/L in STZ-treated mice *versus* 8.2 ± 0.5 mmol/L in controls). DHE was used to measure the ROS production in TH cells *in vivo*. Three hours after DHE injection, the number of red fluorescent puncta in TH neurons was significantly higher in diabetic mice than in controls (8 ± 2.3 puncta per cell in diabetic mice *vs* 3.7 ± 1.1 puncta per cell in controls; Fig. 1A). TXNIP is a key regulator of intracellular ROS production, so we determined the TXNIP levels in the striatum and midbrain by Western blot analysis. TXNIP was significantly increased by 3-fold in the midbrain and 2.5-fold in the striatum ($P = 0.019$ in midbrain, $P = 0.024$ in striatum; Fig. 1B).

Autophagy is Inhibited in the Midbrain of Diabetic Mice

We then explored the change in autophagy in the midbrain of diabetic mice. LC3-II, a marker of autophagosomes, was increased by ~1.7-fold ($P = 0.04$), and p62, a substrate of autophagy, was also increased ($P = 0.03$) (Fig. 1C). It has been reported that dysfunctional mitochondria are mainly eliminated *via* the PINK1–Parkin-mediated autophagic pathway [14]. We found that PINK1 was decreased by 50% in the midbrain of diabetic mice compared with controls ($P = 0.04$; Fig. 1D). However, Parkin did not change in diabetic mice. These results indicated that autophagic flux is blocked in the midbrain of diabetic mice.

MPTP-induced Loss of TH^+ Neurons is Accelerated in Diabetic Mice

Seven days after STZ administration, the mice were intraperitoneally injected with MPTP daily for 5 days to create the PD model. The DA neurons in the SNc and ventral tegmental area were stained with TH antibody (Fig. 2A). MPTP injection induced a 41% loss of TH-positive cells in the SNc in normal mice ($P = 0.002$, *vs* controls), and a 57% loss in diabetic mice ($P = 0.020$ *vs*

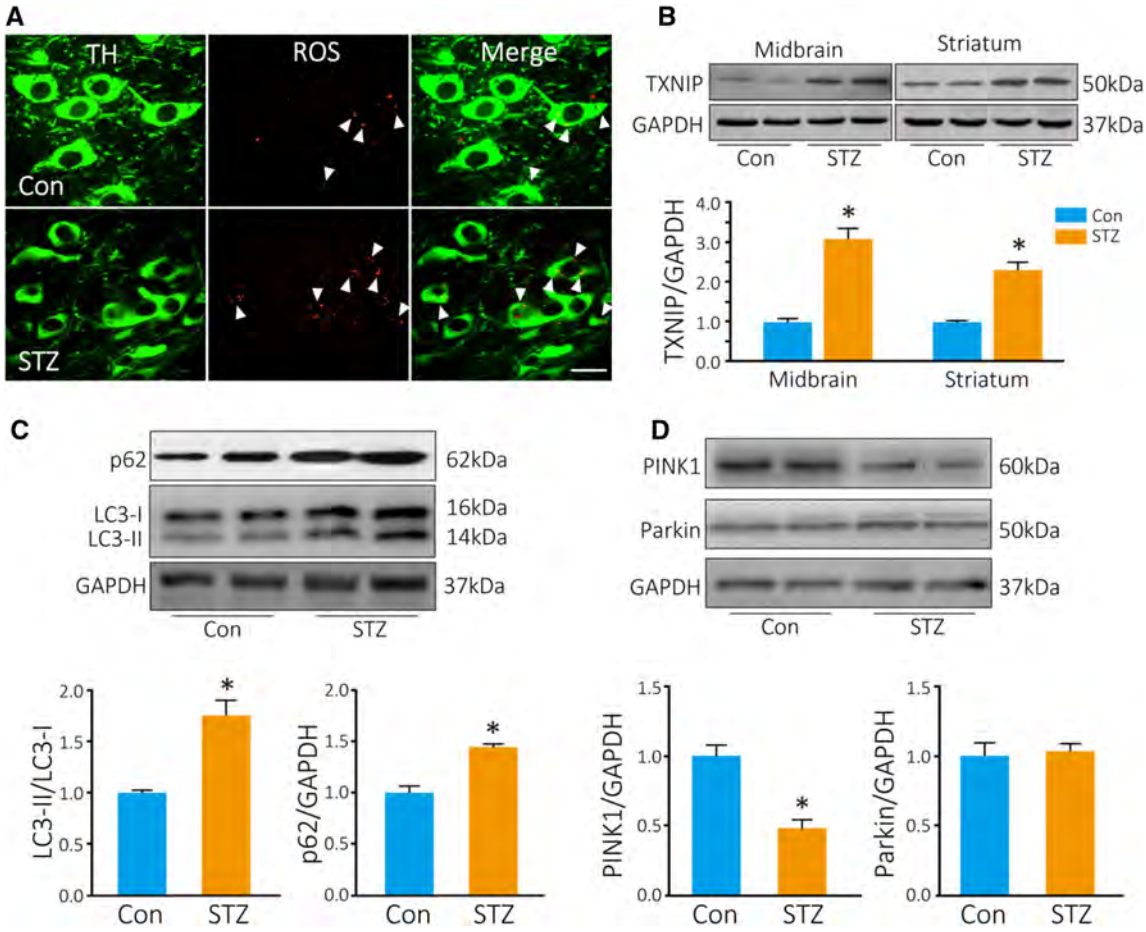

Fig. 1 ROS and TXNIP are increased in TH^+ neurons in diabetic mice. **A** Photomicrographs of *in situ* ROS as assessed by DHE (red, arrowheads); dopaminergic neurons are stained by TH antibody (green). **B** Western blots and analysis of TXNIP. Autophagy is inhibited in the midbrain of diabetic mice. **C**, **D** Western blots and analyses of LC3, p62, PINK1, and Parkin in diabetic (STZ) and control (Con) mice ($^*P < 0.05$ *vs* controls; $n = 4$; scale bar, 20 μm).

MPTP-injected mice; Fig. 2A). No difference was found in TH expression in the midbrain between the control and diabetic mice before MPTP injection (Fig. 2B). However, TH was decreased by ~68% in diabetic mice ($P = 0.003$), whereas it was only decreased by 55% in normal mice after MPTP injection ($P = 0.001$) (Fig. 2B). TH in the dorsal striatum can be used to evaluate the nigrostriatal DA pathway. The TH-positive fiber density in the dorsal striatum decreased after MPTP injection both in normal and diabetic mice ($P = 0.031$; Fig. 2C). In addition, DA decreased to 0.38 ± 0.07 μg/g tissue in diabetic mice after MPTP injection, while it only decreased to 0.48 ± 0.08 μg/g tissue in normal mice after MPTP injection (Fig. 2D). Similarly, DOPAC, a metabolite of DA, also showed a further decline in diabetic mice compared to normal mice after MPTP injection ($P = 0.013$; Fig. 2D). In addition, we used the pole test to assess the motor activity, and to determine whether the MPTP-induced PD model displayed bradykinesia. The T-total increased on days 1, 3, and 5 after MPTP injection (Fig. 2E). Meanwhile, STZ further aggravated the MPTP-induced bradykinesia on days 1, 3, and 5 after MPTP injection ($P < 0.05$; Fig. 2E). These results suggest that DA neurons are more vulnerable to damage under the hyperglycemic conditions in diabetes.

Effect of HG on PC12 Cell Viability

The MTT assay was used to measure the effect of HG on neuronal cell death. PC12 cells were treated with various concentrations of glucose from 5 to 500 mmol/L for 48 h. HG significantly decreased the viability of PC12 cells compared with controls (Fig. 3A), and the IC_{50} was 75.06 mmol/L (Fig. 3B). Glucose at 50 mmol/L was selected for HG treatment, and 5 mmol/L for the control in further studies. In addition, HG/6-OHDA co-treatment further increased the death of PC12 cells compared with those exposed to 6-OHDA alone ($P < 0.001$; Fig. 3C). These data suggest that DA neurons are damaged under HG conditions. Moreover, HG may be a risk factor in the pathological conditions of PD.

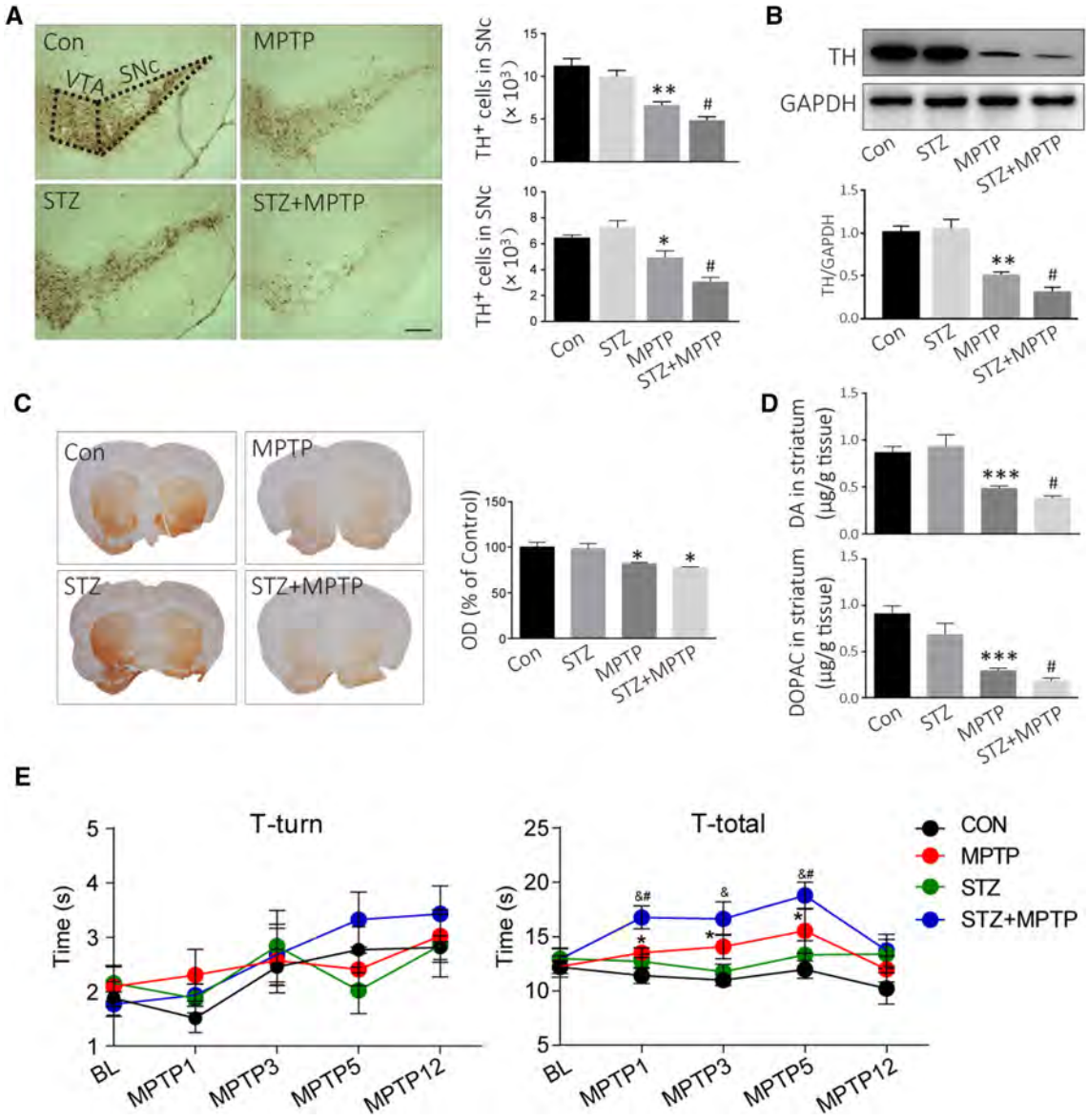

Fig. 2 Hyperglycemia accelerates the loss of TH^+ neurons induced by MPTP, and aggravates MPTP-induced bradykinesia. **A** Representative images and analyses for DA neurons assessed by TH immunohistochemistry (scale bar, 200 μm). **B** Western blots and analysis for TH expression in the midbrain. **C** TH-positive fibers in the dorsal striatum assessed by TH immunohistochemistry. **D** DA and DOPAC in the striatum analyzed using LC-MS/MS. **E** Motor activity as assessed by the pole test. $^{***}P < 0.001$, $^{**}P < 0.01$, $^{*}P < 0.05$ *vs* controls; $^{\#}P < 0.05$ *vs* MPTP-treated mice; $n = 4$; $^{\&}P < 0.05$ *vs* STZ-treated mice; $n = 6$–8 for the pole test.

TXNIP is Upregulated in PC12 Cells after HG Treatment

We used H2DCFDA to assess the intracellular ROS and found that, it was significantly increased by 1.5-fold in HG-treated PC12 cells compared with controls ($P = 0.006$; Fig. 4A, B). While several studies have reported that TXNIP is induced by HG treatment, the effect of HG on TXNIP expression in neurons was not clear. To determine the expression of TXNIP, we performed Western blot experiments using PC12 cells incubated at low (5 mmol/L) or high (100 mmol/L) glucose concentrations for 6, 12, and 24 h. We found that HG significantly increased TXNIP expression by 1.8-fold at 24 h compared with controls ($P = 0.006$; Fig. 4D). This finding indicates that TXNIP is involved in the injury of PC12 cells induced by HG treatment.

HG Results in Autophagy Dysfunction

We next explored the effect of HG on autophagy. The results showed that LC3-II was increased by ~3.5-fold in

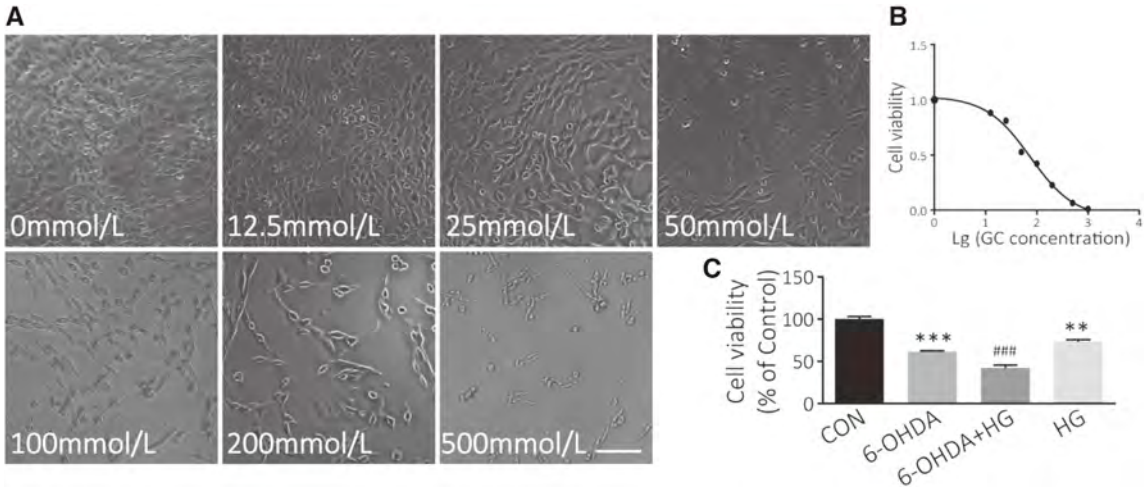

Fig. 3 HG treatment induces PC12 cell death. **A** Bright-field images of cell morphology at different glucose concentrations (scale bar, 200 μm). **B** Survival curve of PC12 cells after exposure to different concentrations of glucose for 48 h (IC_{50} = 75.06 mmol/L). **C** PC12 cell viability determined by MTT assays. PC12 cells were exposed to 50 mmol/L glucose for 24 h followed by 100 μmol/L 6-OHDA for another 24 h (**$P < 0.01$, ***$P < 0.001$ *vs* controls; $^{\#\#\#}P < 0.001$ *vs* 6-OHDA-treated group; $n = 3$).

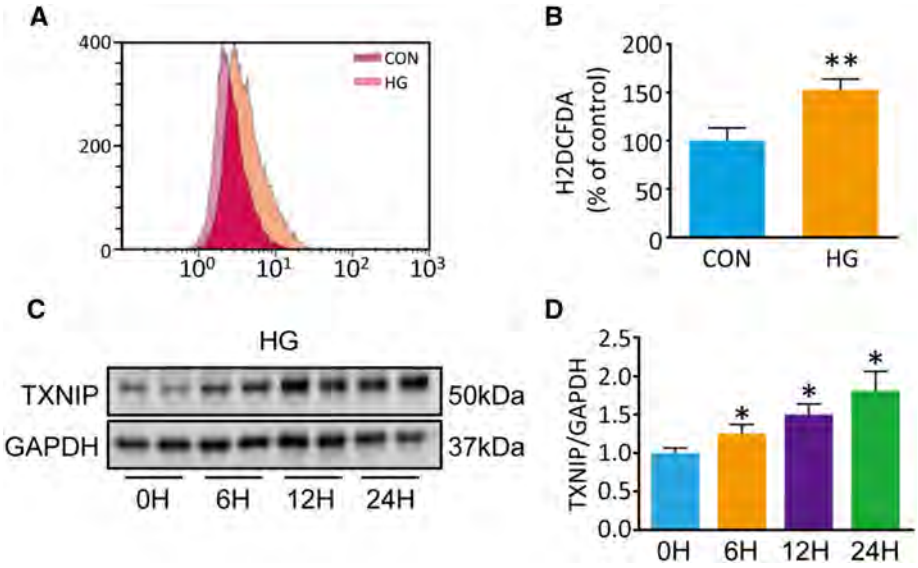

Fig. 4 Intracellular ROS and TXNIP are notably increased in PC12 cells after 50 mmol/L HG treatment compared with controls (5 mmol/L glucose). **A** Flow cytometry for intracellular ROS stained by H2DCFDA. **B** Quantification of ROS (**$P < 0.01$ *vs* controls; $n = 3$). **C**, **D** Western blots and analysis for TXNIP (*$P < 0.05$ *vs* 0 h group; $n = 3$).

PC12 cells that were incubated in HG for 48 h ($P < 0.001$; Fig. 5A). This indicated that autophagosomes were induced in PC12 cells under HG. However, p62, a marker of autophagic degradation, accumulated in HG-treated cells ($P = 0.002$; Fig. 5A). Furthermore, PINK1 declined by ~25% in whole-cell homogenates of HG-treated PC12 cells ($P = 0.033$; Fig. 5B). However, Parkin, another important regulator in mitophagy, did not change in whole-cell homogenates after HG treatment ($P = 0.903$). To assess whether PINK1 transcription is also regulated by HG, we assessed PINK1 mRNA in PC12 cells treated with HG for 48 h or CCCP (20 μmol//L, a widely used inducer of mitophagy) for 6 h. PINK1 mRNA was increased by CCCP treatment ($P = 0.012$; Fig. 5C). However, PINK1 mRNA did not change following HG treatment. These data indicate that the decrease in PINK1 protein expression following HG treatment is not driven by a decrease in PINK1 transcription.

There is evidence that Parkin is recruited to damaged mitochondria, and mitophagy is dependent on the accumulation of Parkin in the outer mitochondrial membrane. So, next we measured Parkin in the mitochondrial fraction. First, the purity of the isolated mitochondrial fractions was confirmed by the absence of the cytosolic protein α-tubulin and the presence of the mitochondrial protein COX IV (Fig. 5D). HG treatment decreased the Parkin level in the

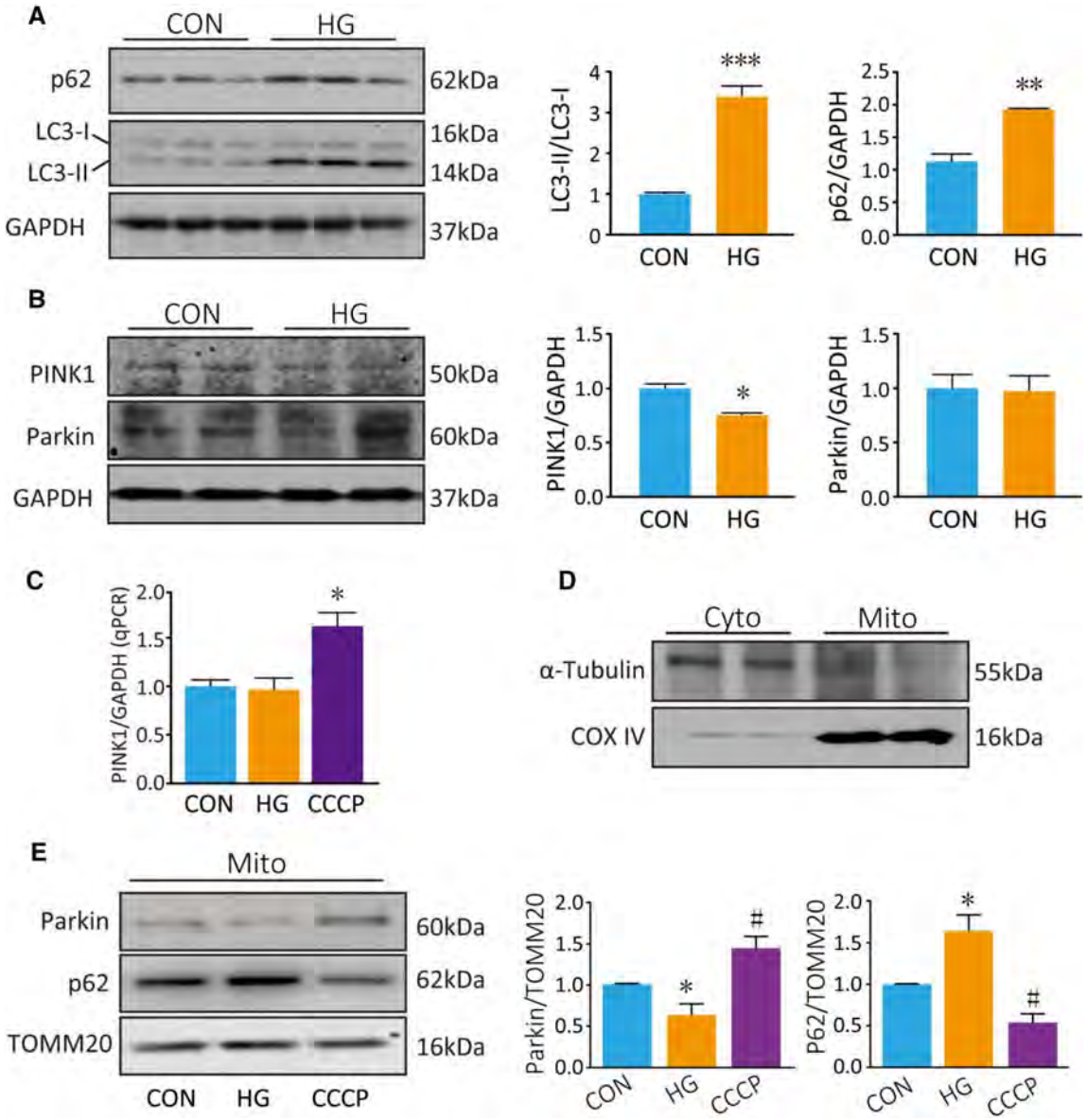

Fig. 5 HG blocks autophagic flux and inhibits Parkin/PINK1-mediated mitophagy in PC12 cells. **A**, **B** Western blots and analyses for LC3, p62, PINK1, and Parkin after HG treatment for 48 h. **C** qPCR analysis of PINK1 mRNA. **D** Western blots of the cytosolic protein α-tubulin and mitochondrial protein COX IV cytosolic (Cyto) and mitochondrial (Mito) fractions. **E** Western blots and analyses for Parkin and p62 in the mitochondrial fraction. COX IV served as a loading control for mitochondrial protein. $^{*}P < 0.05$, $^{**}P < 0.01$, $^{***}P < 0.001$ *vs* controls; $^{\#}P < 0.05$ *vs* HG group; $n = 3$.

mitochondrial fraction ($P = 0.020$; Fig. 5E), but CCCP led to an increased Parkin level in the mitochondrial fraction ($P = 0.020$; Fig. 5E) as previously described [23, 24]. Furthermore, p62 accumulated in the mitochondrial fraction after HG treatment ($P = 0.016$; Fig. 5E), but was downregulated after CCCP treatment ($P < 0.001$) as previously described [23]. p62 is a known target for autophagic degradation. Taken together, these results point out that HG treatment blocks the autophagic flux in PC12 cells.

HG Blocks Mitophagy

To confirm that the inhibition of mitophagy resulted from HG, we measured the co-localization of mitochondria and lysosomes in PC12 cells. As noted above, mitophagy is a selective degradation pathway for damaged mitochondria through double-membrane autophagosomes, which then fuse with lysosomes to form autolysosomes in which mitochondria are degraded. LAMP1 is a lysosomal P-type transport ATPase, and is considered to be a lysosome marker. COX IV and LAMP1 immunofluorescence

staining was used to observe mitochondria and lysosomes, respectively. Under normal conditions, little co-staining of COX IV and LAMP1 was observed (Fig. 6). CCCP induced co-localization of mitochondrial COX IV and lysosomal LAMP1, indicating mitophagy (Fig. 6). However, pretreatment with HG for 48 h inhibited the co-localization of COX IV and LAMP1 induced by CCCP (Fig. 6). Taken together, these results demonstrate that mitophagy is inhibited in PC12 cells under HG conditions.

TXNIP Inhibits Mitophagy

Our previous study reported that overexpression of TXNIP inhibits autophagic flux [9]. In the present study, we transfected TXNIP plasmid into PC12 cells to explore the effect of TXNIP on mitophagy. First, TXNIP was significantly increased in PC12 cells after transfection (P = 0.041; Fig. 7A). Then, we assessed Parkin and PINK1 by Western blot analysis. Consistent with the results of HG treatment, PINK1 was lower in TXNIP-overexpressing cells than in controls (P = 0.005), as was Parkin (P = 0.025) (Fig. 7A). Mitophagy is important for maintaining mitochondrial quality and the intracellular ROS level, so we assessed intracellular ROS using H2DCFDA. The results showed that ROS was increased in TXNIP-overexpressing cells (P = 0.036; Fig. 7B). Furthermore, the co-localization of COX IV and LAMP1 induced by CCCP was inhibited in PC12 cells under HG conditions (Fig. 7C).

Next, we transfected siRNA into PC12 cells to inhibit TXNIP expression and this decreased TXNIP expression by 70% compared with controls (P = 0.009; Fig. 8A). Moreover, the inhibition of TXNIP decreased the intracellular ROS induced by HG (P = 0.025; Fig. 8B). We used MTT assays to determine the cellular viability and found that the inhibition of TXNIP in PC12 cells relieved the cell injury induced by HG (P = 0.041; Fig. 8C). As noted above, co-localization of COX IV with LAMP1 was rare in PC12 cells under HG+CCCP conditions. However, when TXNIP was inhibited by siRNA transfection, more co-localization occurred between COX IV and LAMP1 under these conditions (Fig. 8D, E). These findings indicate that TXNIP is involved in the mitophagy dysfunction induced by HG.

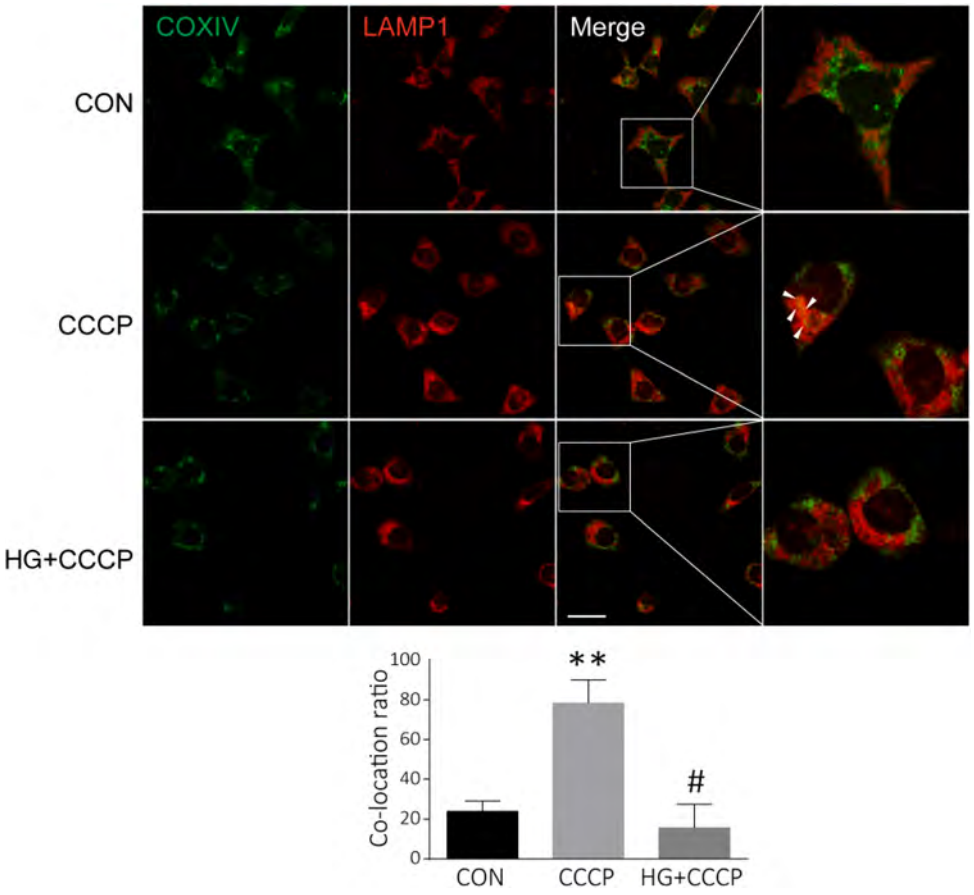

Fig. 6 HG inhibits the mitophagy induced by CCCP. Representative images and analysis of co-localization of the mitochondrial protein COX IV (green) and the lysosomal protein LAMP1 (red) in PC12 cells incubated in low (5 mmol/L) or high (25 mmol/L) glucose medium for 48 h, then treated with CCCP (20 μmol/L) for another 6 h (**$P < 0.01$ *vs* controls; $^{\#}P < 0.05$ *vs* CCCP group; scale bar, 20 μm; three independent experiments were carried out in each group).

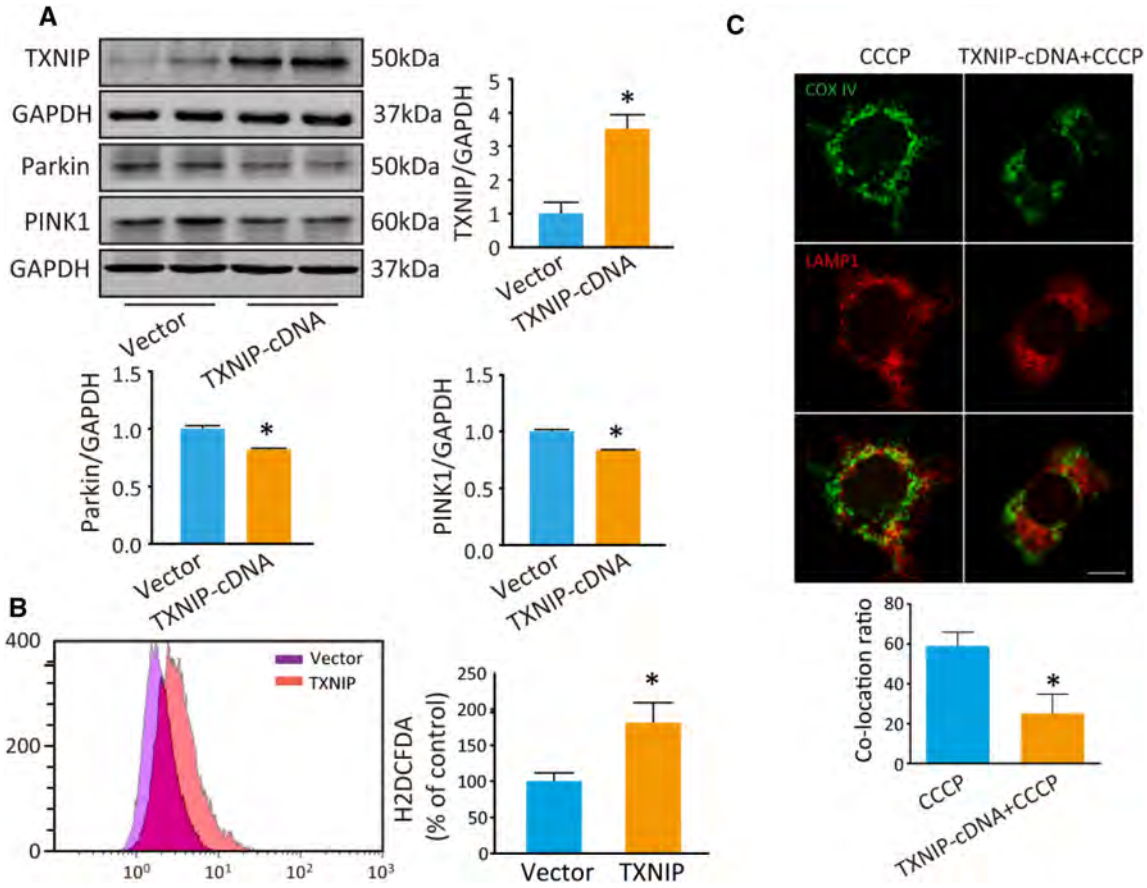

Fig. 7 Overexpression of TXNIP inhibits mitophagy and inhibition of TXNIP decreases intracellular ROS induced by HG. **A** Western blots and analysis of TXNIP, Parkin and PINK1 in PC12 cells after transfection with TXNIP cDNA for 48 h. **B** Intracellular ROS was stained by H2DCDFA and determined by flow cytometry after transfection of TXNIP cDNA. **C** Co-localization analysis of mitochondrial protein COX IV (green) and lysosomal protein LAMP1 (red) to assess mitophagy. $^*P < 0.05$ *vs* vector group; $n = 3$; scale bar, 20 μm; three independent immunofluorescence experiments were carried out in each group.

Discussion

Our results showed that TXNIP was increased and autophagy was inhibited in the midbrain of diabetic mice. Moreover, hyperglycemia accelerated the DA neuron loss induced by MPTP *in vivo*, and HG induced PC12 cell death *in vitro*. In addition, HG increased ROS production and upregulated TXNIP in PC12 cells. Furthermore, autophagic flux was blocked and mitophagy was inhibited in PC12 cells under HG conditions. Moreover, Parkin and PINK1 decreased in PC12 cells transfected with TXNIP cDNA. These findings indicate that hyperglycemia induces mitophagy dysfunction and results in DA neuronal injury in diabetes mellitus.

Blood glucose is commonly increased in diabetes mellitus, and chronic hyperglycemia damages brain cells through increased production of ROS [25]. Diabetes mellitus is associated with worsened motor symptoms and greater striatal DA deficits in the early stage of PD [26], and patients with type 2 diabetes have a higher risk of developing PD [27]. In fact, several dysregulated pathways, such as oxidative stress and inflammation, are common underlying processes that cause PD and diabetes [5, 28–31]. In the present study, we selected PC12 cells, a commonly-used cell line in PD studies *in vitro*, to investigate the effect of HG on DA cells. Similar to other reports [32], we found that HG significantly induced PC12 cell death. Different concentrations of glucose were used in HG-induced injury in PC12 cells, ranging from 25 to 100 mmol/L, and we selected 50 mmol/L glucose to induce PC12 cell injury based on the survival curve [33, 34]. Moreover, we found that HG further promotes cell death when cells were co-treated with HG and 6-OHDA. In experimental models, the DA neuronal degeneration induced by MPTP is exacerbated in mice with type 2 diabetes [35]. These findings suggest that HG or hyperglycemia is a risk factor for DA neuron death in PD.

Chronic hyperglycemia damages brain cells through increased production of ROS. An elevated level of cellular ROS is a key mediator of glucose-induced neurotoxicity

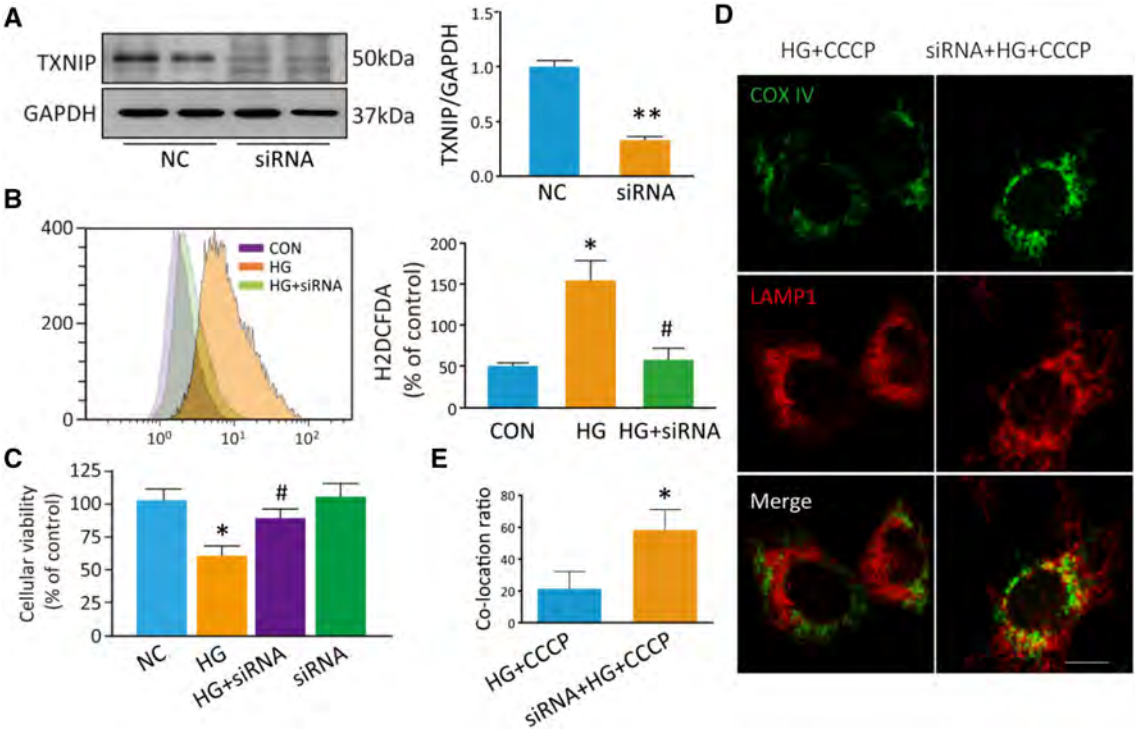

Fig. 8 Inhibition of TXNIP relieves the PC12 cell injury induced by HG, and restores mitophagy induced by CCCP under HG conditions. **A** Western blots and analysis for TXNIP after transfection with TXNIP siRNA for 48 h. **B** Flow cytometry and analysis for intracellular ROS stained by H2DCDFA after transfection with TXNIP siRNA. **C** MTT assays of cellular viability. **D** Images of co-localization of the mitochondrial protein COX IV (green) and the lysosomal protein LAMP1 (red) to assess mitophagy. **E** Co-localization analysis of mitochondrial protein COX IV and lysosomal protein LAMP1. $^{*}P < 0.05$, $^{**}P < 0.01$ *vs* controls; $^{\#}P < 0.05$ *vs* HG group; $n = 3$; scale bar, 20 μm; three independent immunofluorescence experiments were carried out in each group.

[36, 37]. We found that ROS was notably increased in PC12 cells after HG treatment. TXNIP promotes oxidative stress by binding to thioredoxin [6] and TXNIP increases under oxidative stress conditions. In addition, it is strongly induced by glucose and increased in diabetes, while it promotes β-cell apoptosis [38] and diabetic retinopathy [39] and nephropathy[20]. However, few studies have reported whether HG induces TXNIP expression in DA cells. We found that TXNIP was significantly upregulated in PC12 cells incubated with HG, indicating that TXNIP is involved in the DA cell injury induced by HG treatment.

Since mitochondria are considered to be the main source of intracellular ROS, we explored the effect of HG on mitophagy in PC12 cells. Mitochondrial dysfunction has been reported both in diabetes or diabetic complications (such as diabetic retinopathy and cardiomyopathy) [40] and in PD [41–43]. TXNIP induces mitochondrial dysfunction through the p38/MAPK pathway in diabetic retinopathy [8], while TXNIP inhibits autophagic flux and induces α-synuclein accumulation under pathological PD conditions [9]. Under normal conditions, dysfunctional mitochondria are removed through mitophagy, which maintains the mitochondrial number to match metabolic demand and exerts mitochondrial quality control [44]. PINK1-dependent activation of Parkin is a major route of mitophagy. Under basal conditions, PINK1 is imported into mitochondria through the translocases of the outer and inner membrane complexes. Usually, PINK1 is integrated into the outer membrane but is rapidly cleaved by proteases, generating a cleaved form of PINK1 [45], which is released into the cytosol, where it is degraded by the ubiquitin proteasome system. However, PINK1 turnover is disrupted when mitochondria are damaged by toxins. Full-length PINK1 is stabilized on the damaged mitochondrial membrane [46] and phosphorylates Parkin, which is recruited to the damaged mitochondria. Then, the activated Parkin polyubiquitinates mitochondrial outer membrane proteins to initiate mitophagy. Full-length PINK1 is essential for mitophagy to remove impaired mitochondria [47]. A decrease in full-length PINK1 has been reported under conditions of mitophagy inhibition in human induced pluripotent stem cell-based PD models [48]. In the present study, full-length PINK1 accumulated significantly in the mitochondrial fraction after treatment with CCCP, a mitochondrial depolarizing agent, and this result is consistent with published studies [48, 49]. However, full-length PINK1 was decreased in HG-treated or TXNIP-transfected cells. There was no significant change of PINK1 mRNA

levels under HG conditions, indicating that the decreased PINK1 protein expression following HG treatment is not driven by a decrease in PINK1 transcription. PINK1 is activated by PTEN [50], which is inhibited by TXNIP [51]. This mechanism may account for the decreased full-length PINK1 in PC12 cells under HG conditions. Failure of mitophagy results in the accumulation of damaged mitochondria and oxidative stress induced by ROS [44]. The inhibition of TXNIP reduces intracellular ROS, which we assessed with H2DCFDA. ROS detected by H2DCFDA is not selective for mitochondrial ROS – MitoSOX is more appropriate for evaluating mitochondria ROS. It has been reported that downregulation of TXNIP reverses the inhibition of mitophagy induced by HG in HK2 cells [52]. In our study, PINK1 was significantly inhibited in PC12 cells after HG treatment. Meanwhile, both PINK1 and Parkin were notably decreased in cells overexpressing TXNIP. Moreover, when TXNIP was inhibited by siRNA transfection in PC12 cells, more co-localization occurred between COX IV and LAMP1 under HG+CCCP conditions. These results suggest that HG causes mitophagy dysfunction *via* the upregulation of TXNIP. It has recently been reported that ROS is necessary for PINK1-mediated mitophagy [53]. This seems to contradict our results, in which a decrease of TXNIP inhibited the intracellular ROS level. We speculate that TXNIP can regulate PINK1/Parkin-mediated mitophagy *via* a mechanism other than ROS. For instance, TXNIP may interact with PINK1, and prevent the translocation of PINK1 to mitochondria. There are still shortcomings in the present study. We do not know the exact role of TXNIP in the regulation of PINK1/Parkin-mediated mitophagy, and this deserves further study. Moreover, we plan to explore the effect of HG on Parkin-independent mitophagy, which was not evaluated in this paper.

In summary, HG increased the expression of TXNIP, an endogenous protein promoting oxidative stress, resulting in Parkin/PINK1-mediated mitophagy dysfunction in DA cells. All these results suggested that TXNIP is involved in the Parkin/PINK1-mediated mitophagy dysfunction induced by HG, and that TXNIP is a promising therapeutic target for reducing the risk of PD under hyperglycemic conditions.

Acknowledgements This work was supported by the National Science Foundation of China (81601098 and 81603181), the Natural Science Foundation of Jiangsu Province (BK20150302, BK2017 0004), the Natural Science Foundation of the Jiangsu Higher Education Institutions of China (19KJB310016), Suzhou Science and Technology for People's Livelihood (SYS201706), and the Natural Science Foundation of Suzhou (SYSD2018099).

Conflict of interest The authors declare no potential conflicts of interest with respect to the research, authorship, and/or publication of this article.

References

1. Luitse MJ, Biessels GJ, Rutten GE, Kappelle LJ. Diabetes, hyperglycaemia, and acute ischaemic stroke. Lancet Neurol 2012, 11: 261–271.
2. Liu RY, Wang JJ, Qiu X, Wu JM. Acute hyperglycemia together with hematoma of high-glucose blood exacerbates neurological injury in a rat model of intracerebral hemorrhage. Neurosci Bull 2014, 30: 90–98.
3. Biosa A, Outeiro TF, Bubacco L, Bisaglia M. Diabetes mellitus as a risk factor for Parkinson's disease: a molecular point of view. Mol Neurobiol 2018, 55: 8754–8763.
4. Kaplan M, Aviram M, Hayek T. Oxidative stress and macrophage foam cell formation during diabetes mellitus-induced atherogenesis: role of insulin therapy. Pharmacol Ther 2012, 136: 175–185.
5. Pickering RJ, Rosado CJ, Sharma A, Buksh S, Tate M, de Haan JB. Recent novel approaches to limit oxidative stress and inflammation in diabetic complications. Clin Transl Immunol 2018, 7: e1016.
6. Nasoohi S, Ismael S, Ishrat T. Thioredoxin-interacting protein (TXNIP) in cerebrovascular and neurodegenerative diseases: regulation and implication. Mol Neurobiol 2018, 55: 7900–7920.
7. Li X, Kover KL, Heruth DP, Watkins DJ, Guo Y, Moore WV, *et al.* Thioredoxin-interacting protein promotes high-glucose-induced macrovascular endothelial dysfunction. Biochem Biophys Res Commun 2017, 493: 291–297.
8. Wei J, Wu H, Zhang H, Li F, Chen S, Hou B, *et al.* Anthocyanins inhibit high glucose-induced renal tubular cell apoptosis caused by oxidative stress in db/db mice. Int J Mol Med 2018, 41: 1608–1618.
9. Su CJ, Feng Y, Liu TT, Liu X, Bao JJ, Shi AM, *et al.* Thioredoxin-interacting protein induced alpha-synuclein accumulation via inhibition of autophagic flux: Implications for Parkinson's disease. CNS Neurosci Ther 2017, 23: 717–723.
10. Macdonald R, Barnes K, Hastings C, Mortiboys H. Mitochondrial abnormalities in Parkinson's disease and Alzheimer's disease: can mitochondria be targeted therapeutically? Biochem Soc Trans 2018, 46: 891–909.
11. Weil R, Laplantine E, Curic S, Genin P. Role of optineurin in the mitochondrial dysfunction: potential implications in neurodegenerative diseases and cancer. Front Immunol 2018, 9: 1243.
12. Fivenson EM, Lautrup S, Sun N, Scheibye-Knudsen M, Stevnsner T, Nilsen H, *et al.* Mitophagy in neurodegeneration and aging. Neurochem Int 2017, 109: 202–209.
13. Yuan Y, Zhang X, Zheng Y, Chen Z. Regulation of mitophagy in ischemic brain injury. Neurosci Bull 2015, 31: 395–406.
14. Ordureau A, Paulo JA, Zhang W, Ahfeldt T, Zhang J, Cohn EF, *et al.* Dynamics of PARKIN-dependent mitochondrial ubiquitylation in induced neurons and model systems revealed by digital snapshot proteomics. Mol Cell 2018, 70: 211–227 e218.
15. Yamada T, Murata D, Adachi Y, Itoh K, Kameoka S, Igarashi A, *et al.* Mitochondrial stasis reveals p62-mediated ubiquitination in Parkin-independent mitophagy and mitigates nonalcoholic fatty liver disease. Cell Metab 2018, 28: 588–604.e5.
16. Burte F, Carelli V, Chinnery PF, Yu-Wai-Man P. Disturbed mitochondrial dynamics and neurodegenerative disorders. Nat Rev Neurol 2015, 11: 11–24.
17. Piano I, Novelli E, Della Santina L, Strettoi E, Cervetto L, Gargini C. Involvement of autophagic pathway in the progression of retinal degeneration in a mouse model of diabetes. Front Cell Neurosci 2016, 10: 42.
18. Kitada T, Asakawa S, Hattori N, Matsumine H, Yamamura Y, Minoshima S, *et al.* Mutations in the parkin gene cause autosomal recessive juvenile parkinsonism. Nature 1998, 392: 605–608.

19. Valente EM, Abou-Sleiman PM, Caputo V, Muqit MM, Harvey K, Gispert S, *et al.* Hereditary early-onset Parkinson's disease caused by mutations in PINK1. Science 2004, 304: 1158–1160.
20. Kumar A, Mittal R. Mapping Txnip: key connexions in progression of diabetic nephropathy. Pharmacol Rep 2018, 70: 614–622.
21. Andrews ZB, Horvath B, Barnstable CJ, Elsworth J, Yang L, Beal MF, *et al.* Uncoupling protein-2 is critical for nigral dopamine cell survival in a mouse model of Parkinson's disease. J Neurosci 2005, 25: 184–191.
22. Lu M, Su C, Qiao C, Bian Y, Ding J, Hu G. Metformin prevents dopaminergic neuron death in MPTP/P-induced mouse model of Parkinson's disease *via* autophagy and mitochondrial ROS clearance. Int J Neuropsychopharmacol 2016, 19. https://doi.org/10.1093/ijnp/pyw047
23. Youn CK, Kim HB, Wu TT, Park S, Cho SI, Lee JH. 53BP1 contributes to regulation of autophagic clearance of mitochondria. Sci Rep 2017, 7: 45290.
24. Suen DF, Narendra DP, Tanaka A, Manfredi G, Youle RJ. Parkin overexpression selects against a deleterious mtDNA mutation in heteroplasmic cybrid cells. Proc Natl Acad Sci U S A 2010, 107: 11835–11840.
25. Kwon KJ, Lee EJ, Kim MK, Kim SY, Kim JN, Kim JO, *et al.* Diabetes augments cognitive dysfunction in chronic cerebral hypoperfusion by increasing neuronal cell death: implication of cilostazol for diabetes mellitus-induced dementia. Neurobiol Dis 2015, 73: 12–23.
26. Pagano G, Polychronis S, Wilson H, Giordano B, Ferrara N, Niccolini F, *et al.* Diabetes mellitus and Parkinson disease. Neurology 2018, 90: e1654–e1662.
27. Yue X, Li H, Yan H, Zhang P, Chang L, Li T. Risk of Parkinson disease in diabetes mellitus: an updated meta-analysis of population-based cohort studies. Medicine (Baltimore) 2016, 95: e3549.
28. Burbulla LF, Song P, Mazzulli JR, Zampese E, Wong YC, Jeon S, *et al.* Dopamine oxidation mediates mitochondrial and lysosomal dysfunction in Parkinson's disease. Science 2017, 357: 1255–1261.
29. Chitnis T, Weiner HL. CNS inflammation and neurodegeneration. J Clin Invest 2017, 127: 3577–3587.
30. Shimobayashi M, Albert V, Woelnerhanssen B, Frei IC, Weissenberger D, Meyer-Gerspach AC, *et al.* Insulin resistance causes inflammation in adipose tissue. J Clin Invest 2018, 128: 1538–1550.
31. Yuan H, Zheng JC, Liu P, Zhang SF, Xu JY, Bai LM. Pathogenesis of Parkinson's disease: oxidative stress, environmental impact factors and inflammatory processes. Neurosci Bull 2007, 23: 125–130.
32. Namazi Sarvestani N, Saberi Firouzi S, Falak R, Karimi MY, Davoodzadeh Gholami M, Rangbar A, *et al.* Phosphodiesterase 4 and 7 inhibitors produce protective effects against high glucose-induced neurotoxicity in PC12 cells *via* modulation of the oxidative stress, apoptosis and inflammation pathways. Metab Brain Dis 2018, 33: 1293–1306.
33. Aminzadeh A. Protective effect of tropisetron on high glucose induced apoptosis and oxidative stress in PC12 cells: roles of JNK, P38 MAPKs, and mitochondria pathway. Metab Brain Dis 2017, 32: 819–826.
34. Chen M, Zheng H, Wei T, Wang D, Xia H, Zhao L, *et al.* High glucose-induced PC12 cell death by increasing glutamate production and decreasing methyl group metabolism. Biomed Res Int 2016, 2016: 4125731.
35. Wang L, Zhai YQ, Xu LL, Qiao C, Sun XL, Ding JH, *et al.* Metabolic inflammation exacerbates dopaminergic neuronal degeneration in response to acute MPTP challenge in type 2 diabetes mice. Exp Neurol 2014, 251: 22–29.
36. Nishikawa T, Araki E. Impact of mitochondrial ROS production in the pathogenesis of diabetes mellitus and its complications. Antioxid Redox Signal 2007, 9: 343–353.
37. Wei W, Liu Q, Tan Y, Liu L, Li X, Cai L. Oxidative stress, diabetes, and diabetic complications. Hemoglobin 2009, 33: 370–377.
38. Alhawiti NM, Al Mahri S, Aziz MA, Malik SS, Mohammad S. TXNIP in metabolic regulation: physiological role and therapeutic outlook. Curr Drug Targets 2017, 18: 1095–1103.
39. Lu L, Lu Q, Chen W, Li J, Li C, Zheng Z. Vitamin D3 protects against diabetic retinopathy by inhibiting high-glucose-induced activation of the ROS/TXNIP/NLRP3 inflammasome pathway. J Diabetes Res 2018, 2018: 8193523.
40. Mishra M, Kowluru RA. DNA methylation-a potential source of mitochondria DNA base mismatch in the development of diabetic retinopathy. Mol Neurobiol 2019, 56: 88–101.
41. Wang S, Zhao Z, Fan Y, Zhang M, Feng X, Lin J, *et al.* Mst1 inhibits Sirt3 expression and contributes to diabetic cardiomyopathy through inhibiting Parkin-dependent mitophagy. Biochim Biophys Acta 2019, 1865: 1905–1914.
42. Park JS, Davis RL, Sue CM. Mitochondrial dysfunction in Parkinson's disease: new mechanistic insights and therapeutic perspectives. Curr Neurol Neurosci Rep 2018, 18: 21.
43. He L, Chen L, Li L. The TBK1-OPTN axis mediates crosstalk between mitophagy and the innate immune response: a potential therapeutic target for neurodegenerative diseases. Neurosci Bull 2017, 33: 354–356.
44. Wei H, Liu L, Chen Q. Selective removal of mitochondria *via* mitophagy: distinct pathways for different mitochondrial stresses. Biochim Biophys Acta 2015, 1853: 2784–2790.
45. Greene AW, Grenier K, Aguileta MA, Muise S, Farazifard R, Haque ME, *et al.* Mitochondrial processing peptidase regulates PINK1 processing, import and Parkin recruitment. EMBO Rep 2012, 13: 378–385.
46. Lin W, Kang UJ. Characterization of PINK1 processing, stability, and subcellular localization. J Neurochem 2008, 106: 464–474.
47. Gladkova C, Maslen SL, Skehel JM, Komander D. Mechanism of parkin activation by PINK1. Nature 2018, 559: 410–414.
48. Oh CK, Sultan A, Platzer J, Dolatabadi N, Soldner F, McClatchy DB, *et al.* S-Nitrosylation of PINK1 attenuates PINK1/Parkin-dependent mitophagy in hiPSC-based Parkinson's disease models. Cell Rep 2017, 21: 2171–2182.
49. Narendra DP, Jin SM, Tanaka A, Suen DF, Gautier CA, Shen J, *et al.* PINK1 is selectively stabilized on impaired mitochondria to activate Parkin. PLoS Biol 2010, 8: e1000298.
50. Singh LP. Thioredoxin interacting protein (TXNIP) and pathogenesis of diabetic retinopathy. J Clin Exp Ophthalmol 2013, 4. https://doi.org/10.4172/2155-9570.1000287
51. Lee S, Kim SM, Lee RT. Thioredoxin and thioredoxin target proteins: from molecular mechanisms to functional significance. Antioxid Redox Signal 2013, 18: 1165–1207.
52. Huang C, Zhang Y, Kelly DJ, Tan CY, Gill A, Cheng D, *et al.* Thioredoxin interacting protein (TXNIP) regulates tubular autophagy and mitophagy in diabetic nephropathy through the mTOR signaling pathway. Sci Rep 2016, 6: 29196.
53. Xiao B, Goh JY, Xiao L, Xian H, Lim KL, Liou YC. Reactive oxygen species trigger Parkin/PINK1 pathway-dependent mitophagy by inducing mitochondrial recruitment of Parkin. J Biol Chem 2017, 292: 16697–16708.

Neurosci. Bull. April, 2020, 36(4):359–371
https://doi.org/10.1007/s12264-019-00436-y

www.neurosci.cn
www.springer.com/12264

ORIGINAL ARTICLE

Homeobox B8 Targets Sterile Alpha Motif Domain-Containing Protein 9 and Drives Glioma Progression

Wenping Ma[1,2,3] · Hongze Jin[4] · Wenjie Liu[5] · Xiaojuan Li[6] · Xingang Zhou[7] · Xinwu Guo[8] · Runfa Tian[2] · Qi Cui[1] · Junjie Luo[1] · Yueying Jiao[1] · Youtao Yu[9] · Haifeng Yang[10] · Hongshan Zhao[1]

Received: 14 April 2019 / Accepted: 27 May 2019 / Published online: 23 October 2019

Abstract Gliomas are the most commonly occurring tumors of the central nervous system. Glioblastoma multiforme (GBM) is the most malignant and aggressive brain cancer in adults. Further understanding of the mechanisms underlying the aggressive nature of GBM is urgently needed. Here we identified homeobox B8 (HOXB8), a member of the homeobox family, as a crucial contributor to the aggressiveness of GBM. Data mining of publicly accessible RNA sequence datasets and our patient cohorts confirmed a higher expression of HOXB8 in the tumor tissue of GBM patients, and a strong positive correlation between the expression level and pathological grading of tumors and a negative correlation between the expression level and the overall survival rate. We next showed that HOXB8 promotes the proliferation and migration of glioblastoma cells and is crucial for the activation of the PI3K/AKT pathway and expression of epithelial–mesenchymal transition-related genes, possibly through direct binding to the promoter of SAMD9 (Sterile Alpha Motif Domain-Containing Protein 9) and activating its transcription. Collectively, we identified HOXB8 as a critical contributor to the aggressiveness of GBM, which provides insights into a potential therapeutic target for GBM and opens new avenues for improving its treatment outcome.

Keywords HOXB8 · Glioma · Aggressiveness · SAMD9 · Treatment

Electronic supplementary material The online version of this article (https://doi.org/10.1007/s12264-019-00436-y) contains supplementary material, which is available to authorized users.

✉ Youtao Yu
yuyoutao@126.com

✉ Haifeng Yang
429810560@qq.com

✉ Hongshan Zhao
hongshan@bjmu.edu.cn

1 Department of Medical Genetics, School of Basic Medical Sciences, Peking University Health Science Center, Beijing 100191, China

2 Department of Neurosurgery, Beijing Tiantan Hospital, Capital Medical University, Beijing 100050, China

3 Beijing Neurosurgical Institute, Beijing 100050, China

4 The Second Affiliated Hospital of Zhejiang University School of Medicine, Changxing Campus, Changxing 313100, China

5 Department of Hepatobiliary Surgery, National Cancer Center/Cancer Hospital, Chinese Academy of Medical Sciences and Peking Union Medical College, Beijing 100021, China

6 Department of Radiology, The First Hospital of Harbin Medical University, Harbin 150001, China

7 Department of Pathology, Beijing Ditan Hospital, Capital Medical University, Beijing 100015, China

8 Sansure Biotech Inc., Changsha 410205, China

9 Department of Intervention Therapy, The Fourth Medical Center of PLA General Hospital, Beijing 100037, China

10 Department of Neurosurgery, Sanbo Brain Hospital, Capital Medical University, Beijing 100093, China

Introduction

Glioma is a set of primary brain tumors which account for almost 80% of all malignant primary tumors of the brain [1]. They are classified according to their presumed cell of origin and include astrocytic tumors, oligodendrogliomas, ependymomas, and mixed gliomas [2–5]. The World Health Organization classifies gliomas pathologically as grades I to IV based on the level of malignancy as determined by histopathological criteria [6, 7]. Glioblastoma multiforme (GBM) is the most aggressive type of tumor and has been designated Grade IV [8]. The global incidence of GBM is < 10 per 100,000 people. However, the poor prognosis and survival rate after diagnosis makes it a crucial public health issue [9–11]. Currently, the etiology of gliomas remains poorly understood and the aggressiveness of GBM needs urgent investigation in order to develop more effective treatment strategies to improve the poor prognosis of patients with this high-grade glioma.

Hox genes are a group of related genes, each of which contains a well-conserved DNA sequence known as the homeobox [12]. The protein product of each *Hox* gene is a transcription factor. In mammals, 39 *Hox* genes have been identified that are clustered in four genomic loci, the *HoxA*, *HoxB*, *HoxC* and *HoxD* complexes, which control the body plan of the embryo along the head-tail axis [13, 14]. In addition, *Hox* proteins regulate numerous other processes including apoptosis, receptor signaling, differentiation, motility, and angiogenesis [15, 16]. Aberrations in *Hox* gene expression have been reported in malignancy, indicating that altered expression of *Hox* genes could be important for both oncogenesis and tumor suppression, depending on context [17, 18].

HOXB8 is located at 17q21.32, is composed of 5 exons, and encodes 243 amino-acids. In addition to its critical role in the development of the central nervous system, accumulating evidence suggests a significant role of HOXB8 in colorectal cancer [19], liver cancer [20], gastric cancer [21], and ovarian cancer [22]. However, its role in the development and progression of glioma is unclear.

Therefore, in this study, we set out to determine the role of HOXB8 in the development of glioma.

Materials and Methods

Ethics Statement

Human brain tissue microarrays were provided by Shanghai Outdo Biotech Co. Ltd., comprising 3 from normal brain tissue and 87 from glioma patients (3 with grade I, 16 with grade II, 26 with grade III, and 42 with grade IV) (Cat No. HBraG090PG01, Lot No. XT16-017).

Tissues from 26 glioma cases (13 with grade III and 13 with grade IV) were provided by Beijing Tiantan Hospital and individual informed consent was given by all patients. Normal brain tissues were acquired from patients who underwent brain surgery for unrelated causes. We confirm that the procedures involving experiments on human subjects met the ethical standards of the Helsinki Declaration in 1975. This study was approved by the Ethics Committee of Peking University Health Science Center.

Bioinformatics Analysis of HOXB8 Expression

HOXB8 mRNA expression data from gliomas were downloaded and extracted from three datasets [European Bioinformatics Institute (EBI) ArrayExpress data, Chinese Glioma Genome Atlas (CGGA) data, and Gene Expression Omnibus (GEO) data]. The Kruskal-Wallis rank sum test was performed to assess the difference in HOXB8 expression between non-tumor brain tissue and gliomas, and between low-grade and high-grade gliomas. Gene Set Enrichment Analysis (GSEA) was also used to find significantly enriched gene sets and pathways. The relationship between HOXB8 mRNA expression levels and tumor patient survival was analyzed online using Oncolnc (http://www.oncolnc.org/), which linked the survival data to mRNAs, miRNAs, and lncRNAs from The Cancer Genome Atlas.

Cell Culture

Human glioma cell lines U251 (Sigma-Aldrich, 0906301, Porton Down, UK), U87 (American Type Culture Collection, HTB-14, Manassas, VA), A172 (American Type Culture Collection, CRL-1620), GOS-3 (German Collection of Microorganisms and Cell Cultures, ACC 408, Braunschweig, Germany), and rat C6 glioma cells (American Type Culture Collection, CCL-107) were cultured in RPMI 1640 medium (pH 7.4) supplemented with 10% fetal bovine serum (FBS) and 100 IU/mL penicillin and streptomycin (all from Gibco, Thermo Scientific, NY, USA) in a humidified atmosphere of 5% CO_2 at 37°C.

Plasmids and Antibodies

Full-length HOXB8 was cloned into the pcDNA3.1 vector. Anti-HOXB8 antibody (Abcam, ab125727, WB 1:1000, ICC 1:200) and anti-SAMD9 antibody (Abcam, ab13603, WB 1:1000, ICC 1:100) were from Abcam. MMP2 (#13132, D8N9Y), MMP3 (#14351, D7F5B), MMP-9 (#13667, D6O3H), Slug (#9585, C19G7), Snail (#3879, C15D3), PI3K kinase p85 (#4942), phospho-PI3 kinase p85 (#4228,1:1000,Tyr458)/p55 (Tyr199), E-cadherin (#3195, 24E10), N-cadherin (#13116,D4R1H), p44/42 MAPK

(#4695, Erk1/2) (137F5), phospho-p44/42 MAPK (#9101, Erk1/2) (Thr202/Tyr204), Akt (#4691, pan) (C67E7), phospho-Akt (#4060, Ser473) (D9E), vimentin (#5741, D21H3), β-actin (#3700, 8H10D10), and GAPDH (#8884, D16H11) were from Cell Signaling Technology (Massachusetts, USA). Mouse anti-rabbit IgG-HRP (BE0107-100, Shenzhen, China) was from EASYBIO and KI67 rabbit polyclonal antibody was from Proteintech (27309-1-AP, Rosemont, USA).

si-RNA Sequences

The small interfering (si)-RNA sequences were designed and synthesized by GenePharma (Shanghai, China). U251 and U87 cells were transfected with Smart pool siRNAs against HOXB8 or SAMD9 (20 nmol/L) using Lipofectamine 3000 (Thermo Fisher Scientific Transfection, Waltham, MA). The sequences were as follows: siRNA HOXB8 1, 5′-CCUAUUUAAUCCCUAUCUGTT-3′; siRNA HOXB8 2, 5′-UCAACUCACUGUUCUCCAATT-3′; siRNA SAMD9, 5′-GUGCAUUCGAGAGCCAAGAUU-3′; siNC, 5′-GUGCAUUCAAGAGCCAAGAUU-3′.

Lentivirus Infection

Lentiviruses carrying short hairpin (sh)-RNA targeting human HOXB8 were constructed by GeneChem (GIDL0158539, Shanghai, China). Cells were infected by the viruses for 48 h, then they were cultured in medium containing puromycin for selecting stable HOXB8-knockdown cells. The knockdown efficiency was verified by Western blotting. The shRNA sequences were as follows: HOXB8 5′-GCAAATCCAGGAGTTCTAC-3′, non-targeting control: 5′-TTCTCCGAACGTGTCACGT -3′.

Cell Survival Assay

Cells were assayed using Cell Counting Kit-8 (CCK-8) (Beijing Solarbio Science & Technology Co., Ltd, CA1210). The cells were plated in 96-well plates (100 μL cell suspensions, 3×10^3 cells), 10 μL of CCK8 per well was added at 0, 12, 24, 36, 48, and 72 h, incubated for 2–4 h in a 37°C cell incubator, then the absorbance (OD) at 450 nm was measured using a microplate reader (Thermo, Waltham, MA).

Colony Formation

Approximately 200 stably-transfected cells were plated into a 12-well plate. Two weeks later, visible colonies were fixed in 4% paraformaldehyde and stained with 0.1% crystal violet (Selleck Chemicals, S1917, Houston, TX). All experiments were performed in triplicate wells.

Cell Migration Assays

Migration assays were conducted by seeding 1×10^4 U251 or U87 glioma cells in the upper chamber of a Transwell plate (Corning, NY, USA). The glioma cells were cultured without serum for 12 h before each experiment; a single cell suspension (300 μL) in serum-free medium was added to the upper chamber, then 700 μL of complete medium containing 10% FBS was added to the lower level. After incubation at 37°C for 24 h, the cells in the lower chamber were fixed in 4% formalin and stained with 0.1% crystal violet. The migrated cells were counted in three randomly-selected fields from each membrane and each experiment was performed three times.

Cell Invasion Assay

Invasion assays were performed by seeding 1×10^4 U251 or U87 glioma cells in the upper chamber of a Transwell plate (Corning). Matrigel (0.5%) in a coating buffer solution (BD Biosciences, NJ, USA) was added to the upper chamber prior to seeding the cells. The glioma cells were cultured without serum for 12 h before each experiment and an appropriate amount (300 μL) of a single-cell suspension in serum-free medium was added to the upper chamber, and complete medium containing 10% FBS (700 μL) was then added to the lower layer. After incubation at 37°C for 24 h, the cells in the lower chamber were fixed in 4% formalin and stained with 0.1% crystal violet. The migrated cells were counted in three randomly-selected fields from each membrane; each experiment was performed three times.

Western Blotting

Glioma cells were harvested and lysed in RIPA buffer (Beyotime, P0013C, Beijing, China), containing complete mini protease inhibitor cocktail (Roche, 04693124001, Basel, Switzerland). Proteins were separated by SDS-PAGE and transferred to polyvinylidene fluoride membranes (GE, PVDF 0.45 μmol/L, 10600023). Non-specific binding was blocked using 5% non-fat milk and the primary antibody was incubated at 4°C overnight; then the secondary antibody was incubated at room temperature for 1 h. Signals were visualized by chemiluminescence (Millipore Corp., Billerica, MA).

RNA Sequencing and Target Gene Search by qPCR

U251 cells were treated with HOXB8 siRNA and siRNA NC for 48 h, each with 3 technical replicates. RNA was extracted using TRIzol (Invitrogen, 15596-026, Grand Island, NY) according to the manufacturer's protocol. Total RNA was reverse transcribed using an RT-PCR kit

(Tiangen, KR103-03, Beijing, China) according to the manufacturer's protocol. The sequencing reads were generated using the BGISEQ-500 platform following the manufacturer's recommendations. The paired-end clean reads were aligned to the reference human genome (UCSC version hg19) using TopHat v2.0.12. HTSeq v0.6.1 was used to count the read numbers mapped to each gene and the gene expression levels were calculated with RSEM version v1.2.31. Fragments per kilobase of transcript per million mapped reads for each gene were calculated based on the length of the gene and the read-count mapped to that gene, all these were provided by the Beijing Genomics Institute (Beijing, China). We used MA, volcano, scatter, and heatmap plots to show the distributions of differentially-expressed genes. A Holm's corrected *P*-value of 0.005 and log2 (fold-change) of 1 were set as the threshold for significant differential expression. Then functional enrichment analysis was performed on Gene Ontology and Kyoto Encyclopedia of Genes and Genomes pathways. Subsequently, qPCR was performed using Go Taq qPCR Master Mix (Cat No. A6001, Promega Corp., Madison, WI). Cycling conditions were as follows: 5 min at 95°C followed by 45 cycles each consisting of 10 s at 95°C, 20 s at 60°C, and 30 s at 72°C. The relative concentrations of genes were normalized to β-actin. Fold-change was calculated using the $2^{-\Delta\Delta Ct}$ method. The primers are listed in Table S1.

Semi-quantitative Immunohistochemistry

Paraffin sections were made as previously described [23–25]. After deparaffinization, sections were immersed in 100% ethanol (2×), 96% ethanol (2×), and 70% ethanol (2×) followed by heat-induced antigen retrieval at 120°C for 10 min in citrate buffer (pH 6), then allowed to cool to room temperature. After blocking endogenous enzyme activity and non-specific protein binding sites, each slide was incubated overnight at 4°C with the primary antibody followed by incubation with the secondary antibody for 1 h. Color development was produced using 3, 3-diaminobenzidine tetrahydrochloride (Beijing Solarbio Science & Technology Co., Ltd, DA1010-10) for 5 min, and counterstained with hematoxylin (Selleck Chemicals, S2384).

HOXB8 expression was evaluated independently by two experienced pathologists using the following method. A: Cell staining intensity (at 10×20 magnification, 5 different fields of view were selected randomly and observed under the microscope; the average of the combined counts of 5 fields was calculated): negative staining, 0 point; weakly positive staining, 1 point; positive staining but with light brown background, 2 points; positive staining without background, 3 points. B: Area staining intensity (at 10 × 4 magnification the total positive area was observed and evaluated): positive area = 0%, 0 point; positive area = 1%–25%, 1 point; positive area = 26%–50%, 2 points; positive area = 51%–75%, 3 points; positive area > 75%, 4 points. C: The degree of positive staining for each section was determined by multiplication of the values for A and B: 1–3 was classified as weakly positive (+); 4–6 as positive (++); and 7–12 as strongly positive (+++).

Nuclear Protein Extraction and Electrophoretic Mobility Shift Assay (EMSA)

Nuclear extracts were isolated from shNC U251 and shHOXB8 U251 cells with Nuclear and Cytoplasmic Extraction Reagents (Pierce, Cat: 78833, NY, USA) according to the manufacturer's instructions. Protein concentrations were determined with a BCA protein assay kit (Pierce, Cat: 23227). Nuclear extracts were stored at − 80°C until use. We predicted HOXB8 binding sites in the SAMD9 promoter and designed three biotin end-labeled probes (probe 1 sequence, AAGAGTAATTAAGTTA, location − 778 to − 794 bp; probe 2 sequence, CTCTGCAA-TAAATGAA, location − 488 to − 478 bp; probe 3 sequence, ACCCTTAAAGGCCAGT, − 370 to − 386 bp), synthesized by Sangon Biotech (Shanghai, China). EMSA was carried out using the LightShift® Chemiluminescent EMSA Kit (Pierce, Cat: 89880, NY, USA) according to the manufacturer's instructions. DNA binding reactions were detected in 20-μL volumes containing biotin-labeled oligonucleotides and nuclear extracts. Unlabeled oligonucleotides were added as competition controls. The reaction products were incubated at 4°C for 20 min, then the reaction mixtures were separated by electrophoresis, transferred to a nylon membrane (Roche) and detected by chemiluminescence (Millipore Corp.).

Statistical Analysis

Quantitative data are presented as the mean ± SD. Differences in the mean of two samples were analyzed using Student's *t*-test. Correlation between HOXB8 and SAMD9 expression levels was analyzed using the Spearman rank correlation test. Correlations between HOXB8 expression and various clinical pathological variables were analyzed using the Kruskal-Wallis test. Overall survival rates were determined using the Kaplan-Meier method. All statistical tests were two-tailed exact tests with a $P < 0.05$ considered significant. All statistical analyses were performed using SPSS software (version 15.0)/R version 3.4.4 (http://www.cran.r-project.org).

Results

HOXB8 is Involved in the Pathogenesis of Gliomas

We first turned to publicly-accessible databases for evidence of involvement of HOXB8 in the pathogenesis of gliomas. We found that the expression level of HOXB8 was significantly higher in gliomas than in non-tumor tissue (Fig. 1A). To further explore the clinical significance of HOXB8 in glioma progression, we took advantage of data from the CGGA database and found a strong positive correlation between the expression level of HOXB8 and the pathological grading of tumors (Fig. 1B). These findings were supported by data from a cohort of glioma patients from the GEO database (Table S2). A strong negative correlation was found between the expression

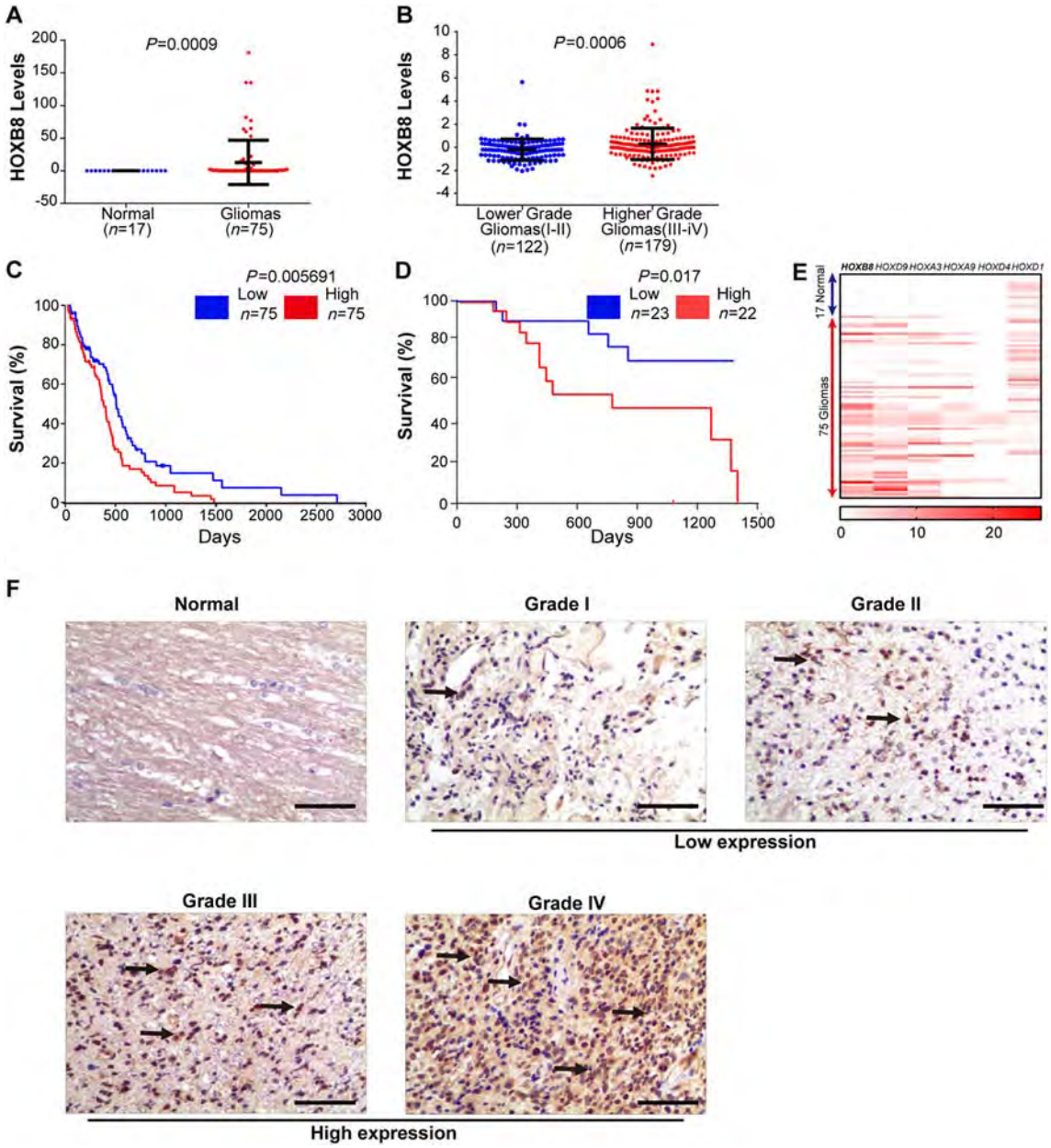

Fig. 1 HOXB8 expression in gliomas in relation to their grades. **A** HOXB8 expression in gliomas and non-tumor brain tissue from EBI ArrayExpress data (17 non-tumor brain tissues and 75 gliomas). ***$P < 0.001$. **B** HOXB8 expression in low-grade and high-grade gliomas from CGGA data (122 low-grade and 179 high-grade). ***$P < 0.001$. **C** Overall survival of glioma patients with high and low expression of HOXB8. Data from OncoLnc (http://www.oncolnc.org/). *$P < 0.05$. **D** Overall survival of glioma patients with high and low expression of HOXB8. Data from our cohort of patients. *$P < 0.05$. **E** Expression of *HOX* family members including *HOXB8* in gliomas from the GSEA database (17 non-tumor controls and 75 gliomas). **F** Immunohistochemical analysis of HOXB8 expression in gliomas of different pathological grades. Data are presented as the mean ± SD. Scale bars, 50 μm.

Table 1 HOXB8-related factor analysis in grade I–IV gliomas

Variable	Total	(−)	(+)	(++)	(+++)	*P* value
Age (years)						
> 50	26	6	4	7	9	0.432788
≤ 50	50	18	10	7	15	
Gender						
Male	38	9	8	8	16	0.146729
Female	38	15	6	9	8	
Glioma grade						
I–II	19	11	4	3	1	0.005443
III–IV	57	13	10	11	23	

level of HOXB8 and patients' overall survival rate (Fig. 1C), which was confirmed in our cohort of glioma patients (23 low grade and 22 high grade) (Fig. 1D). It is noteworthy that, according to data derived from the GSEA database (75 gliomas and 17 non-tumor controls), many HOX family members were strongly expressed in gliomas, including HOXB8 (Fig. 1E). We confirmed the stronger expression of HOXB8 in gliomas in our cohort of patients by immunohistochemistry staining (IHC) (Fig. 1F). Consistent with the above data-mining results, HOXB8 expression in our cohort was also correlated with pathological grading (Table 1).

HOXB8 Promotes Proliferation of Glioma Cells

We screened several glioma cell lines with grade IV glioma tissue as a positive control. Consequently, we selected U251 and U87 glioma cells for subsequent experiments based on the abundant expression of HOXB8 in these two cell lines (Fig. 2A). After transient knockdown of HOXB8 in the glioma cells, proliferation experiments showed that the knockdown of HOXB8 reduced their ability to proliferate (Fig. S1A, B). The knockdown efficiency in these cells was verified by western blotting (Fig. S2A). Stable silencing of HOXB8 in U251 and U87 glioma cells was achieved using a lentivirus-mediated knockdown system. Silencing HOXB8 significantly reduced the proliferative capacity (Fig. 2B). Consistently, over-expression of HOXB8 promoted the proliferation of glioma cells (Fig. 2C). Silencing HOXB8 also significantly reduced the colony-forming ability (Fig. 2D, E). To explore the mechanism underlying the decreased proliferation of glioma cells following knockdown of HOXB8, we investigated the activation of the AKT pathway and found that it was significantly decreased (Fig. 2F). Conversely, overexpression of HOXB8 increased the activation of the PI3K/AKT pathway (Fig. 2G). We also examined the ERK pathway and found no notable difference (Fig. S2C).

HOXB8 Promotes Migration of Glioma Cells

Transient silencing of HOXB8 in glioma cells reduced their migration and invasion ability (Fig. S1C, D). Consistently, stable silencing of HOXB8 produced the same results (Fig. 3A, B). Epithelial-mesenchymal transition (EMT)-related proteins were examined to reveal the relationship between HOXB8 and the EMT process. We detected upregulation of an epithelial cell marker (E-cadherin) and downregulation of mesenchymal cell markers (N-cadherin and vimentin) after transient knockdown of HOXB8 (Fig. S2A, B). Similar results were obtained in stably-transfected cells (Fig. 3E). Consistently, overexpression of HOXB8 significantly decreased the epithelial cell markers and increased the mesenchymal cell markers (Fig. 3C, D, F). These results indicated that HOXB8 is involved in the process of epithelial-to-mesenchymal transition.

SAMD9 is a Potential Target of HOXB8 and Induces Proliferation, Migration, and Invasion of Glioma Cells

To gain better insight into the molecular mechanisms involving HOXB8 during the proliferation, migration, and invasion of glioma cells, we performed whole genome RNA sequencing in U251 cells transfected with control siRNA and siRNA against HOXB8. We found down-regulation of 62 genes and up-regulation of 18 genes among the differentially-expressed genes (Fig. 4A). We analyzed numerous differentially-expressed genes, including *HOXB8, SAMD9, OSA3, IFI44L, RSAD2, IFIT1, HERC6, PPFIA4, KRT15, KRT13, SEMA7A, NME1-NME2, MX1*, and *MX2* (Fig. 4B). Based on the role of HOXB8 in promoting the proliferation, migration, and invasion of tumor cells, 14 genes associated with metastasis were identified from the top genes with a 20-fold change (Table S3). Three out of 14 genes were down-regulated in siRNA HOXB8-treated U251 cells by qPCR analysis (Fig. 4C). Among these genes, SAMD9 is closely associated with tumorigenesis. To test if HOXB8 binds directly to the promoter of SAMD9, we designed three probes in the SAMD9 promotor region and analyzed the possible protein motif for HOXB8 (Fig. 4D). We performed EMSA experiments and showed that HOXB8 directly binds to the promoter of SAMD9 and transactivates SAMD9 (Fig. 4E). More importantly, SAMD9 was also elevated in gliomas compared to non-tumor brain tissue (Fig. 5A). Similar to HOXB8, we found that the expression level of SAMD9 had a positive correlation with the glioma clinical pathology data (Fig. 5B) and a negative correlation with the overall survival rate in the CGGA database (Fig. 5C). These findings were further supported

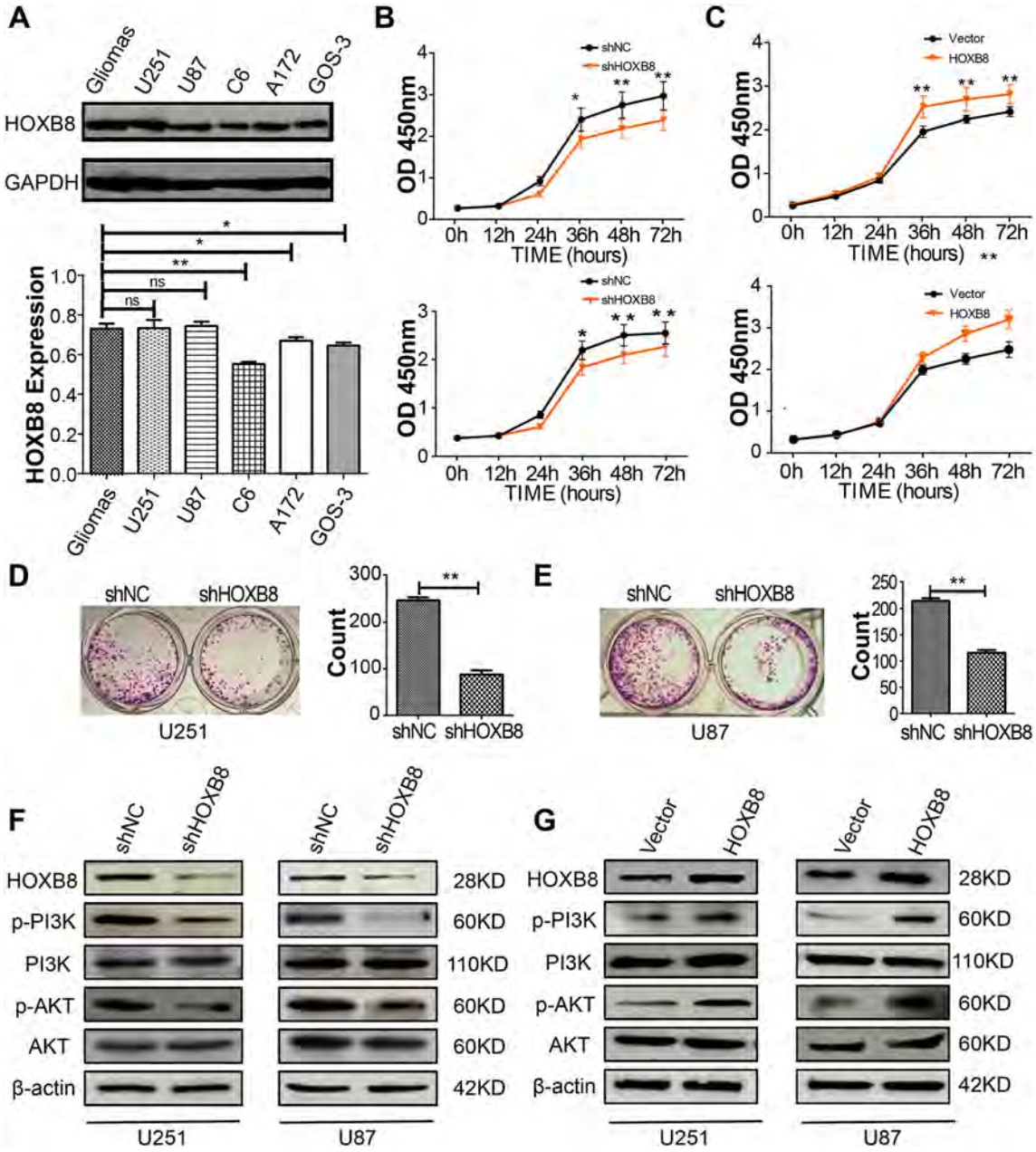

Fig. 2 HOXB8 promotes proliferation of glioma cells and affects activation of the AKT/PI3K pathway. **A** Expression of HOXB8 assessed by western blot in glioma samples. Upper panel, blots of U251, U87, C6, A172, GOS-3 cells; lower panel, statistical analysis of grayscale values. **B** Proliferation assays in U251 cells (upper) and U87 (lower) with stable expression of shHOXB8. **C** Proliferation assays in U251 (upper) and U87 (lower) cells with overexpression of HOXB8. **D** Colony formation assays in U251 cells (left) with stable expression of shHOXB8 and statistical results (right; 3 independent experiments). **E** Colony formation assays in U87 cells (left) with stable expression of shHOXB8, and statistical results (right: 3 independent experiments). **F**, **G** Western blots of PI3K and AKT, and phosphorylation of these proteins in U251 and U87 cells with stable expression of shHOXB8 (**F**) and overexpression of HOXB8 (**G**). Data are shown as the mean ± SD and were pooled from 3 independent experiments. $*P < 0.05$, $**P < 0.01$.

by data from a cohort of glioma patients from the GEO database (Table S4). Using semi-quantitative IHC analysis of 1 normal brain and 9 gliomas (Fig. 5D), we found that HOXB8 expression correlated with SAMD9 expression (Fig. 5E) and p-AKT expression (Fig. 5F); we also found that SAMD9 expression correlated with p-AKT expression (Fig. 5G). Transient knockdown of SAMD9 in glioma cells reduced their ability to proliferate (Fig. 6A, B) and decreased the activation of the AKT pathway (Fig. 6C). Silencing of SAMD9 in glioma cells reduced their

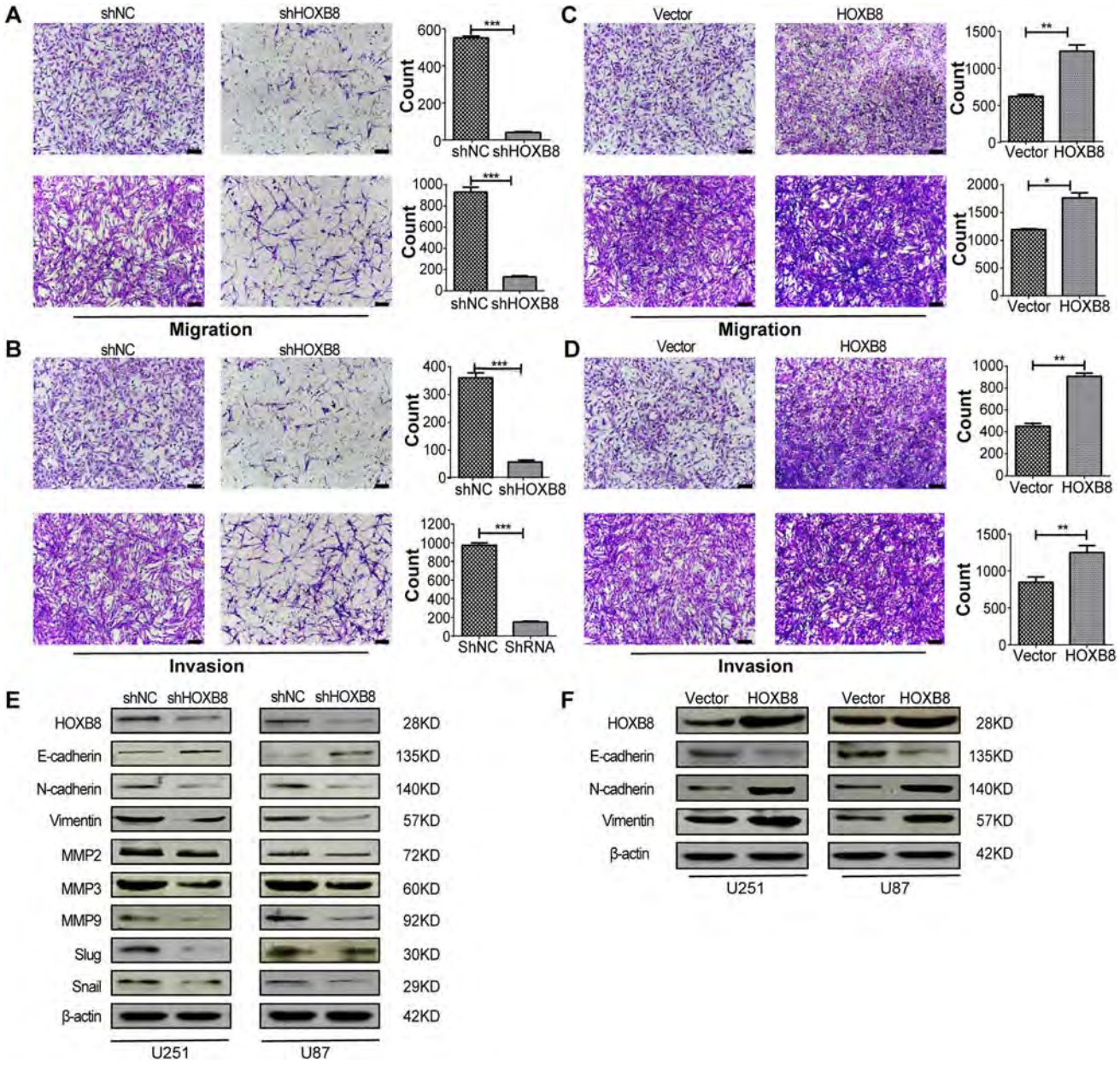

Fig. 3 HOXB8 promotes migration of glioma cells and upregulates EMT-related genes. **A**, **B** Migration (**A**) and invasion (**B**) assays in U251 (upper) and U87 (lower) cells with stable expression of shHOXB8. **C**, **D** Migration (**C**) and invasion (**D**) assays in U251 (upper) and U87 (lower) cells with overexpressed HOXB8. **E** Western blots of EMT-related proteins (E-cadherin, N-cadherin, vimentin, MMP2, MMP3, MMP9, Slug, and Snail) in U251 and U87 cells with stable expression of shHOXB8. **F** Western blots of EMT-related proteins E-cadherin, N-cadherin and vimentin in U251 cells with HOXB8 overexpression. Data are shown as the mean ± SD and were pooled from three independent experiments. Scale bars, 100 μm. $^{*}P < 0.05$, $^{**}P < 0.01$, $^{***}P < 0.001$.

migration and invasion ability (Fig. 6D, E). We revealed upregulation of an epithelial cell marker (E-cadherin) and downregulation of mesenchymal cell markers (N-cadherin and vimentin) after transient knockdown of SAMD9 (Fig. 6F). Taken together, these data suggest the working model that HOXB8/SAMD9 drives the development of glioma cells through the PI3K/AKT signaling pathway (Fig. 7).

Discussion

Increased expression of HOXB8 is associated with a wide variety of cancers. Higher expression of HOXB8 promotes gastric cancer cell migration, invasion, and the EMT, possibly through interacting with ZEB2 [21]. HOXB8 knockdown inhibits the proliferation and invasion of colon cancer cells *in vitro* as well as carcinogenesis and

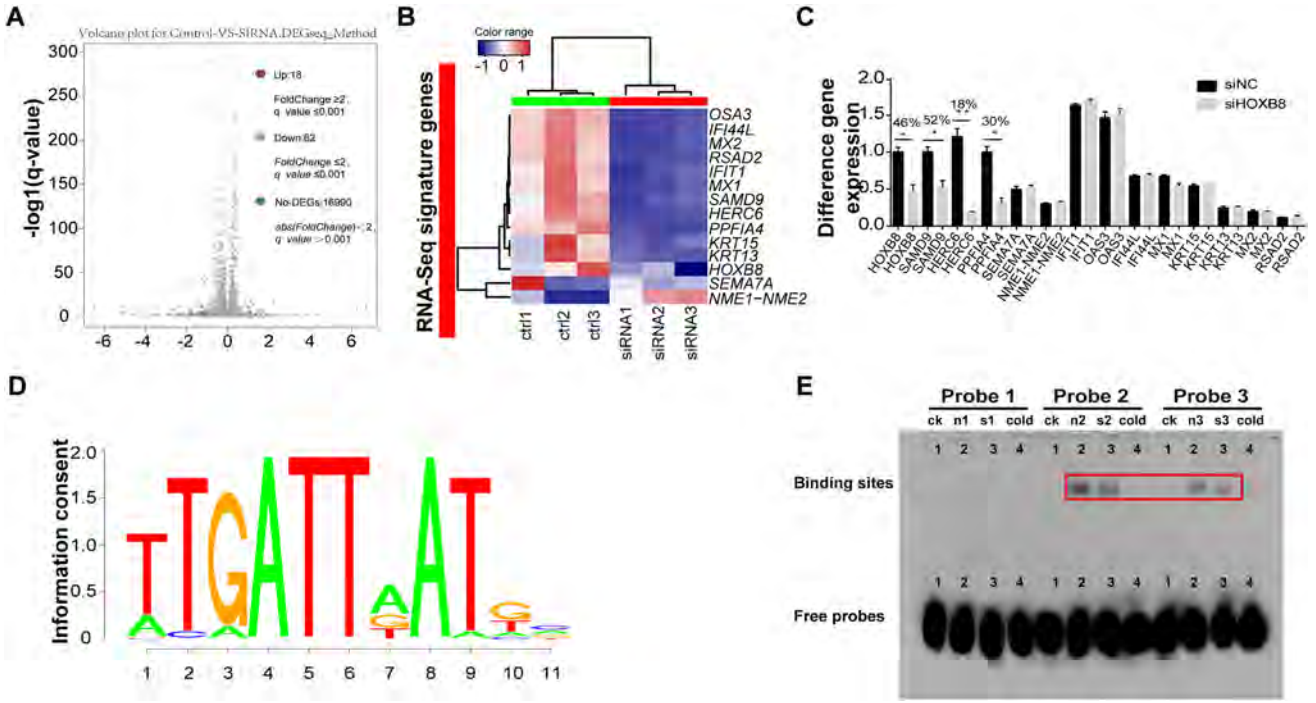

Fig. 4 SAMD9 is one of the mediators of HOXB8 in glioma cells. **A** Volcano plot depicting a log transformation plot of the fold-change of different genes by whole genome RNA sequencing in U251 cells transfected with control siRNA and HOXB8 siRNA. **B** Top differentially-expressed genes in RNA-seq results. **C** Top differentially-expressed genes in RNA sequencing confirmed in U251 cells by qPCR. $*P < 0.05$, $**P < 0.01$. **D** *De novo* motifs recovered by the MD module from the HOXB8 binding sites with a RefSeq gene within 2 kb. **E** EMSA of biotinylated SMAD9 promoter probes in nuclear extracts from siNC-treated and HOXB8 siRNA-treated U251 cells. Biotinylated probes were detected with HRP-streptavidin. "ck" and "cold" indicate competitor and unlabeled probe negative controls, respectively. Data are shown as the mean ± SD and were pooled from three independent experiments.

metastasis *in vivo*. HOXB8 also induces the EMT in colon cancer cells, and this is characterized by the down-regulation of AKT phosphorylation [26]. Higher HOXB8 expression in effusions is associated with shorter overall and progression-free survival in serous ovarian carcinoma [22]. Consistent with these findings, we found higher expression of HOXB8 in human gliomas than in non-tumor tissue (Fig. 1A). Furthermore, we found that the expression level of HOXB8 was strongly correlated with tumor pathological grading (Fig. 1B) and negatively correlated with the overall survival rate (Fig. 1C, D). We also demonstrated that strong expression of HOXB8 was critical for the proliferation (Fig. 2B), migration, and invasion (Fig. 3A, B) of glioblastoma cells and that HOXB8 might also induce the EMT in glioblastoma cells. The EMT of tumor cells is a major step towards invasion and metastasis. After knockdown of HOXB8, the epithelial marker E-cadherin was up-regulated, while Snail was down-regulated (Fig. 3E). Snail plays an important role in tumor metastasis by transcriptionally regulating a variety of factors involved in the EMT process. Vimentin was also down-regulated (Fig. 3E). Vimentin is an intermediate microfilament protein specifically expressed in mesenchymal cells and its presence indicates that cancer cells have changed from an epithelial phenotype to a mesenchymal phenotype. Nevertheless, whether the dysregulation of EMT-related proteins is directly responsible for the increased proliferation, migration, and invasion of glioma cells by HOXB8 overexpression needs further investigation.

Activation of the PI3K-AKT pathway plays an important role in the malignant proliferation of tumor cells. This pathway is considered to be one of the most basic survival signaling pathways in tumors. It is abnormally activated in many tumor types including glioma and is closely associated with the aggressiveness of glial tumors. PI3K/AKT further activates its downstream target mTOR through the TSC1/2 complex. In head and neck tumors, PI3K/AKT activation up-regulates the expression of MMP9, which degrades E-cadherin on the cell surface and promotes cell invasion and migration. We identified SAMD9 as a downstream target gene of HOXB8 in glioma cells (Fig. 4E). SAMD9 is involved in the control of cell proliferation and functions as a tumor suppressor in some cancers. Deleterious mutations in the SAMD9 gene are known to cause normophosphatemic familial tumoral carcinosis, a rare autosomal recessive disease [27]. In malignant glioma, SAMD9 is involved in death signaling in response to inactivated Sendai virus particles (HVJ-E) or

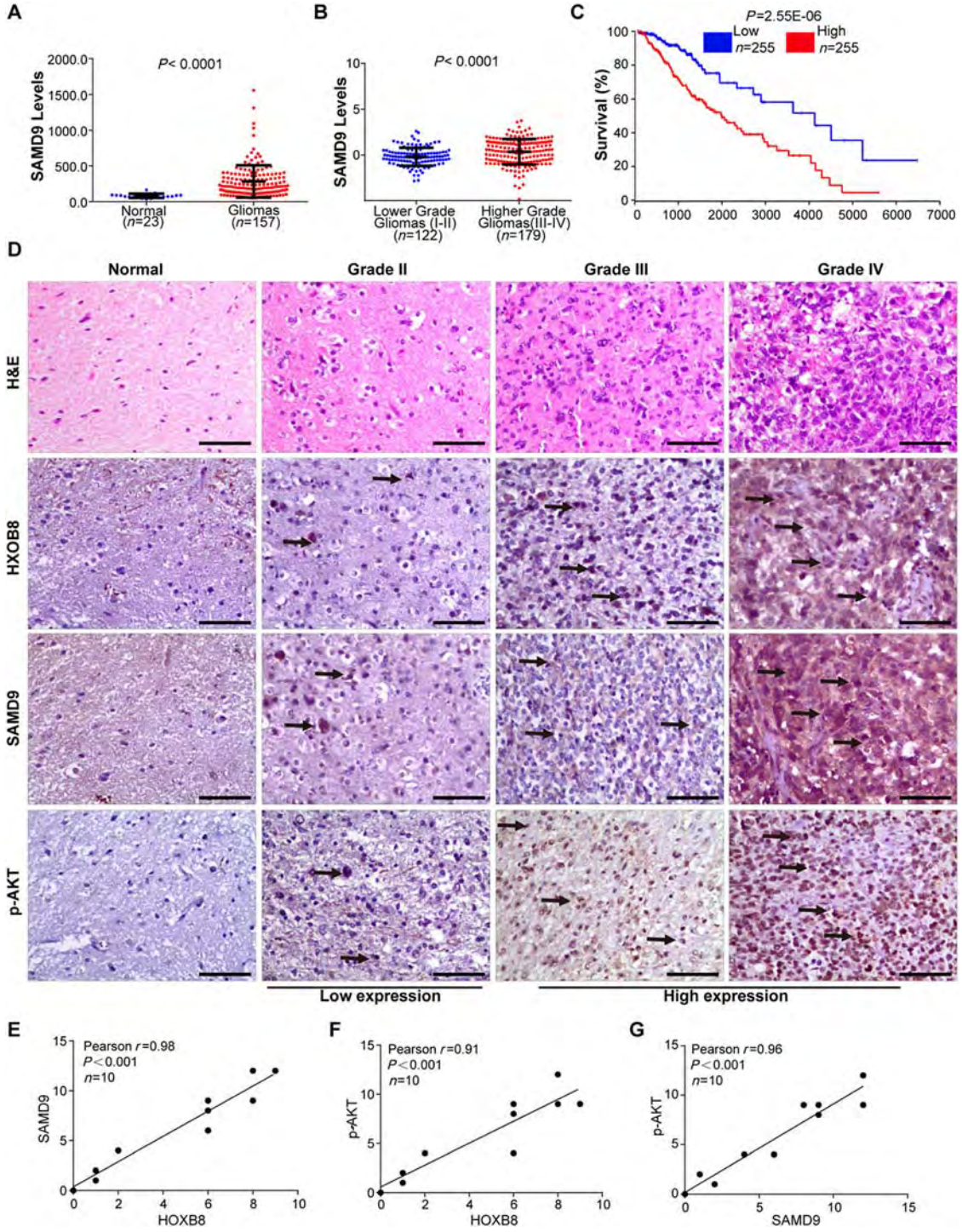

Fig. 5 SAMD9 expression in glioma cells and its correlation with HOXB8. **A** SAMD9 expression in gliomas from GEO data (23 non-tumor brain tissue samples and 157 gliomas). ***$P < 0.001$. **B** SAMD9 expression levels in higher and lower grade gliomas from CGGA data (122 low-grade and 179 high-grade). ***$P < 0.001$. **C** Overall survival of glioma patients with high and low expression of SAMD9. Data from OncoLnc (http://www.oncolnc.org/). ***$P < 0.001$. **D** One normal brain sample and 9 gliomas stained with hematoxylin and eosin (H&E) and for HOXB8, SAMD9, and p-AKT. The arrows show the positive protein expression. **E** Correlation analysis of HOXB8 and SAMD9 immunohistochemical scores. X-axis, HOXB8 staining score; y-axis, SAMD9 staining score; correlation coefficient $r = 0.96$; ***$P < 0.001$. **F** Correlation analysis of HOXB8 and p-AKT immunohistochemical scores. X-axis, HOXB8 staining score; y-axis, p-AKT staining score; correlation coefficient $r = 0.91$; ***$P < 0.001$. **G** Correlation analysis of SAMD9 and p-AKT immunohistochemical scores. X-axis, SAMD9 staining score; y-axis, p-AKT staining score; correlation coefficient $r = 0.96$; ***$P < 0.001$. Data are shown as the mean ± SD. Scale bars, 50 μm.

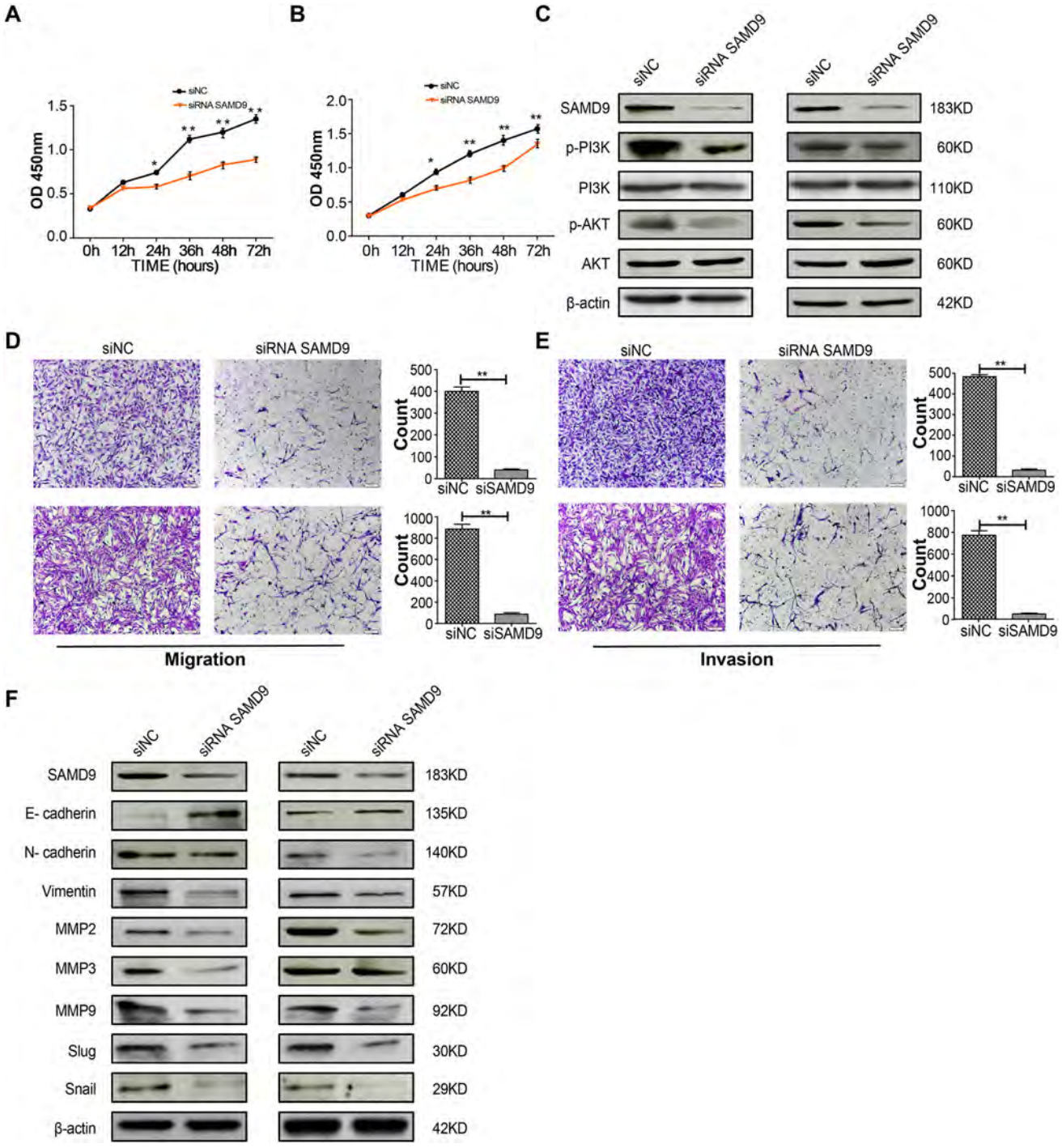

Fig. 6 SAMD9 mediates the proliferation, migration, and invasion of glioma cells and affects the activation of the AKT/PI3K pathway and expression of EMT-related genes. **A**, **B** Transient silencing of SAMD9 in U251 cells (**A**) and U87 cells (**B**) decreased the rate of proliferation. **C** Western blots of phosphorylation of PI3K and AKT in U251 and U87 cells with transiently silenced SAMD9. **D** Transient silencing of HOXB8 in U251 (upper) and U87 (lower) cells decreased the rate of migration. **E** Transient silencing of SAMD9 in U251 (upper) and U87 (lower) cells decreased the rate of invasion. **F** Western blots of EMT-related proteins (E-cadherin, N-cadherin, vimentin, MMP2, MMP3, MMP9, Slug, and Snail) in U251 and U87 cells with transiently silenced SAMD9. Data are shown as the mean ± SD and were pooled from three independent experiments. Scale bars, 100 μm. $^{*}P < 0.05$, $^{**}P < 0.01$.

type I interferon treatment. When SAMD9 expression is knocked down by RNA interference, the apoptotic cell death induced by HVJ-E is blocked in U251 cells [28]. Studies have shown that SAMD9 is closely associated with invasive fibromatosis [29]. Overexpression of SAMD9 inhibits the proliferation and invasion of non-

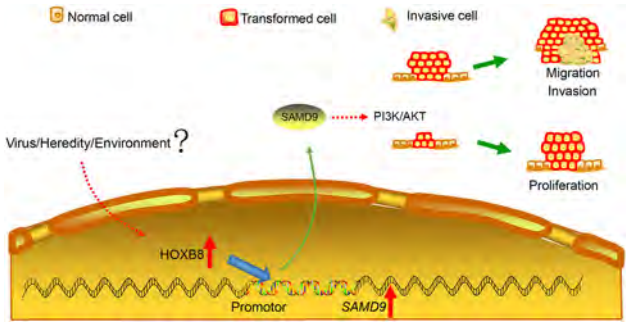

Fig. 7 Working model. Schematic showing the speculation that HOXB8/SAMD9 drives the proliferation, migration, and invasion of glioma cells and involves the PI3K/AKT signaling pathway.

small-cell lung carcinoma cells [30]. SAMD9 is significantly up-regulated in highly metastatic esophageal carcinoma, suggesting that it plays an important role in tumor metastasis [31]. Bioinformatics analysis found that SAMD9 was higher in gliomas than normal brain tissue (Fig. 5A), and its expression was positively correlated with glioma pathological grading (Fig. 5B). SAMD9 was highly expressed in gliomas and positively correlated with pathological grades from the GEO database (Table S4). Subsequent overexpression and knockdown assays showed a similar phenotype for HOXB8. However, whether dysregulated PI3K/AKT activation plays a direct role downstream of both HOXB8 and SAMD9 in the proliferation, migration, and invasion of glioma cells is not clear. In addition, further investigation is needed to fully establish SAMD9 is a direct effector gene for the HOXB8-mediated proliferation, migration, and invasion of glioma cells. Nevertheless, similar to other neural disorders [32], there is a critical need for biomarkers for diagnosis and prognosis in glioma treatment. Currently, one clinical trial is recruiting patients to evaluate and identify effective prognostic biomarkers for malignant glioma [33, 34]. HOXB8 expression evaluation in initial diagnostic biopsy sections could provide a valuable indicator in terms of prognosis.

In conclusion, our study identified HOXB8 as a crucial contributor to the aggressiveness of GBM. With further detailed mechanistic investigation, HOXB8 may prove to be an interesting prognostic biomarker and therapeutic target, blockade of which increases the sensitivity of glioma cells to current treatment.

Acknowledgements We would like to give special thanks to Dr. Wangshu Xu for her helpful editing improvements and Dr. Hongqiang Du for his contributions to trial management. This work was supported by the National Natural Science Foundation of China (31571298).

Conflict of interest The authors declare no competing interests.

References

1. Ostrom QT, Gittleman H, Stetson L, Virk SM, Barnholtz-Sloan JS. Epidemiology of gliomas. Cancer Treat Res 2015, 163: 1–14.
2. Schwab DE, Lepski G, Borchers C, Trautmann K, Paulsen F, Schittenhelm J. Immunohistochemical comparative analysis of MAP-2, NOGO-A, OLIG-2 and WT-1 expression in WHO 2016 classified neuroepithelial tumours and their prognostic value. Pathol Res Pract 2018, 214: 15–24.
3. DeWeerdt S. The genomics of brain cancer. Nature 2018, 561: S54–S55.
4. Xie H, Wang M, Bonaldo Mde F, Rajaram V, Stellpflug W, Smith C, *et al.* Epigenomic analysis of Alu repeats in human ependymomas. Proc Natl Acad Sci U S A 2010, 107: 6952–6957.
5. Venteicher AS, Tirosh I, Hebert C, Yizhak K, Neftel C, Filbin MG, *et al.* Decoupling genetics, lineages, and microenvironment in IDH-mutant gliomas by single-cell RNA-seq. Science 2017, 355.
6. Perry A, Wesseling P. Histologic classification of gliomas. Handb Clin Neurol 2016, 134: 71–95.
7. Birk HS, Han SJ, Butowski NA. Treatment options for recurrent high-grade gliomas. CNS Oncol 2017, 6: 61–70.
8. Ceccarelli M, Barthel FP, Malta TM, Sabedot TS, Salama SR, Murray BA, *et al.* Molecular profiling reveals biologically discrete subsets and pathways of progression in diffuse glioma. Cell 2016, 164: 550–563.
9. Sehmer EA, Hall GJ, Greenberg DC, O'Hara C, Wallingford SC, Wright KA, *et al.* Incidence of glioma in a northwestern region of England, 2006-2010. Neuro Oncol 2014, 16: 971–974.
10. Lu VM, Welby JP, Mahajan A, Laack NN, Daniels DJ. Reirradiation for diffuse intrinsic pontine glioma: a systematic review and meta-analysis. Childs Nerv Syst 2019, 35: 739–746.
11. Kieran MW, Goumnerova L, Manley P, Chi SN, Marcus KJ, Manzanera AG, *et al.* Phase I study of gene-mediated cytotoxic immunotherapy with AdV-tk as adjuvant to surgery and radiation for pediatric malignant glioma and recurrent ependymoma. Neuro Oncol 2019, 21: 537–546.
12. Shah N, Sukumar S. The Hox genes and their roles in oncogenesis. Nat Rev Cancer 2010, 10: 361–371.
13. Quinonez SC, Innis JW. Human HOX gene disorders. Mol Genet Metab 2014, 111: 4–15.
14. Kutejova E, Engist B, Self M, Oliver G, Kirilenko P, Bobola N. Six2 functions redundantly immediately downstream of Hoxa2. Development 2008, 135: 1463–1470.
15. Domsch K, Papagiannouli F, Lohmann I. The HOX-apoptosis regulatory interplay in development and disease. Curr Top Dev Biol 2015, 114: 121–158.
16. Bakalenko NI, Novikova EL, Nesterenko AY, Kulakova MA. Hox gene expression during postlarval development of the polychaete Alitta virens. Evodevo 2013, 4: 13.
17. Pastori C, Kapranov P, Penas C, Peschansky V, Volmar CH, Sarkaria JN, *et al.* The Bromodomain protein BRD4 controls HOTAIR, a long noncoding RNA essential for glioblastoma proliferation. Proc Natl Acad Sci U S A 2015, 112: 8326–8331.
18. Hutlet B, Theys N, Coste C, Ahn MT, Doshishti-Agolli K, Lizen B, *et al.* Systematic expression analysis of Hox genes at adulthood reveals novel patterns in the central nervous system. Brain Struct Funct 2016, 221: 1223–1243.
19. Vider BZ, Zimber A, Hirsch D, Estlein D, Chastre E, Prevot S, *et al.* Human colorectal carcinogenesis is associated with deregulation of homeobox gene expression. Biochem Biophys Res Commun 1997, 232: 742–748.
20. Sugimachi K, Matsumura T, Hirata H, Uchi R, Ueda M, Ueo H, *et al.* Identification of a bona fide microRNA biomarker in serum

exosomes that predicts hepatocellular carcinoma recurrence after liver transplantation. Br J Cancer 2015, 112: 532–538.
21. Ding WJ, Zhou M, Chen MM, Qu CY. HOXB8 promotes tumor metastasis and the epithelial-mesenchymal transition via ZEB2 targets in gastric cancer. J Cancer Res Clin Oncol 2017, 143: 385–397.
22. Stavnes HT, Holth A, Don T, Kaern J, Vaksman O, Reich R, *et al.* HOXB8 expression in ovarian serous carcinoma effusions is associated with shorter survival. Gynecol Oncol 2013, 129: 358–363.
23. Kelppe J, Thoren H, Ristimaki A, Haglund C, Sorsa T, Hagstrom J. BRAF V600E expression in ameloblastomas-A 36-patient cohort from Helsinki University Hospital. Oral Dis 2019, 25: 1169–1174.
24. Nishida H, Kashima K, Yano S, Daa T, Arakane M, Oyama Y, *et al.* A biotin tagging immunoelectron microscopy for paraffin-embedded sections. Appl Immunohistochem Mol Morphol 2019. https://doi.org/10.1097/pai.0000000000000735.
25. Sousa DA, Silva K, Cascon CM, Silva FBF, Mello MFV, Leite JDS, *et al.* Epidermal growth factor receptor 2 immunoexpression in gastric cells of domestic cats with H. heilmannii infection. Acta Histochem 2019, 121: 413–418.
26. Schimanski CC, Frerichs K, Rahman F, Berger M, Lang H, Galle PR, *et al.* High miR-196a levels promote the oncogenic phenotype of colorectal cancer cells. World J Gastroenterol 2009, 15: 2089–2096.
27. Hershkovitz D, Gross Y, Nahum S, Yehezkel S, Sarig O, Uitto J, *et al.* Functional characterization of SAMD9, a protein deficient in normophosphatemic familial tumoral calcinosis. J Invest Dermatol 2011, 131: 662–669.
28. Tanaka M, Shimbo T, Kikuchi Y, Matsuda M, Kaneda Y. Sterile alpha motif containing domain 9 is involved in death signaling of malignant glioma treated with inactivated Sendai virus particle (HVJ-E) or type I interferon. Int J Cancer 2010, 126: 1982–1991.
29. Li CF, MacDonald JR, Wei RY, Ray J, Lau K, Kandel C, *et al.* Human sterile alpha motif domain 9, a novel gene identified as down-regulated in aggressive fibromatosis, is absent in the mouse. BMC Genomics 2007, 8: 92.
30. Ma Q, Yu T, Ren YY, Gong T, Zhong DS. Overexpression of SAMD9 suppresses tumorigenesis and progression during non small cell lung cancer. Biochem Biophys Res Commun 2014, 454: 157–161.
31. Tang S, Zheng X, He L, Qiao L, Jing D, Ni Z, *et al.* Significance of SAMD9 expression in esophageal squamous cell carcinoma. Xi Bao Yu Fen Zi Mian Yi Xue Za Zhi 2014, 30: 411–413.
32. Yan X, Mai L, Lin C, He W, Yin G, Yu J, *et al.* CSF-based analysis for identification of potential serum biomarkers of neural tube defects. Neurosci Bull 2017, 33: 436–444.
33. Paech D, Dreher C, Regnery S, Meissner JE, Goerke S, Windschuh J, *et al.* Relaxation-compensated amide proton transfer (APT) MRI signal intensity is associated with survival and progression in high-grade glioma patients. Eur Radiol 2019, 29: 4957–4967.
34. Liu C, Sage JC, Miller MR, Verhaak RG, Hippenmeyer S, Vogel H, *et al.* Mosaic analysis with double markers reveals tumor cell of origin in glioma. Cell 2011, 146: 209–221.

Neurosci. Bull. April, 2020, 36(4):372–384
https://doi.org/10.1007/s12264-019-00442-0

www.neurosci.cn
www.springer.com/12264

ORIGINAL ARTICLE

Epidural Spinal Cord Stimulation Promotes Motor Functional Recovery by Enhancing Oligodendrocyte Survival and Differentiation and by Protecting Myelin after Spinal Cord Injury in Rats

Gang Li[1,2] · Zhong-Kai Fan[3] · Guang-Fei Gu[1,2] · Zhi-Qiang Jia[4] · Qiang-Qiang Zhang[3] · Jun-Yu Dai[3] · Shi-Sheng He[1,2]

Received: 29 April 2019 / Accepted: 23 July 2019 / Published online: 16 November 2019

Abstract Epidural spinal cord stimulation (ESCS) markedly improves motor and sensory function after spinal cord injury (SCI), but the underlying mechanisms are unclear. Here, we investigated whether ESCS affects oligodendrocyte differentiation and its cellular and molecular mechanisms in rats with SCI. ESCS improved hindlimb motor function at 7 days, 14 days, 21 days, and 28 days after SCI. ESCS also significantly increased the myelinated area at 28 days, and reduced the number of apoptotic cells in the spinal white matter at 7 days. SCI decreased the expression of 2′,3′-cyclic-nucleotide 3′-phosphodiesterase (CNPase, an oligodendrocyte marker) at 7 days and that of myelin basic protein at 28 days. ESCS significantly upregulated these markers and increased the percentage of Sox2/CNPase/DAPI-positive cells (newly differentiated oligodendrocytes) at 7 days. Recombinant human bone morphogenetic protein 4 (rhBMP4) markedly downregulated these factors after ESCS. Furthermore, ESCS significantly decreased BMP4 and p-Smad1/5/9 expression after SCI, and rhBMP4 reduced this effect of ESCS. These findings indicate that ESCS enhances the survival and differentiation of oligodendrocytes, protects myelin, and promotes motor functional recovery by inhibiting the BMP4-Smad1/5/9 signaling pathway after SCI.

Keywords Spinal cord injury · Epidural spinal cord stimulation · Oligodendrocyte · Differentiation · Remyelination

Introduction

Spinal cord injury (SCI) leads to motor, sensory, and autonomic dysfunction below the site of injury [1]. In the USA, the recent estimated number of persons with SCI was ~291,000, with ~17,730 new cases each year (www.uab.edu/nscisc). Although there have been numerous studies on SCI, effective treatment is still lacking [2]. Accumulating evidence indicates that epidural spinal cord stimulation (ESCS) not only effectively relieves neuropathic pain [3, 4], but also significantly improves motor function [5–9], and even restores cough after SCI [10]. As a result, ESCS is becoming a leading candidate for the treatment of SCI [11]. Apart from activating residual neuronal pathways [12, 13], ESCS also promotes anatomical plasticity of the nervous system after SCI [7, 12–14]. However, it is unclear whether ESCS promotes oligodendrocyte differentiation or reduces myelin loss after SCI.

Oligodendrocytes wrap axons with myelin sheaths, provide trophic support, and protect neurons and their axons [15]. Oligodendrocyte loss and axonal demyelination are major pathological events hindering functional recovery after SCI [16]. Increased numbers of mature oligodendrocytes can significantly improve motor functional recovery [17]. Although inhibition of oligodendrocyte apoptosis after SCI reduces axonal demyelination and

✉ Shi-Sheng He
heshishengtj@163.com

1 Department of Orthopedics, Shanghai Tenth People's Hospital, Tongji University School of Medicine, Shanghai 200072, China

2 Spinal Pain Research Institute, Tongji University School of Medicine, Shanghai 200072, China

3 Department of Orthopaedics, The First Affiliated Hospital, Jinzhou Medical University, Jinzhou 121001, China

4 Department of Spinal Surgery, The Second Affiliated Hospital, Henan University of Science and Technology, Luoyang 471003, China

promotes neurological recovery, stimulating oligodendrocyte differentiation is also a promising approach for replacing damaged oligodendrocytes and enhancing remyelination [18–23]. Studies have shown that spontaneous oligodendrocyte replacement and remyelination occur naturally from both endogenous neural stem cells (eNSCs) and oligodendrocyte progenitor cells (eOPCs) in several animal models of SCI [16, 18, 19, 24–28]. However, this self-repair response is not sufficient to compensate for the oligodendrocyte loss and demyelination caused by SCI, ultimately leading to spinal cord dysfunction [16, 29]. Therefore, exploring novel therapeutic strategies for promoting oligodendrocyte differentiation and remyelination is key to enhancing functional recovery after SCI [30, 31].

ESCS is an important neuromodulatory approach, whereby an electrode is implanted into the spinal epidural space and directly stimulates the spinal cord tissue with a suitable current to exert a therapeutic effect [32]. Many studies have suggested that other electrical stimulation methods also enhance neurological functional recovery by promoting eNSC proliferation and their differentiation into oligodendrocytes, thereby stimulating axonal remyelination after SCI [33–36]. For example, Becker *et al.* [36] reported that electrical stimulation promotes the proliferation of endogenous neural progenitor cells and their differentiation into oligodendrocytes after SCI in adult rats. Geng *et al.* [34] reported that electroacupuncture promotes the proliferation of eNSCs and their differentiation into oligodendrocytes by inhibiting the activation of the Notch signaling pathway after SCI in rats. During CNS development, bone morphogenetic proteins (BMPs) repress oligodendrogenesis while enhancing the development of astrocytes [37]. BMP4 suppresses the differentiation of adult eOPCs into oligodendrocytes, and inhibition of BMP4 signaling promotes remyelination and functional recovery from CNS demyelinating disease [38]. Our previous studies showed that ESCS promotes eNSC proliferation (unpublished), but the effects of ESCS on oligodendrocyte differentiation and myelination after SCI are still unclear. Therefore, in the present study, we investigated whether ESCS affects oligodendrocyte differentiation in the spinal cord white matter after SCI, and explored the underlying mechanisms.

Materials and Methods

Animals, Chemicals, Electrodes, and External Electrical Stimulator

All the adult female Sprague-Dawley rats (250 g–300 g) were provided by the Experimental Animals Center of Jinzhou Medical University. All the animal experiments were conducted strictly following the National Institutes of Health Guide for the Care and Use of Laboratory Animals and were approved by the Animal Care Ethics Commission of Shanghai Tenth People's Hospital. Recombinant human bone morphogenetic protein 4 (rhBMP4, HY-P7007, MedChemexpress, Monmouth Junction, NJ) was dissolved in dimethyl sulfoxide (DMSO). The stimulating electrodes were independently developed by the Control Science and Engineering Department of Huazhong University of Science and Technology (Fig. 1A). The external electrical stimulator (Isostim A320) was from World Precision Instruments Inc. (Sarasota, FL).

Experimental Groups and Drug Administration

Sprague-Dawley rats were randomly divided into four groups: Sham (T10 and T13 laminectomy only), SCI (T10 contusive injury and T13 laminectomy), SCI+ESCS (abbreviated to ESCS), and SCI+ESCS+rhBMP4 (ESCS+BM; 2.5 μL, 1 μg/μL rhBMP4 [39]) groups. Rats in the sham and SCI groups were not given electrical stimulation. Rats in the ESCS and ESCS+rhBMP4 groups were given monophasic direct current pulse stimulation immediately after the incision was sutured [14], and this treatment lasted for 30 min per day over the course of 1 week [7, 40]. The rats in the ESCS+rhBMP4 group were given rhBMP4 immediately after SCI, while the rats in the Sham, SCI, and ESCS groups received an equivalent volume of DMSO. A microsyringe (F519159, Sangon Biotech, Shanghai, China) was used to inject 2.5 μL rhBMP4 at 0.5 μL/min into the spinal cord [41]. Each group was randomly divided into three subgroups for subsequent experiments: (A) assessment of hindlimb motor function for 7 days and 28 days [42, 43] (n = 6); (B) semi-quantitative reverse transcription-polymerase chain reaction (RT-PCR) and western blot (n = 6 each); (C) immunofluorescent labeling, fluorescence TUNEL staining, and Luxol fast blue (LFB) (n = 6 each) histological examination when the hindlimb motor function test was finished at 28 days after SCI. Myelin basic protein (MBP) and LFB staining were assessed at 28 days, while other indicators were measured at 7 days after SCI.

SCI Model Establishment, Epidural Electrode Implantation, and Stimulation Parameters

Adult rats were anesthetized with pentobarbital sodium (40 mg/kg, i.p.). The incomplete contusive SCI model was established using a self-made Allen's impact device and postoperative care was as described previously [44]. In brief, after anesthesia and sterilization, the skin and muscle overlying the spinal column were incised and a

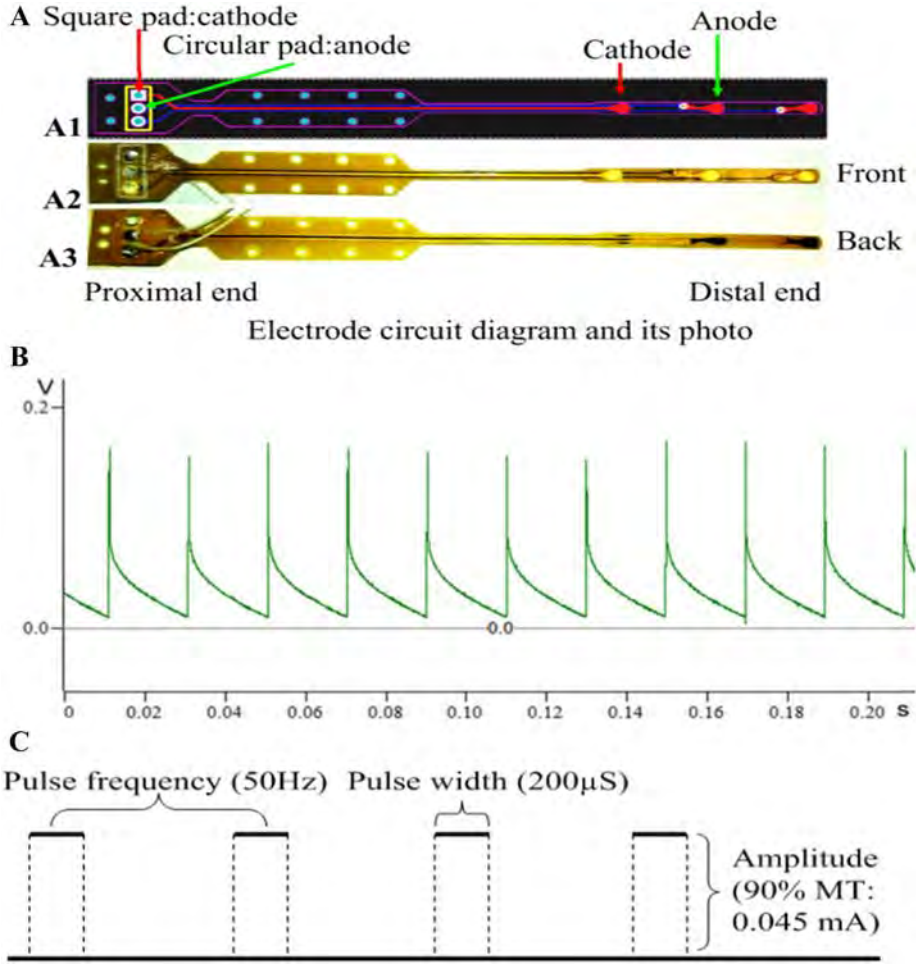

Fig. 1 Electrode and direct-current square-wave pulses. **A** Electrode circuit diagram (**A1**) and front (**A2**) and back (**A3**) photographs. The electrode is made by a flexible circuit board technique and implanted into the dorsal epidural space. The electrode material is polyimine, which has good biocompatibility. Three circular gold contacts 1 mm in diameter are separated by 7 mm gaps, while eight small holes at the center and two at the proximal end are used to fix the electrode to the paravertebral ligament and muscles [47]. We set the middle gold contact as the anode and the proximal gold contact as the cathode. **B** Traces of direct-current square-wave pulses in a simulated rat environment. **C** Parameters of ESCS (frequency 50 Hz, pulse width 200 μS, amplitude 90% MT: 0.045 mA). MT, motor threshold.

laminectomy was performed at T10 and T13, leaving the dura intact. A firing pin (20 g in weight and 2 mm in diameter) was then dropped onto the exposed T10 region through a glass casing (2.2 mm inner diameter) from a height of 25.0 mm. After SCI, the stimulating electrode was implanted into the epidural space from the T13 segment with the distal end of the electrode oriented rostrally and the anode center facing the epicenter of the lesion of T10, and the positioning holes on the electrode were fixed to the paravertebral ligament and muscles. The cathode and anode wires were tunneled to the animal's neck, where plugs were attached firmly to the skin. As the motor threshold (MT) could not be measured after SCI due to the severity of injury and possible spinal shock, we measured it in rats after sham operation. These rats were given direct-current square-wave pulse stimulation (frequency 2 Hz, pulse width 200 μs) when they were awake; the current intensity was gradually increased until the first occurrence of symmetrical contractions of the lower trunk and/or hindlimbs was seen or palpated; the current intensity at that point was the MT [45]. The MT was 0.05 ± 0.009 mA (n = 6), so the stimulus parameters were set at a frequency of 50 Hz, pulse width 200 μS, and intensity 0.045 mA [7, 45, 46] (Fig. 1B, C).

Basso, Beattie, and Bresnahan (BBB) Score Assessment

The BBB score has 22 grades ranging from 0 to 21, and is used to assess the recovery of hindlimb motor function after SCI in rats [48]. A score of 0 indicates complete paralysis, and the score of 21 indicates that motor function is completely normal. The BBB scores were collected and analyzed by two evaluators who were blinded to the experimental groups at 1 day, 7 days, 14 days, 21 days, and 28 days after SCI.

Semi-quantitative RT-PCR

At 7 days and 28 days after SCI, 6 mm of spinal cord (3 mm at the rostral and caudal ends of the epicenter) was removed and equally divided into two parts centered the epicenter. One part was used to extract total RNA with TRIzol reagent (Invitrogen, Waltham, MA), and the other

part was used for extracting total protein. The purity of the RNA was evaluated by the A260/A280 ratio (normal range 1.7–2.1) using a NanoDrop 2000 Spectrophotometer (Thermo Fisher Scientific, Waltham, MA). RT-PCR was performed following the instructions in the PrimeScript™ One Step RT-PCR Kit Ver.2 (Takara, Beijing, China). A 50-μL reaction system containing 0.5 μg RNA was placed in an S1000 PCR instrument (Bio-Rad, Hercules, CA) with the reaction conditions described in the operating instructions. The expression of 2′,3′-cyclic-nucleotide 3′-phosphodiesterase (CNPase) and MBP was assessed using the following primers sets (Beijing Dingguochangsheng Biotechnology Co., Ltd, Beijing, China): CNPase; F–GAG ACA TAG TGC CCG CAA AG, R–ATC TTG GTG CCG TTG TGG TA (287 bp); MBP; F–GAC GAG CTT CAG ACC ATC CA, R–CCA TAG TTC CTC TAC GCC TCG (263 bp); β-actin F–CTC TGT GTG GAT TGG TGG CT, R–AGC TCA GTA ACA GTC CGC CT (136 bp). Products of RT-PCR and a 50-bp DNA ladder marker (MD1001, Simgen, China) were separated by 2% agarose gel electrophoresis and the imaging results were recorded with ethidium bromide staining. NIH ImageJ software was used to determine the relative band intensity.

Western Blot Analysis

The protein extract was transferred to a 0.22- or 0.45- μm polyvinylidene fluoride (PVDF) membrane after separation on 12% SDS-polyacrylamide gel. The PVDF membranes were blocked with 0.1% bovine serum albumin at room temperature for 2 h, and then incubated with the primary antibody on a shaking table at 4°C overnight. The primary antibodies were as follows: anti-CNPase (marker of oligodendrocytes, ab6319, 1:250; Abcam, Cambridge, UK), anti-MBP (78896S, 1:1000; CST, Danvers, MA), anti-BMP4 (ab39973, 1:1000; Abcam, Cambridge, UK), anti-phospho-Smad1/5/9 (#13820, 1:1000; CST, Danvers, MA), anti-Smad1/5/9 (ab66737, 1:1500; Abcam, Cambridge, UK), and β-actin (sc-47778, 1:1000; Santa Cruz Biotechnology, Inc., Santa Cruz, CA). After fully cleaning the PVDF membrane, the corresponding secondary antibodies [goat anti-rabbit and goat anti-mouse IgG-HRP (sc-2004 or sc-2005; all 1:2000; Santa Cruz Biotechnology, Inc.)] were incubated for 2 h at room temperature. The PVDF membranes were illuminated with electrochemiluminescence and photographed with a gel imaging system. ImageJ was used to measure the gray values of the target proteins and β-actin bands, and target proteins were normalized to β-actin to reflect their relative expression levels.

Immunofluorescent Single and Double Labeling

The rats were sacrificed and the injured spinal cords were fixed in 4% paraformaldehyde at 7 days and 28 days after SCI. Then 6 mm of spinal cord (3 mm at the rostral and caudal ends of the epicenter) were removed and used to cut coronal and sagittal frozen sections. The coronal sections were cut after trimming 1 mm from the epicenter of the lesion. Sagittal sections with gray and white matter on both sides were cut parallel to the posterior median sulcus. Serial 10-μm frozen sections were used for histological examination. Sections were permeabilized with 0.25% Triton X-100 for 20 min, and then incubated with 5% normal goat serum (abs933, Absin, Shanghai, China) for 1 h at room temperature to block non-specific binding sites. The sections were incubated with the primary antibodies (diluted in 5% normal goat serum) anti-CNPase (ab6319, 1:50; Abcam, Cambridge, UK), anti-Sox2 (marker of NSCs, ab97959, 1:400; Abcam, Cambridge, UK), anti-MBP (78896S, 1:200; CST, Danvers, MA), anti-BMP4 (ab39973, 1:200; Abcam, Cambridge, UK), and anti-phospho-Smad1/5/9 (#13820, 1:250; CST, Danvers, MA) in a humidified chamber at 4°C overnight. After fully cleaning the unbound primary antibody from the sections, they were incubated with the secondary antibodies Alexa Fluor 594 goat anti-mouse IgG and/or Alexa Fluor 488 goat anti-rabbit IgG (A-11005 and A-11034, all 1:250; Thermo Fisher Scientific, Waltham, MA) for 2 h at room temperature in the dark. After immunostaining, the sections were incubated with 4′,6-diamidino-2-phenylindole (DAPI, 1 μg/mL) for 2 min in the dark to mark the nuclei. The primary antibody was replaced with PBS buffer in the negative control. A fluorescence microscope (Leica DMI4000B, Wetzlar, Germany) was used to visualize all indicators. Two sections separated by >100 μm for each indicator in one rat were used for immunofluorescent labeling. The counting function in Photoshop CS3 was used to count the numbers of sox2/CNPase double-positive and phospho-Smad1/5/9-positive cells. and ImageJ was used to quantify the mean fluorescence intensity of CNPase, MBP, and BMP4. Mean fluorescence intensity = integrated density / area; percentage immunopositive cells = 100 × number of immunopositive cells / total number of cells (DAPI-stained cells) [44].

Fluorescence TUNEL Staining

Serial 10-μm transverse frozen sections (two sections separated by 100 μm per rat) were prepared for TUNEL labeling which was performed according to the *In Situ* Cell Death Detection Kit, TMR red (Roche, Basel, Switzerland). After TUNEL staining, all the sections were incubated with 1 μg/mL DAPI for 2 min to counterstain nuclei.

Apoptotic cells (red) in the spinal white matter were visualized under a fluorescence microscope and counted using the counting function of Photoshop CS3 [49]. Percentage apoptotic cells = 100 × (red cells / blue cells).

LFB Staining

Serial 10-μm transverse frozen sections (two sections separated by 100 μm per rat) were incubated in 1×PBS for 20 min and then stained according to the instructions with the LFB kit (G3245, Beijing Solarbio Science and Technology Co., Ltd, Beijing, China). Finally, these sections were observed under a light microscope. The proportion of LFB-positive area in the spinal white matter at 28 days after SCI was analyzed with ImageJ [50].

Statistical Analysis

All data are expressed as the mean ± SD, and were analyzed using one-way analysis of variance (ANOVA) with the LSD-*t* test. SPSS version 19.0 was used for all analyses. $P < 0.05$ was considered statistically significant.

Results

ESCS Improves Hindlimb Motor Function at 7 Days, 14 Days, 21 Days, and 28 Days after SCI in Rats

BBB scores were lower in the SCI group than in the sham group at 7 days, 14 days, 21 days, and 28 days ($P < 0.05$). In contrast, compared with the SCI group, the BBB scores were markedly higher in the ESCS group on these days ($P < 0.05$). In addition, the BBB scores were lower in the ESCS+BM group than in the ESCS group at 7 days, 14 days, and 28 days ($P < 0.05$). These results indicate that ESCS improves hindlimb motor function at 7 days, 14 days, 21 days, and 28 days following SCI in rats (Fig. 2).

ESCS Reduces Myelin Loss in Spinal White Matter 28 Days after SCI

The LFB stain binds myelin to reveal the myelin structure of neural tissue. The relative LFB-stained area can therefore be used to compare myelination among groups [50]. Compared with the Sham group, the relative (proportional) LFB-stained area was reduced in the SCI group at 28 days ($P < 0.05$). Notably, this area was markedly higher in the ESCS group than in the SCI group ($P < 0.05$). Moreover, in the ESCS+BM group, the area was lower than in the ESCS group ($P < 0.05$). These results demonstrate that ESCS reduces myelin loss in the spinal white matter by inhibiting the BMP4-Smad1/5/9 signaling pathway after SCI (Fig. 3).

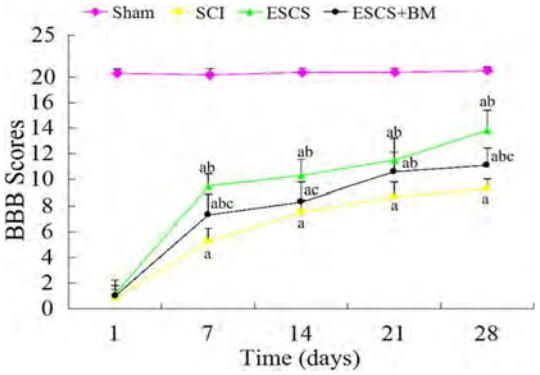

Fig. 2 Effects of ESCS on hindlimb motor dysfunction at 1 day, 7 days, 14 days, 21 days, and 28 days after SCI in rats ($n = 6$). $^{a}P < 0.05$ *vs* Sham, $^{b}P < 0.05$ *vs* SCI, $^{c}P < 0.05$ *vs* ESCS.

ESCS Inhibits Apoptosis in Spinal White Matter 7 Days after SCI

TUNEL staining showed that, compared with the sham group, the percentage of apoptotic cells in the white matter was higher in the SCI group ($P < 0.05$). Furthermore, compared with the SCI group, this percentage was lower in the ESCS group ($P < 0.05$). There was no significant difference between the ESCS+BM and ESCS groups ($P > 0.05$) (Fig. 4).

ESCS Up-regulates CNPase Expression 7 Days after SCI in Rats

CNPase is an enzyme expressed by immature and mature oligodendrocytes, and is therefore used as an oligodendrocyte marker [51, 52]. We used RT-PCR and western blotting to evaluate CNPase expression to assess the effects of ESCS on oligodendrocyte survival. The mRNA and protein levels of CNPase were lower in the SCI group than in the sham group ($P < 0.05$; Fig. 5), indicating oligodendrocyte loss after SCI. Notably, compared with the SCI group, CNPase expression was markedly higher in the ESCS group ($P < 0.05$), suggesting that ESCS reduces oligodendrocyte loss after SCI. In the ESCS+BM group, CNPase expression was lower than in the ESCS group ($P < 0.05$), suggesting that ESCS reduces oligodendrocyte loss after SCI by inhibiting the BMP4-Smad1/5/9 signaling pathway.

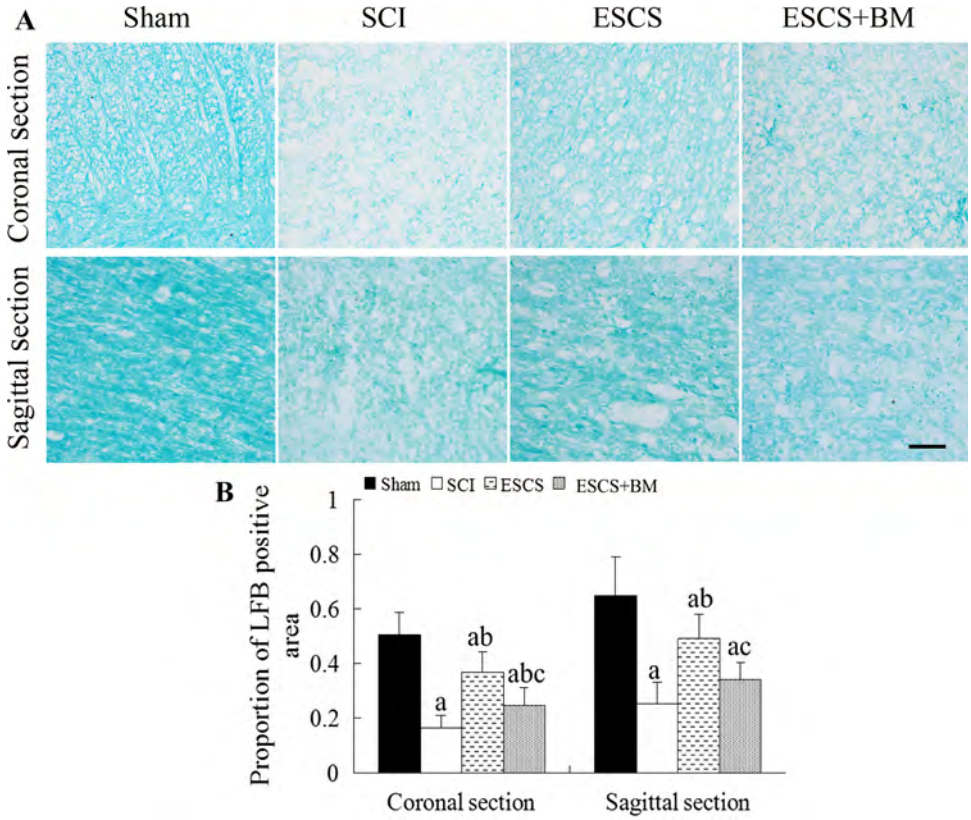

Fig. 3 Effects of ESCS on the proportion of LFB-positive area in the spinal white matter at 28 days after SCI (n = 6). **A** Representative images of LFB staining (scale bar, 100 μm). **B** Quantification of the proportion of LFB-positive area ($^{a}P < 0.05$ *vs* Sham, $^{b}P < 0.05$ *vs* SCI, $^{c}P < 0.05$ *vs* ESCS).

ESCS Promotes Oligodendrocyte Differentiation after SCI

Sox2 is a universal marker of eNSCs and endogenous neural progenitor cells [50, 53], and is also expressed by eOPCs [54]. We performed immunofluorescence double labeling for Sox2/CNPase/DAPI (newly-differentiated oligodendrocytes) [51, 53–55] to investigate the effects of ESCS on oligodendrocyte differentiation in the spinal white matter 7 days after SCI. As shown in Fig. 6, the mean fluorescence intensity of CNPase (Fig. 5) was consistent with the RT-PCR and western blot results. Moreover, the percentage of newly-differentiated oligodendrocytes increased after SCI compared with the sham group ($P < 0.05$). Interestingly, the percentage of newly-differentiated oligodendrocytes increased after ESCS compared with the SCI group ($P < 0.05$), suggesting that ESCS promotes oligodendrocyte differentiation. rhBMP4 decreased the percentage of newly-differentiated oligodendrocytes compared with the ESCS group ($P < 0.05$; Fig. 6). These results suggest that ESCS reduces oligodendrocyte loss and promotes oligodendrocyte differentiation by inhibiting the BMP4-Smad1/5/9 signaling pathway after SCI.

ESCS Increases MBP Expression in Spinal White Matter 28 Days after SCI

MBP is a structural protein in the plasma membrane of oligodendrocytes that plays a critical role in myelin compaction and thickening in the CNS [56]. Mature oligodendrocytes express myelin proteins, among which MBP is one of the most abundant [51]. We used RT-PCR, western blots, and immunofluorescence staining to evaluate MBP expression after SCI. The MBP mRNA and protein expression levels were markedly lower after SCI compared with the sham group ($P < 0.05$). In contrast, compared with the SCI group, MBP expression was higher in the ESCS group ($P < 0.05$). Moreover, in the ESCS+BM group, MBP expression was decreased compared with the ESCS group ($P < 0.05$), indicating that ESCS protects the myelin in the spinal white matter after SCI by inhibiting the BMP4-Smad1/5/9 signaling pathway (Fig. 7).

ESCS Inhibits the BMP4-Smad1/5/9 Signaling Pathway 7 Days after SCI in Rats

The BMP4-Smad1/5/9 signaling pathway regulates the proliferation and differentiation of OPCs and NSCs [38, 57, 58]. To further clarify the mechanisms by which ESCS affects oligodendrocyte differentiation and

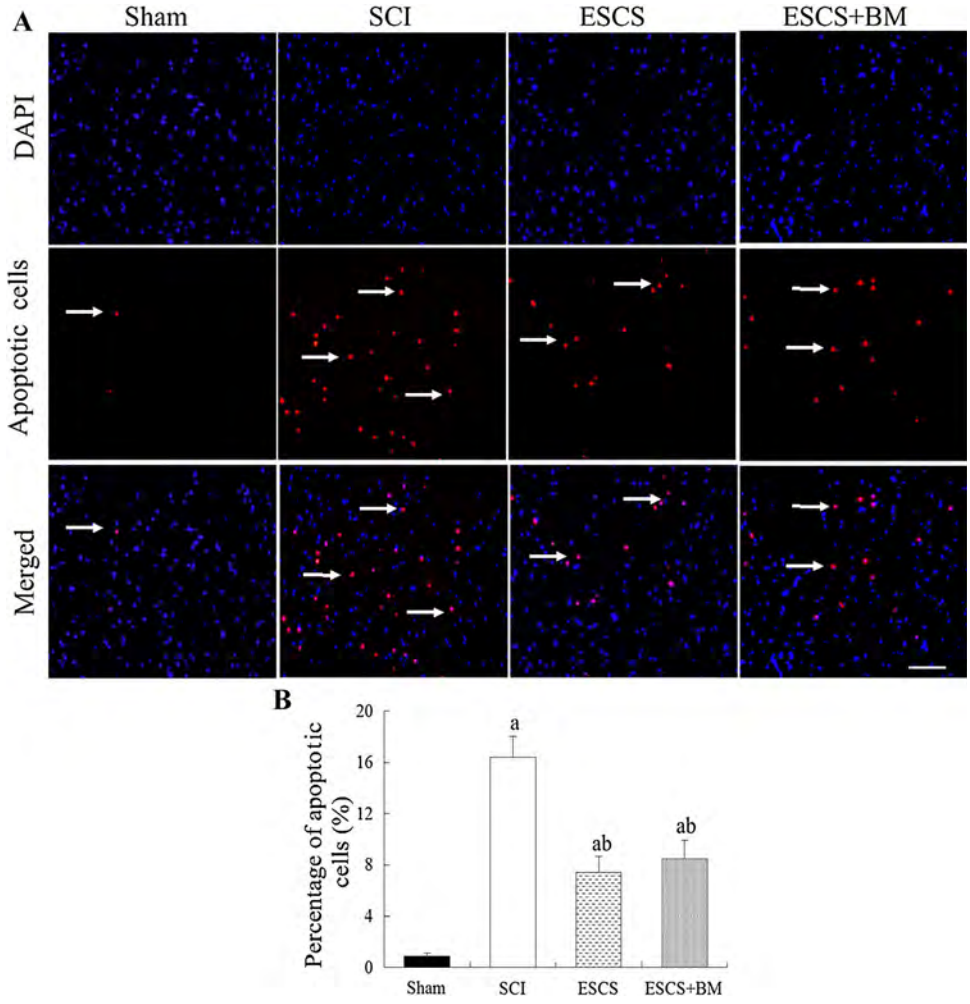

Fig. 4 ESCS decreased apoptosis in the spinal white matter at 7 days after SCI (n = 6). **A** Representative images of fluorescent TUNEL staining in the spinal white matter (arrows, apoptotic cells; scale bar, 100 μm). **B** Quantitative analysis of apoptosis ($^{a}P < 0.05$ *vs* Sham, $^{b}P < 0.05$ *vs* SCI, $^{c}P < 0.05$ *vs* ESCS).

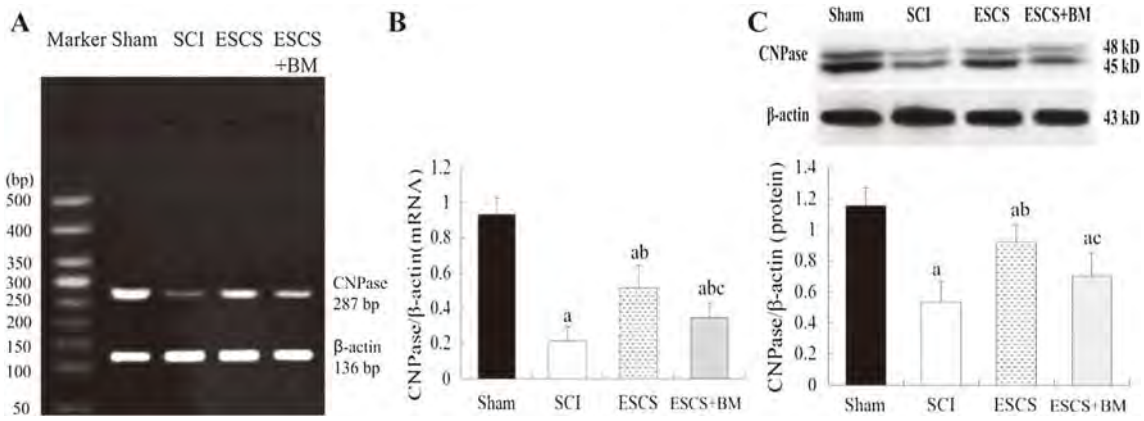

Fig. 5 Effects of ESCS on the CNPase expression 7 days after SCI. **A** Representative images of RT-PCR. **B** Quantitative analysis of CNPase (n = 6). **C** Representative images of western blots and quantitative analysis of CNPase (n = 6). $^{a}P < 0.05$ *vs* Sham, $^{b}P < 0.05$ *vs* SCI, $^{c}P < 0.05$ *vs* ESCS.

myelination, we examined the expression of BMP4 and p-Smad1/5/9 after SCI by western blot and immunofluorescence staining. As shown in Fig. 8A–C, compared with the sham group, the expression levels of BMP4 and p-Smad1/5/9 were higher in the SCI group ($P < 0.05$), suggesting that the BMP4-Smad1/5/9 signaling pathway is activated after SCI. These levels were lower in the ESCS group than in the SCI group ($P < 0.05$). Moreover,

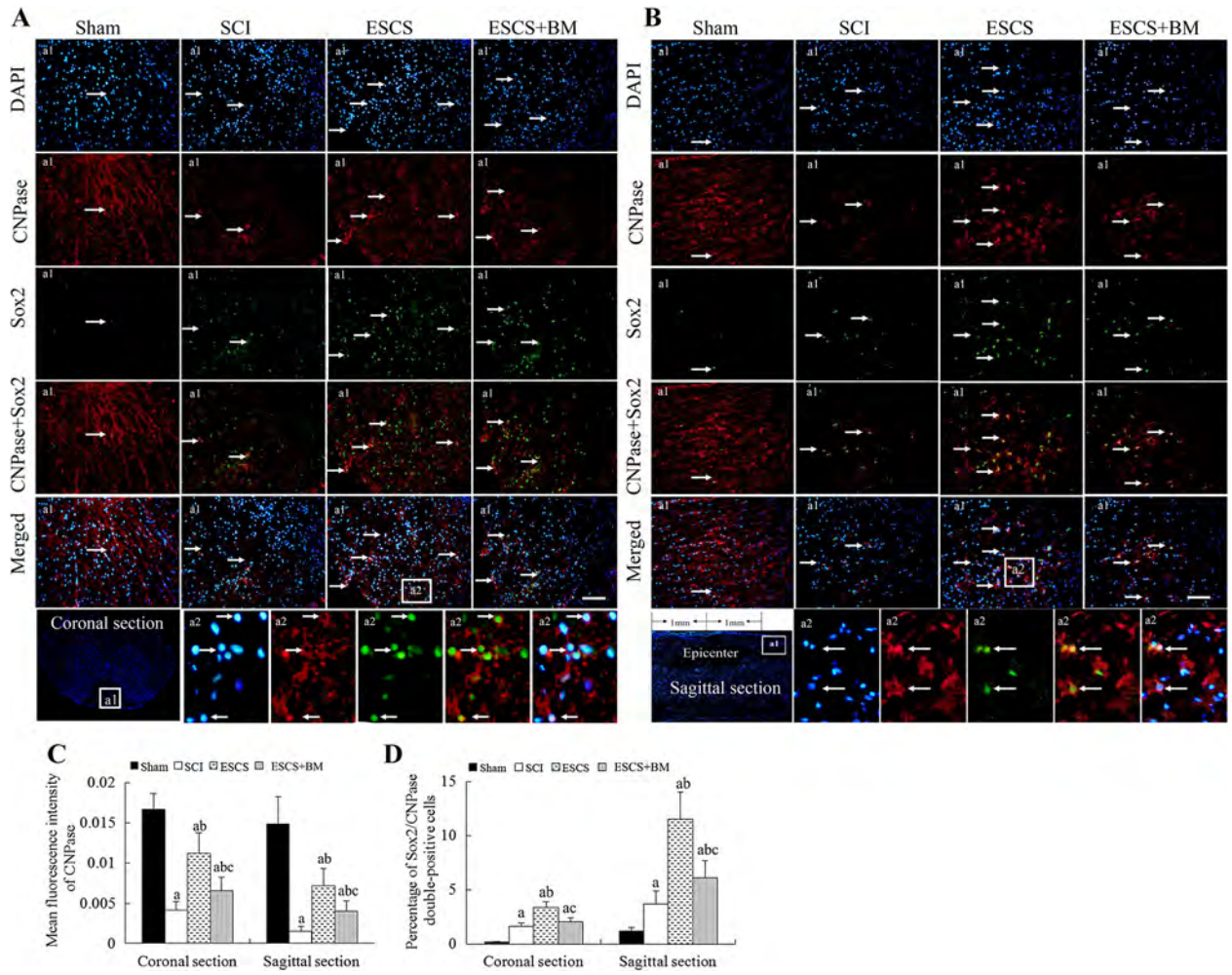

Fig. 6 Effects of ESCS on oligodendrocyte differentiation at 7 days after SCI. **A–D** Representative images of Sox2/CNPase/DAPI immunofluorescent double labeling (coronal sections in **A**; sagittal sections in **B**; arrows, eOPCs; boxes mark the enlarged area; scale bar, 100 μm) and quantitative analysis (mean fluorescence in **C** and double-labeling in **D**; $n = 6$; $^{a}P < 0.05$ *vs* Sham, $^{b}P < 0.05$ *vs* SCI, $^{c}P < 0.05$ *vs* ESCS).

compared with the ESCS group, p-Smad1/5/9 expression was markedly higher in the ESCS+BM group ($P < 0.05$).

Immunofluorescence staining for BMP4 and p-Smad1/5/9 (Fig. 8D–G) confirmed the western blot results (Fig. 8A–C). Compared with the sham group, the BMP4 mean fluorescence intensity and percentage of p-Smad1/5/9-positive cells were higher in the SCI group ($P < 0.05$). Compared with the SCI group, these proteins were downregulated in the ESCS group ($P < 0.05$). Furthermore, these proteins were upregulated in the ESCS+BM group compared with the ESCS group ($P < 0.05$; Fig. 8D–G). These findings indicate that ESCS reduces oligodendrocyte loss, promotes oligodendrocyte differentiation, and protects myelin after SCI by inhibiting the BMP4-Smad1/5/9 signaling pathway.

Discussion

SCI is common and devastating; it results in motor, sensory and autonomic dysfunction. ESCS is becoming a promising treatment for SCI [11]. Studies indicate that, apart from the activation of residual neuronal pathways, ESCS also promotes anatomical plasticity of the nervous system after SCI [7, 12–14]. However, the effects of ESCS on oligodendrocyte differentiation and myelination after SCI remain unclear. In this study, we found that ESCS treatment reduced oligodendrocyte and myelin loss, and enhanced oligodendrocyte differentiation in the spinal white matter after SCI by inhibiting the BMP4-Smad1/5/9 signaling pathway.

Oligodendrocyte loss and widespread demyelination [59] contribute to the loss of motor functions after SCI [22, 60, 61]. Electrical stimulation has been shown to promote the proliferation and differentiation of eNSCs and

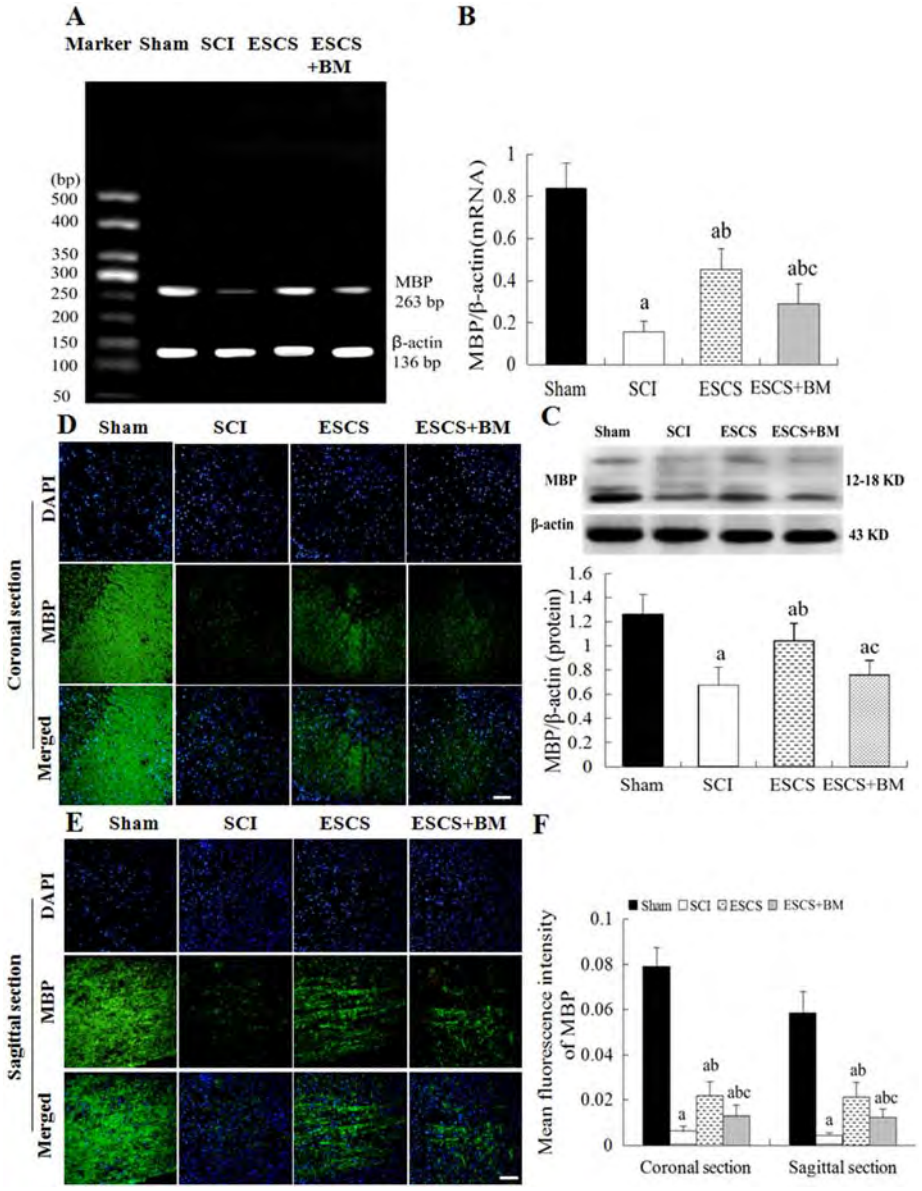

Fig. 7 Effects of ESCS on the expression of MBP in the spinal white matter 28 days after SCI. **A**, **B** Representative images of RT-PCR (**A**) and quantitative analysis of MBP (**B**, $n = 6$). **C** Representative western blots and quantitative analysis of MBP ($n = 6$). **D**, **E** Representative images of immunofluorescent labeling in the spinal white matter (coronal sections in **D**; sagittal sections in **E**; scale bars, 100 μm). **F** Quantification of MBP ($n = 6$; $^{a}P < 0.05$ *vs* Sham, $^{b}P < 0.05$ *vs* SCI, $^{c}P < 0.05$ *vs* ESCS).

eOPCs, and improve neurological function after CNS injury [34, 36, 55, 62–66]. For example, electroacupuncture promotes functional recovery in the brain by enhancing the proliferation of eNSCs and by stimulating their differentiation into astrocytes, oligodendrocytes, and neurons after cerebral ischemic injury in rodents [65, 66]. Following SCI, electroacupuncture significantly enhances the proliferation of eNSCs and eOPCs, promotes eOPC differentiation, and inhibits oligodendrocyte death. Together, these effects promote remyelination and motor functional recovery in rats [35, 63].

In the present study, ESCS significantly alleviated locomotor dysfunction at 7 days, 14 days, 21 days, and 28 days after SCI, supporting previous research findings [5–9]. ESCS also reduced apoptosis in the spinal white matter 7 days after SCI. Furthermore, the protein and mRNA expression levels of CNPase were significantly decreased, while the percentage of newly-differentiated oligodendrocytes was increased after SCI. Notably, ESCS significantly upregulated CNPase and the percentage of newly-differentiated oligodendrocytes 7 days after SCI. These findings indicate that ESCS reduces oligodendrocyte loss by inhibiting apoptosis and promoting oligodendrocyte differentiation in the spinal white matter after SCI in rats, and support previous studies [22, 34, 36, 55, 62–64]. Although in some studies Sox2 has been used as a marker of eNSCs [50, 53], it is also expressed in eOPCs [54]. Therefore, it is unclear whether the newly-differentiated oligodendrocytes in this study were derived from eOPCs, eNSCs, or both.

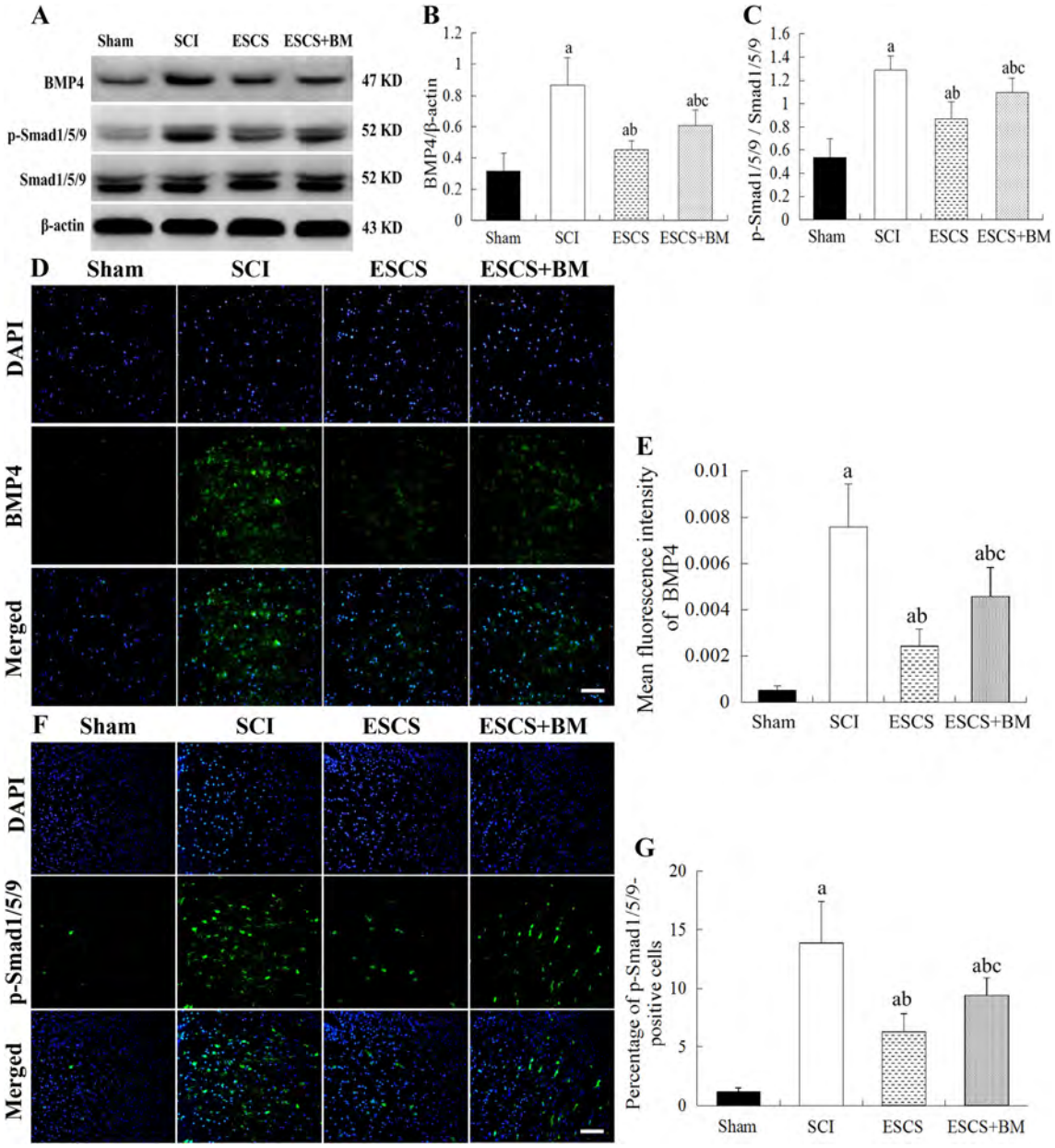

Fig. 8 Effects of ESCS on the BMP4 and Smad1/5/9 expression and their phosphorylation levels 7 days after SCI. **A–C** Representative western blots **(A)** and quantitative analysis of BMP4 (**B**), and Smad1/5/9 and p-Smad1/5/9 (**C**) (n = 6). **D–G** Representative images of immunofluorescent labeling (**D**, **F**; scale bars, 100 μm) and quantification of BMP4 (**E**) and p-Smad1/5/9 (**G**) (n = 6). $^{a}P < 0.05$ *vs* Sham, $^{b}P < 0.05$ *vs* SCI, $^{c}P < 0.05$ *vs* ESCS.

Myelin integrity is essential for the control of motor function and for integrating sensory information, and remyelination plays a critical role in the reconnection of neuronal pathways after SCI [67]. Mature oligodendrocytes are the main cells expressing myelin proteins such as MBP, and are derived from eOPCs [51, 68]. Therefore, promoting the differentiation of eOPCs or eNSCs into mature oligodendrocytes may contribute to remyelination [69] and motor functional recovery after SCI [70]. Oscillating field stimulation has been shown to improve motor function by promoting the differentiation of eOPCs and remyelination after SCI in rats [71]. In the current study, MBP mRNA and protein levels in the white matter of the spinal cord were significantly decreased at 28 days after SCI, and ESCS markedly upregulated their levels. ESCS also significantly increased the myelinated area 28 days after SCI, indicating that it significantly reduces the loss of myelin from neuronal axons in the spinal white matter, likely by inhibiting oligodendrocyte loss and promoting their differentiation.

Following SCI, eOPCs that differentiate into oligodendrocytes are few, and some differentiate into astrocytes [72]. Moreover, Uemura *et al.* [73] reported that upregulation of BMP4 stimulates the differentiation of eOPCs into astrocytes and simultaneously inhibits their proliferation and differentiation into oligodendrocytes, thereby aggravating white matter damage after chronic cerebral hypoperfusion. Notably, studies have shown that inhibiting the activation of the BMP signaling pathway is an effective strategy for promoting oligodendrocyte differentiation and remyelination and for improving motor function after SCI [74, 75]. In the present study, rhBMP4 markedly reduced CNPase expression and the percentage of newly-differentiated oligodendrocytes at 7 days, as well as MBP expression and the myelinated area 28 days after ESCS treatment. Moreover, ESCS significantly inhibited the upregulation of BMP4 and p-Smad1/5/9 after SCI, while rhBMP4 increased the levels of BMP4 and p-Smad1/5/9 after ESCS treatment. These results indicate that ESCS promotes oligodendrocyte differentiation and reduces myelin loss by inhibiting the BMP4-Smad1/5/9 signaling pathway after SCI in rats. However, perplexingly, if inhibition of the BMP4-Smad1/5/9 signaling pathway promotes oligodendrocyte differentiation and reduces myelin loss, why then do activation of the BMP4-Smad1/5/9 signaling pathway and induction of oligodendrocyte differentiation occur simultaneously following SCI? The reason is likely to be complex, but we speculate that multiple factors [76] and signaling pathways [34, 77] are involved in spontaneous oligodendrocyte differentiation after SCI.

In conclusion, ESCS treatment reduces oligodendrocyte and myelin loss and enhances oligodendrocyte differentiation in the spinal white matter by inhibiting the BMP4-Smad1/5/9 signaling pathway after SCI. However, further study is needed to clarify the anti-apoptotic mechanisms of ESCS as well as its effect on neurons. Nevertheless, our study provides important insight into the therapeutic mechanism of action of ESCS and suggests that ESCS in combination with other treatments which promote oligodendrocyte differentiation and enhance remyelination may have better therapeutic efficacy after SCI.

Acknowledgements This research was supported by the Natural Science Foundation of Liaoning Province (201602277), and the Science and Technology Planning Project of Liaoning Province (LJQ2014091). We thank Barry Patel, PhD, for editing the English text of a draft of this manuscript.

Conflict of interest The authors declare that they have no conflicts of interest, financial or otherwise.

References

1. Park HW, Oh S, Lee KH, Lee BH, Chang MS. Olig2-expressing mesenchymal stem cells enhance functional recovery after contusive spinal cord injury. Int J Stem Cells 2018, 11: 177–186.
2. Tran AP, Silver J. Neuroscience. Systemically treating spinal cord injury. Science 2015, 348: 285–286.
3. Reck TA, Landmann G. Successful spinal cord stimulation for neuropathic below-level spinal cord injury pain following complete paraplegia: a case report. Spinal Cord Ser Cases 2017, 3: 17049.
4. Huang Q, Duan W, Sivanesan E, Liu S, Yang F, Chen Z, *et al.* Spinal cord stimulation for pain treatment after spinal cord injury. Neurosci Bull 2019, 35: 527–539.
5. Darrow D, Balser DY, Netoff T, Krassioukov AV, Phillips AA, Parr AM, *et al.* Epidural Spinal Cord Stimulation facilitates immediate restoration of dormant motor and autonomic supraspinal pathways after chronic neurologically complete spinal cord injury. J Neurotrauma 2019, 36: 2325–2336.
6. Wagner FB, Mignardot JB, Le Goff-Mignardot CG, Demesmaeker R, Komi S, Capogrosso M, *et al.* Targeted neurotechnology restores walking in humans with spinal cord injury. Nature 2018, 563: 65–71.
7. Li H, Dong X, Jin M, Cheng W. The protective effect of spinal cord stimulation postconditioning against spinal cord ischemia/reperfusion injury in rabbits. Neuromodulation 2018, 21: 448–456.
8. Carhart MR, He J, Herman R, D'Luzansky S, Willis WT. Epidural spinal-cord stimulation facilitates recovery of functional walking following incomplete spinal-cord injury. IEEE Trans Neural Syst Rehabil Eng 2004, 12: 32–42.
9. Ichiyama RM, Gerasimenko YP, Zhong H, Roy RR, Edgerton VR. Hindlimb stepping movements in complete spinal rats induced by epidural spinal cord stimulation. Neurosci Lett 2005, 383: 339–344.
10. Hachmann JT, Calvert JS, Grahn PJ, Drubach DI, Lee KH, Lavrov IA. Review of epidural spinal cord stimulation for augmenting cough after spinal cord injury. Front Hum Neurosci 2017, 11: 144.
11. James ND, McMahon SB, Field-Fote EC, Bradbury EJ. Neuromodulation in the restoration of function after spinal cord injury. Lancet Neurol 2018, 17: 905–917.
12. Hassannejad Z, Yousefifard M, Azizi Y, Zadegan SA, Sajadi K, Sharif-Alhoseini M, *et al.* Axonal degeneration and demyelination following traumatic spinal cord injury: A systematic review and meta-analysis. J Chem Neuroanat 2019, 97: 9–22.
13. Smith AC, Knikou M. A Review on locomotor training after spinal cord injury: reorganization of spinal neuronal circuits and recovery of motor function. Neural Plast 2016, 2016: 1216258.
14. Zhang C, Zhang G, Rong W, Wang A, Wu C, Huo X. Early applied electric field stimulation attenuates secondary apoptotic responses and exerts neuroprotective effects in acute spinal cord injury of rats. Neuroscience 2015, 291: 260–271.
15. Baumann N, Pham-Dinh D. Biology of oligodendrocyte and myelin in the mammalian central nervous system. Physiol Rev 2001, 81: 871–927.
16. Almad A, Sahinkaya FR, McTigue DM. Oligodendrocyte fate after spinal cord injury. Neurotherapeutics 2011, 8: 262–273.
17. Imai T, Katoh H, Suyama K, Kuroiwa M, Yanagisawa S, Watanabe M. Amiloride promotes oligodendrocyte survival and remyelination after spinal cord injury in rats. J Clin Med 2018, 7.
18. Plemel JR, Keough MB, Duncan GJ, Sparling JS, Yong VW, Stys PK, *et al.* Remyelination after spinal cord injury: is it a target for repair? Prog Neurobiol 2014, 117: 54–72.

19. Hesp ZC, Goldstein EZ, Miranda CJ, Kaspar BK, McTigue DM. Chronic oligodendrogenesis and remyelination after spinal cord injury in mice and rats. J Neurosci 2015, 35: 1274–1290.
20. McTigue DM, Wei P, Stokes BT. Proliferation of NG2-positive cells and altered oligodendrocyte numbers in the contused rat spinal cord. J Neurosci 2001, 21: 3392–3400.
21. Wang HF, Liu XK, Li R, Zhang P, Chu Z, Wang CL, *et al.* Effect of glial cells on remyelination after spinal cord injury. Neural Regen Res 2017, 12: 1724–1732.
22. Li Q, Brus-Ramer M, Martin JH, McDonald JW. Electrical stimulation of the medullary pyramid promotes proliferation and differentiation of oligodendrocyte progenitor cells in the corticospinal tract of the adult rat. Neurosci Lett 2010, 479: 128–133.
23. Stirling DP, Khodarahmi K, Liu J, McPhail LT, McBride CB, Steeves JD, *et al.* Minocycline treatment reduces delayed oligodendrocyte death, attenuates axonal dieback, and improves functional outcome after spinal cord injury. J Neurosci 2004, 24: 2182–2190.
24. Salgado-Ceballos H, Guizar-Sahagun G, Feria-Velasco A, Grijalva I, Espitia L, Ibarra A, *et al.* Spontaneous long-term remyelination after traumatic spinal cord injury in rats. Brain Res 1998, 782: 126–135.
25. Papastefanaki F, Matsas R. From demyelination to remyelination: the road toward therapies for spinal cord injury. Glia 2015, 63: 1101–1125.
26. Alizadeh A, Karimi-Abdolrezaee S. Microenvironmental regulation of oligodendrocyte replacement and remyelination in spinal cord injury. J Physiol 2016, 594: 3539–3552.
27. Horky LL, Galimi F, Gage FH, Horner PJ. Fate of endogenous stem/progenitor cells following spinal cord injury. J Comp Neurol 2006, 498: 525–538.
28. Assinck P, Duncan GJ, Plemel JR, Lee MJ, Stratton JA, Manesh SB, *et al.* Myelinogenic plasticity of oligodendrocyte precursor cells following spinal cord contusion injury. J Neurosci 2017, 37: 8635–8654.
29. Barnabe-Heider F, Goritz C, Sabelstrom H, Takebayashi H, Pfrieger FW, Meletis K, *et al.* Origin of new glial cells in intact and injured adult spinal cord. Cell Stem Cell 2010, 7: 470–482.
30. Yang XH, Ding Y, Li W, Zhang RY, Wu JL, Ling EA, *et al.* Effects of electroacupuncture and the retinoid X receptor (RXR) signalling pathway on oligodendrocyte differentiation in the demyelinated spinal cord of rats. Acupunct Med 2017, 35: 122–132.
31. Shi Y, Shao Q, Li Z, Gonzalez GA, Lu F, Wang D, *et al.* Myt1L promotes differentiation of oligodendrocyte precursor cells and is necessary for remyelination after lysolecithin-induced demyelination. Neurosci Bull 2018, 34: 247–260.
32. Fontaine D. Neurosurgical treatment of chronic pain. Rev Prat 2013, 63: 805–809.
33. Zhu Y, Wu Y, Zhang R. Electro-acupuncture promotes the proliferation of neural stem cells and the survival of neurons by downregulating miR-449a in rat with spinal cord injury. EXCLI J 2017, 16: 363–374.
34. Geng X, Sun T, Li JH, Zhao N, Wang Y, Yu HL. Electroacupuncture in the repair of spinal cord injury: inhibiting the Notch signaling pathway and promoting neural stem cell proliferation. Neural Regen Res 2015, 10: 394–403.
35. Wu H, Hu M, Yuan D, Wang Y, Wang J, Li T, *et al.* Electroacupuncture promotes the proliferation of endogenous neural stem cells and oligodendrocytes in the injured spinal cord of adult rats. Neural Regen Res 2012, 7: 1138–1144.
36. Becker D, Gary DS, Rosenzweig ES, Grill WM, McDonald JW. Functional electrical stimulation helps replenish progenitor cells in the injured spinal cord of adult rats. Exp Neurol 2010, 222: 211–218.
37. Hall AK, Miller RH. Emerging roles for bone morphogenetic proteins in central nervous system glial biology. J Neurosci Res 2004, 76: 1–8.
38. Cheng X, Wang Y, He Q, Qiu M, Whittemore SR, Cao Q. Bone morphogenetic protein signaling and olig1/2 interact to regulate the differentiation and maturation of adult oligodendrocyte precursor cells. Stem Cells 2007, 25: 3204–3214.
39. Pang EK, Im SU, Kim CS, Choi SH, Chai JK, Kim CK, *et al.* Effect of recombinant human bone morphogenetic protein-4 dose on bone formation in a rat calvarial defect model. J Periodontol 2004, 75: 1364–1370.
40. Maeda Y, Ikeuchi M, Wacnik P, Sluka KA. Increased c-fos immunoreactivity in the spinal cord and brain following spinal cord stimulation is frequency-dependent. Brain Res 2009, 1259: 40–50.
41. Shao Z, Lv G, Wen P, Cao Y, Yu D, Lu Y, *et al.* Silencing of PHLPP1 promotes neuronal apoptosis and inhibits functional recovery after spinal cord injury in mice. Life Sci 2018, 209: 291–299.
42. Li ZW, Tang RH, Zhang JP, Tang ZP, Qu WS, Zhu WH, *et al.* Inhibiting epidermal growth factor receptor attenuates reactive astrogliosis and improves functional outcome after spinal cord injury in rats. Neurochem Int 2011, 58: 812–819.
43. Hu R, Zhou J, Luo C, Lin J, Wang X, Li X, *et al.* Glial scar and neuroregeneration: histological, functional, and magnetic resonance imaging analysis in chronic spinal cord injury. J Neurosurg Spine 2010, 13: 169–180.
44. Li G, Cao Y, Shen F, Wang Y, Bai L, Guo W, *et al.* Mdivi-1 inhibits astrocyte activation and astroglial scar formation and enhances axonal regeneration after spinal cord injury in rats. Front Cell Neurosci 2016, 10: 241.
45. Smits H, Ultenius C, Deumens R, Koopmans GC, Honig WM, van Kleef M, *et al.* Effect of spinal cord stimulation in an animal model of neuropathic pain relates to degree of tactile "allodynia". Neuroscience 2006, 143: 541–546.
46. Meuwissen KPV, Gu JW, Zhang TC, Joosten EAJ. Conventional-SCS vs. burst-SCS and the behavioral effect on mechanical hypersensitivity in a rat model of chronic neuropathic pain: effect of amplitude. Neuromodulation 2018, 21: 19–30.
47. Xu Q, Hu D, Duan B, He J. A fully implantable stimulator with wireless power and data transmission for experimental investigation of epidural spinal cord stimulation. IEEE Trans Neural Syst Rehabil Eng 2015, 23: 683–692.
48. Basso DM, Beattie MS, Bresnahan JC. A sensitive and reliable locomotor rating scale for open field testing in rats. J Neurotrauma 1995, 12: 1–21.
49. Li G, Jia Z, Cao Y, Wang Y, Li H, Zhang Z, *et al.* Mitochondrial division inhibitor 1 ameliorates mitochondrial injury, apoptosis, and motor dysfunction after acute spinal cord injury in rats. Neurochem Res 2015, 40: 1379–1392.
50. Hong JY, Lee SH, Lee SC, Kim JW, Kim KP, Kim SM, *et al.* Therapeutic potential of induced neural stem cells for spinal cord injury. J Biol Chem 2014, 289: 32512–32525.
51. Bernardo A, De Simone R, De Nuccio C, Visentin S, Minghetti L. The nuclear receptor peroxisome proliferator-activated receptor-gamma promotes oligodendrocyte differentiation through mechanisms involving mitochondria and oscillatory Ca2+ waves. Biol Chem 2013, 394: 1607–1614.
52. Wang LC, Almazan G. Role of sonic hedgehog signaling in oligodendrocyte differentiation. Neurochem Res 2016, 41: 3289–3299.
53. Shin DC, Ha KY, Kim YH, Kim JW, Cho YK, Kim SI. Induction of endogenous neural stem cells by extracorporeal shock waves after spinal cord injury. Spine (Phila Pa 1976) 2018, 43: E200–E207.

54. Ossola B, Zhao C, Compston A, Pluchino S, Franklin RJ, Spillantini MG. Neuronal expression of pathological tau accelerates oligodendrocyte progenitor cell differentiation. Glia 2016, 64: 457–471.
55. Ahn SM, Kim YR, Kim HN, Shin YI, Shin HK, Choi BT. Electroacupuncture ameliorates memory impairments by enhancing oligodendrocyte regeneration in a mouse model of prolonged cerebral hypoperfusion. Sci Rep 2016, 6: 28646.
56. Eftekharpour E, Karimi-Abdolrezaee S, Wang J, El Beheiry H, Morshead C, Fehlings MG. Myelination of congenitally dysmyelinated spinal cord axons by adult neural precursor cells results in formation of nodes of Ranvier and improved axonal conduction. J Neurosci 2007, 27: 3416–3428.
57. Lu HZ, Wang YX, Zou J, Li Y, Fu SL, Jin JQ, *et al.* Differentiation of neural precursor cell-derived oligodendrocyte progenitor cells following transplantation into normal and injured spinal cords. Differentiation 2010, 80: 228–240.
58. Wislet-Gendebien S, Bruyere F, Hans G, Leprince P, Moonen G, Rogister B. Nestin-positive mesenchymal stem cells favour the astroglial lineage in neural progenitors and stem cells by releasing active BMP4. BMC Neurosci 2004, 5: 33.
59. Wu B, Sun L, Li P, Tian M, Luo Y, Ren X. Transplantation of oligodendrocyte precursor cells improves myelination and promotes functional recovery after spinal cord injury. Injury 2012, 43: 794–801.
60. Bambakidis NC, Miller RH. Transplantation of oligodendrocyte precursors and sonic hedgehog results in improved function and white matter sparing in the spinal cords of adult rats after contusion. Spine J 2004, 4: 16–26.
61. Lytle JM, Wrathall JR. Glial cell loss, proliferation and replacement in the contused murine spinal cord. Eur J Neurosci 2007, 25: 1711–1724.
62. Beaumont E, Guevara E, Dubeau S, Lesage F, Nagai M, Popovic M. Functional electrical stimulation post-spinal cord injury improves locomotion and increases afferent input into the central nervous system in rats. J Spinal Cord Med 2014, 37: 93–100.
63. Huang S, Tang C, Sun S, Cao W, Qi W, Xu J, *et al.* Protective effect of electroacupuncture on neural myelin sheaths is mediated via promotion of oligodendrocyte proliferation and inhibition of oligodendrocyte death after compressed spinal cord injury. Mol Neurobiol 2015, 52: 1870–1881.
64. Braun R, Klein R, Walter HL, Ohren M, Freudenmacher L, Getachew K, *et al.* Transcranial direct current stimulation accelerates recovery of function, induces neurogenesis and recruits oligodendrocyte precursors in a rat model of stroke. Exp Neurol 2016, 279: 127–136.
65. Kim YR, Kim HN, Ahn SM, Choi YH, Shin HK, Choi BT. Electroacupuncture promotes post-stroke functional recovery via enhancing endogenous neurogenesis in mouse focal cerebral ischemia. PLoS One 2014, 9: e90000.
66. Yang Z, Yu H, Rao X, Liu Y, Pi M. Effects of electroacupuncture at the conception vessel on proliferation and differentiation of nerve stem cells in the inferior zone of the lateral ventricle in cerebral ischemia rats. J Tradit Chin Med 2008, 28: 58–63.
67. Falnikar A, Li K, Lepore AC. Therapeutically targeting astrocytes with stem and progenitor cell transplantation following traumatic spinal cord injury. Brain Res 2015, 1619: 91–103.
68. Dusart I, Marty S, Peschanski M. Demyelination, and remyelination by Schwann cells and oligodendrocytes after kainate-induced neuronal depletion in the central nervous system. Neuroscience 1992, 51: 137–148.
69. Patel JR, Klein RS. Mediators of oligodendrocyte differentiation during remyelination. FEBS Lett 2011, 585: 3730–3737.
70. Whittaker MT, Zai LJ, Lee HJ, Pajoohesh-Ganji A, Wu J, Sharp A, *et al.* GGF2 (Nrg1-beta3) treatment enhances NG2+ cell response and improves functional recovery after spinal cord injury. Glia 2012, 60: 281–294.
71. Jing JH, Qian J, Zhu N, Chou WB, Huang XJ. Improved differentiation of oligodendrocyte precursor cells and neurological function after spinal cord injury in rats by oscillating field stimulation. Neuroscience 2015, 303: 346–351.
72. Sozmen EG, Rosenzweig S, Llorente IL, DiTullio DJ, Machnicki M, Vinters HV, *et al.* Nogo receptor blockade overcomes remyelination failure after white matter stroke and stimulates functional recovery in aged mice. Proc Natl Acad Sci U S A 2016, 113: E8453–E8462.
73. Uemura MT, Ihara M, Maki T, Nakagomi T, Kaji S, Uemura K, *et al.* Pericyte-derived bone morphogenetic protein 4 underlies white matter damage after chronic hypoperfusion. Brain Pathol 2018, 28: 521–535.
74. Wang Y, Cheng X, He Q, Zheng Y, Kim DH, Whittemore SR, *et al.* Astrocytes from the contused spinal cord inhibit oligodendrocyte differentiation of adult oligodendrocyte precursor cells by increasing the expression of bone morphogenetic proteins. J Neurosci 2011, 31: 6053–6058.
75. Hampton DW, Asher RA, Kondo T, Steeves JD, Ramer MS, Fawcett JW. A potential role for bone morphogenetic protein signalling in glial cell fate determination following adult central nervous system injury *in vivo*. Eur J Neurosci 2007, 26: 3024–3035.
76. Ramos-Cejudo J, Gutierrez-Fernandez M, Otero-Ortega L, Rodriguez-Frutos B, Fuentes B, Vallejo-Cremades MT, *et al.* Brain-derived neurotrophic factor administration mediated oligodendrocyte differentiation and myelin formation in subcortical ischemic stroke. Stroke 2015, 46: 221–228.
77. Guardiola-Diaz HM, Ishii A, Bansal R. Erk1/2 MAPK and mTOR signaling sequentially regulates progression through distinct stages of oligodendrocyte differentiation. Glia 2012, 60: 476–486.

Neurosci. Bull. April, 2020, 36(4):385–395
https://doi.org/10.1007/s12264-019-00435-z

www.neurosci.cn
www.springer.com/12264

ORIGINAL ARTICLE

Blockade of c-Src Within the Paraventricular Nucleus Attenuates Inflammatory Cytokines and Oxidative Stress in the Mechanism of the TLR4 Signal Pathway in Salt-Induced Hypertension

Qing Yang[1] · Xiao-Jing Yu[1] · Qing Su[1] · Qiu-Yue Yi[1,2] · Xin-Ai Song[1] · Xiao-Lian Shi[3] · Hong-Bao Li[1] · Jie Qi[1] · Guo-Qing Zhu[4] · Yu-Ming Kang[1]

Received: 17 June 2019 / Accepted: 9 August 2019 / Published online: 22 October 2019

Abstract Toll-like receptor 4 (TLR4) and cellular Src (c-Src) are closely associated with inflammatory cytokines and oxidative stress in hypertension, so we designed this study to explore the exact role of c-Src in the mechanism of action of the TLR4 signaling pathway in salt-induced hypertension. Salt-sensitive rats were given a high salt diet for 10 weeks to induce hypertension. This resulted in higher levels of TLR4, activated c-Src, pro-inflammatory cytokines, oxidative stress, and arterial pressure. Infusion of a TLR4 blocker into the hypothalamic paraventricular nucleus (PVN) decreased the activated c-Src, while microinjection of a c-Src inhibitor attenuated the PVN levels of nuclear factor-kappa B, pro-inflammatory cytokines, and oxidative stress. Our findings suggest that a long-term high-salt diet increases TLR4 expression in the PVN and this promotes the activation of c-Src, which upregulates the expression of pro-inflammatory cytokines and results in the overproduction of reactive oxygen species. Therefore, inhibiting central c-Src activity may be a new target for treating hypertension.

Keywords Toll-like receptor 4 · Cellular Src · Inflammatory cytokines · Oxidative stress · Hypothalamic paraventricular nucleus · Salt-induced hypertension

Introduction

Hypertension is a common cardiovascular disease which is controlled by hereditary and environmental factors. It is also a disease with high rates of morbidity, disability, and mortality. According to epidemiological studies, long-term high-salt intake as an important environmental factor can raise blood pressure and lead to hypertension. In high salt-induced hypertensive rats, there are not only organizational and functional changes in the heart, but the central and peripheral rennin-angiotensin system is also activated. Meanwhile, a long-term high-salt diet is closely associated with inflammatory cytokines and oxidative stress. Hypertension is accompanied by chronic low-grade inflammation, and inflammatory cytokines such as interleukin (IL)-1β, IL-6, and IL-10 are considered to be important factors in the occurrence and development of hypertension. The hypothalamic paraventricular nucleus (PVN) plays important roles in sympathetic nerve activity, blood pressure stability, and neurohumoral regulation [1, 2]. Previous studies in our laboratory have shown that a high-salt intake upsets the balance of inflammatory cytokines peripherally and centrally. Neurons positive for IL-1β and IL-6 show higher expression, but the IL-10 is lower in the PVN of

Qing Yang and Xiao-Jing Yu have contributed equally to this work.

✉ Jie Qi
jie-qi@xjtu.edu.cn

✉ Yu-Ming Kang
ykang@mail.xjtu.edu.cn

1 Department of Physiology and Pathophysiology, Xi'an Jiaotong University School of Basic Medical Sciences, Key Laboratory of Environment and Genes Related to Diseases of the Ministry of Education, Xi'an Jiaotong University, Xi'an 710061, China

2 Department of Cardiovascular Surgery, First Affiliated Hospital of Xi'an Jiaotong University, Xi'an 710061, China

3 Department of Pharmacology, School of Basic Medical Sciences, Xi'an Jiaotong University Health Science Center, Xi'an 710061, China

4 Key Laboratory of Cardiovascular Disease and Molecular Intervention, Department of Physiology, Nanjing Medical University, Nanjing 210029, China

hypertensive rats [3, 4]. This indicates that an imbalance of central pro-inflammatory cytokines (PICs) and anti-inflammatory cytokines contributes to the pathogenesis of hypertension.

In addition, a high salt intake can also induce central oxidative stress. In hypertensive rats, neurons positive for NAD(P)H oxidase isoforms, such as NOX2 and NOX4, in the PVN show higher expression [5, 6]. The fluorescence intensity of dihydroethidium (DHE) in the PVN showed an increasing trend in the high-salt diet group, which means that oxidative stress is activated in the PVN. In addition, other indicators of oxidative stress such as NAD(P)H oxidase and malondialdehyde (MDA) are increased, but glutathione (GSH) and superoxide dismutase (SOD) are decreased after high-salt stimulation [7]. Combined with previous research, the inflammatory cytokines and oxidative stress in the PVN in hypertension play an important role in the pathogenesis of salt-induced hypertension.

Toll-like receptor 4 (TLR4), a member of the TLR family, is a pattern-recognition receptor mainly expressed by immune cells. TLR4 is involved in sterile inflammatory responses and plays an important role in the innate immune system and the subsequent development of adaptive immunity. In a number of recent studies, TLR4 has been shown to have a close relationship with inflammatory cytokines and oxidative stress and is considered to be a modulator of the inflammatory responses in various cardiovascular diseases such as coronary arterial disease, heart failure, and hypertension [8, 9]. Activation of the TLR4 signaling pathway increases the expression of PICs in order to induce hypertension [10]. In previous studies, chronic bilateral PVN infusion of the TLR4 inhibitor telmisartan reduces the inflammatory reaction *via* inhibiting the TLR4 pathway, which decreases blood pressure [11]. In addition, previous studies found that after stimulating several NAD(P)H oxidase isoforms, oxidative stress is involved in the TLR-dependent signaling pathway in cells from immune and non-immune origins [12]. Meanwhile, the result from our laboratory showed that the central inflammatory cytokines and oxidative stress are decreased by blocking the TLR4 pathway in the PVN, and finally decrease the peripheral renal sympathetic activation [9]. Therefore, TLR4 in the PVN plays an important role in the development of hypertension by promoting the expression of inflammatory cytokines and the production of oxidative stress. However, whether TLR4 regulates inflammatory cytokines and oxidative stress by direct action or by some intermediate is unknown.

Cellular Src (c-Src) is a typical non-receptor membrane-combining tyrosine kinase. Studies have shown that c-Src is involved in cell proliferation, motility, and even apoptosis. And c-Src is also considered to play an important role in a variety of cellular signal transduction pathways [13–15]. Studies have shown that c-Src activated in vascular smooth muscle cells (VSMCs) is involved in the angiotensin II-induced oxidative stress responses, which lead to the overproduction of reactive oxygen species (ROS) [16–18]. And the NAD(P)H oxidase subunit may also be a downstream target of c-Src in human VSMCs [14]. In addition, c-Src is also closely associated with the inflammatory response. Activated c-Src is involved in mediating inflammatory responses in synovial fibroblasts in osteoarthritis and the airway smooth muscle cells of asthmatic patients, leading to up-regulation of IL-6 expression [19, 20]. Recently, c-Src has been found in the brain, and may participate in the central regulation of oxidative stress [15]. However, in high salt-induced hypertensive responses, whether c-Src in the PVN is involved in the pathogenesis of hypertension by regulating inflammatory cytokines and oxidative stress, and whether TLR4 in the PVN regulates peripheral sympathetic activity *via* c-Src is not clear. And no studies have investigated the relationship between c-Src and TLR4 in salt-induced hypertension. Therefore, we proposed the following hypothesis: in high salt-induced hypertension, TLR4 in the PVN is activated, and this activates c-Src to regulate ROS and PICs, then leading to regulation of peripheral sympathetic excitation, elevation of blood pressure, and participation in the occurrence and development of hypertension.

Materials and Methods

Animals

Male Dahl salt-sensitive (S) rats (150 g–200 g body weight) were fed and operated with approval by Xi'an Jiaotong University Animal Care and Use Committee in accordance with the Guidelines for the Care and Use of Experimental Animals of the National Institutes of Health (NIH Publication No. 85-23, revised 1996).

General Experimental Protocol

The rats were randomly divided into two diet intervention groups (0.3% NaCl, NS and 8% NaCl, HS) for 10 weeks and their blood pressure was monitored. After 10 weeks on a diet, the bilateral PVN was infused *via* minipump with the selective TLR4 blocker TAK-242 (10 μg/h) or artificial cerebrospinal fluid (aCSF) for two weeks or microinjected with the selective c-Src inhibitor 4-amino-5-(4-chlorophenyl)-7-(t-butyl) pyrazolo [3,4-d] pyrimidine (PP2, 0.1 nmol) or vehicle. The rats were randomly assigned to eight groups ($n = 7$ per group): HS + TAK-242; HS + aCSF; NS + TAK-242; NS + aCSF; HS + PP2;

HS + vehicle; NS + PP2; and NS + vehicle. All the procedures were carried out under anesthesia with a ketamine (90 mg/kg) and xylazine (10 mg/kg) mixture *via* intraperitoneal injection, using a stereotaxic apparatus.

Bilateral PVN Osmotic Minipump for Chronic Drug Intervention

After anesthesia, the rat's head was fixed in the stereotaxic apparatus for sterile surgery. The skull was then exposed through a midline incision, and a stainless steel double cannula was implanted into the PVN according to the Paxinos and Watson [21] rat atlas (1.8 mm posterior to bregma, 0.4 mm from midline, and 7.9 mm below the skull surface). The cannula was fixed to the cranium with dental acrylic and two stainless-steel screws [2]. A minipump (Alzet Osmotic Pumps, Model 2004, 0.25 μL/h) was implanted subcutaneously at the back of the neck and connected to the cannula for two weeks of continuous infusion of TAK-242 or aCSF into the PVN as described previously [9, 22]. Rats received subcutaneous buprenorphine (0.03 mg/kg) immediately after surgery and 12 h later.

Microinjection Through Bilateral PVN Cannulae for Chronic Drug Intervention

Due to the storage conditions (− 20°C), a minipump could not be used to infuse PP2 into the PVN. So we microinjected through bilateral PVN cannulae for chronic PP2 intervention. After anesthesia, the stereotaxic procedure was carried out as described previously [2]. A stainless-steel double cannula (Plastics One, Inc.) with a center-to-center distance of 0.5 mm was implanted into the PVN using an introducer, at the stereotaxic coordinates 1.8 mm caudal to the bregma, 0.4 mm lateral to midline, and 7.9 mm below the skull surface [7], and the cannulae were fixed to the cranium with dental acrylic and two stainless steel screws. PP2 (0.1 nmol) or vehicle was microinjected into each side in a volume of 50 nL completed in 1 min [23]. This microinjection was carried out once per day for 14 days. Rats received buprenorphine (0.03 mg/kg, subcutaneous) immediately after surgery and 12 h later.

Mean Arterial Pressure Measurement

Arterial pressure was measured non-invasively *via* a tail-cuff instrument and its recording system (BP100A, 113 Chengdu Techman Software Co., Ltd, China) throughout the study. The tail artery blood pressure was measured in conscious rats. The method for mean arterial pressure (MAP) has been previously described [11, 24]. The rats were trained in the daily blood pressure measure for at least 7 days to minimize stress-induced blood pressure fluctuations, and were warmed to an ambient temperature of 32°C by placing them in a holding device mounted on a thermostatically-controlled warming plate to achieve the steady pulse. Animals were allowed to acclimate to the tail cuffs for 10 min prior to each pressure recording session. The data collected by the tail-cuff instrument system were the mean value from each group rats each day.

Electrophysiological Recordings

Under anesthesia and after a retroperitoneal laparotomy, the left renal sympathetic nerve was isolated under a stereomicroscope, placed on a platinum electrode, and covered by paraffin oil tampons to record the renal sympathetic nerve activity (RSNA) as described previously [25]. The maximum RSNA was induced by sodium nitroprusside (SNP, 10 μg, intravenous). At the end of the experiment, the background noise, defined as the signal recorded postmortem, was subtracted from the actual RSNA and subsequently expressed as a percentage of maximum (in response to SNP).

Collection of Blood and Tissue Samples

At the end of two weeks of drug intervention and blood pressure measurements, one group of rats was perfused through the left ventricle under anesthesia to collect the brain. The brains were embedded in OCT and cut into 18-μm transverse sections at ∼ 1.8 mm from bregma (the PVN) for immunofluorescence staining. Each of the remaining rats was decapitated under anesthesia to collect PVN tissue and blood samples. The PVN tissue was isolated according to microdissection procedures and immediately stored in liquid nitrogen for western blotting and real-time PCR (RT-PCR). The blood samples were centrifuged at 3000 rpm for 15 min and stored at −80°C.

Immunofluorescence Staining

Under anesthesia and after thoracotomy, rats were transcardially perfused through the left ventricle with 200 mL of 1% phosphate-buffered saline (PBS), followed by 400 mL of 4% buffered paraformaldehyde (pH 7.4). The brain was removed and immersed in 4% buffered paraformaldehyde for 48 h, and then immersed in 30% sucrose for at least 2 days. The brain was embedded in OCT and cut into 18-μm transverse sections ∼ 1.8 mm from bregma (the PVN). The free-floating sections were incubated with 0.3% Triton-X for 20 min and with 5% goat serum for 30 min. The sections were then incubated with primary antibody diluted in 0.01 mol/L PBS at 4°C overnight followed by incubation with secondary antibody

(1:200, green or red fluorescence; Invitrogen, Carlsbad, CA) for 60 min at 37°C. The primary antibodies TLR4 (sc-293072, 1:200), nuclear factor-kappa B (NF-κB) p65 (ab16502, 1:500), NOX2 (sc-130549, 1:200), and NOX4 (ab133303, 1:500) were from Santa Cruz Biotechnology and Abcam. Positive immunofluorescence-stained cells in the PVN were observed under a fluorescence microscope (Nikon, Tokyo, Japan). Superoxide anion levels in the PVN were determined by fluorescence-labeled dihydroethidium staining (DHE, Molecular Probes). All the procedures were performed as previously described [26].

Western Blotting

After measurement of RSNA, the rats were euthanized to collect PVN tissue. The tissue homogenates were subjected to Western blotting for measurement of IL-1β, IL-10, NOX2, NOX4, SOD1, c-Src, and phosphorylated Src (Tyr416) (p-Src) expression in the PVN. The tissue samples were lysed in a RIPA buffer with protease inhibitor and phosphatase inhibitor cocktail. After sonication, the protein content of the resulting samples was determined by a modified BCA protein assay. The samples were then subjected to sodium dodecyl sulfate-polyacrylamide gel electrophoresis using Electrophoresis and Blotting Apparatus (Bio-Rad). Protein products were separated by SDS-PAGE electrophoresis and transferred to nitrocellulose membranes. Then the membranes were blocked with 3.0% BSA in TBST buffer (TBS plus 0.1% Tween-20) for 1.5 h at room temperature and incubated with primary antibodies overnight at 4°C [7]. The primary antibodies against IL-1β (sc12742, 17 kDa, 1:500), IL-10 (sc-365858, 20 kDa, 1:500), NOX2 (sc-130549, 91 kDa, 1:500), NOX4 (ab133303, 67 kDa, 1:2000), and SOD1 (sc-8637, 23 kDa, 1:500) were from Santa Cruz Biotechnology and Abcam. Protein loading was controlled by probing all western blots with β-actin antibody and normalizing the IL-1β, IL-10, NOX2, NOX4, and SOD1 protein intensities to that of β-actin. The p-Src (Tyr416) has activity and the ratio of p-Src (Tyr416) to c-Src represents the activation of c-Src. The c-Src antibody (2109s, 60 kDa, 1:1000) and p-Src (Tyr416) antibody (6943s, 60 kDa, 1:1000) were from Gene Company Ltd. The protein intensity of p-Src (Tyr416) was normalized to that of c-Src. Band densities were analyzed using NIH ImageJ software [27].

Real-Time PCR

The rat brains were isolated and cut into a coronal segment from − 0.92 mm to − 2.13 mm posterior to bregma, and a block of the hypothalamus containing the PVN was excised from the coronal segment. The details of PVN microdissection were as described previously [2]. Total RNA isolation, cDNA synthesis, and RT-PCR were performed as previously described [8]. Total RNA was isolated using RNeasy kits (Qiagen) according to the manufacturer's instructions, and 1 μg of purified RNA was reverse-transcribed with a high-capacity cDNA reverse transcription kit (Bio-Rad). Specific primers for NOX2, NOX4, and SOD1 are shown in Table 1. The fold-changes in mRNA expression were determined relative to glyceraldehyde 3-phosphate dehydrogenase (GAPDH) mRNA levels in each corresponding group [28].

ELISA Studies

The MDA, SOD, GSH, and NAD(P)H oxidase activity in the PVN was quantified using rat ELISA kits (Invitrogen Corp., Carlsbad, CA). The norepinephrine (NE) in plasma was quantified using rat ELISA kits (Invitrogen) [29]. All the protocols were according to the manufacturer's instructions. The standards or sample diluents were added and incubated in the appropriate well of a microtiter plate pre-coated with a specific antibody. Conjugate was added and incubated for 1 h at 37°C and then washed. The reactions were stopped with stop solution and read using a microtiter plate reader (MK3, Thermo Fisher Scientific, Waltham, MA).

Statistical Analysis

Data are expressed as the mean ± SEM and $P < 0.05$ was considered statistically significant. Statistical analyses were performed using Prism (GraphPad Software, Inc.; version 5.0). For the tail blood pressures, the MAP was analyzed by repeated measures ANOVA. One-way ANOVA with Tukey's *post hoc* test was applied to the statistical analyses for RSNA, protein levels in the PVN, plasma NE, numbers of positive neurons, fluorescence intensity, and western blotting data.

Results

Effect of Infusion of TAK-242 into the PVN on Mean Arterial Pressure

The high-salt diet induced a significant increase in MAP compared with control rats (at day 14, 168 ± 7 mmHg *vs* 103 ± 5 mmHg, $P < 0.05$). Bilateral PVN infusion of TAK-242 significantly decreased the MAP compared with the salt-induced hypertensive rats (146 ± 5 mmHg *vs* 168 ± 7 mmHg, $P < 0.05$; Fig. 1A).

Table 1 Primers used for real-time PCR.

Rat genes	Forward (5′–3′)	Reverse (5′–3′)
NOX2	CTGCCAGTGTGTCGGAATCT	TGTGAATGGCCGTGTGAAGT
NOX4	GGATCACAGAAGGTCCCTAGC	AGAAGTTCAGGGCGTTCACC
SOD1	GGTGGGCCAAAGGATGAAGAG	CCACAAGCCAAACGACTTCC
GAPDH	AGACAGCCGCATCTTCTTGT	CTTGCCGTGGGTAGAGTCAT

NOX2, NADPH oxidase subunit 2; NOX4, NADPH oxidase subunit 4; SOD1, superoxide dismutase 1; GAPDH, glyceraldehyde 3-phosphate dehydrogenase.

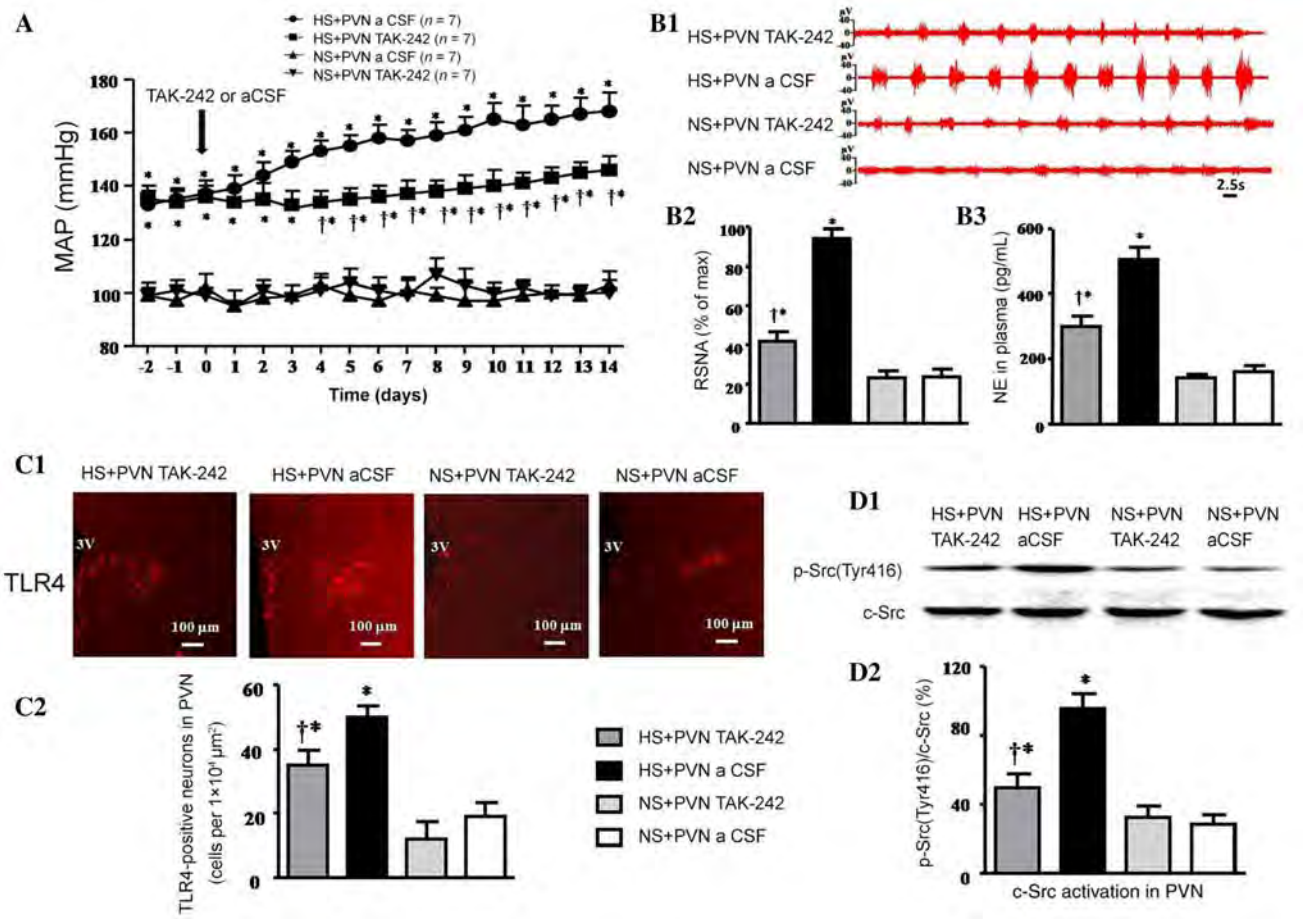

Fig. 1 Bilateral PVN infusion of TAK-242 or aCSF on mean arterial pressure, sympathetic nerve activity, TLR4 expression, and c-Src activation in salt-induced hypertensive rats. **A** Mean arterial pressure (MAP) increased in the high-salt (HS) group. Bilateral PVN infusion of TAK-242 attenuated the HS-induced increase in blood pressure compared with the HS + PVN aCSF group. **B1** Representative renal sympathetic nerve activity (RSNA) in different groups. **B2** Bar graph comparing the RSNA in different groups. RSNA was increased in the HS groups, and bilateral PVN infusion of TAK-242 made the RSNA lower than in the control group. **B3** Bar graph comparing norepinephrine (NE) in the plasma of different groups. The plasma NE in the HS + PVN TAK-242 group was lower than in the control group. **C1** Immunofluorescence for TLR4 (red) in the PVN in different groups. **C2** Numbers of TLR4-positive neurons in the PVN in different groups. **D1** Representative immunoblots of p-Src(Tyr416) and c-Src. **D2** Densitometric analysis of protein expression of p-Src(Tyr416)/c-Src in the PVN in different groups. Values are expressed as the mean ± SEM. $^{*}P < 0.05$ *vs* NS groups (NS + PVN TAK-242 or NS + PVN aCSF); $^{\dagger}P < 0.05$ HS + PVN TAK-242 *vs* HS + PVN aCSF.

Effect of Infusion of TAK-242 into the PVN on Sympathetic Nerve Activity

The RSNA (% of max) and plasma NE induced by HS diet were 395% and 315% of control rats ($P < 0.05$). Bilateral PVN infusion of TAK-242 resulted in a 55.3% decrease in RSNA and a 40.5% decrease in plasma NE in salt-induced hypertensive rats ($P < 0.05$). NS + PVN TAK-242 did not attenuate RSNA when compared with NS + PVN aCSF (Fig. 1B1–B3).

Effect of Infusion of TAK-242 into the PVN on TLR4 and c-Src Activation

The HS groups had a high level of expression of TLR4 and p-Src(Tyr416)/c-Src, and they were lower in the HS + PVN TAK-242 group. The immunofluorescence results revealed that the number of TLR4-positive neurons induced by HS diet was 263% of control rats ($P < 0.05$; Fig. 1C1, C2). Bilateral PVN infusion of TAK-242 caused a 30% decrease in the number of TLR4-positive neurons in hypertensive rats ($P < 0.05$). Western blotting indicated that the protein expression level of activated c-Src (p-Src(Tyr416)/c-Src) in the PVN of the hypertensive rats was 343% of that in the control group ($P < 0.05$; Fig. 1D1, D2). Bilateral PVN infusion of TAK-242 resulted in a 47.9% decrease in the protein expression of activated c-Src compared with salt-induced rats ($P < 0.05$).

Effect of Microinjection of PP2 into the PVN on Mean Arterial Pressure

The MAP in the HS + PVN Vehicle group was higher than that in control animals (at day 14, 167 ± 5 mmHg *vs* 101 ± 3 mmHg, $P < 0.05$). Bilateral PVN microinjection of PP2 decreased the MAP compared with the HS + PVN Vehicle group (at day 14, 144 ± 6 mmHg *vs* 167 ± 5 mmHg, $P < 0.05$) (Fig. 2A).

Effect of Microinjection of PP2 into the PVN on Sympathetic Nerve Activity

The RSNA and plasma NE induced by HS diet were 518% and 294% of the control ($P < 0.05$). Bilateral PVN microinjection of PP2 resulted in a 48.7% decrease in RSNA and a 36.2% decrease in plasma NE in salt-induced hypertensive rats ($P < 0.05$). NS + PVN PP2 did not show any significant change in RSNA and plasma NE compared with NS + PVN Vehicle at the end of the experiment (Fig. 2B1–B3).

Effect of Microinjection of PP2 into the PVN on NF-κB p65, IL-1β, IL-10, and c-Src Activation

The HS groups had high levels of NF-κB p65, IL-1β, and p-Src(Tyr416)/c-Src expression, but lower level of IL-10 expression. And the p-Src(Tyr416)/c-Src of HS + PVN PP2 was lower than that of the HS + PVN Vehicle. The immunofluorescence results (Fig. 2C1, C2) revealed that the number of NF-κB p65-positive neurons induced by the HS diet was 480% of the control ($P < 0.05$). Bilateral PVN microinjection of PP2 caused a 45.8% decrease in the number of NF-κB p65-positive neurons in the PVN in hypertensive rats at the end of the experiment. The Western blotting results (Fig. 2D1–D4) indicated that the protein level of IL-1β and the activated c-Src (p-Src (Tyr416)/c-Src) of salt-induced hypertensive rats were 667% and 544% in the PVN compared with that in the control rats ($P < 0.05$), but the IL-10 in the PVN was lower than that in control rats. Bilateral microinjection of PP2 into the PVN caused a 41.7% decrease in IL-1β and a 56.1% decrease in activated c-Src, but increased the IL-10 protein level compared with salt-induced hypertensive rats ($P < 0.05$).

Effect of Microinjection of PP2 into the PVN on NOX2 and SOD1

The immunofluorescence results revealed that the number of NOX2-positive neurons induced by the HS diet was 525% of the control ($P < 0.05$). However, bilateral PVN microinjection of PP2 caused a 49.2% decrease in NOX2-positive neurons in the PVN in hypertensive rats at the end of the experiment (Fig. 3A1, A2). The western blotting results indicated that the protein level of NOX2 in salt-induced hypertensive rats was 945% of the control, but SOD1 was decreased in the PVN compared with control rats ($P < 0.05$). Bilateral PVN microinjection of PP2 into the PVN caused a 48.1% decrease in NOX2 but increased the SOD1 protein level compared with salt-induced hypertensive rats ($P < 0.05$) (Fig. 3B1–B3).

Effect of Microinjection of PP2 into the PVN on NOX4

The immunofluorescence results (Fig. 3C1, C2) revealed that the number of NOX4-positive neurons induced by the HS diet was 722% compared with control rats ($P < 0.05$). However, bilateral PVN microinjection of PP2 resulted in a 55.4% decrease in NOX4 in the PVN in hypertensive rats at the end of the experiment. The western blotting results (Fig. 3D1, D2) indicated that the protein level of NOX4 in salt-induced hypertensive rats was 115% in the PVN compared with control rats ($P < 0.05$). Bilateral microinjection of PP2 into the PVN resulted in a 47.8% decrease in the NOX4 protein level compared with salt-induced hypertensive rats ($P < 0.05$).

Effect of Microinjection of PP2 into the PVN on the Superoxide Level and the mRNA Levels of NOX2, NOX4, and SOD1

The HS groups had higher ROS activity as measured by DHE (Fig. 3E1, E2). Bilateral PVN microinjection of PP2 reduced the levels of superoxide in the PVN of HS rats. The superoxide level in the HS diet group was 410% of the control ($P < 0.05$). Bilateral PVN microinjection of PP2 caused a 25.6% decrease in superoxide in the PVN of

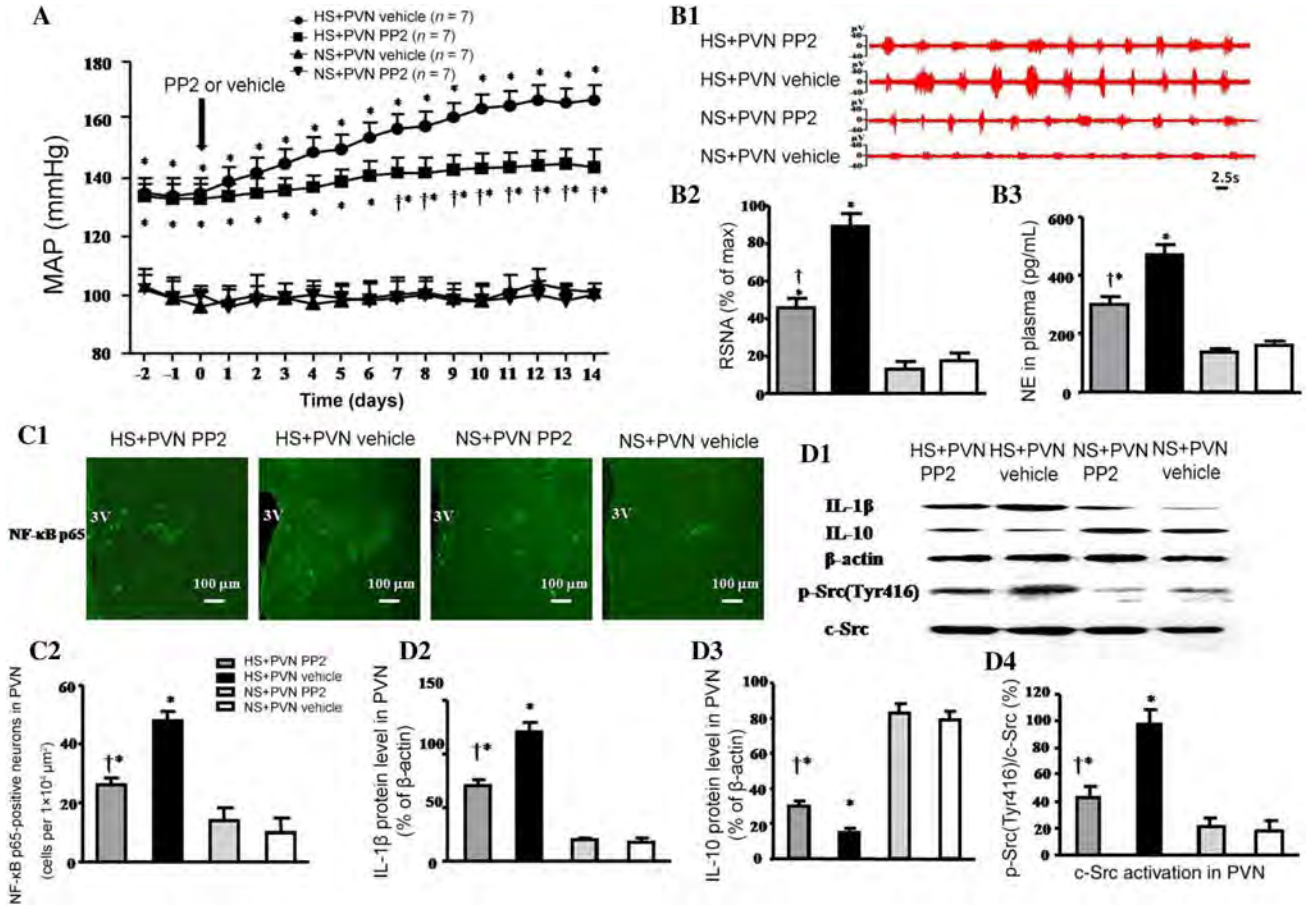

Fig. 2 Effects of bilateral PVN microinjection of PP2 or vehicle on mean arterial pressure, sympathetic nerve activity, NF-κB p65 activation, inflammatory cytokines, and c-Src activation in salt-induced hypertensive rats. **A** The MAP in the HS groups was higher than that in the NS groups. Bilateral PVN microinjections of PP2 for 14 days attenuated the HS-induced increase in blood pressure compared with HS + PVN vehicle. **B1** Representative renal sympathetic nerve activity (RSNA) in the different groups. **B2** Bar graph comparing RSNA in the different groups. The RSNA was higher in the HS groups, and bilateral PVN microinjection of PP2 reduced it to lower than the control group. **B3** Bar graph comparing plasma NE in the different groups. The plasma NE in the HS + PVN PP2 group was lower than in the control group. **C1** Immunofluorescence for NF-κB p65 (green) in the PVN in the different groups. **C2** Numbers of NF-κB p65-positive neurons in the PVN in the different groups. **D1** Representative immunoblots of IL-1β, IL-10, p-Src(Tyr416), and c-Src. **D2–D4** Densitometric analysis of protein expression of IL-1β, IL-10, and p-Src(Tyr416)/c-Src in the PVN in the different groups. Values are expressed as the mean ± SEM. $^{*}P < 0.05$ *vs* NS groups (NS + PVN PP2 or NS + PVN Vehicle); $^{\dagger}P < 0.05$ HS + PVN PP2 *vs* HS + PVN Vehicle.

hypertensive rats at the end of the experiment ($P < 0.05$). The RT-PCR results (Fig. 3F) indicated that the protein levels of NOX2 and NOX4 induced by the HS diet were 288% and 365% in the PVN compared with control rats, but SOD1 was decrased ($P < 0.05$). Bilateral PVN microinjection of PP2 resulted in a 56.7% decrease in the mRNA level of NOX2 and a 59.7% decrease in NOX4, but SOD1 was increased compared with the salt-induced hypertensive rats ($P < 0.05$).

Effect of TAK-242 and PP2 on Oxidative Stress in the PVN

Compared with the NS rats, the hypertensive rats had higher levels of MDA and NAD(P)H oxidase activity, but lower levels of SOD and GSH in the PVN. Infusion of TAK-242 or microinjection of PP2 into the PVN attenuated the levels of the MDA and NAD(P)H oxidase activity, and also augmented the levels of the SOD activity and GSH in the PVN of the HS groups (Table 2).

Discussion

In this study, we mainly investigated how activated c-Src acts in the PVN during the hypertensive responses by an induced high-salt diet. The novel findings of this study are: (1) the HS diet increased the expression of TLR4 and PICs, increased ROS production, and enhanced the activation of c-Src in the PVN; (2) TLR4 regulated blood pressure by

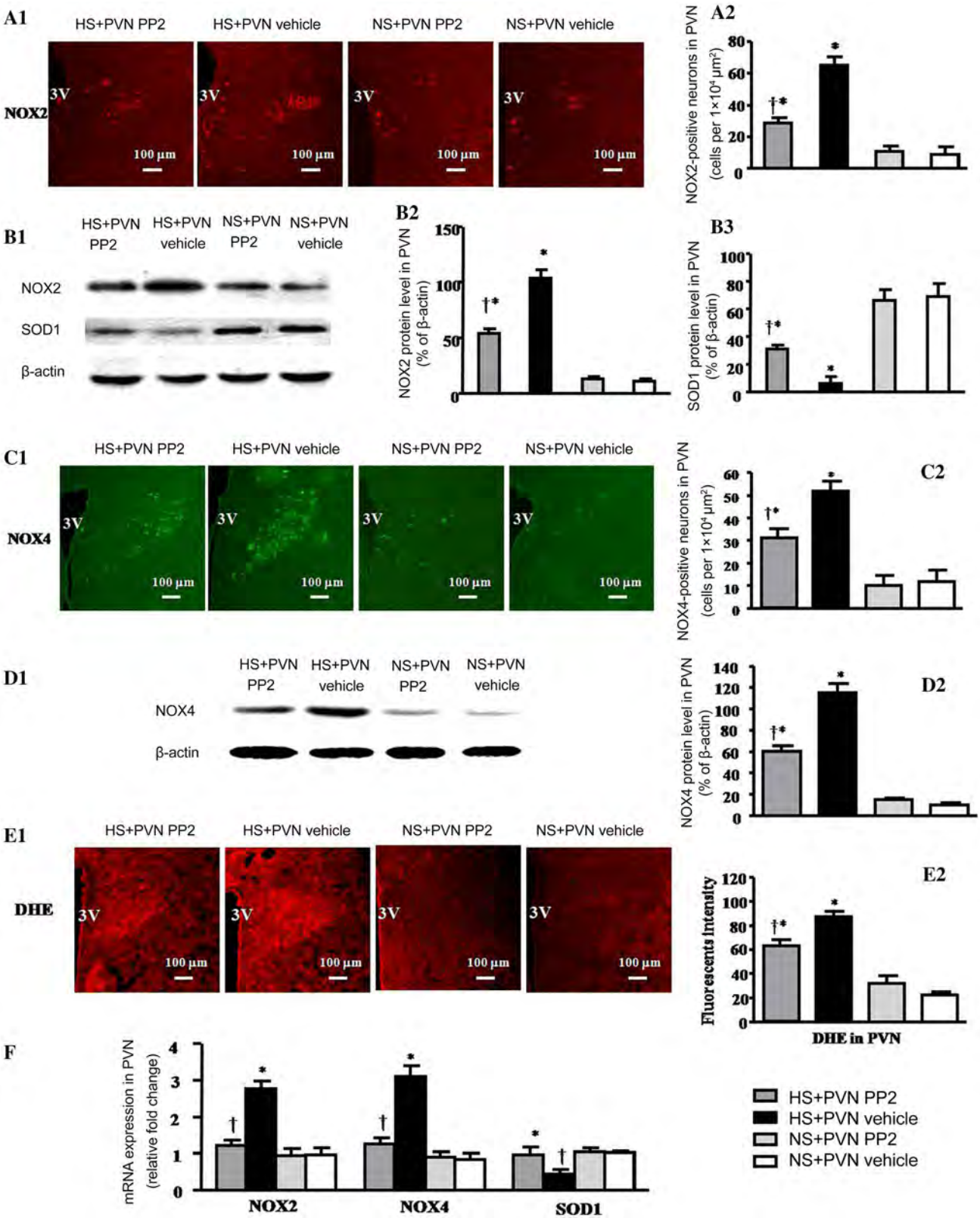
A1
HS+PVN PP2
HS+PVN vehicle
NS+PVN PP2
NS+PVN vehicle
NOX2
3V
100 μm
A2
NOX2-positive neurons in PVN
(cells per 1×10⁴ μm²)
B1
HS+PVN PP2
HS+PVN vehicle
NS+PVN PP2
NS+PVN vehicle
NOX2
SOD1
β-actin
B2
NOX2 protein level in PVN
(% of β-actin)
B3
SOD1 protein level in PVN
(% of β-actin)
C1
NOX4
C2
NOX4-positive neurons in PVN
(cells per 1×10⁴ μm²)
D1
NOX4
β-actin
D2
NOX4 protein level in PVN
(% of β-actin)
E1
DHE
E2
Fluorescents Intensity
DHE in PVN
F
mRNA expression in PVN
(relative fold change)
NOX2
NOX4
SOD1
HS+PVN PP2
HS+PVN vehicle
NS+PVN PP2
NS+PVN vehicle

◀**Fig. 3** Effects of bilateral PVN microinjection of PP2 or vehicle on oxidative stress in salt-induced hypertensive rats. **A1** Immunofluorescence for NOX2 (red) in the PVN in the different groups. **A2** Numbers of NOX2-positive neurons in the PVN in the different groups. **B1** Representative immunoblots of NOX2 and SOD1. **B2**, **B3** Densitometric analysis of protein expression of NOX2 and SOD1 in the PVN in the different groups. **C1** Immunofluorescence for NOX4 (green) in the PVN in the different groups. **C2** Numbers of NOX4-positive neurons in the PVN in the different groups. **D1** Representative immunoblots of NOX4. **D2** Densitometric analysis of protein expression of NOX4 in the PVN in the different groups. **E1** Immunofluorescence for superoxide in the PVN in the different groups. **E2** Immunofluorescence intensity of DHE in the PVN in the different groups. **F** mRNA expression of NOX2, NOX4, and SOD1 in the PVN in the different groups. Values are expressed as the mean ± SEM. $^{*}P < 0.05$ *vs* NS groups (NS + PVN PP2 or NS + PVN Vehicle); $^{\dagger}P < 0.05$ HS + PVN PP2 *vs* HS + PVN Vehicle.

increasing the activation of c-Src in the PVN; (3) activation of c-Src in the PVN increased the expression of PICs by regulating the activation of NF-κB; and (4) in the PVN, the activated c-Src increased the production of the ROS in salt-induced hypertension. Thereby, c-Src participates in the development of salt-induced hypertension through regulating the PICs and ROS. We conclude that in salt-induced hypertension, TLR4 in the PVN increases the c-Src activity, and then the activated c-Src increases the PICs and ROS, which lead to increased sympathetic nerve activity and blood pressure. Therefore, inhibition of c-Src activity in the PVN may be a new target for the treatment of salt-induced hypertension.

It is well known that a long-term salt diet increases BP. Previous research focused on peripheral regulation of hypertension, but in recent studies, the central regulation of blood pressure has received more attention, and the PVN as a cardiovascular regulatory center plays a very important role in sympathetic nervous activity, BP control, and neurohumoral regulation. Our previous studies showed that oxidative stress and inflammatory cytokines in the PVN are involved in the regulation of sympathetic activity and blood pressure [2–4]. Chronic inflammatory responses have been noted as a factor in hypertension. The inflammatory cytokines, such as TNF-α, IL-1β, IL-6, and IL-10, are also considered to be important factors in the development of hypertension [30, 31]. Blocking TNF-α in the PVN reduces MAP and improves cardiac hypertrophy [32]. Chronic bilateral PVN intervention with an IL-1β inhibitor reduces the expression of NLRP3 (NOD-like receptor family pyrin domain-containing 3) protein on sympathetic neurons and thus affects the occurrence and development of hypertension [3]. In this study, we found that, in the high salt-induced hypertension, the expression of IL-1β and activated NF-κB in the PVN were increased and the expression of the anti-inflammatory cytokine IL-10 was decreased. So inflammatory cytokines in the PVN are involved in the process of hypertension. In addition, oxidative stress is an important link in the pathogenesis and development of hypertension, and an HS diet induces ROS production in central and peripheral tissues. Our results also indicated that the levels of NAD(P)H oxidase isoforms in the PVN were increased, and the excessive ROS production stimulated hypertensive responses and increased sympathetic outflow in high salt-induced hypertensive rats. The above results are consistent with the studies from our laboratory and other laboratories [4, 33].

TLR4, an important innate immune system receptor, is closely associated with inflammation [34, 35]. Studies have shown that TLR4 regulates the expression of PICs by increasing the activity of NF-κB [10], and TLR4 plays an important role in the progression of hypertension [32]. Other studies have shown that TLR-dependent signaling pathways in some immune or non-immune cells induce oxidative stress by stimulating several NAD(P)H oxidase isoforms [12, 36]. In this study, the HS diet increased the levels of TLR4 in the PVN, and blocking the expression of TLR4 suppressed the effect of HS on the hypertensive responses. Previous experiments in our laboratory also demonstrated that inhibiting TLR4 expression down-

Table 2 Effects of TAK-242 and PP2 on MDA, SOD, and GSH levels, and NAD(P)H oxidase activity.

Parameters	MDA (mmol/mgp)	SOD (U/mgp)	GSH (μmol/mgp)	NAD(P)H oxidase (RLU/mg/s)
HS + PVN TAK-242	4.4 ± 0.5*†	7.03 ± 0.34*†	3.27 ± 0.23*†	2.21 ± 1.24*†
HS + PVN aCSF	6.03 ± 0.37*	3.79 ± 0.11*	0.853 ± 0.20*	4.14 ± 1.17*
NS + PVN TAK-242	2.11 ± 0.76	9.18 ± 0.39	4.27 ± 0.25	1.13 ± 0.43
NS + PVN aCSF	1.94 ± 0.4	9.16 ± 1.27	4.736 ± 0.27	1.15 ± 0.15
HS + PVN PP2	3.97 ± 0.47*†	4.91 ± 0.28*†	1.84 ± 0.26*†	3.10 ± 1.1*†
HS + PVN vehicle	5.7 ± 0.38*	3.5 ± 0.22*	1.00 ± 0.15*	4.93 ± 1.73*
NS + PVN PP2	2.65 ± 0.7	7.83 ± 0.47	3.4 ± 0.18	1.435 ± 0.52
NS + PVN vehicle	2.6 ± 0.36	7.79 ± 0.59	3.00 ± 0.21	1.56 ± 0.22

n = 7/group; NS, normal salt diet; HS, high salt diet; mgp, mg protein; $^{*}P < 0.05$ *vs* NS groups, $^{\dagger}P < 0.05$ HS + PVN TAK-242 or HS + PVN PP2 *vs* HS control groups.

regulates PICs and ROS, and regenerates neurotransmitter balance in the PVN [9]. Thus, combined with this study and previous studies from our laboratory, it has been demonstrated that TLR4 regulates PICs and ROS in salt-induced hypertension. However, we do not know the specific mechanism by which TLR4 acts on PICs and ROS, so we suggest the following experiments and speculations.

c-Src is a non-receptor membrane-bound tyrosine kinase that plays an important role in various cell signaling pathways [13–15]. c-Src is closely associated with both inflammatory cytokines [19, 20] and oxidative stress [16–18, 37]. In this study, we found that the expression of activated c-Src in the PVN was higher in the high salt-induced hypertensive rats than in the control group, and the RSNA and BP were higher in the salt-induced hypertension group. After chronic bilateral PVN intervention with a TLR4 blocker, the activation of c-Src in the PVN was decreased, along with the sympathetic excitability and BP. These results indicated that TLR4 regulates the activity of c-Src in the PVN in salt-induced hypertension. After bilateral PVN administration of a c-Src blocker, the activation of NF-κB, the expression of PICs, and the level of ROS were decreased in the PVN. At the same time, the RSNA, NE, and BP were decreased. The results of these experiments indicated that the activated c-Src regulates NF-κB, PICs, and ROS in the PVN in salt-induced hypertension. Therefore, combining the results of the two sets of experiments, we can infer that TLR4 augments the activation of c-Src, and the activated c-Src increases the NF-κB, PICs, and ROS to regulate the RSNA and BP in salt-induced hypertension. Previous research in our laboratory found that PICs and ROS in the PVN are down-regulated after blocking TLR4 [9] and that TLR4 regulates PICs and ROS *via* regulating the activation of NF-κB, and then regulates hypertensive responses [9, 11]. Meanwhile, some studies have suggested that c-Src has an effect on the ROS and PICs in cells by regulating the activation of NF-κB [19] and the levels of NAD(P)H oxidase [38]. Therefore, we conclude that in salt-induced hypertension, the activated c-Src in the PVN is augmented by TLR4, and then the activated c-Src regulates PICs and ROS *via* enhancing the activation of NF-κB and NAD(P)H oxidase, so as to regulate sympathetic activity and BP (Fig. 4).

Conclusion

We found that a long-term high-salt diet increases TLR4 expression in the PVN and activates the TLR4 signal pathway. And the high expression of TLR4 promotes the activation of c-Src. Blocking the activation of c-Src attenuates the effectiveness of the TLR4 pathway. This result suggests that c-Src may be a modulator in the TLR4 signaling pathway which regulates inflammatory cytokines and oxidative stress to increase the sympathetic activity and blood pressure in salt-induced hypertension. Therefore, inhibiting central c-Src activity may become a new target for treating salt-induced hypertension.

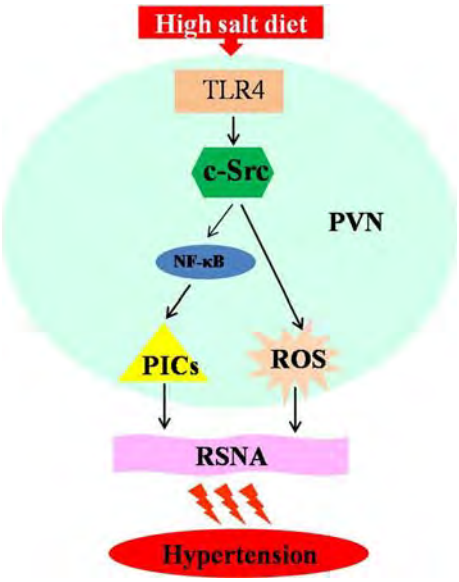

Fig. 4 Schematic representation of the hypothesis. c-Src acts as a modulator in the TLR4 signal pathway which regulates inflammatory cytokines and oxidative stress responses, and then increases peripheral sympathetic activation and raises blood pressure in salt-induced hypertension.

Acknowledgements This work was supported by the National Natural Science Foundation of China (81770426, 81600333, 81600330, and 81800373), China Postdoctoral Science Foundation (2016M602835), and Shaanxi Postdoctoral Science Foundation (2016BSHEDZZ91).

Conflict of interest The authors report no conflicts of interest.

References

1. Sriramula S, Haque M, Majid DS, Francis J. Involvement of tumor necrosis factor-alpha in angiotensin II-mediated effects on salt appetite, hypertension, and cardiac hypertrophy. Hypertension 2008, 51: 1345–1351.
2. Li HB, Qin DN, Cheng K, Su Q, Miao YW, Guo J, *et al.* Central blockade of salusin beta attenuates hypertension and hypothalamic inflammation in spontaneously hypertensive rats. Sci Rep 2015, 5: 11162.
3. Qi J, Zhao XF, Yu XJ, Yi QY, Shi XL, Tan H, *et al.* Targeting interleukin-1 beta to suppress sympathoexcitation in hypothalamic paraventricular nucleus in Dahl salt-sensitive hypertensive rats. Cardiovasc Toxicol 2016, 16: 298–306.
4. Su Q, Liu JJ, Cui W, Shi XL, Guo J, Li HB, *et al.* Alpha lipoic acid supplementation attenuates reactive oxygen species in hypothalamic paraventricular nucleus and sympathoexcitation in high salt-induced hypertension. Toxicol Lett 2016, 241: 152–158.

5. Gao HL, Yu XJ, Qi J, Yi QY, Jing WH, Sun WY, *et al.* Oral CoQ10 attenuates high salt-induced hypertension by restoring neurotransmitters and cytokines in the hypothalamic paraventricular nucleus. Sci Rep 2016, 6: 30301.
6. Zhang M, Qin DN, Suo YP, Su Q, Li HB, Miao YW, *et al.* Endogenous hydrogen peroxide in the hypothalamic paraventricular nucleus regulates neurohormonal excitation in high salt-induced hypertension. Toxicol Lett 2015, 235: 206–215.
7. Su Q, Huo CJ, Li HB, Liu KL, Li X, Yang Q, *et al.* Renin-angiotensin system acting on reactive oxygen species in paraventricular nucleus induces sympathetic activation via AT1R/PKCgamma/Rac1 pathway in salt-induced hypertension. Sci Rep 2017, 7: 43107.
8. Dange RB, Agarwal D, Teruyama R, Francis J. Toll-like receptor 4 inhibition within the paraventricular nucleus attenuates blood pressure and inflammatory response in a genetic model of hypertension. J Neuroinflammation 2015, 12: 31.
9. Wang ML, Yu XJ, Li XG, Pang DZ, Su Q, Saahene RO, *et al.* Blockade of TLR4 within the paraventricular nucleus attenuates blood pressure by regulating ROS and inflammatory cytokines in prehypertensive rats. Am J Hypertens 2018, 31: 1013–1023.
10. Kawai T, Akira S. TLR signaling. Cell Death Differ 2006, 13: 816–825.
11. Li HB, Li X, Huo CJ, Su Q, Guo J, Yuan ZY, *et al.* TLR4/MyD88/NF-kappaB signaling and PPAR-gamma within the paraventricular nucleus are involved in the effects of telmisartan in hypertension. Toxicol Appl Pharmacol 2016, 305: 93–102.
12. Lugrin J, Rosenblatt-Velin N, Parapanov R, Liaudet L. The role of oxidative stress during inflammatory processes. Biol Chem 2014, 395: 203–230.
13. Touyz RM, He G, Wu XH, Park JB, Mabrouk ME, Schiffrin EL. Src is an important mediator of extracellular signal-regulated kinase 1/2-dependent growth signaling by angiotensin II in smooth muscle cells from resistance arteries of hypertensive patients. Hypertension 2001, 38: 56–64.
14. Touyz RM, Yao G, Schiffrin EL. c-Src induces phosphorylation and translocation of p47phox: role in superoxide generation by angiotensin II in human vascular smooth muscle cells. Arterioscler Thromb Vasc Biol 2003, 23: 981–987.
15. Khanna S, Roy S, Park HA, Sen CK. Regulation of c-Src activity in glutamate-induced neurodegeneration. J Biol Chem 2007, 282: 23482–23490.
16. Cheng SE, Lee IT, Lin CC, Kou YR, Yang CM. Cigarette smoke particle-phase extract induces HO-1 expression in human tracheal smooth muscle cells: role of the c-Src/NADPH oxidase/MAPK/Nrf2 signaling pathway. Free Radic Biol Med 2010, 48: 1410–1422.
17. Salter MW, Kalia LV. Src kinases: a hub for NMDA receptor regulation. Nat Rev Neurosci 2004, 5: 317–328.
18. Gianni D, Bohl B, Courtneidge SA, Bokoch GM. The involvement of the tyrosine kinase c-Src in the regulation of reactive oxygen species generation mediated by NADPH oxidase-1. Mol Biol Cell 2008, 19: 2984–2994.
19. Hou CH, Fong YC, Tang CH. HMGB-1 induces IL-6 production in human synovial fibroblasts through c-Src, Akt and NF-kappaB pathways. J Cell Physiol 2011, 226: 2006–2015.
20. Hsu CK, Lee IT, Lin CC, Hsiao LD, Yang CM. Sphingosine-1-phosphate mediates COX-2 expression and PGE2 /IL-6 secretion *via* c-Src-dependent AP-1 activation. J Cell Physiol 2015, 230: 702–715.
21. Paxinos G, Watson G. The Rat Brain in Stereotaxic Coordinates. 6th ed. San Diego: Academic Press, 2007.
22. Kang YM, Zhang ZH, Xue B, Weiss RM, Felder RB. Inhibition of brain proinflammatory cytokine synthesis reduces hypothalamic excitation in rats with ischemia-induced heart failure. Am J Physiol Heart Circ Physiol 2008, 295: H227–H236.
23. Han Y, Yuan N, Zhang SJ, Gao J, Shi Z, Zhou YB, *et al.* c-Src in paraventricular nucleus modulates sympathetic activity and cardiac sympathetic afferent reflex in renovascular hypertensive rats. Pflugers Arch 2011, 461: 437–446.
24. Gu JW, Bailey AP, Tan W, Shparago M, Young E. Long-term high salt diet causes hypertension and decreases renal expression of vascular endothelial growth factor in Sprague-Dawley rats. J Am Soc Hypertens 2008, 2: 275–285.
25. Su Q, Qin DN, Wang FX, Ren J, Li HB, Zhang M, *et al.* Inhibition of reactive oxygen species in hypothalamic paraventricular nucleus attenuates the renin-angiotensin system and proinflammatory cytokines in hypertension. Toxicol Appl Pharmacol 2014, 276: 115–120.
26. Kang YM, Ma Y, Zheng JP, Elks C, Sriramula S, Yang ZM, *et al.* Brain nuclear factor-kappa B activation contributes to neurohumoral excitation in angiotensin II-induced hypertension. Cardiovasc Res 2009, 82: 503–512.
27. Li Z, You Z, Li M, Pang L, Cheng J, Wang L. Protective effect of resveratrol on the brain in a rat model of epilepsy. Neurosci Bull 2017, 33: 273–280.
28. Kong X, Wei J, Wang D, Zhu X, Zhou Y, Wang S, *et al.* Upregulation of spinal voltage-dependent anion channel 1 contributes to bone cancer pain hypersensitivity in rats. Neurosci Bull 2017, 33: 711–721.
29. Li HB, Qin DN, Ma L, Miao YW, Zhang DM, Lu Y, *et al.* Chronic infusion of lisinopril into hypothalamic paraventricular nucleus modulates cytokines and attenuates oxidative stress in rostral ventrolateral medulla in hypertension. Toxicol Appl Pharmacol 2014, 279: 141–149.
30. Agarwal D, Dange RB, Raizada MK, Francis J. Angiotensin II causes imbalance between pro- and anti-inflammatory cytokines by modulating GSK-3beta in neuronal culture. Br J Pharmacol 2013, 169: 860–874.
31. Kang YM, Zhang DM, Yu XJ, Yang Q, Qi J, Su Q, *et al.* Chronic infusion of enalaprilat into hypothalamic paraventricular nucleus attenuates angiotensin II-induced hypertension and cardiac hypertrophy by restoring neurotransmitters and cytokines. Toxicol Appl Pharmacol 2014, 274: 436–444.
32. Cardinale JP, Sriramula S, Mariappan N, Agarwal D, Francis J. Angiotensin II-induced hypertension is modulated by nuclear factor-kappaB in the paraventricular nucleus. Hypertension 2012, 59: 113–121.
33. Iranloye BO, Oludare GO, Morakinyo AO, Esume NA, Ekeh LC. Reproductive parameters and oxidative stress status of male rats fed with low and high salt diet. J Hum Reprod Sci 2013, 6: 267–272.
34. Li T, Wang Y, Liu C, Hu Y, Wu M, Li J, *et al.* MyD88-dependent nuclear factor-kappaB activation is involved in fibrinogen-induced hypertrophic response of cardiomyocytes. J Hypertens 2009, 27: 1084–1093.
35. Liu-Bryan R, Scott P, Sydlaske A, Rose DM, Terkeltaub R. Innate immunity conferred by Toll-like receptors 2 and 4 and myeloid differentiation factor 88 expression is pivotal to monosodium urate monohydrate crystal-induced inflammation. Arthritis Rheum 2005, 52: 2936–2946.
36. Gill R, Tsung A, Billiar T. Linking oxidative stress to inflammation: Toll-like receptors. Free Radic Biol Med 2010, 48: 1121–1132.
37. Martel-Gallegos G, Casas-Pruneda G, Ortega-Ortega F, Sanchez-Armass S, Olivares-Reyes JA, Diebold B, *et al.* Oxidative stress induced by P2X7 receptor stimulation in murine macrophages is mediated by c-Src/Pyk2 and ERK1/2. Biochim Biophys Acta 2013, 1830: 4650–4659.
38. Igwe OJ. Prooxidant-induced c-Src/nuclear factor kappa B-coupled signalling in sensory ganglia mediates cutaneous hyperalgesia. Eur J Pain 2013, 17: 1027–1038.

Neurosci. Bull. April, 2020, 36(4):396–406
https://doi.org/10.1007/s12264-019-00438-w

www.neurosci.cn
www.springer.com/12264

ORIGINAL ARTICLE

Contribution of Baroreflex Afferent Pathway to NPY-Mediated Regulation of Blood Pressure in Rats

Yang Liu[1,2] · Shu-Yang Zhao[1] · Yan Feng[1] · Jie Sun[1] · Xiao-Long Lu[3] · Qiu-Xin Yan[1] · Ying Li[1] · Zhuo Liu[1,4] · Lu-Qi Wang[1] · Xun Sun[1] · Shijun Li[2] · Guo-Fen Qiao[1] · Bai-Yan Li[1]

Received: 14 April 2019 / Accepted: 22 May 2019 / Published online: 29 October 2019

Abstract Neuropeptide Y (NPY), a metabolism-related cardiovascular factor, plays a crucial role in blood pressure (BP) regulation *via* peripheral and central pathways. The expression of NPY receptors (Y_1R/Y_2R) specific to baroreflex afferents impacts on the sexually dimorphic neural control of circulation. This study was designed to investigate the expression profiles of NPY receptors in the nodose ganglion (NG) and nucleus tractus solitary (NTS) under hypertensive conditions. To this end, rats with hypertension induced by N^G-nitro-L-arginine methylester (L-NAME) or high fructose drinking (HFD), and spontaneously hypertensive rats (SHRs) were used to explore the effects/mechanisms of NPY on BP using functional, molecular, and electrophysiological approaches. The data showed that BP was elevated along with baroreceptor sensitivity dysfunction in model rats; Y_1R was up- or down-regulated in the NG or NTS of male and female HFD/L-NAME groups, while Y_2R was only down-regulated in the HFD groups as well as in the NG of the male L-NAME group. In SHRs, Y_1R and Y_2R were both down-regulated in the NTS, and not in the NG. In addition to NPY-mediated energy homeostasis, leptin-melanocortin activation may be essential for metabolic disturbance-related hypertension. We found that leptin and α-melanocyte stimulating hormone (α-MSH) receptors were aberrantly down-regulated in HFD rats. In addition, α-MSH concentrations were reduced and NPY concentrations were elevated in the serum and NTS at 60 and 90 min after acute leptin infusion. Electrophysiological recordings showed that the decay time-constant and area under the curve of excitatory post-synaptic currents were decreased by Y_1R activation in A-types, whereas, both were increased by Y_2R activation in Ah- or C-types. These results demonstrate that sex- and afferent-specific NPY receptor expression in the baroreflex afferent pathway is likely to be a novel target for the clinical management of metabolism-related and essential hypertension.

Keywords Neuropeptide Y · Hypertension · Nucleus of the solitary tract · Excitatory post-synaptic current · Baroreflex

Yang Liu and Shu-Yang Zhao have contributed equally to this work.

Electronic supplementary material The online version of this article (https://doi.org/10.1007/s12264-019-00438-w) contains supplementary material, which is available to authorized users.

✉ Guo-Fen Qiao
qiaogf88@163.com

✉ Bai-Yan Li
liby@ems.hrbmu.edu.cn

[1] Department of Pharmacology, State-Province Key Laboratories of Biomedicine-Pharmaceutics of China, Key Laboratory of Cardiovascular Medicine Research, Ministry of Education, College of Pharmacy, Harbin Medical University, Harbin 150081, China

[2] Department of Clinical Laboratory, The First Affiliated Hospital of Dalian Medical University, Dalian 116011, China

[3] Department of Pharmacology, College of Pharmacy, Dalian Medical University, Dalian 116044, China

[4] Riley Heart Center, Wells Center for Pediatric Research, Indiana University School of Medicine, Indianapolis, IN 46202, USA

Introduction

Neuropeptide Y (NPY), discovered in 1982 [1], is a neurotransmitter widely expressed in the central and peripheral nervous systems. By binding to different receptors, NPY has wide physiological functions in food intake

[2, 3], metabolic disorders [4], and cardiovascular regulation [5]. Peripherally, NPY activates adrenaline by coupling to type-I NPY receptors (Y_1Rs) and modulates vasoconstrictor or vasopressor responses [6], while centrally, these effects play the opposite role, and are usually anti-hypertensive [7]. On the other hand, type-II NPY receptors (Y_2Rs) are quite different from Y_1Rs; they are abundantly distributed in presynaptic neurons and regulate neurotransmitter release [8]. Recently, we reported [9] the direct activation of Y_1Rs and Y_2Rs expressed in the nodose ganglia (NG) that contain the cell bodies of the first-order neurons in the afferent loop of the baroreflex. Several lines of evidence also imply that NPY and its agonists have central hypotensive effects on the nucleus of the solitary tract (NTS), a baroreflex center [7, 10]. However, the specific role of NPY and different expression of NPY receptors have not yet been established in the baroreflex afferent pathway under hypertensive conditions.

Hypertension affects more than 1 billion people worldwide [11, 12] and the American Heart Association estimates this number will double by 2050. It is well-recognized that hypertension is a common complication of metabolic diseases. As reported previously [13, 14], NPY levels are not only closely associated with endothelial dysfunction but also metabolic syndrome and hypertension. It has been shown [15] that blockade of nitric oxide synthase (NOS) causes NO deficiency and impaired vascular relaxation leading to a sustained increase in blood pressure (BP). Likewise, NPY promotes positive energy balance in part by suppressing α-melanocyte-stimulating hormone (α-MSH), which binds to and activates melanocortin 3/4 receptors to inhibit food intake as an anorexigenic peptide [4, 16]. In contrast, the protein hormone leptin contributes to the regulation of the sympathetic nervous system [17] and is counterbalanced by NPY in the hypothalamus and peripheral autonomic nervous system. Nevertheless, the mechanisms and interactions between leptin, α-MSH, and NPY in the baroreflex afferent pathway remain unclear. Therefore, in this study, we investigated the effects of NPY and its receptors in the baroreflex afferent pathway of rats with hypertension induced by N^G-nitro-L-arginine methylester (L-NAME) or high fructose-drinking (HFD) as models of secondary hypertension and compared them with essential hypertension using spontaneously hypertensive rats (SHRs).

Electrophysiological and pharmacological studies have shown that activation of Y_1Rs and Y_2Rs mediates differential neuronal excitation and Ca^{2+} channel modulation in myelinated A-, Ah- and unmyelinated C-type baroreceptor neurons (BRNs) in the NG and participates in the regulation of peripheral BP [9]. In addition, along with the solitary tract pathway, baroreceptor reflexes can be initiated directly within the medial NTS by incoming action potentials with no intervening synapse [18, 19] and glutamate is the primary neurotransmitter released from all vagal afferents to transfer information to the NTS [20–22]. The underlying cellular mechanisms of NPY within the NTS are not yet clear. Here, we recorded evoked excitatory post-synaptic currents (EPSCs) in horizontal brainstem slices to test whether NPY alters afferent synaptic integration at the second-order baroreceptive neurons of the NTS and provide evidence to support the role of Y_1R and/or Y_2R expression in the NG and NTS in the neural control of BP regulation under hypertensive conditions.

Materials and Methods

All the animal protocols were approved by the Institutional Animal Care and Use Committee of Harbin Medical University, and were in accord with the recommendations of the Panel on Euthanasia of the American Veterinary Medical Association and the National Institutes of Health Guide for the Care and Use of Laboratory Animals (http://www.nap.edu/readingroom/books/labrats/). Systolic artery BP was measured by tail-cuff (BP-98A, Saffron, Japan). NG and NTS tissues were collected for molecular and immunohistochemical studies to assess Y_1R and Y_2R expression and distribution. The concentrations of metabolic regulators (α-MSH and NPY) were measured by ELISA. The baroreceptor sensitivity (BRS) was assessed by the injection of vasoactive drugs. Horizontal brainstem slices were prepared for recording solitary tract-evoked EPSCs in baroreceptive neurons of the NTS [23]. Details are available in the Online-only Supplement.

Data Analysis

Clampfit (Molecular Devices, Sunnyvale, CA) was used for initial patch-clamp recording. Excel and Origin (Microsoft, Northampton, MA) were used for statistical analysis and graphing. Fluorescence intensity was measured using Image J-pro plus 5.0 (Media Cybernetics, Rockville, MD) and the Odyssey Infrared Imaging System (LI-COR Inc., Lincoln, NE). Student's *t*-test and one-way ANOVA were applied to compare the significance of differences between and among groups and averaged data are presented as the mean ± SD. The $P \leq 0.05$ was considered to show a significant difference.

Results

Dysregulation of NPYRs in Hypertension Induced by High-Fructose Drinking

To explore the relationship between NPY and baroreflex afferent function under metabolic syndrome-related

hypertensive conditions, the rat model of high fructose-drinking-induced hypertension (HFD-HTN) was established using male and age-matched female rats. Our preliminary data showed that the systemic BP and serum concentration of NPY were significantly and continuously higher in male and female HFD-HTN rats during 4 weeks of HFD than in normal controls (Fig. S1). The results from immunohistochemistry and whole section visualization of the NG and NTS showed that both Y_1Rs and Y_2Rs (Fig. 1A, E) were distributed in the cell membrane and cytoplasm of myelinated afferents (HCN1-positive), whereas they were only detected in the cell-membrane of unmyelinated afferents (HCN1-negative). The mean fluorescence intensity was significantly higher in HCN1-positive than HCN1-negative neurons. Meanwhile, they were all expressed in the NTS region (Fig. 1B, F). Quantification (Table S1) showed that the mean fluorescent intensity was higher in the HCN1-positive population and lower in the HCN1-negative population, respectively, in the HFD-HTN group ($P < 0.05$). In the NTS, the intensity of Y_1R and Y_2R expression was lower in the HFD-HTN group than in controls ($P < 0.05$, Table S2). Furthermore, the mRNA and protein levels of Y_1Rs and Y_2Rs in the NG and NTS were confirmed by qRT-PCR and western blot (Fig. 1C, D, G, H). Interestingly, the expression profiles in the NG were in stark contrast to those in the NTS. First, at the receptor level, up-regulated Y_1R and down-regulated Y_2R expression were clearly seen in the NG of HFD-HTN rats, and these expression changes further support their functional roles in the neural control of BP [9] and that they are responsible at least partially for the development of hypertension; second, at the NG and NTS level, an opposite expression profile for Y_1R and synergistic expression profile of Y_2R were also recognized, and these findings are consistent with the roles of the NG [9] and NTS [7] in the management of BP under normal and disease conditions. Although a sex difference in Y_1R and Y_2R expression in the NG under physiological conditions has been reported [9], this difference in the expression pattern of both receptors has not yet been detected under hypertensive disease conditions.

Expression of Other Metabolic Factors in the NG and NTS

The published data from another group have shown that hypothalamic neuropeptides such as NPY and α-MSH interact closely with leptin, an anorexic peptide produced mainly by adipose tissue and involved in the regulation of appetite, energy balance, and sympathetic nervous system activity [24]. The pilot experimental results showed that significant changes in BP were not reached with systemic application of leptin, but BP declined after NG microinjection of leptin (data not shown), suggesting a collaborative mechanism among leptin, NPY, and α-MSH. Thus, it is necessary to clarify the effects of expression of leptin and α-MSH receptors on the baroreflex afferent pathway in HFD-HTN rats. Of the five melanocortin receptor subtypes identified to date, MC3R and MC4R are expressed primarily in the brain and influence cardiovascular action [25, 26]. The current immunohistochemical findings in the NG showed that the mean fluorescence intensity of MC3R and MC4R expressed on myelinated and unmyelinated neurons were clearly reduced in HFD-HTN rats (Fig. 2A, B), and identical expression also occurred in the NTS (Fig. 2C). Importantly, similar expression patterns for leptin receptors were also found in the NG and NTS under similar experimental conditions (data not shown). These data suggested that metabolic factors play an important role in the pathogenesis of hypertension.

Direct Effect of Leptin on Changes in NPY and α-MSH in Serum and NTS

The results above showed that leptin and α-MSH are both expressed in the baroreflex afferent pathway and very likely to contribute to the development of hypertension. Thus, it was essential to confirm the direct effect of leptin on BP. Thus, we delivered leptin systemically and surprisingly, there was no significant change in BP, further suggesting a likely collaborative change between NPY and α-MSH in BP stabilization from the functional point of view. To test this hypothesis, blood and NTS tissue were collected from all groups immediately after intravenous administration of 100 μg/kg leptin and measurement of MAP. These data demonstrated that BP was maintained for 90 min after leptin administration (data not shown); however, the α-MSH levels both in serum and NTS tissue were significantly lower at 60 and 90 min (Fig. 3A) along with a significant elevation of NPY ($\sim$ 2-fold) (Fig. 3B). These results implied that NPY and its receptors (Y_1R and Y_2R) play a key role in the neural control of BP *via* the baroreflex afferent pathway, in collaboration with other metabolic factors/neuropeptides, such as leptin and α-MSH.

Expression Changes in NPY Receptors in Hypertension Induced by L-NAME

Previous studies have demonstrated that NO plays a critical role as a molecular mediator in a variety of biological processes, including vasodilatation and neurotransmission [27]. To explore the interaction between NPY and NO in cardiovascular dysregulation and the potential involvement of baroreflex afferents, we induced hypertension in rats

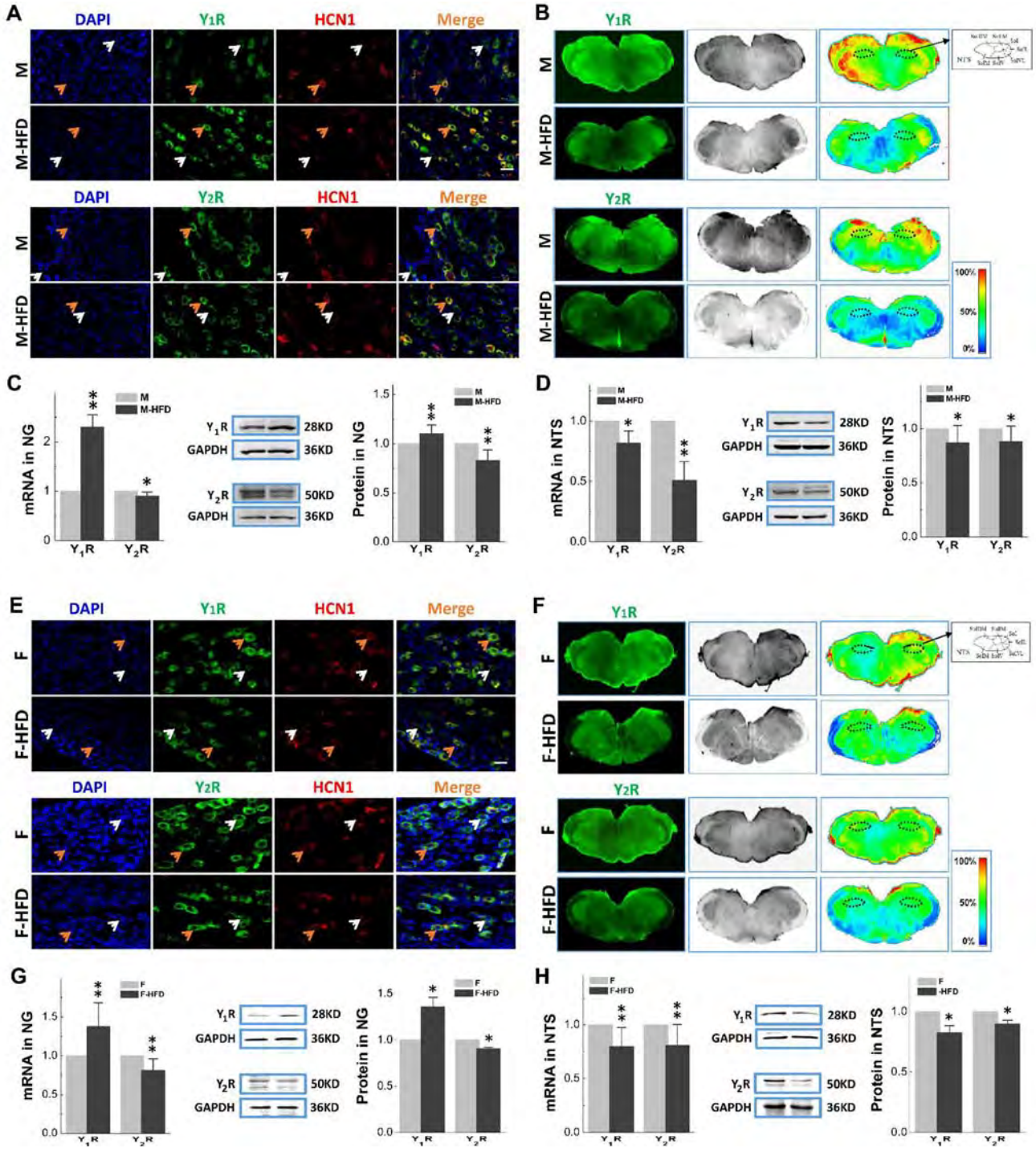
A
DAPI
Y1R
HCN1
Merge
M
M-HFD
DAPI
Y2R
HCN1
Merge
M
M-HFD
B
Y1R
M
M-HFD
Y2R
M
M-HFD
100%
50%
0%
C
mRNA in NG
M
M-HFD
Y1R
Y2R
Y1R
GAPDH
28KD
36KD
Y2R
GAPDH
50KD
36KD
Protein in NG
M
M-HFD
Y1R
Y2R
D
mRNA in NTS
M
M-HFD
Y1R
Y2R
Y1R
GAPDH
28KD
36KD
Y2R
GAPDH
50KD
36KD
Protein in NTS
M
M-HFD
Y1R
Y2R
E
DAPI
Y1R
HCN1
Merge
F
F-HFD
DAPI
Y2R
HCN1
Merge
F
F-HFD
F
Y1R
F
F-HFD
Y2R
F
F-HFD
100%
50%
0%
G
mRNA in NG
F
F-HFD
Y1R
Y2R
Y1R
GAPDH
28KD
36KD
Y2R
GAPDH
50KD
36KD
Protein in NG
F
F-HFD
Y1R
Y2R
H
mRNA in NTS
F
F-HFD
Y1R
Y2R
Y1R
GAPDH
28KD
36KD
Y2R
GAPDH
50KD
36KD
Protein in NTS
F
F-HFD
Y1R
Y2R

◀**Fig. 1** NPYR expression in the NG and NTS in male and female HFD-HTN rats. **A** Y_1R and Y_2R immunostaining in the NG of male (M) control and HFD rats. Neurons were labeled by the antibodies against HCN1 (red) and Y_1R/Y_2R (green). 4′,6-Diamidino-2-phenylindole (DAPI) staining was used to label nuclei. White arrowheads, neurons with unmyelinated (HCN1-negative) afferents; orange arrowheads, neurons with myelinated (HCN1-positive) afferents. Scale bar, 50 μm. **B** Immunostained brainstem section (35 μm; bregma, −12.60 mm) showing the distribution of Y_1R/Y_2R protein in the NTS regions of male (M) control and HFD rats. **C** mRNA and protein expression levels of Y_1R/Y_2R in the NG of male (M) control and HFD rats; n = 4–6 duplications from 9–12 rats for PCR; n = 12–16 tissue samples from 24–32 rats of each group for western. **D** mRNA and protein expression levels of Y_1R/Y_2R in the NTS of male (M) control and HFD rats; n = 5–7 duplications from 6–8 rats for PCR; n = 12 duplications from 16 rats for western. **E** Y_1R and Y_2R immunostaining in the NG of female (F) control and HFD rats. **F** Immunostaining of whole brainstem sections (35 μm; bregma, −12.60 mm) showing the distribution of Y_1R/Y_2R protein within the NTS region of female (F) control and HFD rats. **G** mRNA and protein expression levels of Y_1R/Y_2R in the NG of female (F) control and HFD rats; n = 11–19 tissue samples from 15–21 rats for PCR; n = 3–4 duplications from 24 rats for western. **H** mRNA and protein expression levels of Y_1R/Y_2R in the NTS of female (F) control and HFD rats; n = 10–12 duplications from 10–12 rats for PCR; n = 8–9 tissue samples from 16 rats for western. Student's t-test was used to compare the differences between control and experimental rats and data are presented as the mean ± SD. $^*P < 0.05$, $^{**}P < 0.01$ *vs* male/female rats.

with L-NAME, which causes NO deficiency and impaired vascular relaxation, leading to a sustained BP increase by blocking NOS under experimental conditions. Compared with controls, systemic BP was significantly elevated to 155 ± 12.6 mmHg in male and 146 ± 8.19 mmHg in female rats (baseline male, 124 ± 4.3 mmHg and female, 115 ± 4.5 mmHg; $P < 0.01$) and diastolic BP was also markedly increased from 93.9 ± 2.8 mmHg to 116 ± 11 mmHg for males and from 88.3 ± 2.7 mmHg to 112 ± 10.8 mmHg for females ($P < 0.01$) 4 weeks after intraperitoneal injection of the NO synthase inhibitor L-NAME (Fig. S2A, B). Importantly, we further investigated the changes in BRS by intravenous injection of phenylephrine (2–10 μg/kg) in the control and L-NAME groups (Fig. S2C, D). Our data clearly showed that the BRS was significantly down-regulated in the L-NAME group ($P < 0.05$ or $P < 0.01$), suggesting that the BP elevation induced by L-NAME was due at least partially to a dysfunction of the baroreflex afferent function. In addition, the echocardiographic results in the short axis M-mode showed that the diameter of the left ventricular anterior wall was larger in male L-NAME rats than in controls (Fig. S3), but not in female L-NAME rats, implying that an unknown mechanism contributes to the protective effect on cardiac function in females. To further understanding, serum NPY was also assessed by ELISA (Fig. S3). As expected, NPY was significantly higher in L-NAME rats ($P < 0.05$). In addition, using the same model, the gene and protein expression of Y_1R and Y_2R was determined in the NG and NTS and the results showed that Y_1R was up-regulated in the NG and down-regulated in the NTS in both males and females (Fig. 4). Meanwhile,

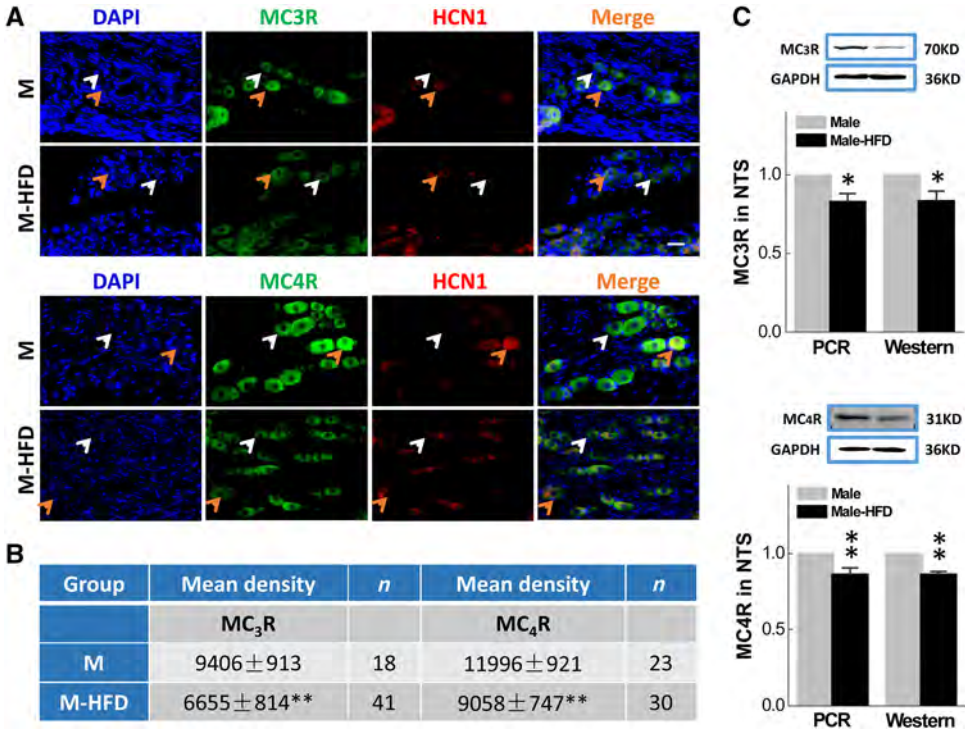

Group	Mean density	n	Mean density	n
	MC_3R		MC_4R	
M	9406±913	18	11996±921	23
M-HFD	6655±814**	41	9058±747**	30

Fig. 2 Quantification of α-MSH receptors in NG neurons and NTS tissue of male control and HFD rats. **A** Immunostaining of MC3R and MC4R on NG neurons (white arrowheads, HCN1 (unmyelinated)-negative neurons; orange arrowheads, HCN1 (myelinated)-positive neurons; scale bar, 50 μm). **B** Mean fluorescence density in individual neurons. **C** Representative protein bands and summarized results for MC3R and MC4R in the NTS (n = 3 duplications from 6 rats for PCR; n = 3 duplications from 12 rats for western; data are presented as the mean ± SD; $^*P < 0.05$, $^{**}P < 0.01$ *vs* control male rats, Student's t-test).

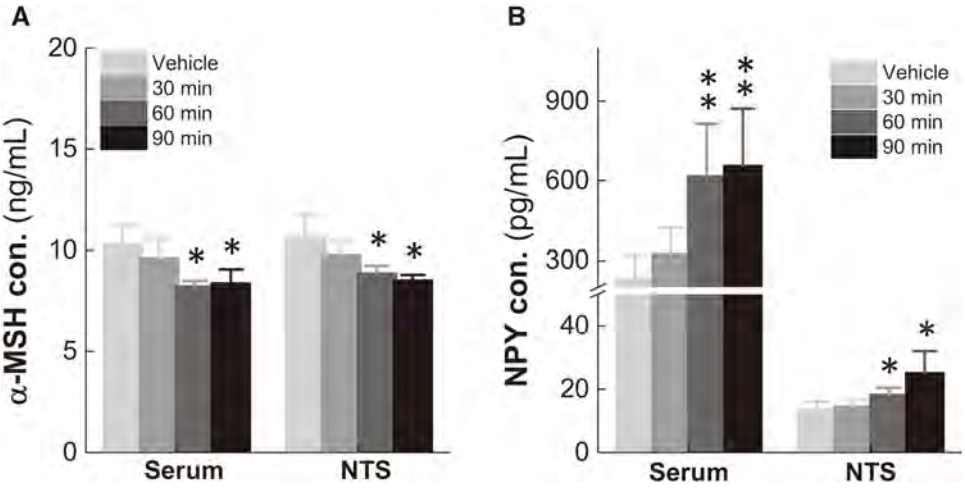

Fig. 3 Changes in α-MSH and NPY after intravenous leptin injection in male rats. α-MSH (**A**) and NPY (**B**) in the serum and NTS at 30, 60, and 90 min after leptin injection (n = 3–6/group; data presented as the mean ± SD; $^{*}P < 0.05$, $^{**}P < 0.01$ *vs* vehicle, paired *t*-test).

similar expression profiles for Y_2R were not found in female L-NAME rats (Fig. 4E–H). These data strongly suggest that, first, the NG and NTS play opposite roles in BP regulation; second, Y_1R mediates BP elevation and Y_2R mediates its reduction at the NG level; and finally, the sex difference in Y_2R expression well explains the protective action (less elevated BP in female *vs* male L-NAME rats without ventricular wall modification). Whether or not estrogen participates in this protective effect needs further investigation.

Expression Changes in NPY Receptors of Spontaneously Hypertensive Rats

To understand a potential role of NPY and its receptors in the development of a genetic form of hypertension as well as the possible involvement of baroreflex afferent pathway in this pathophysiological process, the BP was also monitored in SHRs (Fig. S4A). The systemic BP was higher ($P < 0.01$) in SHRs (202 ± 8.8 mmHg) than in WKY rats (122 ± 9 mmHg), however no significant difference of serum NPY concentration was found between them (163 ± 58 pg/mL in WKY *vs* 146 ± 74 pg/mL in SHR; $P > 0.05$) (Fig. S4B), suggesting that serum NPY itself is not the causal factor affecting the basal BP in SHRs. Furthermore, to confirm the Y_1R and Y_2R expression profiles, we collected NG and NTS tissues. Unlike HFD-HTN and L-NAME rats, no change in the expression of either Y_1R or Y_2R was found in the NG; however, both receptors were down-regulated ($P < 0.05$ *vs* WKY) in the NTS (Fig. 5), indicating that, even though the NG does not participate in the neural control of BP in SHRs, the driving force favoring BP reduction is significantly attenuated. These data once again emphasize that NPY receptors play a prominent role in the CNS, especially the baroreflex afferent pathway, by regulating sympathetic activity and maintaining a state of hypertension in SHRs.

Differentiation of Y_1R or Y_2R-Mediated Central Integration of Baroreflex Afferent Information

The NTS is an important cardiovascular center that receives and integrates baroreflex afferent signals from the baroreceptor terminals, so, alteration of NPY receptor expression in this region would imply a regulatory role of NPY in primary hypertension. Based on our published data [9], we have discovered that Y_1R or Y_2R mediates similar down-regulation of neuromodulation in myelinated A-type BRNs by the inhibition of L-type Ca^{2+} channels. These results provide a clue that Y_1R activation-mediated reduction in the current density of I_{Ca} may change neurotransmission in the NTS. In this regard, we investigated EPSCs in capsaicin (Cap)-insensitive A-type BRNs and the results showed that the peak, decay time constant, and the area under the curve (AUC) of EPSCs were dramatically decreased with solitary tract-evoked single or five stimuli after removing rapid desensitization at post-synaptic terminals with 100 μmol/L cyclothiazide (CTZ), suggesting less glutamate release from presynaptic membrane by Y_1R activation (100 nmol/L Pro34, a selective Y_1R agonist) (Fig. 6A–F), further indicating that direct Y_1R activation in the NTS also causes a BP response similar to direct Y_1R activation in the NG [9], and this finding is not consistent with the published evidence [7].

In stark contrast, the peak, decay time constant, and AUC were further increased by direct application of the Y_2R agonist into the brainstem slice recording chamber, ($P < 0.05$ or 0.01 *vs* artificial cerebrospinal fluid) in Cap-insensitive Ah-type BRNs of the NTS in the presence of NPY13-36 (a selective Y_2R agonist; 100 nmol/L) after CTZ by single or a burst of 5 solitary tract stimuli (Fig. 6G–L), suggesting that the direct activation of Y_2R at the level of the NTS increases presynaptic glutamate release and consequent reflex BP reduction, which is

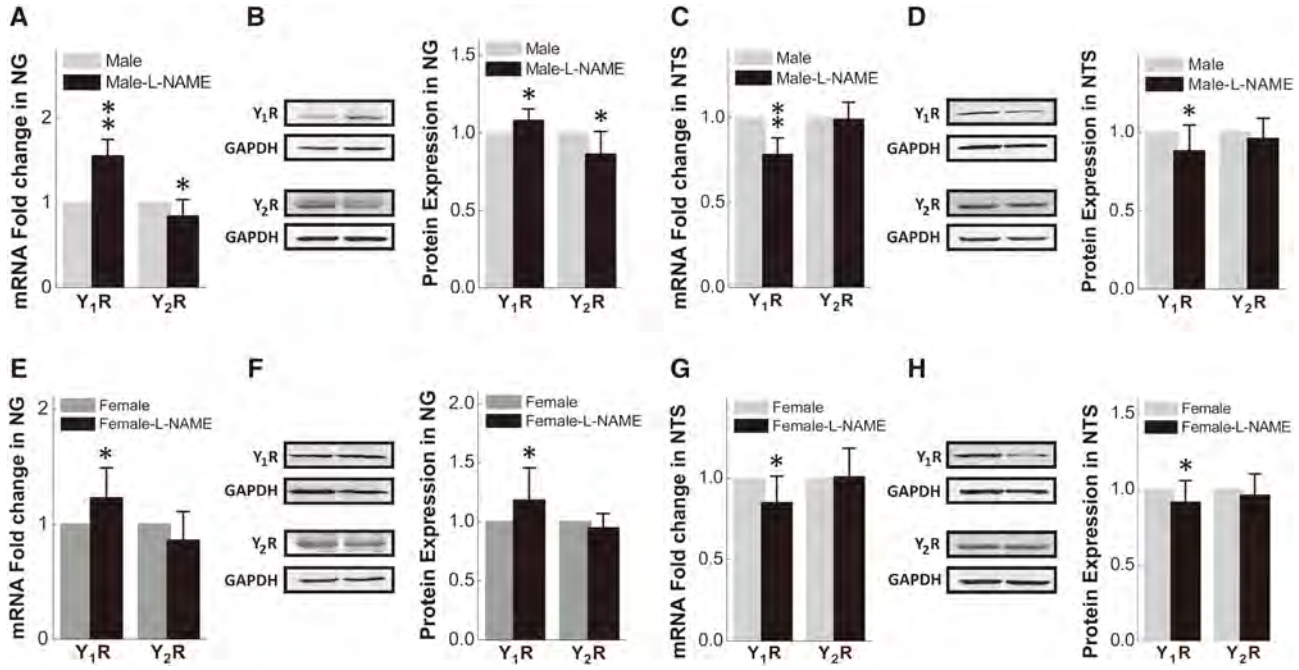

Fig. 4 Dysregulation of NPY receptors at the mRNA and protein levels in the NG and NTS in rats with hypertension induced by L-NAME. **A–D** mRNA and protein expression of Y_1R/Y_2R in the NG and NTS of males (n = 9–12 from 8–15 rats for PCR; n = 12–16 tissue samples from 24–32 rats for western). **E–F** mRNA and protein expression of Y_1R/Y_2R in the NG and NTS of females (n = 6–11 from 8–15 rats for PCR; n = 7–16 tissue samples from 24–32 rats for western; data are presented as the mean ± SD; $^*P < 0.05$, $^{**}P < 0.01$ *vs* control group, Student's *t*-test).

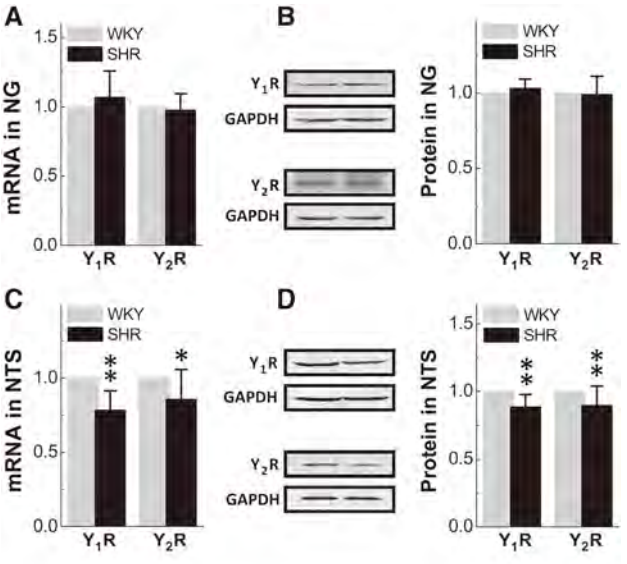

Fig. 5 Changes in mRNA and protein expression of Y_1R and Y_2R in the NG and NTS from male spontaneously hypertensive rats (SHRs). **A**, **B** Representative protein bands and summary data for Y_1R and Y_2R in the NG (n = 9–10 from 12 rats for PCR; n = 10 tissue samples from 24 rats for western). **C**, **D** Representative protein bands and summary data for Y_1R and Y_2R in the NTS (n = 8–12 from 10–12 rats for PCR; n = 12–14 tissue samples from 16–20 rats for western; data are presented as the mean ± SD; $^*P < 0.05$, $^{**}P < 0.01$ *vs* WKY, Student's *t*-test.

consistent with the findings for direct Y_2R activation at the NG level.

In identified Cap-sensitive and Dil-positive C-type BRNs in the NTS, Y_1R or Y_2R activation had similar effects on the peak, decay time constant, and AUC of EPSCs under these experimental conditions, and they were remarkably increased after removing the rapid sensitization with CTZ (Fig. S5; Table S3) and this action would lead to more glutamate and reflex BP reduction.

Discussion

Expression Profiles of Y_1Rs and Y_2Rs in Secondary or Primary Hypertension

It has been well documented that NPY is closely associated with metabolic syndrome-related hypertension [28, 29] and essential hypertension [30, 31]. Combined with our previous report [32], significantly elevated systolic and diastolic BP were recorded in HFD-HTN and L-NAME-induced hypertension with impaired BRS in both male and female rats; similar phenomena were also seen in SHRs, suggesting the dysregulation of baroreflex afferent function in the development of these models of hypertension. The first question that needed to be answered was if NPY contributes to the development of hypertension *via* its

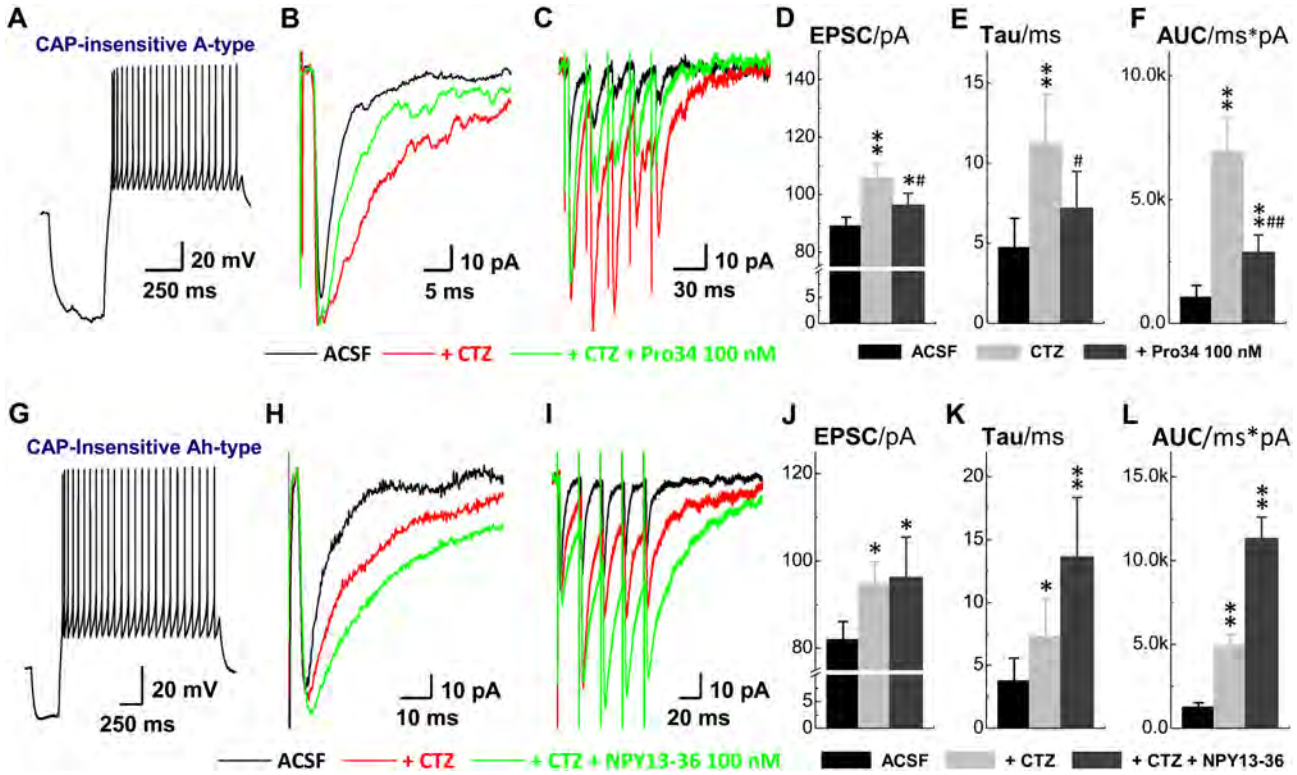

Fig. 6 Effects of NPYR agonists on EPSCs in myelinated neurons. **A** A-type neuron identified by AP discharge (Cap-insensitive and non-delayed-excitation). **B** Superimposed EPSCs induced by a single stimulus before and after desensitization using cyclothiazide (CTZ) and Y_1R activation (Pro34). **C** Superimposed EPSCs induced by a burst of five 200-μs current pulses before and after CTZ without/with Y_1R activation. **D–F** Summary data of the peak EPSC, tau, and AUC ($n = 5$, $^{*}P < 0.05$, $^{**}P < 0.01$ *vs* artificial cerebrospinal fluid (ACSF); $^{\#}P < 0.05$, $^{\#\#}P < 0.01$ *vs* CTZ, Student's *t*-test between groups followed by one-way ANOVA with post-hoc Turkey test among groups). **G** Ah-type neuron identified by AP discharge (Cap-insensitive and non-delayed-excitation). **H** Superimposed EPSCs evoked by a single stimulus before (ACSF) and after desensitization (CTZ) without/with Y_2R activation (NPY13-36). **I** Superimposed EPSCs evoked by a burst of five 200-μs current pulses before and after CTZ without/with Y_2R activation. **J–L** Summary data of the peak EPSCs, tau, and AUC ($n = 5$, $^{*}P < 0.05$, $^{**}P < 0.01$ *vs* ACSF, Student's *t*-test between groups followed by one-way ANOVA with *post-hoc* Turkey test among groups).

peripheral vasoconstriction and our findings have not excluded this possibility since serum NPY was elevated without sexual difference in all models except for SHRs.

Upon dysregulation of BRS, changes in the expression profiles of NPYRs under hypertensive conditions are to be expected. Interestingly, by using qRT-PCR along with immunoblotting, the expression profiles of Y_1R and/or Y_2R changed in favor of BP elevation in the NG and NTS of all hypertensive models (HFD-HTN, L-NAME-induced, and SHRs), which led us to the partial conclusion that (1) Y_1Rs and Y_2Rs contribute differently to the development of hypertension at the NG level *via* opposite expression; and (2) even though the Y_1R expression patterns in the NTS were in stark contrast, while those for Y_2R were identical, from the functional point of view, the NG and NTS play similar roles in BP regulation and the development of hypertension through the variable expression of NPYRs. All the noted molecular changes regarding NPYRs at the tissue level from different model rats were validated by immunostaining showing similar trends in HCN1-positive and HCN1-negative neurons. Although this latter partial conclusion seems to conflict with the previous notion that NPY increases or decreases BP through the NG or NTS [7, 9], it is an indisputable fact that NPY and its receptor are closely involved in BP regulation *via* the baroreflex afferent pathway under both physiological and hypertensive conditions.

Afferent-Specific Role of Baroreceptive Neurons in the NTS in NPY-Mediated Glutamate Release

The current evidence demonstrated a similar trend in NPYR expression in the NG and NTS in either metabolism-related or a genetic form of hypertension, which all favor the development of hypertension. However, cellular mechanism of NPY-mediated glutamate release is likely to be distinct between myelinated A- and Ah-type baroreceptive neurons (the 2nd-order) of NTS, which may play a differential role in NPY-autonomic control of BP regulation simply because of the unique expression patterns for

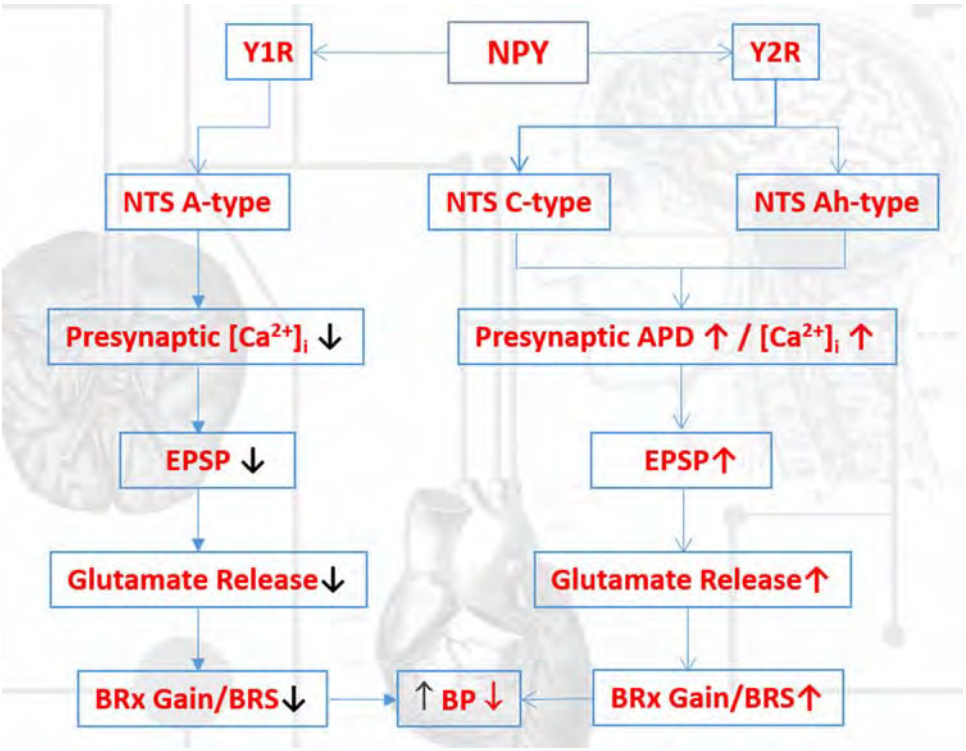

Fig. 7 Summary of potential mechanisms of the central neuromodulation of blood pressure mediated by NPY.

Y_1R and Y_2R confirmed in identified BRNs (the 1st-order) of NG. As shown in our previous study, Y_1R and Y_2R are only expressed in Ah-types and A-types [9], this leads us to hypothesize that A- and Ah-type baroreceptive neurons of NTS are very likely to play an opposite role in baroreflex integration even if the N-type Ca^{2+} currents expressed in their 1st-order neurons show similar responses in the presence of Y_1 (Pro34) or Y_2 (NPY13-36) agonist. As expected, presynaptic glutamate release was dramatically reduced in A- and enhanced in Ah-types, even though they are all myelinated afferents, which was clearly revealed by evaluation of the peak, decay time constant, and the AUC of EPSCs after removing the fast desensitization of the synapse. This electrophysiological data combined with our molecular findings point out that complicated processes are involved in the NPY-mediated BP regulation through the baroreflex afferent pathway under normal and disease conditions; this clearly requires a balance of the expression of Y_1R and Y_2R and an integrative balance between the NG and NTS, as well as a functional balance between A-type and Ah-type BRNs.

NPYR-Mediated Central Integration in the NTS

Based on our previous work [9], activation of Y_1Rs in the ND elevates BP without altering the action potential duration of A-type neurons, while activation of Y_2R does. Meanwhile, activation of Y_2Rs and Y_1R/Y_2R in Ah- and C-type neurons have a frequency-dependent prolonged duration. From the electrophysiological point of view, the central integration underlying the activation of different types of BRNs by NPYRs in the NTS needs further investigation. The early study demonstrated that AP broadening causes the presynaptic enhancement of synaptic transmission, presumably as a result of an increased influx of Ca^{2+} [33–35], so frequency-dependent spike broadening would be efficient means of intracellular Ca^{2+} accumulation. As expected, Y_2R activation dramatically enhances the neurotransmission in Cap-insensitive BRNs of the NTS by increasing presynaptic glutamate release in a frequency-dependent manner.

Our present finding has demonstrated for the first time that differential neurotransmission responses to Y_1R and Y_2R activation also occur in Cap-insensitive/myelinated BRNs of the NTS, in which the coupling mechanism between KCa1.1 and N-type Ca^{2+} channel [36, 37] on the presynaptic membrane is likely the key to result in the distinct neurotransmission induced by Y_1R and Y_2R activation [38]. This result is consistent with our recent finding that glutamate release is enhanced in almost half of the Cap-insensitive BRNs in the NTS in the presence of iberiotoxin (data not shown). In other words, this coupling mechanism not only exists on the somatic membrane of first-order BRNs but may also be expressed on the presynaptic membrane, suggesting that the somatic membrane shares adaptive and biophysical properties with the peripheral and central projections [39] (Fig. 7).

Neuropeptide-Mediated Sympathetic Regulation

NPY is widely distributed in the central and peripheral nervous systems. An earlier study indicated that microinjection of NPY into the NTS decreases BP and attenuates baroreflex control in anesthetized Sprague-Dawley rats [40]. In contrast, we have previously reported [9] that NPY dramatically mediates sympathetic vasoconstriction by NG microinjection. Meanwhile, leptin acts as a homeostatic agent by inhibiting NPY neurons and simultaneously activating pro-opiomelanocortin neurons in the hypothalamus, leading to the production of α-MSH, which in turn activates melanocortin 3/4 receptors [28], so it was imperative to investigate the expression of leptin and melanocortin receptors in the baroreflex afferent pathway. In this study, we have shown that both α-MSH and leptin receptors were down-regulated in the NG and NTS in HFD-HTN rats. In addition, intracerebroventricular injection of leptin or α-MSH elevated the sympathetic tone and BP [41, 42]. These findings indicate that leptin-resistance exists in hypertension, and α-MSH may share a similar signaling pathway in controlling BP. However, it is interesting to note that intravenous injection of a high dose of leptin increases endothelial NO production to slightly reduce BP [43], which may offset the pressor response induced by leptin-mediated sympathetic activation. On the other hand, we also found significantly decreased α-MSH and increased NPY concentrations at 60 and 90 min after acute leptin infusion, which reinforces the idea that a negative feedback regulation mechanism may exist, and the contribution of NPY to regulation of the cardiovascular system is likely to be balanced by leptin and α-MSH.

Perspectives

Altogether, our study shows that the baroreflex afferent pathway plays an important role in NPY-mediated BP regulation. This was evidenced by using three types of hypertension model rats with male and age-matched female groups to evaluate the expression of NPY receptors in both the NG and NTS. Furthermore, the interaction of metabolic regulators provides a new perspective on the neural control of BP regulation under physiological and hypertensive disease conditions. Whether the suppressed sympathetic activation in HFD-HTN rats is because of the change in NPYRs expression or mediation by other neuropeptides deserves further investigation. As part of the integration of the baroreflex, electrophysiological study of the baroreceptive neurons in the NTS showed potential mechanisms of the central neuromodulation of BP mediated by NPY. We expect that NPY or other peptides may be potential targets for the clinical management of hypertension, obesity, metabolic disorder, and cardiovascular diseases in the near future.

Acknowledgements This work was supported by grants from the National Natural Science Foundation of China (31171122, 81573431, 81773731, 81971326, and 8190130222).

Conflict of interest The authors declare that they have no conflict of interest.

References

1. Tatemoto K, Carlquist M, Mutt V. Neuropeptide Y–a novel brain peptide with structural similarities to peptide YY and pancreatic polypeptide. Nature 1982, 296: 659–660.
2. Lang UE, Beglinger C, Schweinfurth N, Walter M, Borgwardt S. Nutritional aspects of depression. Cell Physiol Biochem 2015, 37: 1029–1043.
3. Bouret SG. Development of Hypothalamic Circuits That Control Food Intake and Energy Balance. In: Harris RBS (Ed.). Appetite and Food Intake: Central Control. Boca Raton (FL): CRC Press/ Taylor & Francis, 2017: 135–154.
4. Loh K, Herzog H, Shi YC. Regulation of energy homeostasis by the NPY system. Trends Endocrinol Metab 2015, 26: 125–135.
5. Jacques D, Abdel-Samad D. Neuropeptide Y (NPY) and NPY receptors in the cardiovascular system: implication in the regulation of intracellular calcium. Can J Physiol Pharmacol 2007, 85: 43–53.
6. Kennedy B, Shen GH, Ziegler MG. Neuropeptide Y-mediated pressor responses following high-frequency stimulation of the rat sympathetic nervous system. J Pharmacol Exp Ther 1997, 281: 291–296.
7. Cheng PW, Wu AT, Lu PJ, Yang YC, Ho WY, Lin HC, *et al.* Central hypotensive effects of neuropeptide Y are modulated by endothelial nitric oxide synthase after activation by ribosomal protein S6 kinase. Br J Pharmacol 2012, 167: 1148–1160.
8. Wahlestedt C, Yanaihara N, Hakanson R. Evidence for different pre-and post-junctional receptors for neuropeptide Y and related peptides. Regul Pept 1986, 13: 307–318.
9. Liu Y, Wu D, Qu MY, He JL, Yuan M, Zhao M, *et al.* Neuropeptide Y-mediated sex- and afferent-specific neurotransmissions contribute to sexual dimorphism of baroreflex afferent function. Oncotarget 2016, 7: 66135–66148.
10. Barraco RA, Ergene E, Dunbar JC, Ganduri YL, Anderson GF. Y2 receptors for neuropeptide Y in the nucleus of the solitary tract mediate depressor responses. Peptides 1991, 12: 691–698.
11. Mankin LA. Update in hypertension therapy. Med Clin North Am 2016, 100: 665–693.
12. Tu H, Zhang D, Li YL. Cellular and molecular mechanisms underlying arterial baroreceptor remodeling in cardiovascular diseases and diabetes. Neurosci Bull 2019, 35: 98–112.
13. Potje SR, Munhoz FC, Perassa LA, Graton ME, Pereira AA, Nakamune AC, *et al.* Mechanisms underlying the hypotensive and vasodilator effects of Ru(terpy)(bdq)NO](3 +), a nitric oxide donor, differ between normotensive and spontaneously hypertensive rats. Eur J Pharmacol 2014, 741: 222–229.
14. Yi M, Li H, Wu Z, Yan J, Liu Q, Ou C, *et al.* A promising therapeutic target for metabolic diseases: neuropeptide Y receptors in humans. Cell Physiol Biochem 2018, 45: 88–107.
15. Zemancikova A, Torok J. Cardiovascular effects of high-fructose intake in rats with nitric oxide deficiency. Interdiscip Toxicol 2014, 7: 159–164.

16. Cyr NE, Toorie AM, Steger JS, Sochat MM, Hyner S, Perello M, *et al.* Mechanisms by which the orexigen NPY regulates anorexigenic alpha-MSH and TRH. Am J Physiol Endocrinol Metab 2013, 304: E640–650.
17. do Carmo JM, da Silva AA, Freeman JN, Wang Z, Moak SP, Hankins MW, *et al.* Neuronal suppressor of cytokine signaling 3: Role in modulating chronic metabolic and cardiovascular effects of leptin. Hypertension 2018, 71: 1248–1257.
18. Andresen MC, Kunze DL. Nucleus tractus solitarius–gateway to neural circulatory control. Annu Rev Physiol 1994, 56: 93–116.
19. Browning KN. Excitability of nodose ganglion cells and their role in vago-vagal reflex control of gastrointestinal function. Curr Opin Pharmacol 2003, 3: 613–617.
20. Kawai Y, Senba E. Organization of excitatory and inhibitory local networks in the caudal nucleus of tractus solitarius of rats revealed in in vitro slice preparation. J Comp Neurol 1996, 373: 309–321.
21. Lachamp P, Balland B, Tell F, Crest M, Kessler JP. Synaptic localization of the glutamate receptor subunit GluR2 in the rat nucleus tractus solitarii. Eur J Neurosci 2003, 17: 892–896.
22. Travagli RA, Hermann GE, Browning KN, Rogers RC. Brainstem circuits regulating gastric function. Annu Rev Physiol 2006, 68: 279–305.
23. Jin YH, Bailey TW, Li BY, Schild JH, Andresen MC. Purinergic and vanilloid receptor activation releases glutamate from separate cranial afferent terminals in nucleus tractus solitarius. J Neurosci 2004, 24: 4709–4717.
24. Baltazi M, Katsiki N, Savopoulos C, Iliadis F, Koliakos G, Hatzitolios AI. Plasma neuropeptide Y (NPY) and alpha-melanocyte stimulating hormone (a-MSH) levels in patients with or without hypertension and/or obesity: a pilot study. Am J Cardiovasc Dis 2011, 1: 48–59.
25. Mountjoy KG, Mortrud MT, Low MJ, Simerly RB, Cone RD. Localization of the melanocortin-4 receptor (MC4-R) in neuroendocrine and autonomic control circuits in the brain. Mol Endocrinol 1994, 8: 1298–1308.
26. Matsumura K, Tsuchihashi T, Fujii K, Iida M. Neural regulation of blood pressure by leptin and the related peptides. Regul Pept 2003, 114: 79–86.
27. Puzserova A, Bernatova I. Blood pressure regulation in stress: focus on nitric oxide-dependent mechanisms. Physiol Res 2016, 65: S309–S342.
28. Lim K, Barzel B, Burke SL, Armitage JA, Head GA. Origin of aberrant blood pressure and sympathetic regulation in diet-induced obesity. Hypertension 2016, 68: 491–500.
29. Barzel B, Lim K, Davern PJ, Burke SL, Armitage JA, Head GA. Central proopiomelanocortin but not neuropeptide Y mediates sympathoexcitation and hypertension in fat fed conscious rabbits. J Hypertens 2016, 34: 464–473; discussion 473.
30. Krukoff TL, MacTavish D, Jhamandas JH. Effects of restraint stress and spontaneous hypertension on neuropeptide Y neurones in the brainstem and arcuate nucleus. J Neuroendocrinol 1999, 11: 715–723.
31. Guo XW, Wang XL, Gao ZL. Effect of neuropeptide Y and neurotensin on diurnal rhythm of blood pressure and target organ damage for essential hypertension. Zhonghua Xin Xue Guan Bing Za Zhi 2005, 33: 1006–1009.
32. He JL, Zhao M, Xia JJ, Guan J, Liu Y, Wang LQ, *et al.* FGF21 ameliorates the neurocontrol of blood pressure in the high fructose-drinking rats. Sci Rep 2016, 6: 29582.
33. Li BY, Glazebrook P, Kunze DL, Schild JH. KCa1.1 channel contributes to cell excitability in unmyelinated but not myelinated rat vagal afferents. Am J Physiol Cell Physiol 2011, 300: C1393–1403.
34. Geiger JR, Jonas P. Dynamic control of presynaptic Ca(2 +) inflow by fast-inactivating K(+) channels in hippocampal mossy fiber boutons. Neuron 2000, 28: 927–939.
35. Sabatini BL, Regehr WG. Control of neurotransmitter release by presynaptic waveform at the granule cell to Purkinje cell synapse. J Neurosci 1997, 17: 3425–3435.
36. Mendelowitz D, Kunze DL. Characterization of calcium currents in aortic baroreceptor neurons. J Neurophysiol 1992, 68: 509–517.
37. Mendelowitz D, Reynolds PJ, Andresen MC. Heterogeneous functional expression of calcium channels at sensory and synaptic regions in nodose neurons. J Neurophysiol 1995, 73: 872–875.
38. Blakemore LJ, Levenson CW, Trombley PQ. Neuropeptide Y modulates excitatory synaptic transmission in the olfactory bulb. Neuroscience 2006, 138: 663–674.
39. Harper AA. Similarities between some properties of the soma and sensory receptors of primary afferent neurones. Exp Physiol 1991, 76: 369–377.
40. Shih CD, Chan JY, Chan SH. Tonic suppression of baroreceptor reflex response by endogenous neuropeptide Y at the nucleus tractus solitarius of the rat. Neurosci Lett 1992, 148: 169–172.
41. Matsumura K, Tsuchihashi T, Abe I, Iida M. Central alpha-melanocyte-stimulating hormone acts at melanocortin-4 receptor to activate sympathetic nervous system in conscious rabbits. Brain Res 2002, 948: 145–148.
42. Rahmouni K, Correia ML, Haynes WG, Mark AL. Obesity-associated hypertension: new insights into mechanisms. Hypertension 2005, 45: 9–14.
43. Lembo G, Vecchione C, Fratta L, Marino G, Trimarco V, d'Amati G, *et al.* Leptin induces direct vasodilation through distinct endothelial mechanisms. Diabetes 2000, 49: 293–297.

Neurosci. Bull. April, 2020, 36(4):407–418
https://doi.org/10.1007/s12264-019-00446-w

www.neurosci.cn
www.springer.com/12264

ORIGINAL ARTICLE

DPP-4 Inhibitor Linagliptin is Neuroprotective in Hyperglycemic Mice with Stroke *via* the AKT/mTOR Pathway and Anti-apoptotic Effects

Gang Zhang[1,2] · Samuel Kim[1] · Xiaohuan Gu[1] · Shan Ping Yu[1] · Ling Wei[1,3]

Received: 11 April 2019 / Accepted: 10 August 2019 / Published online: 5 December 2019

Abstract Dipeptidyl peptidase 4 (DPP-4) inhibitors have been shown to have neuroprotective effects in diabetic patients suffering from stroke, but less research has focused on patients with mild hyperglycemia below the threshold for a diagnosis of diabetes. In this investigation, a hyperglycemic mouse model was generated by intraperitoneal injection of streptozotocin and then subjected to focal cerebral ischemia. We demonstrated that the DPP-4 inhibitor linagliptin significantly decreased the infarct volume, reduced neuronal cell death, decreased inflammation, and improved neurological deficit compared with control mice. Linagliptin up-regulated the expression of p-Akt and p-mTOR and regulated the apoptosis factors Bcl-2, Bax, and caspase 9. Taken together, these results suggest that linagliptin exerts a neuroprotective action likely through activation of the Akt/mTOR pathway along with anti-apoptotic and anti-inflammatory mechanisms. Therefore, linagliptin may be considered as a therapeutic treatment for stroke patients with mild hyperglycemia.

Keywords Cerebral ischemia · Hyperglycemia · DPP-4 inhibitor · Linagliptin · Neuroprotection

✉ Ling Wei
lwei7@emory.edu

[1] Department of Anesthesiology, Emory University School of Medicine, Atlanta, GA 30322, USA

[2] Department of Neurology, Children's Hospital of Nanjing Medical University, Nanjing 210000, China

[3] Department of Neurology, Emory University School of Medicine, Atlanta, GA 30322, USA

Introduction

Ischemic stroke is a global health concern that leads to lifelong disability or death [1]. In the USA, approximately 795,000 people experience acute first and recurrent ischemic strokes each year [2]. Despite declining stroke mortality rates, the global burden of stroke is increasing. As of 2010, the total expenditure on the disease was $53 billion/year in the USA and is expected to double by 2030 [3]. Over the past 20 years, the understanding of the pathophysiology, diagnosis, and treatment of acute ischemic stroke has improved significantly [4]. Many causes of stroke have been identified, such as high blood pressure, cardiovascular disease, high cholesterol, diabetes, cigarette smoking or exposure to secondhand smoke, and a personal or family history of stroke. More specifically, the prognosis of acute ischemic stroke is affected by multiple factors such as the patient's glucose level on admission. Retrospective clinical studies have shown that hyperglycemia, an independent risk factor for stroke, is closely associated with the progression, treatment, and prognosis of stroke [5, 6]. Higher admission blood glucose levels are associated with increased morbidity and mortality [7, 8]. Studies have also shown that hyperglycemia increases the area of cerebral infarction in animal models [9–11]. This may occur because hyperglycemia contributes to damaging processes such as increased anaerobic metabolism, hyperosmolarity, lactic acidosis, and focal toxicity of ischemic vascular disease [12–15]. For these reasons, the management of blood glucose levels is especially important in patients with stroke and hyperglycemia.

Hyperglycemia is recognized as an important risk factor for cerebrovascular disease, especially ischemic stroke [16, 17]. Patients with hyperglycemia carry a 1.5–3 times higher risk of stroke compared with the general population

[18]. Stroke mortality is also higher and post-stroke outcomes are poorer in patients with hyperglycemia [19]. Most notably, however, clinical studies have found that effective control of blood glucose effectively improves the prognosis of patients with diabetes complicated with stroke.

Inhibitors of dipeptidyl peptidase 4 (DPP-4) are widely used in clinical settings to treat type 2 diabetes [20, 21] due to their ability to effectively reduce blood sugar levels in diabetics. The effect of DPP-4 inhibitors on reducing stroke incidence tends to vary widely, with some studies suggesting no effect on stroke incidence [22–24] and others suggesting reduced incidence after DPP-4 inhibitor treatment [25]. Despite this, there is evidence that DPP-4 inhibitor treatment promotes neuroprotective effects in patients with diabetes complicated with stroke [26, 27], suggesting that DPP-4 inhibitors may be useful for stroke recovery in patients with conditions such as hyperglycemia. Thus, this investigation focused on markers of neuroprotection such as cell death and sensorimotor deficit, rather than rates of stroke incidence and death that tend to be the focus of clinical trials [28]. In addition, previous studies failed to recognize patients with hyperglycemia below the threshold for a diagnosis of diabetes. Whether DPP-4 inhibitors also promote neuroprotection in the patients that suffer a stroke is not clear. In this study, we established a hyperglycemic mouse model with stroke to determine the potential efficacy of the DPP-4 inhibitor linagliptin. We further investigated its neuroprotective mechanism.

Materials and Methods

Animals

Adult male C57BL/6 mice were housed in standard cages in 12-h light/12-h dark cycle in the Emory University animal facility where the room temperature was kept at 22°C ± 1°C. All experimental procedures were conducted in accordance with the National Institutes of Health (NIH) Guide for the Care and Use of Laboratory Animals and were approved by the Emory University Institutional Animal Care and Use Committee.

Hyperglycemic Mouse Model

All animal experiments and surgical procedures were approved by the Institutional Animal Care and Use Committee at Emory University and met NIH standards. Hyperglycemia was induced in adult male C57BL/6 mice 10–12 weeks old weighing ~ 25 g. Mice were given an intraperitoneal (i.p.) injection of streptozotocin (STZ) dissolved in citrate buffer. All solutions were prepared immediately before use. Controls received i.p. vehicle. After the injections, mice were housed for 2–3 weeks and given food and water *ad libitum*. Every week, blood glucose levels were measured after a 4-h fast using samples from the tail vein with the FreeStyle glucose meter.

Focal Ischemic Stroke Model

The focal cerebral ischemic stroke model in adult male mice was created as previously described [29]. In summary, mice were anesthetized with 4% chloral hydrate. The distal branches of the right middle cerebral artery were permanently ligated, followed by bilateral occlusion of the common carotid arteries and subsequent reperfusion. During surgery and recovery, body temperature was maintained at 37.0 °C ± 0.5° C using a temperature-controlling ventilator and heating pads.

Quantification of Infarct Volume Using 2,3,5-triphenyltetrazolium Chloride (TTC) Staining

Infarct volume was assessed 3 days after ischemia *via* TTC staining. Brains were removed and cut into 1-mm coronal slices using a brain matrix. The slices were incubated in 2% TTC (Sigma) at 37°C for 5 min, then stored in 10% buffered formalin for 24 h. A flatbed scanner was then used to capture digital images of the caudal aspect of each slice. Ipsilateral and contralateral hemispheres and infarct areas were measured using ImageJ software (NIH, Bethesda, MD, USA) and infarct volume was calculated using the indirect method [30].

Cell Death Assay Using Terminal Deoxynucleotidyl Transferase Biotin-dUTP Nick-End Labeling (TUNEL)

A TUNEL assay kit (DeadEnd Fluorometric TUNEL system; Promega, Madison, WI, USA) was used to assess cell death in 10-μm brain sections according to manufacturer's instructions. Briefly, sections were fixed in 10% buffered formalin for 10 min and then permeabilized in 0.2% Triton-X 100 after fixation for 5 min in ethanol:acetic acid (2:1). They were incubated in equilibration buffer for 10 min and then incubated in the dark at 37°C for 60 min in recombinant terminal deoxynucleotidyl transferase and nucleotide mixtures. The reaction was stopped by 2× SSC solution for 15 min, and nuclei were then counterstained with DAPI for 5 min.

Immunohistochemical Staining and Cell Counts

Brain cryosections 10 μm thick were dried on a slide warmer for 30 min, fixed in 10% buffered formalin for 10 min, washed with −20°C ethanol:acetic acid (2:1) for 10 min, permeabilized with 0.2% Triton-X 100 and phosphate-buffered saline (PBS) for 5 min, blocked with 1% fish gel (Sigma) and PBS for 60 min, and incubated with the following primary antibodies overnight at 4°C: mouse anti-NeuN (1:400; Chemicon, Temecula, CA) for mature neurons, rabbit anti-glucose transporter 1 (GLUT-1) (1:400, Chemicon, Millipore) for vessels, and rabbit anti-ionized calcium binding adaptor molecule-1(Iba-1) (1:200; Biocare Medical, CA). After rinsing with PBS, the sections were then exposed for 1 h at room temperature to the relevant secondary antibodies: secondary antibody Alexa Fluor 488 anti-rabbit, anti-goat, anti-mouse IgG (1:200; Invitrogen, Carlsbad, CA), cyanine-3 (Cy3)-conjugated anti-rat, anti-rabbit IgG (1:1000; Invitrogen), or Cy5-conjugated anti-goat IgG (1:400; Invitrogen). DAPI was applied at 1:25,000 for 5 min and washed with PBS. Slides were then mounted with Vectashield (Vector Laboratory, Burlingame, CA) for fluorescence microscopy analysis and imaging.

For systematic random sampling in design-based stereological cell counting, 9 sections, each 90 μm apart, in the region of interest were used. For multi-stage random sampling, 6 fields per section were randomly selected in the penumbra [31] at a magnification of 400× under a fluorescence microscope. This was repeated in 6 separate sections per brain.

Western Blotting

The peri-infarct region was defined by a 500-mm boundary extending from the edge of the infarct core, medial and lateral to the infarct, as previously described [32]. Peri-infarct tissue samples of cortex were collected from each group 3 days after ischemia. Proteins were extracted from the tissue by homogenization in protein lysis buffer (in mmol/L: 25 Tris-HCl [pH 7.6], 150 NaCl, 5 EDTA, 2 sodium orthovanadate, 100 NaF, 0.1% SDS, 1% Triton, leupeptin, aprotinin, and pepstatin). Protein from each sample was loaded into the gradient gel and run at a constant current until the protein markers were sufficiently separated. Protein was transferred onto polyvinyl difluoride membranes that were then probed using a standard protocol [33]. The membranes were then blocked with 5% bovine serum albumin for 1 h and incubated overnight at 4°C with primary antibodies. The primary antibodies used and the dilutions for each were mouse β-actin (1: 5000; Sigma-Aldrich, St. Louis, MO), rabbit mTOR (1:500; Santa Cruz Biotech, Inc., Dallas, TX), rabbit AKT (1:1000; Santa Cruz), rabbit TNF-α (1:1000; Cell Signaling, Danvers, MA), rabbit IL-1β (1:1000; Cell Signaling), rabbit IL-6 (1:1000; Cell Signaling), rabbit Bcl-2 (1:1000; Cell Signaling), rabbit Bax (1:1000; Cell Signaling), cleaved caspase-3 (1:1000; Cell Signaling), p-mTOR (1:1000; Santa Cruz) and p-AKT (1:1000; Santa Cruz). After washing in TBST, the membranes were incubated with ammonium persulfate (AP)-conjugated secondary antibodies (GE Healthcare, Piscataway, NJ) for 1 h at room temperature. The signal was developed using nitro-blue tetrazolium and 5-bromo-4-chloro-3'indolyphophate solution. The band intensities were analyzed using ImageJ. The expression of each target protein was then normalized to β-actin.

Local Cerebral Blood Flow (LCBF) Measurement

Laser scanning imaging was used to measure LCBF at 0 day for baseline and at 21 days after ischemia as previously described. Mice were anesthetized and an incision was made to expose the skull above the right middle cerebral artery. The laser was centered on the right coronal suture. Unlike conventional laser Doppler probes which measure small blood flow points, the scanner method used a laser Doppler perfusion imaging system (PeriFlux System 5000-PF5010 LDPM unit, Perimed, Stockholm, Sweden) to measure a square area of 2.4 mm × 2.4 mm [2]. This measurement largely avoided inaccuracies caused by inconsistent positioning of the laser. Laser scanning imaging measurements and analyses of the area were performed using the PeriScans system and LDPIWin programs (Perimed).

Adhesive Removal Test

The adhesive removal test was used to assess sensorimotor deficits after focal cerebral ischemia in mice. In summary, a small adhesive dot was placed on one forepaw, and the number of times to contact and remove the adhesive dot were recorded. Mice were trained in three sessions before surgery to ensure normal sensorimotor function. A recording was discontinued after 120 s of no contact with the adhesive dot. Three trials were performed by the mice in different groups at 3, 7, and 14 days after ischemia and the mean time was calculated for data analysis.

Statistical Analysis

The mice were randomly separated into sham, stroke, hyperglycemia stroke, and linagliptin treatment + hyperglycemia groups. The behavioral tests and data analyses were done double-blind by 2–3 people without knowledge of grouping. GraphPad Prism 6 (GraphPad Software, San

Diego, CA) was used for statistical analysis and graphic presentation, and sample sizes were tested with G-Power Analysis (University of Dusseldorf, Dusseldorf, Germany) to yield sufficient statistical power. Student's *t*-test was used to compare two groups. Multiple comparisons were done using one-way analysis of variance (ANOVA) followed by Tukey's test for multiple comparisons. One-way analysis followed by Bonferroni selective comparisons was performed for pairwise comparisons. Data with $P \leq 0.05$ were considered significantly different. Data are expressed as the mean ± SEM.

Results

Assessment of the Hyperglycemic Mouse Model

A hyperglycemic mouse model was created in adult male mice by injection of STZ. Two weeks after the injection, animals exhibited significantly elevated levels of blood glucose with respect to age-matched vehicle control mice (Fig. 1A). This hyperglycemic state lasted for at least 3 weeks before we performed ischemic surgery. The results showed that linagliptin treatment (10 mg/kg by gavage) decreased the fasting blood glucose levels (Fig. 1B). However, we did not find that the blood glucose levels were related to the body weight, and linagliptin treatment did not affect the body weight (Fig. 1C and D).

Linagliptin Reduces Infarct Volume after Ischemic Stroke in Hyperglycemic Mice

Compared with animals with stroke and normal blood glucose, the hyperglycemic stroke mice showed a significantly larger brain infarct volume (Fig. 2A–C). Linagliptin treatment significantly reduced the infarct volume compared with the stroke control group (Fig. 2A–C).

Linagliptin Reduces Neuronal Cell Death in Hyperglycemic Mice

To understand the protective mechanism of linagliptin at the cellular level, TUNEL staining in brain tissues harvested 3 days after ischemia was used to determine whether linagliptin treatment affected cell death. Compared with the normal blood glucose group, the hyperglycemic group showed significantly increased numbers of TUNEL-positive cells and TUNEL +/NeuN + co-labeled cells in the penumbra. However, linagliptin treatment significantly reduced the neuronal cell death, as evidenced by a decrease in the number of TUNEL-positive cells double-stained with NeuN, compared with the hyperglycemic stroke control group ($P < 0.05$) (Fig. 3A–C). In addition, we assessed the protein expression of cleaved caspase-3 in the penumbra 3 days after stroke. The data showed that cleaved caspase-3 significantly increased after stroke. Linagliptin treatment decreased the caspase-3 activation ($P < 0.001$) (Fig. 3D).

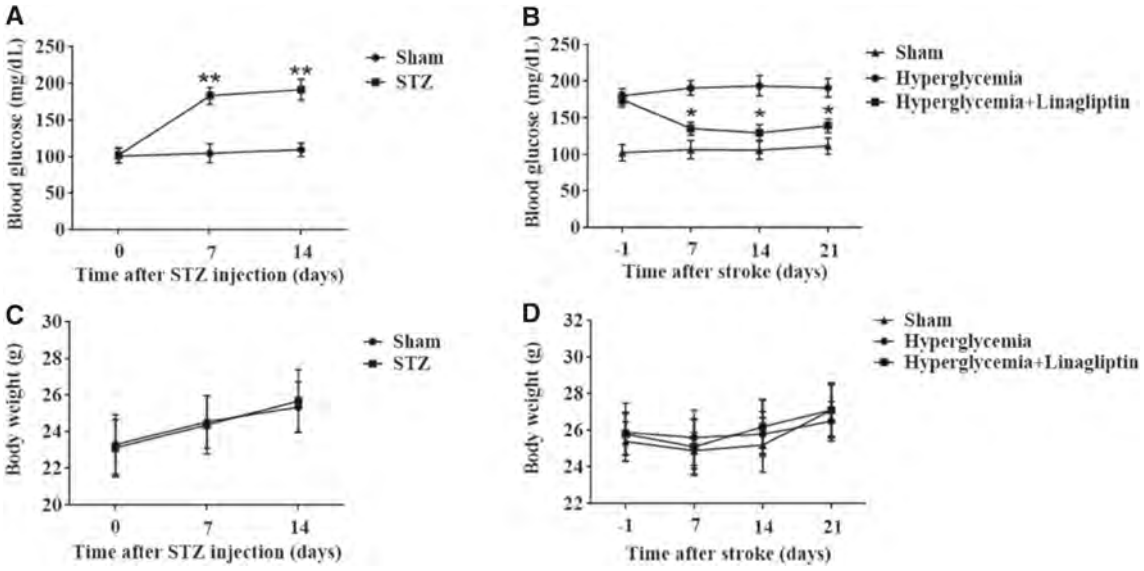

Fig. 1 Changes in body weight and fasting blood glucose. **A** Levels of fasting blood glucose after STZ injection. **B** Levels of fasting blood glucose after daily linagliptin administration after stroke. **C** Body weight after STZ injection. **D** Body weight after daily linagliptin administration after stroke. Values are expressed as the mean ± SEM. *$P < 0.05$, **$P < 0.01$.

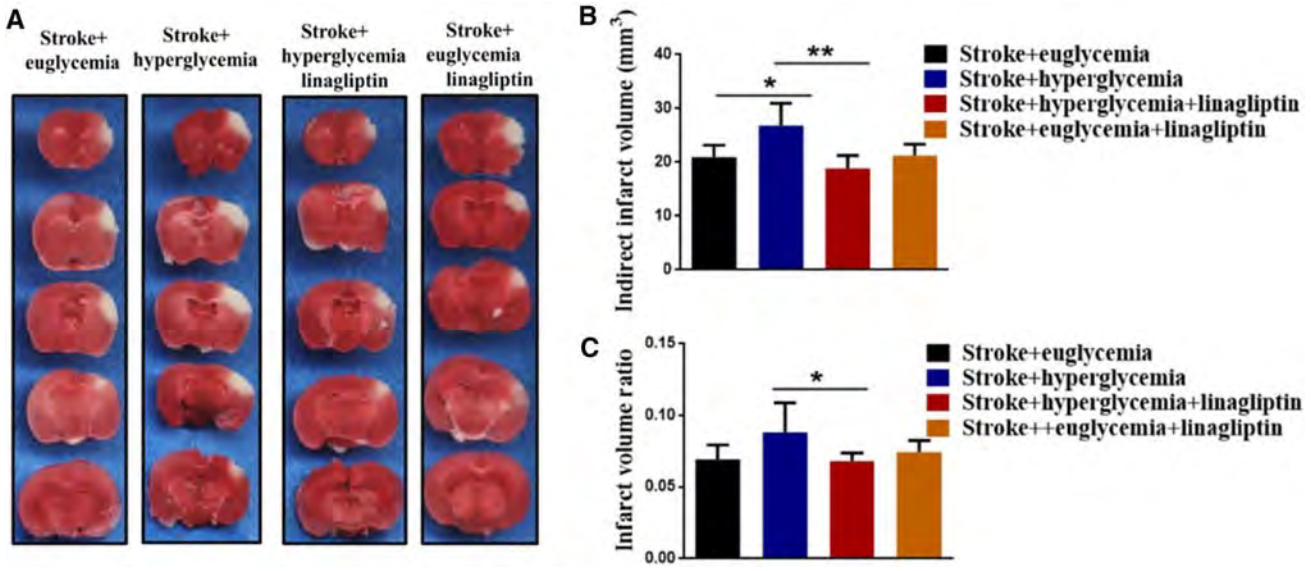

Fig. 2 Linagliptin reduces infarct volume after ischemic stroke in hyperglycemic mice. **A** TTC staining 3 days after stroke to evaluate infarct formation after stroke. **B** Linagliptin treatment significantly reduced the indirect infarct volume. **C** Linagliptin treatment significantly reduced the indirect infarct ratio. Values are expressed as the mean ± SEM. $^{*}P < 0.05$, $^{**}P < 0.01$.

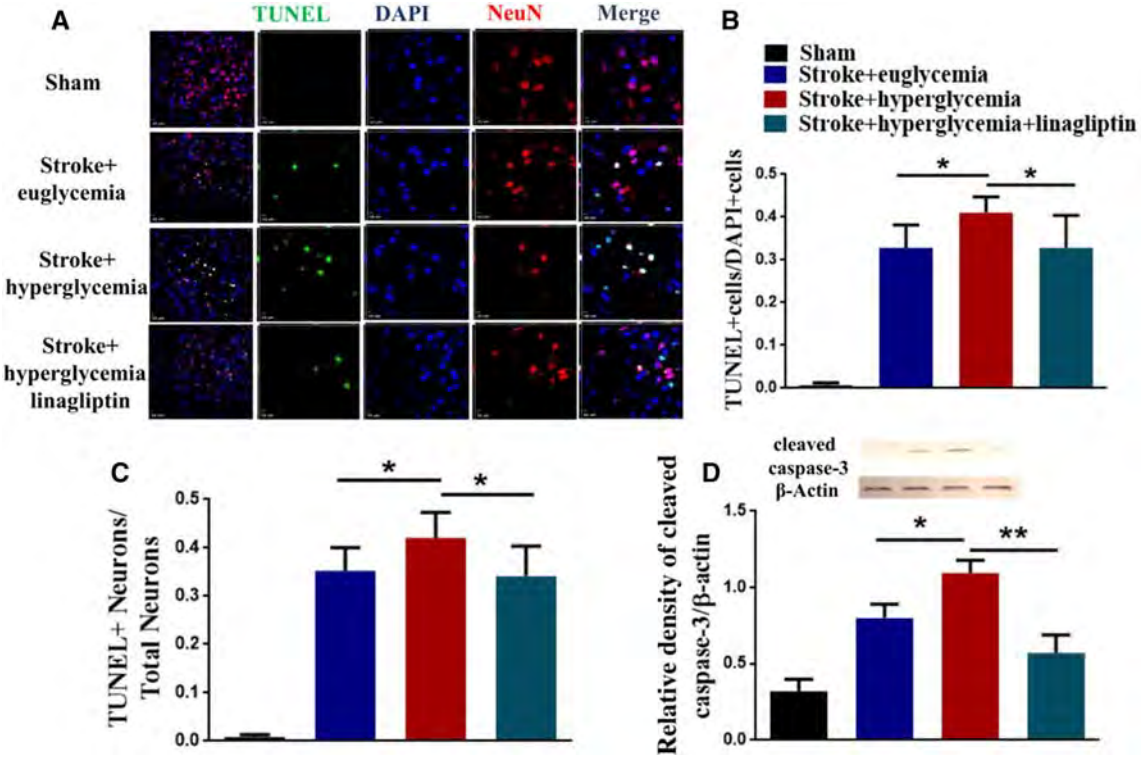

Fig. 3 Linagliptin reduces neuronal cell death in hyperglycemic mice. **A** TUNEL (green), DAPI (blue), and the neuronal marker NeuN (red) staining 3 days after stroke. TUNEL +/NeuN + co-labeled cells indicate dead neurons; TUNEL +/DAPI + co-labeled cells indicate dead cells. **B** The ratio of TUNEL-positive cells to DAPI-positive (blue) cells. **C** The ratio of TUNEL +/NeuN + co-labeled cells to total NeuN + cells. **D** Representative western blots of the protein expression of cleaved caspase-3 in the penumbra 3 days after stroke. Values are expressed as the mean ± SEM. $^{*}P < 0.05$, $^{**}P < 0.01$.

Linagliptin Treatment Decreases Apoptotic Cell Death *via* the Akt/mTOR Pathway

In Western blotting analysis, there were no significant differences in the protein levels of Akt and mTOR between the normal blood glucose and hyperglycemic stroke groups (Fig. 4A–C). The phosphorylated Akt (p-Akt) and phosphorylated mTOR (p-mTOR) proteins, however, were lower in the hyperglycemic stroke group. After treatment with linagliptin, the protein levels were significantly higher (Fig. 4D–F). Compared with the normal blood glucose with stroke group, the Bcl-2 expression in the hyperglycemic group was decreased, and this was prevented by linagliptin treatment ($P < 0.05$) (Fig. 4G–I). On the other hand, compared with the normal blood glucose and stroke group, a higher level of the pro-apoptotic Bax protein was seen in the hyperglycemic group ($P < 0.05$). Consistent with an anti-apoptotic action, the Bax expression was suppressed by linagliptin treatment ($P < 0.05$) (Fig. 4G–I).

Linagliptin Decreases Inflammation in Hyperglycemic Mice

Inflammation and microglial activation play important roles in the pathogenesis of stroke. To measure whether linagliptin influenced the activation of microglia/macrophages, we detected the expression of Iba-1 in the penumbra 3 days after stroke. Compared with the sham group, microglia were significantly activated in the stroke groups. In addition, the number of Iba-1-positive cells was significantly higher in the hyperglycemic group. After treatment with linagliptin, the number of Iba-1-positive cells was significantly decreased (Fig. 5A, B). Some studies have shown that inflammatory factor precursors are released by activated microglia in stroke [34, 35], so we measured the protein expression of inflammatory factors in the penumbra extra 3 days after stroke using western blot. The results showed that the protein levels of the inflammatory factors IL-1β, IL-6, and TNF-α were significantly

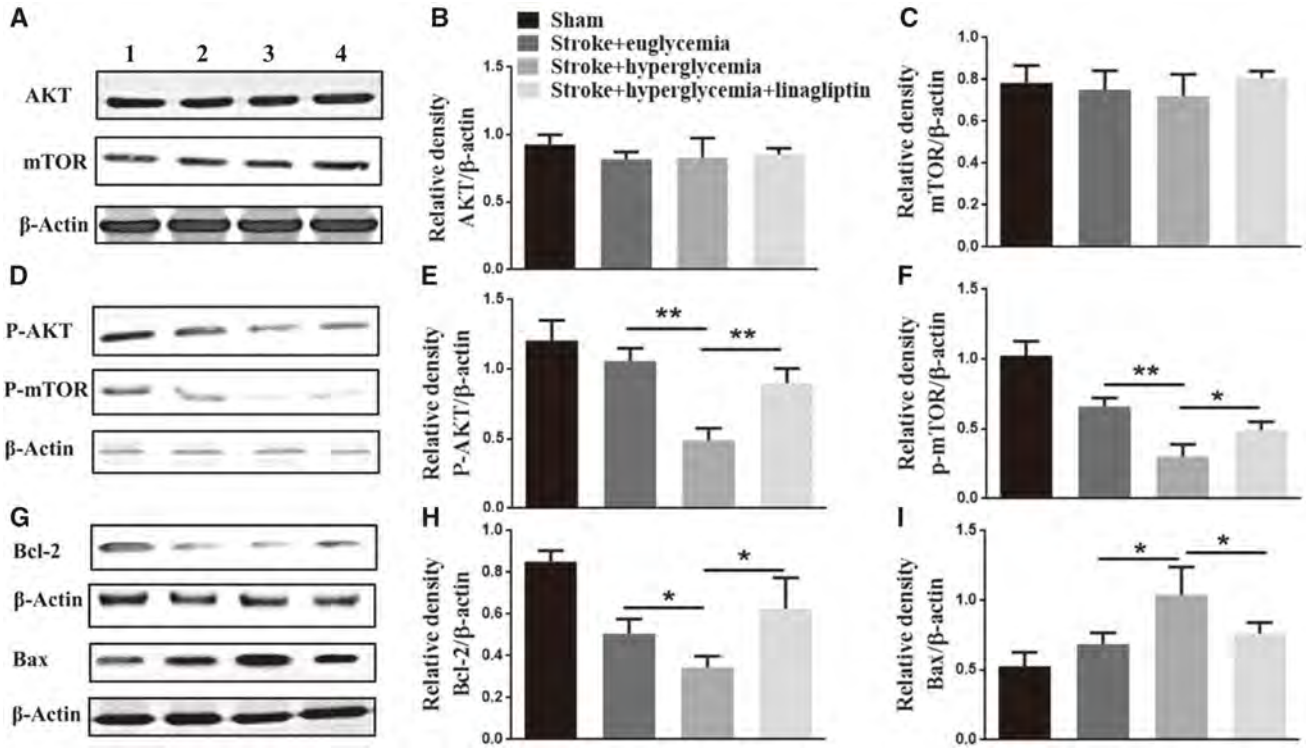

Fig. 4 Linagliptin treatment affects apoptotic cell death *via* the Akt/mTOR pathway. **A–C** The protein expression levels of Akt and mTOR did not significantly differ among groups. **D–F** Representative western blot images and quantification of the protein expression of p-Akt and p-mTOR in the penumbra region. The levels of p-Akt and p-mTOR significantly increased after treatment with linagliptin. **G–I** Representative western blot images and quantification of the protein expression of Bcl-2 and Bax. Bcl-2 levels significantly increased and Bax significantly decreased after treatment with linagliptin. In **A**, **D** and **G**, lane 1, sham group; lane 2, stroke + euglycemia group; lane 3, stroke + hyperglycemia group; and lane 4, stroke + hyperglycemia + linagliptin group. Values are expressed as the mean ± SEM. $^{*}P < 0.05$, $^{**}P < 0.01$.

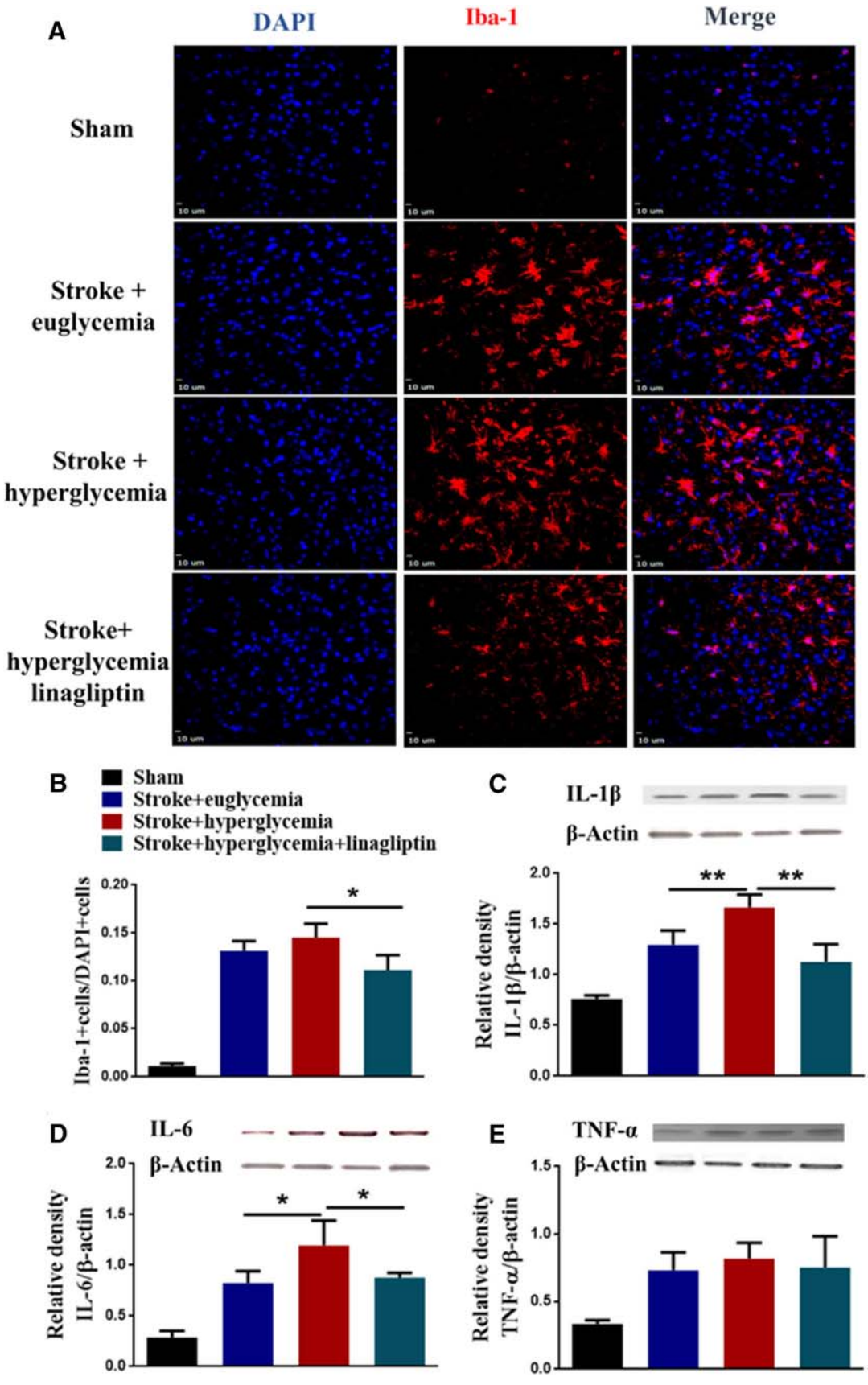
A
DAPI
Iba-1
Merge
Sham
Stroke + euglycemia
Stroke + hyperglycemia
Stroke+ hyperglycemia linagliptin
10 um
B
Sham
Stroke+euglycemia
Stroke+hyperglycemia
Stroke+hyperglycemia+linagliptin
Iba-1+cells/DAPI+cells
0.00
0.05
0.10
0.15
0.20
*
C
IL-1β
β-Actin
Relative density IL-1β/β-actin
0.0
0.5
1.0
1.5
2.0
**
**
D
IL-6
β-Actin
Relative density IL-6/β-actin
*
*
E
TNF-α
β-Actin
Relative density TNF-α/β-actin

◀**Fig. 5** Linagliptin reduces inflammation in hyperglycemic mice. **A** Iba-1 (red) staining shows microglial activation in the penumbra 3 days after stroke. Nuclei were stained using DAPI (blue). **B** The ratio of Iba-1+/DAPI+ cells in each group. **C–E** Representative western blot images of the protein expression of IL-1β, IL-6, and TNF-α in the penumbra 3 days after stroke. Inflammatory factors significantly increased after stroke, and this was significantly ameliorated by linagliptin. Values are expressed as the mean ± SEM. $^{*}P < 0.05$, $^{**}P < 0.01$.

higher in the stroke groups than in the sham group. After treatment with linagliptin, the IL-1β and IL-6 levels were increased compared with the hyperglycemia group ($P < 0.05$) (Fig. 5C–E).

Linagliptin Promotes Recovery of LCBF after Stroke in Hyperglycemic Mice

Recovery of local blood flow is important for cell survival and tissue repair after stroke. To demonstrate that linagliptin promoted angiogenesis and the production of functional blood vessels, we measured the LCBF using a laser Doppler scanner 21 days after stroke. Scanning imaging showed that mice with stroke that received linagliptin treatment had significantly higher LCBF than the stroke-saline group. At the same time, we found that LCBF in the hyperglycemic group was relatively lower than that of the normal blood glucose group ($P < 0.01$) (Fig. 6A, B).

Linagliptin Promotes Functional Recovery after Stroke in Hyperglycemia Mice

We also evaluated whether linagliptin can improve functional deficits after acute stroke. To specifically assess sensorimotor function, we used the adhesive removal test at 0, 3, 7, and 14 days after stroke. The results showed that both normal blood glucose and hyperglycemic mice took significantly more time to detect and remove sticky dots attached to the left paw after ischemic damage to the sensorimotor cortex in the right hemisphere. Linagliptin-treated animals took less time to detect the dot than stroke control hyperglycemic mice at 7 and 14 days after stroke ($P < 0.05$) (Fig. 7A). Linagliptin-treated animals were significantly faster in removing the sticky dot than stroke control hyperglycemic animals at 7 and 14 days after stroke ($P < 0.05$) (Fig. 7B). In addition, there was no significant difference in right paw function.

Discussion

In this study, we investigated whether DPP-4 inhibitors are neuroprotective in a rodent stroke model with hyperglycemia. Although previous large studies have shown that DPP-4 inhibitor treatment does not reduce the incidence of stroke in diabetic patients [22–24], studying factors that promote functional recovery after stroke remains directly relevant to clinical treatment and therapy. Our study demonstrated the neuroprotective effects of acute linagliptin treatment, explored possible mediating mechanisms *via* anti-apoptotic and anti-inflammatory actions, and demonstrated the ability of linagliptin to improve functional sensorimotor recovery in a hyperglycemic stroke mouse model. Previous studies have suggested that DPP-4 inhibitors such as alogliptin and linagliptin have beneficial effects after stroke in normal mice [36, 37] and diabetic patients who suffer strokes [26, 27]. However, we investigated the neuroprotective effects of linagliptin on less-

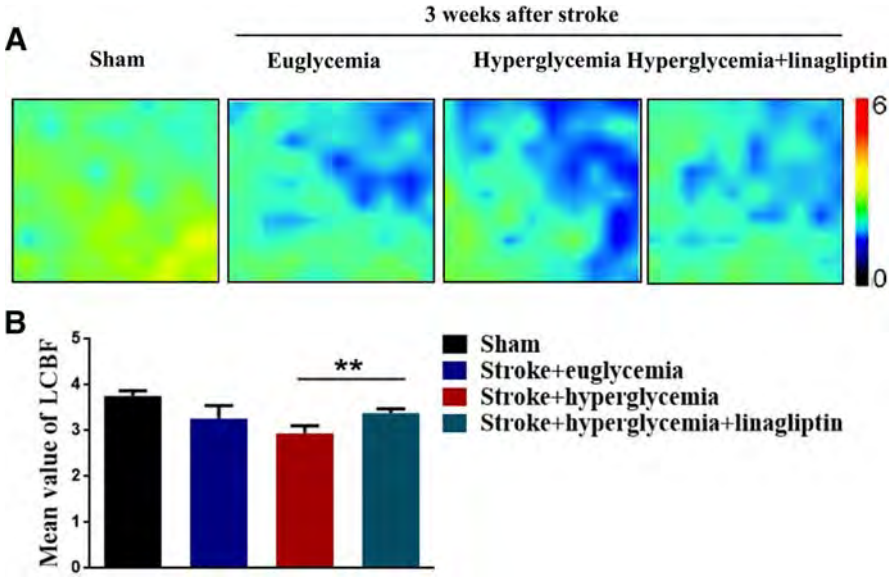

Fig. 6 Linagliptin promotes LCBF recovery after stroke in hyperglycemic mice. **A** Local cerebral blood flow (LCBF) in the penumbra 21 days after stroke measured by laser Doppler in each group. **B** Quantified data showing that animals with stroke that received linagliptin exhibited better LCBF recovery than stroke hyperglycemic animals that did not receive linagliptin. Values are expressed as the mean ± SEM. $^{**}P < 0.01$.

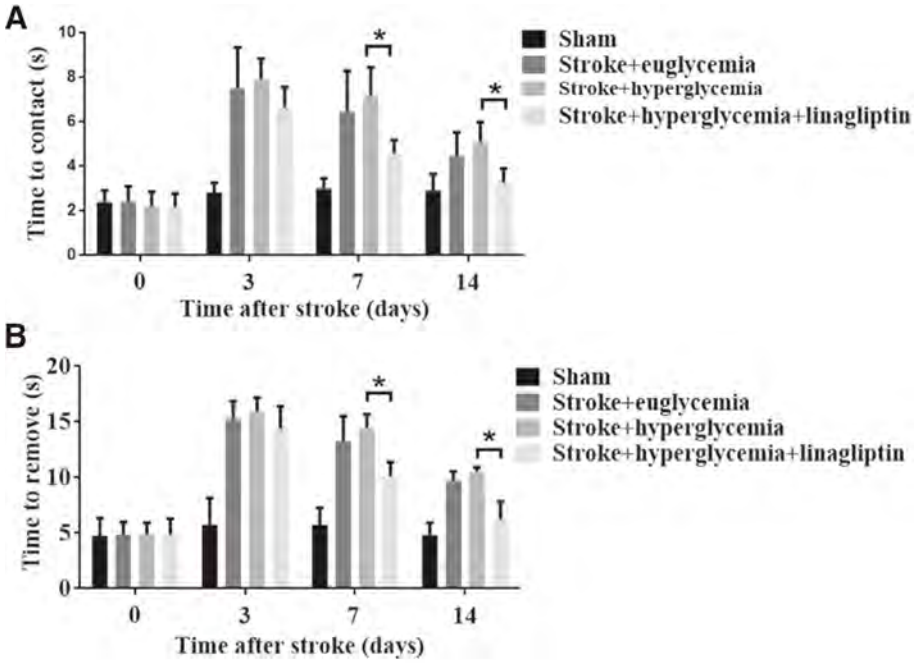

Fig. 7 Linagliptin promotes functional recovery after stroke in hyperglycemic mice. **A** Linagliptin-treated animals took less time to detect the adhesive than stroke hyperglycemic mice that did not receive linagliptin at 7 and 14 days in the adhesive removal test. **B** Linagliptin-treated animals were significantly faster in removing the sticky dot than stroke hyperglycemic animals that did not receive linagliptin at 7 and 14 days. Values are expressed as the mean ± SEM. $^{*}P < 0.05$.

studied hyperglycemic mice and explored the unclear mechanism of the Akt/mTOR pathway.

DPP-4 inhibitors block the enzymatic action of dipeptidyl peptidase-4 and increase the levels of glucagon-like peptide-1 (GLP-1), a peptide hormone secreted by cells in the distal gut and central nervous system (CNS), by preventing the degradation of GLP-1 by DPP-4. GLP-1 increases blood sugar levels *via* direct stimulation of pancreatic β-cells to potentiate insulin secretion [38]. In addition, GLP-1 leads to the feeling of satiety by transmitting signals to the CNS *via* the gut-to-brain axis [39]. GLP-1 receptors have been found in pancreatic tissue and have also been discovered in tissues outside the pancreas, including the heart, kidneys, and brain [40]. They are widely distributed throughout the CNS, with expression in the thalamus, hypothalamus, cerebellum, hippocampus, cortex, and brainstem [41]. Interestingly, GLP-1 has also been identified as a neuropeptide which can cross the blood-brain barrier [42–44].

Recently, the neuroprotective effect of GLP-1 was reported in animal models and clinical work [45–47]. The anti-inflammatory effects of GLP-1 have been found in endothelial islets and pancreatic cells [48–50]. A previous study showed that stimulating GLP-1 receptors reduces the inflammatory response in a rat model of type 1 diabetes [51]. Here, we evaluated the expression of Iba-1 in the penumbra 3 days after stroke. Immunostaining revealed that the number of Iba-1-positive cells was significantly higher in the penumbra than in a sham group. Compared with the normal blood glucose group, the hyperglycemic group showed that Iba-1-positive cells were significantly increased. However, linagliptin treatment significantly reduced the number of Iba-1-positive cells. In addition, we found that the expression of the inflammatory protein was lower in the linagliptin treatment group than in the hyperglycemic group. A previous study has also shown that GLP-1 might be a modulator of inflammation in the CNS by preventing LPS-induced IL-1β mRNA expression [52]. GLP-1 plays a neuroprotective role by alleviating the inflammatory response in neurodegenerative diseases such as Alzheimer's and Parkinson's Disease [45, 53]. Thus, it has been suggested that GLP-1 may be a therapeutic option for targeting inflammation in the brain, although further clinical research is necessary [54, 55]. In addition, we demonstrated that linagliptin improved the recovery of blood flow after stroke, suggesting the mediation of angiogenesis and the preservation of functional blood vessels by DPP-4 inhibitors. This is in line with previous studies demonstrating that linagliptin improves cerebrovascular function and reverses diabetes-mediated cerebral artery remodeling in diabetic rats [56, 57] and provides another important avenue for future investigations of the use of linagliptin treatment for hyperglycemic stroke patients.

In this study, we observed a significant reduction in neuronal apoptosis in the linagliptin-treated group, suggesting that linagliptin may be involved in regulating the apoptotic pathway. A previous study in a mouse model of stroke with diabetes showed significantly increased expression levels of GLP-1 in peripheral blood and significantly reduced ischemic area of brain injury after linagliptin treatment [58]. *In vitro* experiments revealed that GLP-1

promoted the survival and proliferation of neurons and prevented apoptosis and oxidative stress-related cell death in hippocampal cells and glia [59]. GLP-1 mediates neuronal proliferation through the activation of protein kinase A and phosphoinositide 3-kinase, and regulates the apoptotic signaling pathway through decreased Bax and caspase-3 and increased Bcl-2 to enhance cell survival [60–63]. In our study, we found that linagliptin reduced neuronal death in hyperglycemic mice. It is possible that linagliptin might play a neuroprotective role by suppressing serum GLP-1 degradation and activating GLP-1-induced Akt/mTOR signaling pathways. Previous studies have also reported that GLP-1 protects against amyloid-induced neuronal apoptosis *via* the cAMP signaling pathway and oxidative stress-induced apoptosis *via* the MAPK pathway [64, 65]. Our data showed that linagliptin upregulated the anti-apoptotic protein Bcl-2 and downregulated the pro-apoptotic protein Bax. Linagliptin had an inhibitory effect on the cleavage of caspase-3. The Bcl-2 family contains two classes of protein: pro-apoptotic (such as Bax, Bak, Bok, and BAD) and anti-apoptotic proteins (such as Bcl-w, Bcl-2, and Bcl-xL) [66]. The Bcl-2 protein family constitutes a complex of interactions involved in the regulation of apoptosis. The response of cells to apoptotic signals is determined by the relative expression levels of apoptosis-inducing genes and apoptosis-inhibiting genes. When the expression of Bcl-2 is excessive, apoptosis is inhibited; when Bax is overexpressed, apoptosis is promoted; thus, the ratio of Bcl-2 to Bax is very important. In general, a higher ratio of Bcl-2:Bax protein expression is essential for cell survival and the reverse is essential for apoptosis. For example, after cerebral ischemia, both Bax and Bcl-2 mRNA levels are increased in the penumbra. However, Bax is more abundant than Bcl-2, so the former is the key cause of ischemia-induced cell death [67]. Our further experiments demonstrated that the effects of linagliptin might be mediated through the upregulation of AKT/mTOR signal pathway proteins. Although mTOR is a key regulator of cell growth and proliferation [68, 69], it is also involved in the regulation of apoptosis in a variety of cells [70–72]. Many factors lead to apoptosis, such as oxidative stress. Previous studies by Holville and Green suggest that the oxidative stress-induced apoptosis pathways are the Fas, P53/MPTP, NF-kB, and JNK pathways [73, 74]. In this investigation, we simply explored a possible mechanism in one pathway, which leaves the remaining pathways as interesting targets for future investigations.

In summary, the DPP-4 inhibitor linagliptin reduced neuronal death in hyperglycemic mice, and this may be mediated *via* suppression of the degradation of serum GLP-1 and the activation of GLP-1-induced Akt/mTOR signaling pathways. We also demonstrated that linagliptin improves tolerance to inflammatory processes. With regard to long-term recovery, linagliptin induced significantly higher LCBF and also promoted functional recovery after stroke in hyperglycemic mice compared to the stroke-saline group. As a result, the DPP-4 inhibitor linagliptin holds future translational potential in stroke patients with hyperglycemia by promoting functional recovery in stroke survivors.

Acknowledgements This work was supported by the John E. Steinhaus Endowment fund.

Conflict of interest The authors declare no potential conflicts of interest with respect to the research, authorship, and/or publication of this article.

References

1. Benjamin EJ, Muntner P, Alonso A, Bittencourt MS, Callaway CW, Carson AP, *et al.* Heart disease and stroke statistics-2019 update: a report from the American Heart Association. Circulation 2019, 139: e56–e66.
2. Guzik A, Bushnell C. Stroke epidemiology and risk factor management. Continuum (Minneap Minn) 2017, 23: 15–39.
3. Heidenreich PA, Trogdon JG, Khavjou OA, Butler J, Dracup K, Ezekowitz MD, *et al.* Forecasting the future of cardiovascular disease in the United States: a policy statement from the American Heart Association. Circulation 2011, 123: 933–944.
4. National Institute of Neurological Disorders and Stroke rt-PA Stroke Study Group. Tissue plasminogen activator for acute ischemic stroke. N Engl J Med 1995, 333: 1581–1587.
5. Jeremitsky E, Omert LA, Dunham CM, Wilberger J, Rodriguez A. The impact of hyperglycemia on patients with severe brain injury. J Trauma 2005, 58: 47–50.
6. Juvela S, Siironen J, Kuhmonen J. Hyperglycemia, excess weight, and history of hypertension as risk factors for poor outcome and cerebral infarction after aneurysmal subarachnoid hemorrhage. J Neurosurg 2005, 102: 998–1003.
7. Capes SE, Hunt D, Malmberg K, Pathak P, Gerstein HC. Stress hyperglycemia and prognosis of stroke in nondiabetic and diabetic patients: a systematic overview. Stroke 2001, 32: 2426–2432.
8. Demchuk AM, Tanne D, Hill MD, Kasner SE, Hanson S, Grond M, *et al.* Predictors of good outcome after intravenous tPA for acute ischemic stroke. Neurology 2001, 57: 474–480.
9. de Courten-Myers G, Myers RE, Schoolfield L. Hyperglycemia enlarges infarct size in cerebrovascular occlusion in cats. Stroke 1988, 19: 623–630.
10. Nedergaard M. Transient focal ischemia in hyperglycemic rats is associated with increased cerebral infarction. Brain Res 1987, 408: 79–85.
11. Prado R, Ginsberg MD, Dietrich WD, Watson BD, Busto R. Hyperglycemia increases infarct size in collaterally perfused but not end-arterial vascular territories. J Cereb Blood Flow Metab 1988, 8: 186–192.
12. Parsons MW, Barber PA, Desmond PM, Baird TA, Darby DG, Byrnes G, *et al.* Acute hyperglycemia adversely affects stroke outcome: a magnetic resonance imaging and spectroscopy study. Ann Neurol 2002, 52: 20–28.
13. Els T, Klisch J, Orszagh M, Hetzel A, Schulte-Monting J, Schumacher M, *et al.* Hyperglycemia in patients with focal cerebral ischemia after intravenous thrombolysis: influence on

clinical outcome and infarct size. Cerebrovasc Dis 2002, 13: 89–94.
14. Ribo M, Molina CA, Delgado P, Rubiera M, Delgado-Mederos R, Rovira A, *et al.* Hyperglycemia during ischemia rapidly accelerates brain damage in stroke patients treated with tPA. J Cereb Blood Flow Metab 2007, 27: 1616–1622.
15. Baird TA, Parsons MW, Phan T, Butcher KS, Desmond PM, Tress BM, *et al.* Persistent poststroke hyperglycemia is independently associated with infarct expansion and worse clinical outcome. Stroke 2003, 34: 2208–2214.
16. Gray CS, Hildreth AJ, Sandercock PA, O'Connell JE, Johnston DE, Cartlidge NE, *et al.* Glucose-potassium-insulin infusions in the management of post-stroke hyperglycaemia: the UK Glucose Insulin in Stroke Trial (GIST-UK). Lancet Neurol 2007, 6: 397–406.
17. Martini SR, Kent TA. Hyperglycemia in acute ischemic stroke: a vascular perspective. J Cereb Blood Flow Metab 2007, 27: 435–451.
18. Sander D, Kearney MT. Reducing the risk of stroke in type 2 diabetes: pathophysiological and therapeutic perspectives. J Neurol 2009, 256: 1603–1619.
19. Idris I, Thomson GA, Sharma JC. Diabetes mellitus and stroke. Int J Clin Pract 2006, 60: 48–56.
20. Yehya A, Sadhu AR. New therapeutic strategies for type 2 diabetes (CME). Methodist Debakey Cardiovasc J 2018, 14: 281–288.
21. Cahn A, Cernea S, Raz I. An update on DPP-4 inhibitors in the management of type 2 diabetes. Expert Opin Emerg Drugs 2016, 21: 409–419.
22. Zhang Z, Chen X, Lu P, Zhang J, Xu Y, He W, *et al.* Incretin-based agents in type 2 diabetic patients at cardiovascular risk: compare the effect of GLP-1 agonists and DPP-4 inhibitors on cardiovascular and pancreatic outcomes. Cardiovasc Diabetol 2017, 16: 31.
23. Li YR, Tsai SS, Chen DY, Chen ST, Sun JH, Chang HY, *et al.* Linagliptin and cardiovascular outcomes in type 2 diabetes after acute coronary syndrome or acute ischemic stroke. Cardiovasc Diabetol 2018, 17: 2.
24. Barkas F, Elisaf M, Tsimihodimos V, Milionis H. Dipeptidyl peptidase-4 inhibitors and protection against stroke: A systematic review and meta-analysis. Diabetes Metab 2017, 43: 1–8.
25. Gallwitz B. Emerging DPP-4 inhibitors: focus on linagliptin for type 2 diabetes. Diabetes Metab Syndr Obes 2013, 6: 1–9.
26. Darsalia V, Klein T, Nystrom T, Patrone C. Glucagon-like receptor 1 agonists and DPP-4 inhibitors: Anti-diabetic drugs with anti-stroke potential. Neuropharmacology 2018, 136: 280–286.
27. Magkou D, Tziomalos K. Antidiabetic treatment, stroke severity and outcome. World J Diabetes 2014, 5: 84–88.
28. Darsalia V, Larsson M, Klein T, Patrone C. The high need for trials assessing functional outcome after stroke rather than stroke prevention with GLP-1 agonists and DPP-4 inhibitors. Cardiovasc Diabetol 2018, 17: 32.
29. Wei L, Cui L, Snider BJ, Rivkin M, Yu SS, Lee CS, *et al.* Transplantation of embryonic stem cells overexpressing Bcl-2 promotes functional recovery after transient cerebral ischemia. Neurobiol Dis 2005, 19: 183–193.
30. Swanson RA, Morton MT, Tsao-Wu G, Savalos RA, Davidson C, Sharp FR. A semiautomated method for measuring brain infarct volume. J Cereb Blood Flow Metab 1990, 10: 290–293.
31. Whitaker VR, Cui L, Miller S, Yu SP, Wei L. Whisker stimulation enhances angiogenesis in the barrel cortex following focal ischemia in mice. J Cereb Blood Flow Metab 2007, 27: 57–68.
32. Ohab JJ, Fleming S, Blesch A, Carmichael ST. A neurovascular niche for neurogenesis after stroke. J Neurosci 2006, 26: 13007–13016.
33. Choi KE, Hall CL, Sun JM, Wei L, Mohamad O, Dix TA, *et al.* A novel stroke therapy of pharmacologically induced hypothermia after focal cerebral ischemia in mice. FASEB J 2012, 26: 2799–2810.
34. Zhao SC, Ma LS, Chu ZH, Xu H, Wu WQ, Liu F. Regulation of microglial activation in stroke. Acta Pharmacol Sin 2017, 38: 445–458.
35. Lucas SM, Rothwell NJ, Gibson RM. The role of inflammation in CNS injury and disease. Br J Pharmacol 2006, 147 Suppl 1: S232–240.
36. Chiazza F, Tammen H, Pintana H, Lietzau G, Collino M, Nystrom T, *et al.* The effect of DPP-4 inhibition to improve functional outcome after stroke is mediated by the SDF-1alpha/CXCR4 pathway. Cardiovasc Diabetol 2018, 17: 60.
37. Yang D, Nakajo Y, Iihara K, Kataoka H, Yanamoto H. Alogliptin, a dipeptidylpeptidase-4 inhibitor, for patients with diabetes mellitus type 2, induces tolerance to focal cerebral ischemia in non-diabetic, normal mice. Brain Res 2013, 1517: 104–113.
38. Drucker DJ. The biology of incretin hormones. Cell Metab 2006, 3: 153–165.
39. Burcelin R, Serino M, Cabou C. A role for the gut-to-brain GLP-1-dependent axis in the control of metabolism. Curr Opin Pharmacol 2009, 9: 744–752.
40. Holst JJ. The physiology of glucagon-like peptide 1. Physiol Rev 2007, 87: 1409–1439.
41. Alvarez E, Martinez MD, Roncero I, Chowen JA, Garcia-Cuartero B, Gispert JD, *et al.* The expression of GLP-1 receptor mRNA and protein allows the effect of GLP-1 on glucose metabolism in the human hypothalamus and brainstem. J Neurochem 2005, 92: 798–806.
42. Larsen PJ, Holst JJ. Glucagon-related peptide 1 (GLP-1): hormone and neurotransmitter. Regul Pept 2005, 128: 97–107.
43. Trapp S, Richards JE. The gut hormone glucagon-like peptide-1 produced in brain: is this physiologically relevant? Curr Opin Pharmacol 2013, 13: 964–969.
44. Kastin AJ, Akerstrom V, Pan W. Interactions of glucagon-like peptide-1 (GLP-1) with the blood-brain barrier. J Mol Neurosci 2002, 18: 7–14.
45. Zhang L, Li L, Holscher C. Neuroprotective effects of the novel GLP-1 long acting analogue semaglutide in the MPTP Parkinson's disease mouse model. Neuropeptides 2018, 71: 70–80.
46. Yang JL, Chen WY, Chen YP, Kuo CY, Chen SD. Activation of GLP-1 receptor enhances neuronal base excision repair via PI3 K-AKT-induced expression of apurinic/apyrimidinic endonuclease 1. Theranostics 2016, 6: 2015–2027.
47. Chen F, Wang W, Ding H, Yang Q, Dong Q, Cui M. The glucagon-like peptide-1 receptor agonist exendin-4 ameliorates warfarin-associated hemorrhagic transformation after cerebral ischemia. J Neuroinflammation 2016, 13: 204.
48. Cechin SR, Perez-Alvarez I, Fenjves E, Molano RD, Pileggi A, Berggren PO, *et al.* Anti-inflammatory properties of exenatide in human pancreatic islets. Cell Transplant 2012, 21: 633–648.
49. Krasner NM, Ido Y, Ruderman NB, Cacicedo JM. Glucagon-like peptide-1 (GLP-1) analog liraglutide inhibits endothelial cell inflammation through a calcium and AMPK dependent mechanism. PLoS One 2014, 9: e97554.
50. Ceriello A, Novials A, Ortega E, Canivell S, La Sala L, Pujadas G, *et al.* Glucagon-like peptide 1 reduces endothelial dysfunction, inflammation, and oxidative stress induced by both hyperglycemia and hypoglycemia in type 1 diabetes. Diabetes Care 2013, 36: 2346–2350.

51. Kodera R, Shikata K, Kataoka HU, Takatsuka T, Miyamoto S, Sasaki M, *et al.* Glucagon-like peptide-1 receptor agonist ameliorates renal injury through its anti-inflammatory action without lowering blood glucose level in a rat model of type 1 diabetes. Diabetologia 2011, 54: 965–978.
52. Iwai T, Ito S, Tanimitsu K, Udagawa S, Oka J. Glucagon-like peptide-1 inhibits LPS-induced IL-1beta production in cultured rat astrocytes. Neurosci Res 2006, 55: 352–360.
53. Holscher C. Novel dual GLP-1/GIP receptor agonists show neuroprotective effects in Alzheimer's and Parkinson's disease models. Neuropharmacology 2018, 136: 251–259.
54. Athauda D, Foltynie T. The glucagon-like peptide 1 (GLP) receptor as a therapeutic target in Parkinson's disease: mechanisms of action. Drug Discov Today 2016, 21: 802–818.
55. Candeias EM, Sebastiao IC, Cardoso SM, Correia SC, Carvalho CI, Placido AI, *et al.* Gut-brain connection: The neuroprotective effects of the anti-diabetic drug liraglutide. World J Diabetes 2015, 6: 807–827.
56. Hardigan T, Yasir A, Abdelsaid M, Coucha M, El-Shaffey S, Li W, *et al.* Linagliptin treatment improves cerebrovascular function and remodeling and restores reduced cerebral perfusion in Type 2 diabetes. Am J Physiol Regul Integr Comp Physiol 2016, 311: R466–477.
57. Yasir A, Hardigan T, Ergul A. Diabetes-mediated middle cerebral artery remodeling is restored by linagliptin: Interaction with the vascular smooth muscle cell endothelin system. Life Sci 2016, 159: 76–82.
58. Darsalia V, Ortsater H, Olverling A, Darlof E, Wolbert P, Nystrom T, *et al.* The DPP-4 inhibitor linagliptin counteracts stroke in the normal and diabetic mouse brain: a comparison with glimepiride. Diabetes 2013, 62: 1289–1296.
59. Velmurugan K, Bouchard R, Mahaffey G, Pugazhenthi S. Neuroprotective actions of glucagon-like peptide-1 in differentiated human neuroprogenitor cells. J Neurochem 2012, 123: 919–931.
60. Perry T, Haughey NJ, Mattson MP, Egan JM, Greig NH. Protection and reversal of excitotoxic neuronal damage by glucagon-like peptide-1 and exendin-4. J Pharmacol Exp Ther 2002, 302: 881–888.
61. Holst JJ, Burcelin R, Nathanson E. Neuroprotective properties of GLP-1: theoretical and practical applications. Curr Med Res Opin 2011, 27: 547–558.
62. Liu WJ, Jin HY, Lee KA, Xie SH, Baek HS, Park TS. Neuroprotective effect of the glucagon-like peptide-1 receptor agonist, synthetic exendin-4, in streptozotocin-induced diabetic rats. Br J Pharmacol 2011, 164: 1410–1420.
63. Li Y, Tweedie D, Mattson MP, Holloway HW, Greig NH. Enhancing the GLP-1 receptor signaling pathway leads to proliferation and neuroprotection in human neuroblastoma cells. J Neurochem 2010, 113: 1621–1631.
64. Qin Z, Sun Z, Huang J, Hu Y, Wu Z, Mei B. Mutated recombinant human glucagon-like peptide-1 protects SH-SY5Y cells from apoptosis induced by amyloid-beta peptide (1-42). Neurosci Lett 2008, 444: 217–221.
65. Liu J, Yin F, Zheng X, Jing J, Hu Y. Geniposide, a novel agonist for GLP-1 receptor, prevents PC12 cells from oxidative damage via MAP kinase pathway. Neurochem Int 2007, 51: 361–369.
66. Brunelle JK, Letai A. Control of mitochondrial apoptosis by the Bcl-2 family. J Cell Sci 2009, 122: 437–441.
67. Lin CH, Lu YZ, Cheng FC, Chu LF, Hsueh CM. Bax-regulated mitochondria-mediated apoptosis is responsible for the *in vitro* ischemia induced neuronal cell death of Sprague Dawley rat. Neurosci Lett 2005, 387: 22–27.
68. Carter AJ. TOR of the cell cycle: Are there important implications for diabetics in the era of the drug-eluting stent? Catheter Cardiovasc Interv 2004, 61: 233–236.
69. Sarbassov DD, Ali SM, Sabatini DM. Growing roles for the mTOR pathway. Curr Opin Cell Biol 2005, 17: 596–603.
70. Lieberthal W, Fuhro R, Andry CC, Rennke H, Abernathy VE, Koh JS, *et al.* Rapamycin impairs recovery from acute renal failure: role of cell-cycle arrest and apoptosis of tubular cells. Am J Physiol Renal Physiol 2001, 281: F693–706.
71. Woltman AM, de Fijter JW, Kamerling SW, van Der Kooij SW, Paul LC, Daha MR, *et al.* Rapamycin induces apoptosis in monocyte- and CD34-derived dendritic cells but not in monocytes and macrophages. Blood 2001, 98: 174–180.
72. Wu X, Reiter CE, Antonetti DA, Kimball SR, Jefferson LS, Gardner TW. Insulin promotes rat retinal neuronal cell survival in a p70S6 K-dependent manner. J Biol Chem 2004, 279: 9167–9175.
73. Hollville E, Romero SE, Deshmukh M. Apoptotic cell death regulation in neurons. FEBS J 2019, 286: 3276–3298.
74. Green DR, Llambi F. Cell death signaling. Cold Spring Harb Perspect Biol 2015. https://doi.org/10.1101/cshperspect.a006080

Neurosci. Bull. April, 2020, 36(4):419–426
https://doi.org/10.1007/s12264-019-00449-7

www.neurosci.cn
www.springer.com/12264

ORIGINAL ARTICLE

Myelin Deficits Caused by Olig2 Deficiency Lead to Cognitive Dysfunction and Increase Vulnerability to Social Withdrawal in Adult Mice

Xianjun Chen[1,2] · Fei Wang[1] · Jingli Gan[2] · Zhonghua Zhang[2] · Xuejun Liang[2] · Tao Li[1] · Nanxin Huang[1] · Xiaofeng Zhao[3] · Feng Mei[1] · Lan Xiao[1]

Received: 30 May 2019 / Accepted: 27 August 2019 / Published online: 22 November 2019

Abstract Oligodendrocyte (OL) and myelin development are crucial for network integration and are associated with higher brain functions. Accumulating evidence has demonstrated structural and functional impairment of OLs and myelin in serious mental illnesses. However, whether these deficits contribute to the brain dysfunction or pathogenesis of such diseases still lacks direct evidence. In this study, we conditionally deleted *Olig2* in oligodendroglial lineage cells (*Olig2* cKO) and screened the behavioral changes in adult mice. We found that *Olig2* ablation impaired myelin development, which further resulted in severe hypomyelination in the anterior cingulate cortex. Strikingly, *Olig2* cKO mice exhibited an anxious phenotype, aberrant responses to stress, and cognitive deficits. Moreover, *Olig2* cKO mice showed increased vulnerability to social avoidance under the mild stress of social isolation. Together, these results indicate that developmental deficits in OL and myelin lead to cognitive impairment and increase the risk of phenotypes reminiscent of mental illnesses.

✉ Lan Xiao
xiaolan35@hotmail.com

[1] Department of Histology and Embryology, Chongqing Key Laboratory of Neurobiology, Army Medical University (Third Military Medical University), Chongqing 400038, China

[2] Department of Psychiatry, Mental Diseases Prevention and Treatment Institute of The People's Liberation Army (PLA), 988 Hospital of Joint Logistic Support Force of PLA, Jiaozuo 454003, China

[3] Institute of Life Sciences, College of Life and Environmental Sciences, Hangzhou Normal University, Hangzhou 310036, China

Keywords Oligodendrocyte · *Olig2* · Hypomyelination · Cognition · Social withdrawal

Introduction

The oligodendrocytes (OLs) and myelin that underly long-rang connectivity are crucial for complex forms of network integration and many aspects of higher brain function, such as motor-skill learning and the oscillation frequency and synchrony of neuronal activity [1, 2]. OL maturation and myelination are dynamic processes during developmental and early adulthood stages, notably in the cerebral cortex [3]. Notably, the critical period for OL and myelin development coincides with the peak onset of psychiatric disorders, which is concentrated in a very narrow age range from adolescence to young adulthood [4, 5]. In the adolescent brain, the structure and function of neural circuits, including the number and structure of synapses, the availability of neurotransmitters, and the expression of neurotransmitter receptors, are highly dynamic [4]. Furthermore, the function of neural circuits, which are crucial for adolescent emotions and behaviors, is strongly affected by the interactions between neurons and OLs [6, 7].

Accumulating evidence has demonstrated structural and functional impairment of myelin and OL in serious mental illnesses [8]. In schizophrenia, even before disease onset, reduced myelin integrity occurs in frontal areas and this advances in further stages of the disorder to more caudal and posterior regions [9, 10]. A recent postmortem study identified a decrease in the total number of OLs, but not progenitor cells, in the prefrontal cortex (PFC) of the schizophrenic brain [11]. Microarray analysis of dysregulated OL and myelin genes further suggests that OL differentiation defects are involved in the pathogenesis of

schizophrenia [12]. In addition, patients with severe OL and myelin abnormalities, such as the leukodystrophies and multiple sclerosis, also show grave neurological symptoms reminiscent of psychiatric disorders [13, 14]. These findings suggest that OL/myelin developmental deficits are involved in the early pathogenesis of psychiatric disorders.

Notably, cognitive impairment is one of the pivotal common features of major psychiatric disorders [15]. Some evolutionary findings support the hypothesis that OL and myelin development is positively associated with cognition [5]. Multiple clinical studies have further shown that the number of OLs and myelin integrity are correlated with cognition in healthy individuals [16], as well as cognitive dysfunction in those with schizophrenia [17, 18]. Furthermore, our previous study showed that developmental deficits in OL and myelin cause aberrant synaptic transmission of pyramidal neurons in cortex [19], which could be tightly related to cognitive dysfunction in schizophrenia [20, 21]. However, whether and how these developmental deficiencies lead to cognitive deficits and increase the risk of psychiatric disorders still lack direct evidence. Therefore, we set out to determine the effect of OL and myelin deficits on cognitive function by using our previously reported mouse model with specific deletion of *Olig2* in oligodendroglial lineage cells (*CNPase-Cre*).

Materials and Methods

Animals

Olig2-flox mice and *CNP-Cre* mice were as previously described [22, 23]. *Olig2 loxP/loxP* mice were crossed with *CNP-Cre* +/− mice (kindly provided by Dr. Klaus-Armin Nave, Max Planck Institute of Experimental Medicine, Göttingen, Germany) to specifically delete *Olig2* in oligodendroglial lineage cells. All animal experiments were performed according to a protocol approved by the Third Military Medical University Institutional Animal Care and Use Committee.

Immunostaining

Immunostaining was performed as previously described [24]. Briefly, for immunofluorescence staining, free-floating sections were blocked with 5% BSA for 1 h, and then incubated with mouse anti-MBP (1:200; Santa Cruz Biotechnology, Santa Cruz, CA) overnight at 4°C, followed by Alexa fluor 488-conjugated anti-mouse secondary antibody (1:2000; Invitrogen) for 1.5 h.

Western Blotting

Samples containing 50 μg of total protein were denatured in gel-loading buffer and separated on 10% SDS-PAGE gel. Protein samples were transferred to PVDF membranes and visualized by chemiluminescence (ECL plus, GE Healthcare). β-actin was used as a loading control. Quantification of band intensity was analyzed using Image-Pro Plus software 5.0 (Media Cybernetics, Silver Spring, MD). The following primary antibodies were used: mouse anti-MBP (1:1000) and mouse anti-β-actin (1:2000; Santa Cruz Biotechnology).

RNA Extraction and Analysis

RNA extraction, reverse-transcription and quantitative RT-PCR (RT-qPTR) were carried out as previously described [25]. The primers used were: MBP: forward 5′-ACACACGAGAACTACCCATTATGG-3′, reverse 5′-AGAAATGGACTACTGGGTTTTCATCT-3′; PLP: forward 5′-CCCACCCCTATCCGCTAGTT-3′, reverse 5′-CAGGAAAAAAAGCACCATTGTG-3′; MAG: forward 5′-GACTAAGCCCTAGCTCAATCAC-3′, reverse 5′-CCCTCGAGAAGCTGAAATCAT-3′; GAPDH: forward 5′-ACCCAGAAGACTGTGGATGG-3′, reverse 5′-CACATTGGGGGTAGGAACAC-3′.

Electron Microscopy

Electron microscopy was performed as previously described [24]. Briefly, the anterior cingulate cortex (ACC) was removed rapidly and fixed in fresh fixative overnight at 4°C. Tissue cubes were rinsed in PBS, postfixed in 1% OsO_4 in PBS for 2 h, counterstained with uranyl acetate, dehydrated in a graded ethanol series, infiltrated with propylene oxide, and embedded in Epon. Ultrathin sections were cut on an ultramicrotome (LKB-V, LKB Produkter AB, Bromma, Sweden) and were viewed in a transmission electron microscope (HT7700, Hitachi, Japan). The g-ratios of myelinated fibers were calculated as the ratio of the diameter of the axon to the diameter of the axon with the myelin sheath using Image-Pro Plus software. Measurements were made on electron micrographs from three pairs of mice in all cases.

Behavioral Tests

Mice were housed in a controlled environment (25°C) with free access to food and water and maintained on a 12 h/12 h light/dark cycle. In the social isolation experiments, mice were singly housed for 3 to 8 weeks; otherwise, they were group housed (3–4 animals per cage). After each experiment, all apparatus was wiped clean with 70%

ethanol to remove traces of the previous assay. In all the behavioral experiments, investigators were blinded to *Olig2* cKO or wild-type (WT) mice.

Open field tests were performed in an open-field apparatus (Biowill, Shanghai, China) as previously described [26]. Briefly, mice were placed in the center of the open-field box (50 cm × 50 cm × 50 cm), then their activity was recorded for 10 min. The total and center-area distances traveled were measured and the time spent in the central area was recorded.

The forced swim test was used to assess the response to an acute stress. Mice were forced to swim in a glass cylinder (diameter 12 cm, height 24 cm) for 6 min. The first 2 min were regarded as adaptive training. The activity and total immobility times were recorded during the following 4 min.

The prepulse inhibition (PPI) test was conducted in a foam-lined (sound-damping) isolation chamber (Med Associates, Startle Reflex System ENV-022s). The chamber was equipped with an acoustic stimulator (ANL-925) and a platform with a transducer amplifier (PHM-255A and PHM-250B). The mouse was confined to the holder for 10 min under background noise (65 dB), then acclimatized to a startle pulse (120 dB, 40 ms) 5 times. PPI test sessions consisted of 30 trials: pulse-alone trials (120 dB, 40 ms), prepulse + pulse trials, and no-stimulus trials. Prepulse + pulse trials consisted of a prepulse of noise (75 dB, 20 ms) followed 100 ms after prepulse onset by a startle pulse (120 dB, 40 ms). Each kind of trial was given 10 times pseudorandomly with an interval of 10 s to 30 s. The percentage PPI induced by prepulse intensity was calculated as [1 − (startle amplitude on prepulse trial)/(startle amplitude on pulse alone)] × 100%. The startle amplitude on pulse-alone trials was recorded as an acoustic startle response.

The novel object recognition test (NORT) was conducted in an open-field apparatus (50 cm × 50 cm × 50 cm). In habituation training, the animal was exposed to the experimental apparatus in the absence of objects for 10 min per day for 2 days. The training session was conducted 24 h after the last habituation training. During the training session, mice were placed in the experimental apparatus in the presence of two identical objects and allowed to explore for 5 min. After a retention interval of 2 h, the mice were again placed in the apparatus; however, one of the objects was replaced with a novel one. Mice were allowed to explore for 5 min. The objects chosen for this experiment were a plastic cylinder and a plastic rectangular block of the same height. The time spent exploring each object was recorded. The NORT discrimination index was calculated as: time exploring novel object/(time exploring familiar object + time exploring novel object) × 100%.

The social interaction test was conducted as previously described with a slight modification [27]. Two identical plastic cylinders (each 8 cm in diameter, 12 cm in height) were placed in opposite corners of a box (50 cm × 50 cm × 50 cm). Each cylinder was perforated with multiple holes (0.5 cm diameter) to allow air exchange between the interior and exterior of the cylinder. The subject mouse was first placed at the center of the box. After a 10-min adaptation period in which the subject was free to explore each cylinder, a stranger mouse was placed in one of the cylinders. Containing the stranger mouse in a cylinder ensured that all social approach was initiated by the subject mouse without direct physical contact. The number of contacts and time spent by the subject mouse in approaching and exploring each cylinder was measured for 5 min. The social index was calculated as: time exploring stranger mouse cylinder/(time exploring stranger mouse cylinder + time exploring empty cylinder) × 100%.

Statistics

For statistical analyses we used GraphPad Prism 5 software. For between-group comparisons, we used the independent-samples *t*-test, and the Welch correction was applied when the variance was unequal. For the effect of genotype and social isolation on mouse sociability, two-way ANOVA and the Bonferroni *post hoc* test were used. We considered results to be significant at $P < 0.05$.

Results

Conditional Knockout of *Olig2* in Oligodendroglia Leads to Myelin Deficits During Adolescence

The transcription factor Olig2 is crucial for OL development [28]. In a previous study, we demonstrated that specifically knocking out olig2 in myelinating OLs leads to robust impairment of myelination at the juvenile stage [24]. OL differentiation is a key process before myelin sheath formation [29]. To further test the effect of Olig2 loss on postnatal myelin development during adolescence, we stained for myelin basic protein (MBP), which is crucial for myelin membrane compaction and essential in initiating and driving the axonal wrapping process [30]. The myelin deficit was preferentially found in the cerebral cortex of *Olig2* cKO mice through adolescence into young adulthood (P56) (Fig. 1A); MBP protein was markedly lower in the ACC (100.0% ± 18.9% in WT *versus* 7.1% ± 3.2% in *Olig2* cKO, $P = 0.001$) and the corpus callosum (100.0% ± 17.3% in WT *vs* 52.0% ± 9.5% in *Olig2* cKO, $P = 0.032$) in *Olig2* cKO mice (Fig. 1B). Besides, the transcripts of myelin-related genes were robustly lower

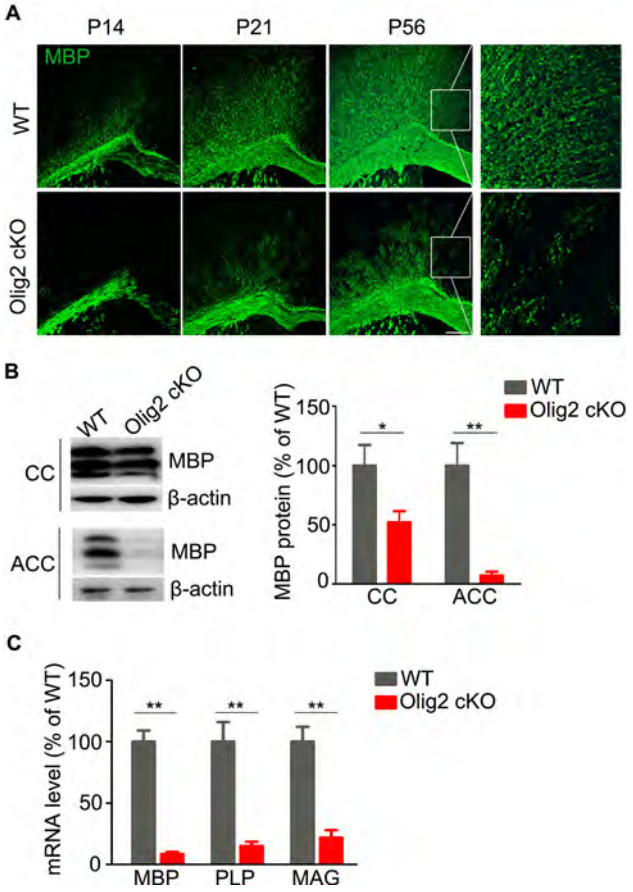

Fig. 1 Impaired myelin development in cortex of *Olig2* cKO mice. **A** Representative images of immunostaining for MBP showing myelin tracts in the cortex of WT and *Olig2* cKO mice at P14, P21, and P56 (white squares enclose the ACC; scale bar, 200 μm). **B** Immunoblots and quantification of MBP in the ACC and corpus callosum of wild-type (WT) and *Olig2* cKO mice ($n = 5$ per group). **C** Quantification of mRNA transcripts of MBP, PLP, and MAG in the ACC of WT and *Olig2* cKO mice ($n = 5$ per group). Data are expressed as the mean ± SEM; $*P < 0.05$, $**P < 0.01$.

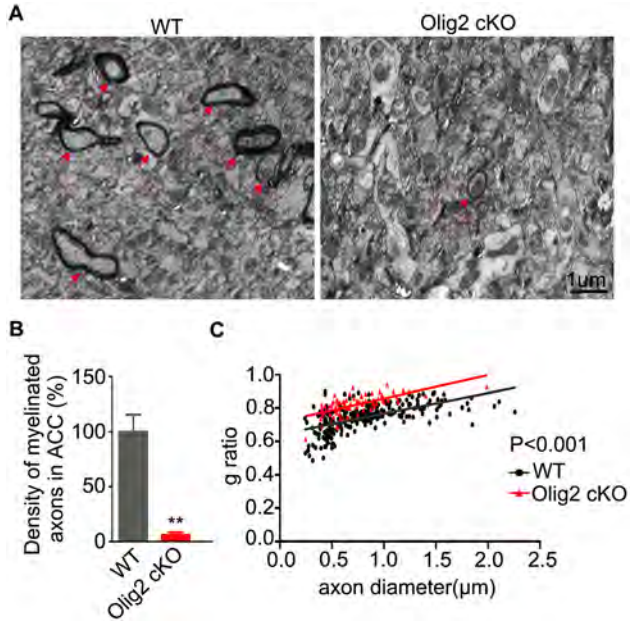

Fig. 2 Analyses of myelin ultrastructure in the ACC of *Olig2* KO and WT mice at P56. **A** Electron micrographs of myelin sheaths in the ACC from WT and *Olig2* cKO mice (arrows indicate myelinated axons; scale bar, 1 μm.). **B** Quantification of the density of myelinated axons in ACC ($n = 3$ animals per group; > 17 000 μm^2 per animal were randomly analyzed). Data are expressed as the mean ± SEM. **C** Scatter-plot of g ratio values of myelinated axons in WT ($n = 253$) and *Olig2* cKO ($n = 79$) mice. $**P < 0.01$.

in the ACC of *Olig2* cKO mice [*MBP*: 100.0% ± 8.6% in WT *vs* 8.5% ± 1.8% in *Olig2* cKO, $P < 0.001$; *PLP* (proteolipid protein): 100.0% ± 16.4% in WT *vs* 15.2% ± 3.6% in *Olig2* cKO, $P = 0.007$; and *MAG* (myelin-associated glycoprotein): 100.0% ± 12.4% in WT *vs* 21.8% ± 6.0% in *Olig2* cKO, $P < 0.001$] (Fig. 1C). This further suggested that myelin gene transcriptional deficits could be responsible for the impairment of myelin development.

To access more details of myelin structure in the ACC, we analyzed the ultra-structural organization of myelin sheaths using a transmission electron microscope. We found that the density of myelinated axons was remarkably lower in the ACC of *Olig2* cKO mice than in WT littermates (Fig. 2A, B; 100.0% ± 15.7% in WT *vs* 5.9% ± 2.7% in *Olig2* cKO, $P = 0.004$). Furthermore, the remaining myelin sheaths in the ACC of *Olig2* cKO mice were also thinner than those in WT controls (Fig. 2C; $P < 0.001$). These results clearly showed that loss of Olig2 caused myelin deficiency in the ACC of young adult mice.

Anxiety and Altered Stress Response in Young Adult *Olig2* cKO Mice

We next tested whether a *de novo* myelin deficit could cause maladaptive behaviors in young adult mice. First, we chose the open field test, a non-conditioned procedure commonly used for assessing locomotor activity in rodents [31]. In this test, *Olig2* cKO mice showed normal locomotor activity by traveling a total distance during a 10-min test similar to WT littermates (Fig. 3A; 65.0 ± 3.6 m in WT *vs* 59.8 ± 3.4 m in *Olig2* cKO, $P = 0.296$). Similar to juveniles as previously reported [24], young adult *Olig2* cKO mice showed a lower ratio of travel distance within the central area to the total travel distance (Fig. 3B; 0.16 ± 0.01 in WT *vs* 0.1 ± 0.01 in *Olig2* cKO, $P = 0.001$) and spent less time in the central area than WT controls (Fig. 3C; 69.3 ± 5.3 s in WT *vs* 49.2 ± 6.5 s in *Olig2* cKO, $P = 0.025$). These results suggest that deleting *Olig2* in oligodendroglia leads to anxiety-like behaviors at the young adult stage.

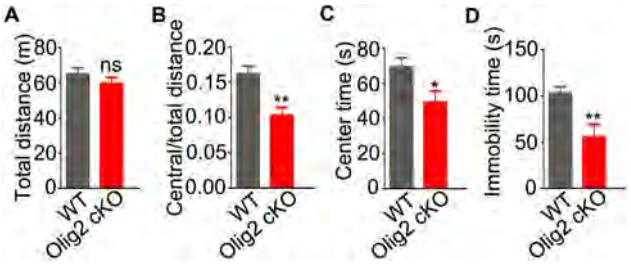

Fig. 3 Anxiety-like behavior and stress response in young adult *Olig2* cKO and WT mice. **A–C** Locomotor activity of WT (n = 12) and *Olig2* cKO (n = 12) mice in the open field test: total distance (**A**), ratio of central to total distance (**B**), and center time (**C**). **D** Immobility time in the forced swim test in WT (n = 15) and *Olig2* cKO (n = 11) mice. Data are expressed as the mean ± SEM; $^{*}P < 0.05$; $^{**}P < 0.01$; ns, no significant difference.

Stress sensitization may be critical in the development or relapse of schizophrenia [32]. The forced swimming test is a well-established paradigm to assess the stress-coping strategy in rodents [33]. In this test, young adult *Olig2* cKO mice spent less time immobile than WT littermates (Fig. 3D; 102.9 ± 6.8 s in WT *vs* 55.6 ± 13.4 s in *Olig2* cKO, P = 0.002), suggesting that deleting *Olig2* in oligodendroglia leads to an aberrant response to acute stress in the young adult.

Behaviors of Young Adult *Olig2* cKO Mice are Analogous to Cognitive Deficits

Cognitive impairment in schizophrenia includes problems in the speed of information processing, attention, learning, and memory [34]. PPI is the most common method to quantify information-processing deficits in schizophrenia with predictive and construct validity [35]. In the present study, we used the PPI test to directly assess the influence of hypomyelination on attention and information processing. First, no significant difference but only a decreasing trend was found in the acoustic startle response between WT and *Olig2* cKO mice (Fig. 4A; 358.0 ± 48.9 in WT *vs* 248.4 ± 45.4 in *Olig2* cKO, P = 0.112). Moreover, to our surprise, *Olig2* cKO mice had lower PPI values than WT littermates (Fig. 4B; 44.0% ± 3.8% in WT *vs* 28.8% ± 5.1% in *Olig2* cKO, P = 0.032), which demonstrated information-processing deficits in young adult *Olig2* cKO mice.

Besides, the NORT is a relatively low-stress, efficient screening method for recognition memory in rodents, and is appropriate for the detection of neuropsychological changes following genetic manipulations [36]. In this test, *Olig2* cKO mice had a lower novel object recognition index than WT littermates (Fig. 4C; 0.56 ± 0.04 in WT *vs* 0.42 ± 0.03 in *Olig2* cKO, P = 0.014), suggesting a non-spatial memory deficit in the *Olig2* cKO mice. Thus, these results demonstrated schizophrenia-like cognitive deficits in young adult *Olig2* cKO mice.

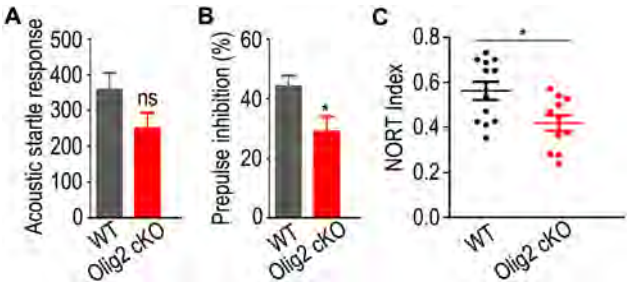

Fig. 4 Analyses of cognitive behaviors in young adult *Olig2* cKO and WT mice. **A, B** PPI test in young adult (P56) WT (n = 13) and *Olig2* KO (n = 17) mice. **A** Acoustic startle response; **B** PPI of acoustic startle response. **C** Novel object recognition test in WT (n = 12) and *Olig2* KO (n = 11) mice. Data are expressed as the mean ± SEM. $^{*}P < 0.05$; ns, no significant difference.

Loss of Olig2 in Oligodendroglial Cells Increases the Susceptibility to Social Withdrawal after Adolescent Isolation

Recent clinical studies have clearly demonstrated social cognitive deficits in patients with schizophrenia [37]. The social interaction test is widely used to analyze sociability in mice [38]. In the present study, young adult *Olig2* cKO mice had numbers of social contacts (Fig. 5A; 12.9 ± 1.3 in WT *vs* 13.6 ± 1.3 in *Olig2* cKO, P = 0.719), durations of approaching stranger mice (Fig. 5B; 82.1 ± 6.2 s in WT *vs* 86.6 ± 6.9 s in *Olig2* cKO, P = 0.635), and durations of contact with stranger mice (Fig. 5C; 65.1 ± 6.3 s in WT *vs* 86.5 ± 10.4 s in *Olig2* cKO, P = 0.077) similar to WT littermates. These results suggest intact sociability in young adult *Olig2* cKO mice.

Social deprivation, which can induce mild neurocognitive impairment, impulsivity, and attentional and social deficits [39], is regarded as an environmental risk factor for schizophrenia. In the present study, social isolation was applied to WT and *Olig2* cKO mice from P35 to P70 to test whether OL and myelin deficits affect vulnerability to environmental stress. To our surprise, both the genetic manipulation of *Olig2* (F = 10.91, P = 0.002) and the duration of isolation (F = 5.16, P = 0.010) had significant effects on sociability (Fig. 5D), while no significant interaction of these two factors was found (F = 1.31, P = 0.280). Interestingly, *Olig2* cKO mice were significantly more susceptible to social withdrawal than WT littermates after 5 weeks of isolation (Fig. 5D). These results suggest that ablating *Olig2* in oligodendroglial cells may increase the risk of social withdrawal when under environmental stress during adolescence.

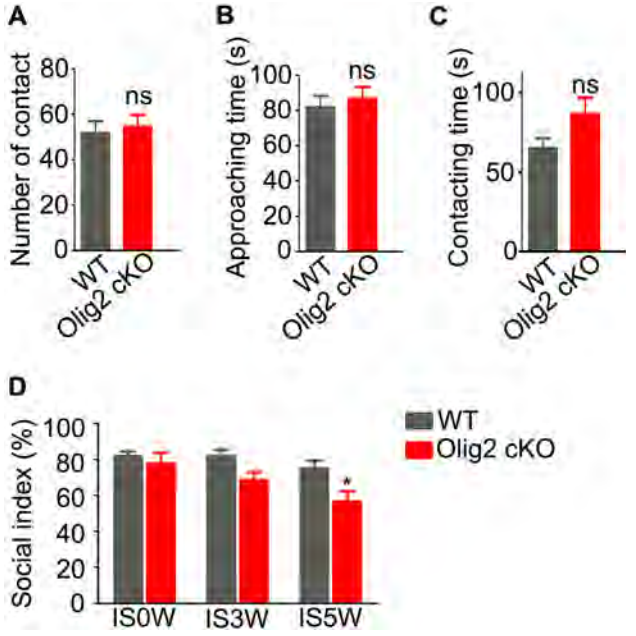

Fig. 5 Sociability of young adult *Olig2* cKO and WT mice in social interaction test. **A** Number of contacts; **B** duration of approaches to stranger mouse; **C** duration of contact in WT and *Olig2* cKO mice. **D** Sociability of *Olig2* cKO mice (n = 6–8) and WT littermates (n = 10–12) after 0, 3, and 5 weeks of social isolation. There were significant effects of genotype (F = 10.91, P = 0.002) and isolation duration (F = 5.16, P = 0.010), but not genotype–isolation interaction (F = 1.31, P = 0.280). Data are expressed as the mean ± SEM. ns, no significant difference. *$P < 0.05$ *vs* WT mice.

Discussion

In this study, we used a mouse model with *de novo* OL and myelin deficits by specific knockout of *Olig2* in oligodendroglial cells. We examined mouse behaviors, especially cognitive-related phenotypes in young adults. Similar to our previously reported phenotypes of juvenile mice, young adult *Olig2* cKO mice showed anxiety-like behaviors. Moreover, we clearly demonstrated cognitive deficits in *Olig2* cKO mice. Strikingly, even though loss of *Olig2* in OLs did not impair sociability, it significantly increased the vulnerability to social withdrawal under the mild stress of social isolation. These results demonstrated that developmental deficits in OL and myelin led to cognitive impairments and increased vulnerability to social withdrawal, providing new evidence that OL and myelin deficiency may be involved in brain dysfunction of psychiatric disorders.

In recent years, increasing numbers of risk genes have been identified by genome-wide association studies and rare mutation findings [40, 41]. Some risk genes, such as *Olig2*, have been recognized to play important roles in OL development and myelination [42]. Notably, two schizophrenia-related single-nucleotide polymorphisms in the *Olig2* gene have been associated with the downregulation of Olig2 in the PFC of schizophrenic patients [43, 44], implying that loss-of-function of *Olig2* increases the risk of psychiatric disorders by interfering with oligodendroglial development. In this study, we used a mouse model in which conditionally deleting *Olig2* in oligodendroglial cells mimicked the genetic deficiency of *Olig2*. Following our previous study [24], we further confirmed that impaired myelin development caused by *Olig2* deletion in oligodendroglial cells lasts throughout adolescence (Fig. 1), and this results in severe hypomyelination in the ACC of young adult mice (Fig. 2). Our finding is consistent with previous studies showing a high capacity of myelination in PFC to be regulated by neuronal activity and social interactions [45–47]. It is known that myelin plasticity, which is produced by mature OLs, occurs from early childhood to adulthood [48]. Mice at P56 may be roughly equivalent to human beings 16 years of age [49], which has been recognized as a key stage of transition from adolescence into young adulthood. Therefore, *Olig2* cKO mice provide an ideal model in which to address the impact of *de novo* OL and myelin developmental deficits on brain function.

In our previous study, juvenile *Olig2* cKO mice exhibited an anxious phenotype and deficits in behavioral inhibition [24]. Unfortunately, cognitive function was not addressed in the study, as the juvenile age (P21) is not suitable for the behavioral training process and cognitive testing in mice. In the present study, we found that young adult *Olig2* cKO mice showed an anxious phenotype and an aberrant response to acute stress (Fig. 3), which further extended our understanding of the effect of OL and myelin deficits on adolescent emotions and actions. More importantly, young adult *Olig2* cKO mice exhibited cognitive dysfunctions, such as deficits in information processing and non-spatial memory (Fig. 4), both of which are core features of psychiatric disorders [34]. To our knowledge, this is the first study to uncover the influence of *de novo* developmental deficits in OL and myelin on higher brain function from the viewpoint of neural development, even though altered myelin structure caused by genetic alterations and chemical toxicants has already been shown to induce brain dysfunction in adults and at older ages [50, 51]. These results may, at least in part, explain why environmental risk factors such as oxidative stress, which suppress OL and myelin development, may increase the risk of psychiatric diseases [52].

Moreover, a recent animal study showed that early social isolation during adolescence results in behavioral

and cognitive dysfunctions which are correlated with myelin alterations in the PFC [46, 53, 54]. Specifically, the influence of social isolation on mouse behaviors occurs at a key period ranging from P21 to P35 [46]. In the present study, we isolated WT and *Olig2* cKO mice from P35 to P70, beyond the previously-reported key period. Importantly, *Olig2* cKO mice were more vulnerable to social withdrawal under the mild stress of social isolation during adolescence (Fig. 5). Together with other studies which demonstrated that social isolation significantly enhances the disruption of PPI in mice [55], these findings support the notion that genetic alterations underlying OL and myelin deficiency increase the vulnerability to psychiatric disorders.

Notably, the ablation of Olig2 in OLs was under the control of the *Cnp* promoter, which is not brain-region specific. As shown in Fig. 1, the ACC was not the only region with hypomyelination, so abnormal behaviors and cognitive deficits could also result from OL and myelin deficits in other brain regions. Future studies are needed to explore whether and how impaired OL and myelin development in specific regions, such as the PFC, affects brain function and contributes to the white matter etiology in psychiatric disorders. Moreover, a recent study showed that the OL myelination process is highly plastic, and this could finely remold and regulate circuit function according to neuron functional demand [7]. Since myelin plasticity is consistently required for higher brain functions in adults [56], we assumed that the hypomyelination caused by Olig2 ablation would also lead to abnormal behaviors in the adult. Besides, developmental deficits in OL and myelin cause a loss of synapses and aberrant synaptic function in adults [19], further providing several possible mechanisms by which OL and myelin deficits lead to behavioral consequences.

In conclusion, even though further investigations are needed to address the mechanisms by which developmental OL and myelin deficits affect the neural circuits responsible for the behavioral abnormalities, our results provide direct evidence for a role of impaired OL development and myelination in brain functions from the viewpoint of neural development, as well as vulnerability to social withdrawal. Our results further strengthen the hypothesis that OL and myelin deficits are involved in the pathogenesis of psychiatric disorders rather than simply accompaniments to pathological abnormalities.

Acknowledgements This work was supported by the National Natural Science Foundation of China (31671117).

Conflict of interest The authors declare that they have no competing interests.

References

1. Pajevic S, Basser PJ, Fields RD. Role of myelin plasticity in oscillations and synchrony of neuronal activity. Neuroscience 2014, 276: 135–147.
2. Xiao L, Ohayon D, McKenzie IA, Sinclair-Wilson A, Wright JL, Fudge AD, *et al.* Rapid production of new oligodendrocytes is required in the earliest stages of motor-skill learning. Nat Neurosci 2016, 19: 1210–1217.
3. Fuster JM. Frontal lobe and cognitive development. J Neurocytol 2002, 31: 373–385.
4. Lee FS, Heimer H, Giedd JN, Lein ES, Sestan N, Weinberger DR, *et al.* Mental health. Adolescent mental health–opportunity and obligation. Science 2014, 346: 547–549.
5. Miller DJ, Duka T, Stimpson CD, Schapiro SJ, Baze WB, McArthur MJ, *et al.* Prolonged myelination in human neocortical evolution. Proc Natl Acad Sci U S A 2012, 109: 16480–16485.
6. Casey BJ, Getz S, Galvan A. The adolescent brain. Dev Rev 2008, 28: 62–77.
7. de Hoz L, Simons M. The emerging functions of oligodendrocytes in regulating neuronal network behaviour. Bioessays 2015, 37: 60–69.
8. Haroutunian V, Katsel P, Roussos P, Davis KL, Altshuler LL, Bartzokis G. Myelination, oligodendrocytes, and serious mental illness. Glia 2014, 62: 1856–1877.
9. Liu X, Lai Y, Wang X, Hao C, Chen L, Zhou Z, *et al.* A combined DTI and structural MRI study in medicated-naive chronic schizophrenia. Magn Reson Imaging 2014, 32: 1–8.
10. Friedman JI, Tang C, Carpenter D, Buchsbaum M, Schmeidler J, Flanagan L, *et al.* Diffusion tensor imaging findings in first-episode and chronic schizophrenia patients. Am J Psychiatry 2008, 165: 1024–1032.
11. Mauney SA, Pietersen CY, Sonntag KC, Woo TW. Differentiation of oligodendrocyte precursors is impaired in the prefrontal cortex in schizophrenia. Schizophr Res 2015, 169: 374–380.
12. Radu A, Hristescu G, Katsel P, Haroutunian V, Davis KL. Microarray database mining and cell differentiation defects in schizophrenia. Adv Exp Med Biol 2011, 696: 67–74.
13. Hyde TM, Ziegler JC, Weinberger DR. Psychiatric disturbances in metachromatic leukodystrophy. Insights into the neurobiology of psychosis. Arch Neurol 1992, 49: 401–406.
14. Feinstein A, Magalhaes S, Richard JF, Audet B, Moore C. The link between multiple sclerosis and depression. Nat Rev Neurol 2014, 10: 507–517.
15. Millan MJ, Agid Y, Brune M, Bullmore ET, Carter CS, Clayton NS, *et al.* Cognitive dysfunction in psychiatric disorders: characteristics, causes and the quest for improved therapy. Nat Rev Drug Discov 2012, 11: 141–168.
16. Muetzel RL, Mous SE, van der Ende J, Blanken LM, van der Lugt A, Jaddoe VW, *et al.* White matter integrity and cognitive performance in school-age children: A population-based neuroimaging study. Neuroimage 2015, 119: 119–128.
17. Perez-Iglesias R, Tordesillas-Gutierrez D, McGuire PK, Barker GJ, Roiz-Santianez R, Mata I, *et al.* White matter integrity and cognitive impairment in first-episode psychosis. Am J Psychiatry 2010, 167: 451–458.
18. Falkai P, Steiner J, Malchow B, Shariati J, Knaus A, Bernstein HG, *et al.* Oligodendrocyte and interneuron density in hippocampal subfields in schizophrenia and association of oligodendrocyte number with cognitive deficits. Front Cell Neurosci 2016, 10: 78.
19. Wang F, Yang YJ, Yang N, Chen XJ, Huang NX, Zhang J, *et al.* Enhancing oligodendrocyte myelination rescues synaptic loss and improves functional recovery after chronic hypoxia. Neuron 2018, 99: 689–701 e685.

20. Moghaddam B, Javitt D. From revolution to evolution: the glutamate hypothesis of schizophrenia and its implication for treatment. Neuropsychopharmacology 2012, 37: 4–15.
21. Kantrowitz JT, Javitt DC. N-methyl-d-aspartate (NMDA) receptor dysfunction or dysregulation: the final common pathway on the road to schizophrenia? Brain Res Bull 2010, 83: 108–121.
22. Lappe-Siefke C, Goebbels S, Gravel M, Nicksch E, Lee J, Braun PE, *et al.* Disruption of Cnp1 uncouples oligodendroglial functions in axonal support and myelination. Nat Genet 2003, 33: 366–374.
23. Yue T, Xian K, Hurlock E, Xin M, Kernie SG, Parada LF, *et al.* A critical role for dorsal progenitors in cortical myelination. J Neurosci 2006, 26: 1275–1280.
24. Chen X, Zhang W, Li T, Guo Y, Tian Y, Wang F, *et al.* Impairment of oligodendroglia maturation leads to aberrantly increased cortical glutamate and anxiety-like behaviors in juvenile mice. Front Cell Neurosci 2015, 9: 467.
25. Chen X, Ku L, Mei R, Liu G, Xu C, Wen Z, *et al.* Novel schizophrenia risk factor pathways regulate FEZ1 to advance oligodendroglia development. Transl Psychiatry 2017, 7: 1293.
26. Xu P, Xu H, Tang X, Xu L, Wang Y, Guo L, *et al.* Liver X receptor beta is essential for the differentiation of radial glial cells to oligodendrocytes in the dorsal cortex. Mol Psychiatry 2014, 19: 947–957.
27. Clapcote SJ, Lipina TV, Millar JK, Mackie S, Christie S, Ogawa F, *et al.* Behavioral phenotypes of Disc1 missense mutations in mice. Neuron 2007, 54: 387–402.
28. Yu Y, Chen Y, Kim B, Wang H, Zhao C, He X, *et al.* Olig2 targets chromatin remodelers to enhancers to initiate oligodendrocyte differentiation. Cell 2013, 152: 248–261.
29. Hardy RJ, Friedrich VL, Jr. Progressive remodeling of the oligodendrocyte process arbor during myelinogenesis. Dev Neurosci 1996, 18: 243–254.
30. Jahn O, Tenzer S, Werner HB. Myelin proteomics: molecular anatomy of an insulating sheath. Mol Neurobiol 2009, 40: 55–72.
31. Bourin M, Petit-Demouliere B, Dhonnchadha BN, Hascoet M. Animal models of anxiety in mice. Fundam Clin Pharmacol 2007, 21: 567–574.
32. Yuii K, Suzuki M, Kurachi M. Stress sensitization in schizophrenia. Ann N Y Acad Sci 2007, 1113: 276–290.
33. Commons KG, Cholanians AB, Babb JA, Ehlinger DG. The rodent forced swim test measures stress-coping strategy, not depression-like behavior. ACS Chem Neurosci 2017, 8: 955–960.
34. Green MF. Cognitive impairment and functional outcome in schizophrenia and bipolar disorder. J Clin Psychiatry 2006, 67 Suppl 9: 3–8; discussion 36–42.
35. Geyer MA, Ellenbroek B. Animal behavior models of the mechanisms underlying antipsychotic atypicality. Prog Neuropsychopharmacol Biol Psychiatry 2003, 27: 1071–1079.
36. Lueptow LM. Novel object recognition test for the investigation of learning and memory in mice. J Vis Exp 2017.
37. Green MF, Horan WP, Lee J. Social cognition in schizophrenia. Nat Rev Neurosci 2015, 16: 620–631.
38. Moy SS, Nadler JJ, Perez A, Barbaro RP, Johns JM, Magnuson TR, *et al.* Sociability and preference for social novelty in five inbred strains: an approach to assess autistic-like behavior in mice. Genes Brain Behav 2004, 3: 287–302.
39. Chugani HT, Behen ME, Muzik O, Juhasz C, Nagy F, Chugani DC. Local brain functional activity following early deprivation: a study of postinstitutionalized Romanian orphans. Neuroimage 2001, 14: 1290–1301.
40. Schizophrenia Working Group of the Psychiatric Genomics Consortium. Biological insights from 108 schizophrenia-associated genetic loci. Nature 2014, 511: 421–427.
41. Purcell SM, Moran JL, Fromer M, Ruderfer D, Solovieff N, Roussos P, *et al.* A polygenic burden of rare disruptive mutations in schizophrenia. Nature 2014, 506: 185–190.
42. Goudriaan A, de Leeuw C, Ripke S, Hultman CM, Sklar P, Sullivan PF, *et al.* Specific glial functions contribute to schizophrenia susceptibility. Schizophr Bull 2014, 40: 925–935.
43. Georgieva L, Moskvina V, Peirce T, Norton N, Bray NJ, Jones L, *et al.* Convergent evidence that oligodendrocyte lineage transcription factor 2 (OLIG2) and interacting genes influence susceptibility to schizophrenia. Proc Natl Acad Sci U S A 2006, 103: 12469–12474.
44. Mitkus SN, Hyde TM, Vakkalanka R, Kolachana B, Weinberger DR, Kleinman JE, *et al.* Expression of oligodendrocyte-associated genes in dorsolateral prefrontal cortex of patients with schizophrenia. Schizophr Res 2008, 98: 129–138.
45. Gibson EM, Purger D, Mount CW, Goldstein AK, Lin GL, Wood LS, *et al.* Neuronal activity promotes oligodendrogenesis and adaptive myelination in the mammalian brain. Science 2014, 344: 1252304.
46. Makinodan M, Rosen KM, Ito S, Corfas G. A critical period for social experience-dependent oligodendrocyte maturation and myelination. Science 2012, 337: 1357–1360.
47. Tomassy GS, Berger DR, Chen HH, Kasthuri N, Hayworth KJ, Vercelli A, *et al.* Distinct profiles of myelin distribution along single axons of pyramidal neurons in the neocortex. Science 2014, 344: 319–324.
48. Rivers LE, Young KM, Rizzi M, Jamen F, Psachoulia K, Wade A, *et al.* PDGFRA/NG2 glia generate myelinating oligodendrocytes and piriform projection neurons in adult mice. Nat Neurosci 2008, 11: 1392–1401.
49. Flurkey K, Currer JM. Pitfalls of animal model systems in ageing research. Best Pract Res Clin Endocrinol Metab 2004, 18: 407–421.
50. Poggi G, Boretius S, Mobius W, Moschny N, Baudewig J, Ruhwedel T, *et al.* Cortical network dysfunction caused by a subtle defect of myelination. Glia 2016, 64: 2025–2040.
51. Wang H, Li C, Mei F, Liu Z, Shen HY, Xiao L. Cuprizone-induced demyelination in mice: age-related vulnerability and exploratory behavior deficit. Neurosci Bull 2013, 29: 251–259.
52. Maas DA, Valles A, Martens GJM. Oxidative stress, prefrontal cortex hypomyelination and cognitive symptoms in schizophrenia. Transl Psychiatry 2017, 7: e1171.
53. Liu J, Dietz K, DeLoyht JM, Pedre X, Kelkar D, Kaur J, *et al.* Impaired adult myelination in the prefrontal cortex of socially isolated mice. Nat Neurosci 2012, 15: 1621–1623.
54. Zhou Y, Fan L, Qiu C, Jiang T. Prefrontal cortex and the dysconnectivity hypothesis of schizophrenia. Neurosci Bull 2015, 31: 207–219.
55. Dai H, Okuda H, Iwabuchi K, Sakurai E, Chen Z, Kato M, *et al.* Social isolation stress significantly enhanced the disruption of prepulse inhibition in mice repeatedly treated with methamphetamine. Ann N Y Acad Sci 2004, 1025: 257–266.
56. McKenzie IA, Ohayon D, Li H, de Faria JP, Emery B, Tohyama K, *et al.* Motor skill learning requires active central myelination. Science 2014, 346: 318–322.

Neurosci. Bull. April, 2020, 36(4):427–431
https://doi.org/10.1007/s12264-019-00454-w

www.neurosci.cn
www.springer.com/12264

LETTER TO THE EDITOR

Topological Shape Changes Weaken the Innate Defensive Response to Visual Threat in Mice

Yan Huang[1,2] · Lei Li[1,2] · Kun Dong[1,2] · Hongsi Tang[1,2] · Qingning Yang[1,2] · Xianglian Jia[1,2] · Yundan Liao[1,2] · Wenbo Wang[3] · Zhen Ren[1,2] · Lin Chen[3] · Liping Wang[1,2]

Received: 3 September 2019 / Accepted: 24 October 2019 / Published online: 7 December 2019

Dear Editor,

Understanding the primitives of visual perception is a fundamental question in the study of vision. To address this question, a theory of topology-based functional hierarchy in visual perception has been proposed [1, 2]. This theory suggests that the extraction of topological properties (TPs) serves as the starting point of object perception. The TP of a figure is the holistic identity which remains constant across various smooth shape-changing transformations of an image [2]. For example, the shape of a rubber sheet can be changed through bending and twisting without changing its TP as long as the sheet does not tear. The number of holes in a geometrical object is a TP because it is retained during such rubber-sheet deformations. Thus the TP of an object is thought to be a basic attribute that is crucial for the stability of perception from variable visual input and is processed with priority during visual perception [2]. The "early topological perception" hypothesis was first demonstrated by a finding showing that the visual system is more sensitive to topological differences than non-topological differences [1, 2]; this hypothesis has been widely tested in the past decades and is backed substantially by evidence from human infants and adults [3–5], other mammals [6], and even insects [7]. However, it is unclear how the TP is rapidly processed. Previous human fMRI data showed that the inferior temporal cortex, which is associated with the late stages of visual processing, is involved in the processing of topological recognition [8, 9]. These neuroimaging results seem to contradict behavioral evidence supporting the early topological perception hypothesis. To address this contradiction, we hypothesized that topological perception is processed in a fast subcortical visual pathway that stems from the superior colliculus (SC).

We used mice to test the subcortical hypothesis. If topological perception is relatively conserved across species, topological perception in animals may be innate and be processed through a conserved subcortical pathway. Here, we present behavioral evidence for innate topological perception and c-fos activation evidence in the SC for subcortical processing of the TP in mice.

A looming visual stimulus is usually presented as an expanding black disk, to mimic the shadow of an approaching aerial predator, and has been extensively adopted to study the innate defensive behaviors of animals and humans [10, 11]. When mice are presented with an upper field looming stimulus, they demonstrate conserved flight-to-nest behavior. The read-out parameters for defensive behavior induced by looming include (i) flight latency: the time from the onset of a looming stimulus to the onset of escape to the nest, (ii) time to the nest: the time taken to

Electronic supplementary material The online version of this article (https://doi.org/10.1007/s12264-019-00454-w) contains supplementary material, which is available to authorized users.

Yan Huang and Lei Li have contributed equally to this work.

✉ Yan Huang
yan.huang@siat.ac.cn

✉ Liping Wang
lp.wang@siat.ac.cn

[1] The Brain Cognition and Brain Disease Institute (BCBDI), Shenzhen Institutes of Advanced Technology, Chinese Academy of Sciences; Shenzhen-Hong Kong Institute of Brain Science-Shenzhen Fundamental Research Institutions, Guangdong Key Lab of Brain Connectomics, Shenzhen 518055, China

[2] University of Chinese Academy of Sciences, Beijing, China

[3] State Key Laboratory of Brain and Cognitive Science, Institute of Biophysics, CAS, University of the CAS, Beijing 100101, China

escape to the nest, and (iii) time in the nest: the time that a mouse spends in the nest after exposure to a stimulus. As reported in previous studies of mice [12], the flight latency to a looming stimulus is an important and sensitive index reflecting the magnitude of the defensive response to an incoming threat. In the looming paradigm of the present study, a topological shape change was inserted briefly into the continuous looming stimulus, to investigate the processing of the TP and the impact of topological shape change on the innate defensive behavior of mice.

The study was approved by the Ethics Committees at the Shenzhen Institutes of Advanced Technology, Chinese Academy of Sciences. Eighty adult (6–8 weeks old) male C57BL/6J mice were used in the behavioral experiments. Mice were placed in a closed Plexiglas box with a dark sheltered nest in one of the corners (Fig. 1A). The looming stimulus was presented on an LCD monitor in the ceiling. Four types of looming stimulus were presented (Fig. 1B): normal looming (no-change, Disk), topologically-changing looming (TP-change, Ring), and two non-topologically-changing looming (non-TP-change, Square and S). The Disk, Square, and S stimuli had the same TP (no hole), so the shape transformations between them were non-TP changes. The Ring stimulus (one hole) was topologically different from the other three, hence a TP-change looming. The S-like figure was specially designed to control the figure area and other potential confounding factors (spatial frequency and perimeter length). Therefore, the main difference between the S (and the Square) and the TP-change (Ring) stimulus was the hole in the ring, i.e., the topological property. The normal looming stimulus was a black disk expanding from 2° to 30° during a 300-ms cycle that was repeated 15 times. The TP-change looming stimulus was almost the same except that during each cycle, an 80-ms topologically different figure—a black ring—was inserted to replace the disk 100 ms after stimulus onset. Similarly, in the non-TP-change looming, a square or an S-like figure was introduced after the expanding disk had been shown for 100 ms and lasted for 80 ms before transforming back to the disk shape. The parameters flight latency, time to nest, and time in nest, were analyzed separately using one-way ANOVAs with stimulus type as the factor (for detailed materials and methods, please refer to the Supplementary Material). We found that flight latency showed a significant main effect ($F(3,168) = 2.921$, $P = 0.035$). Specifically, the average flight latency (Fig. 1C) was higher for the TP-change looming than the other conditions (all $t > 2.22$, $P < 0.05$), while the two non-TP-change looming stimuli had no significant impact on the flight latency compared to normal looming (both $t < 0.49$, $P > 0.6$). Time to nest and time in the nest showed no significant difference between these conditions (both $F(3,168) < 0.894$, $P > 0.445$). These results suggested that the defensive response of mice was weakened by the TP change but was not affected by non-TP shape changes in the looming stimuli.

Previously published evidence shows that the SC is involved in the defensive response [13] and the early stage of topological processing [14]. The effects of a TP change on defensive response may first occur in the SC, so we tested whether c-fos activation in the different layers of the SC decreased for topologically-changing looming stimuli. Mice were exposed to either a no-change or the TP-change looming stimulus. C-fos-positive cells within the SC were manually counted by an individual experimenter blind to the experimental groups. The number of c-fos-positive cells (18 sections for no-change conditions, 12 for the TP-change condition) was submitted to two-way ANOVA with topological change and SC layer as the factors. We found significant main effects for both topological change and SC layer (both $F > 8.298$, $P < 0.001$), and no significant interaction ($F(3,112) = 1.012$, $P = 0.390$). Further t-tests showed a significant decrease in neuron activation in all layers of the SC for the TP-change looming compared to the normal looming stimuli (Fig. 1D–E, all $t > 2.4$, $P < 0.02$). This result indicated that activation of the entire SC was reduced by the topological change, which is in agreement with the weakened defensive response for the TP-change looming stimulus during the behavioral experiment.

It seems plausible that topological change-detection itself takes place in the SC, because a topological change can affect the defensive response to looming stimuli and also affect neuronal activation in the SC. To test this hypothesis, we used constant-sized stimuli, instead of looming stimuli that grow rapidly in time and are associated with danger. Two types of stimuli were used (Fig. 2A). The TP-change stimulus was a transformation back and forth between a disk and an area-matched ring, and the non-TP-change was between a disk and an area-matched square. We found a significant decrease in neuron activation in all SC layers in mice exposed to the TP-change stimulus (26 sections) compared with mice exposed to the non-TP-change stimulus (22 sections, see Fig. 2, all $t > 2.86$, $P < 0.006$). These results suggest that the SC is involved in the detection of topological differences.

Although the theory of early topological perception has been discussed for decades to address the question of the primitives of vision [1]. the processing pathway of topological perception remains unclear. The subcortical hypothesis of early topological perception posits that the TP is processed through a fast subcortical pathway that stems from the SC and ends at the inferior temporal cortex instead of being processed through the classical slow cortical visual pathway [15–17]. Our previous work [14] provided human-brain imaging evidence for this

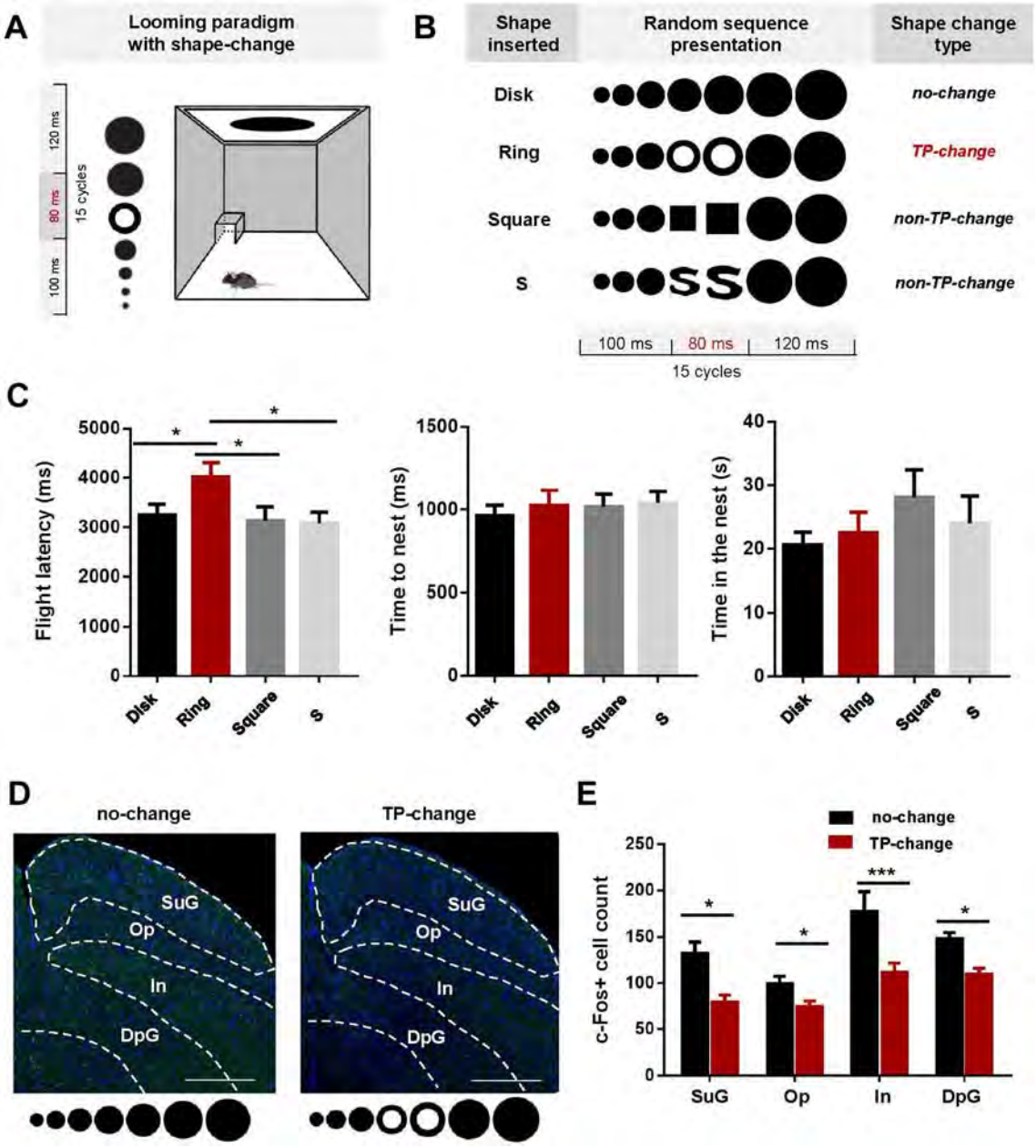

Fig. 1 Topological changes increase flight latency and decrease neuron activation in the SC of mice. **A** Schematic of the looming testing environment. **B** The four visual stimuli. **C** Flight latency, time to nest, and time in nest in response to the four stimuli (80 mice). **D**, **E** Representative immunohistochemistry and quantification showing less c-fos immunoreactivity after TP-change looming stimuli (12 sections) than normal looming stimuli (18 sections) in all layers of the SC (scale bars in (**D**), 500 μm). Graphs show the mean ± SEM; $*P < 0.05$, $***P < 0.001$, Student's *t*-test with Holm-Sidak's correction.

subcortical hypothesis, demonstrating that the TP of an unconscious visual stimulus is processed in the SC and the pulvinar rather than in the lateral geniculate nucleus and the primary visual cortex. In the current study, there were two fundamental questions: (1) whether topological detection in rodents is an innate ability, and (2) whether topological detection occurs at the subcortical level. We used a visual-induced defensive paradigm to test the effect of a topological change inserted into a threatening looming stimulus and compared the results with those using a non-topological change insertion. We found that a topological change in a looming stimulus significantly decreased the magnitude of defensive responses. Our results suggest that topological perception is innate and capable of modifying a well-conserved defensive behavior in mice. This finding provides more evidence supporting the conclusion that topological perception is conserved across species [6, 7]. Furthermore, looming-evoked defensive responses are

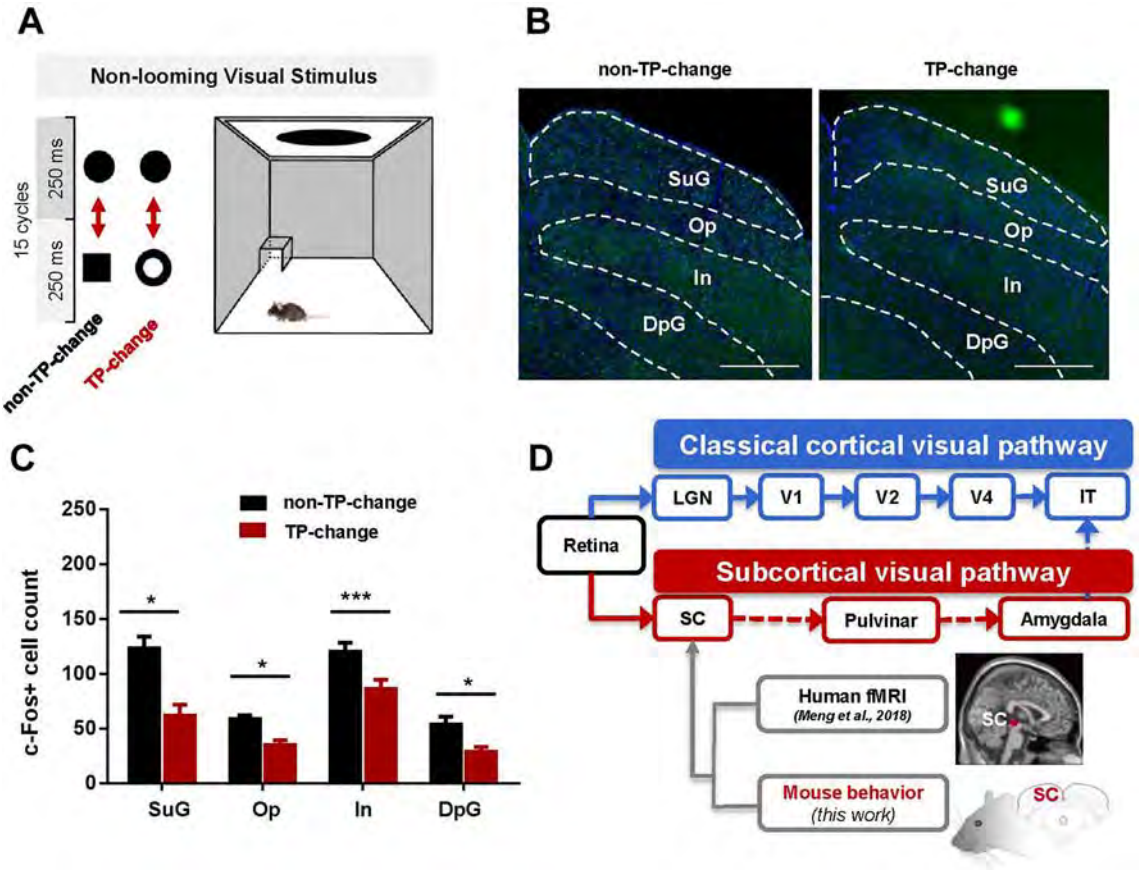

Fig. 2 Continuous non-looming topological changes decrease neuron activation in the SC. **A** Schematic of the non-topologically changing stimulus and the topologically changing stimulus. Note that these two visual stimuli were unlikely to be perceived as threatening and therefore did not trigger a defensive response in mice. **B**, **C** Representative immunohistochemistry and quantification showing that mice had lower c-fos immunoreactivity in all SC layers following the topologically-changing stimulus (26 sections) than the non-topologically changing stimulus (22 sections) (scale bar in (**B**), 500 μm; graphs in (**C**) show the mean ± SEM; $*P < 0.05$, $***P < 0.001$, Student's *t*-tests with Holm-Sidak's corrections). **D** Schematic of the subcortical hypothesis of topological processing and supporting evidence from human-brain imaging [14] and innate mouse behavior.

relatively conserved across rodents [11], monkeys [18] and humans [10]. It is intriguing that perception of a topological change affects a biological function and modulates innate defensive behavior. A possible explanation is that a topological change inserted into a looming stimulus impairs object continuity and reduces the dangerousness of visual stimulation, thus weakening the defensive response in mice.

A topological change in a looming stimulus not only weakened the behavioral defensive responses but also reduced c-fos activation in the SC, which has been reported to be a key nucleus in the subcortical pathway responsible for looming-evoked defensive behaviors. Furthermore, we found that topological changes in non-threatening visual stimuli also modulated activation of the SC in mice even when they were presented with non-alerting visual signals. It is widely accepted that the superficial layer of the SC is associated with visual information-processing and is responsible for the detection of visual motion, and deeper layers are involved in saccades and orienting responses [19]. Our present c-fos activation measurements showed that all the SC layers were less active when mice were exposed to the topologically-changing stimulus than when exposed to non-topologically-changing stimuli in both the looming and non-looming paradigms. Further studies deciphering the detailed mechanism of signal processing by/between different layers of the SC in response to looming stimuli may help to answer questions such as which layers of the SC are first responsible for the modulation of a topological change in looming-evoked behavior.

The present study provides, for the first time, behavioral evidence for innate topological perception in rodents and its influence on conserved defensive behavior. And the c-fos results provide further evidence for subcortical processing of the TP and imply a critical function of subcortical processing of the TP in visual perception. Dissecting the subcortical pathways for topological

perception provides access to the mechanisms underlying the fast processing of the basic visual primitives and also sheds light on the mechanism of interaction between visual perception and innate defensive responses. Furthermore, several brain diseases, such as schizophrenia and autism, have been reported to be associated with dysfunction of subcortical pathways [20]. Future work with varying stimulus parameters such as size, time of change, and speed may help us understand how the SC processes topological perception.

Acknowledgements The work was supported by the Shenzhen Science and Technology Research Funding Program, China (JCYJ20170818161400180 and JCYJ20180508152336419), the National Natural Science Foundation of China (81425010, 31630031, and 31971072), and the Key Laboratory of Brain Connectome of Guangdong Province, China (2017B030301017).

Conflict of interest The authors declare no competing financial interests.

References

1. Chen L. Topological structure in visual perception. Science 1982, 218: 699–700.
2. Chen L. The topological approach to perceptual organization. Vis Cogn 2005, 12: 553–637.
3. Huang Y, Zhou T, Chen L. The precedence of topological change over top-down attention in masked priming. J Vis 2011, 11: 9.
4. Huang Y, He L, Wang W, Meng Q, Zhou T, Chen L. What determines the object-level visual masking: The bottom-up role of topological change. J Vis 2018, 18: 3.
5. Lin YL, Chien SHL, Hu S. An early sensitivity for detecting differences in visual topological property in 0-to 4- day-old human neonates. Pediatric Dimensions 2016, 1: 29–33.
6. Zhu J, Guo XY, Ma Y, Ren F. Different topological properties pattern recognition in mice. Prog Biochem Biophys 2010, 37: 613–617.
7. Chen L, Zhang S, Srinivasan MV. Global perception in small brains: Topological pattern recognition in honey bees. Proc Natl Acad Sci U S A 2003, 100: 6884–6889.
8. Zhou K, Luo H, Zhou T, Zhuo Y, Chen L. Topological change disturbs object continuity in attentive tracking. Proc Natl Acad Sci U S A 2010, 107: 21920–21924.
9. Zhuo Y, Zhou TG, Rao HY, Wang JJ, Meng M, Chen M, *et al.* Contributions of the visual ventral pathway to long-range apparent motion. Science 2003, 299: 417–420.
10. King SM, Dykeman C, Redgrave P, Dean P. Use of a distracting task to obtain defensive head movements to looming visual stimuli by human adults in a laboratory setting. Perception 1992, 21: 245–259.
11. Wallace DJ, Greenberg DS, Sawinski J, Rulla S, Notaro G, Kerr JND. Rats maintain an overhead binocular field at the expense of constant fusion. Nature 2013, 498: 65–69.
12. Li L, Feng X, Zhou Z, Zhang H, Shi Q, Lei Z, *et al.* Stress accelerates defensive responses to looming in mice and involves a locus coeruleus-superior colliculus projection. Curr Biol 2018, 28: 859–871.
13. Shang C, Liu Z, Chen Z, Shi Y, Wang Q, Liu S, *et al.* A parvalbumin-positive excitatory visual pathway to trigger fear responses in mice. Science 2015;, 348: 1472–1477.
14. Meng Q, Huang Y, Cui D, He L, Chen L, Ma Y, *et al.* The dissociations of visual processing of "hole" and "no-hole" stimuli: An functional magnetic resonance imaging study. Brain Behav 2018, 8: e00979.
15. Livingstone M, Hubel D. Segregation of form, color, movement, and depth: anatomy, physiology, and perception. Science 1988, 240: 740–749.
16. Duan J, Fu H, Zhang J. Activation of parvalbumin-positive neurons in both retina and primary visual cortex improves the feature-selectivity of primary visual cortex neurons. Neurosci Bull 2017, 33: 255–263.
17. Erskine D, Taylor JP, Thomas A, Collerton D, McKeith I, Khundakar A, *et al.* Pathological changes to the subcortical visual system and its relationship to visual hallucinations in dementia with lewy bodies. Neurosci Bull 2019, 35: 295–300.
18. Schiff W, Caviness JA, Gibson JJ. Persistent fear responses in rhesus monkeys to the optical stimulus of "looming". Science 1962, 136: 982–983.
19. White BJ, Munoz DP. The Superior Colliculus. Oxford University Press, 2011.
20. Das P, Kemp AH, Flynn G, Harris AW, Liddell BJ, Whitford TJ, *et al.* Functional disconnections in the direct and indirect amygdala pathways for fear processing in schizophrenia. Schizophr Res 2007,90: 284–294.

Neurosci. Bull. April, 2020, 36(4):432–448
https://doi.org/10.1007/s12264-019-00447-9

www.neurosci.cn
www.springer.com/12264

REVIEW

Orexin Receptor Antagonists as Emerging Treatments for Psychiatric Disorders

Ying Han[1] · Kai Yuan[2,3] · Yongbo Zheng[2] · Lin Lu[1,2,3]

Received: 25 April 2019 / Accepted: 27 September 2019 / Published online: 28 November 2019

Abstract Orexins comprise two neuropeptides produced by orexin neurons in the lateral hypothalamus and are released by extensive projections of these neurons throughout the central nervous system. Orexins bind and activate their associated G protein-coupled orexin type 1 receptors (OX1Rs) and OX2Rs and act on numerous physiological processes, such as sleep-wake regulation, feeding, reward, emotion, and motivation. Research on the development of orexin receptor antagonists has dramatically increased with the approval of suvorexant for the treatment of primary insomnia. In the present review, we discuss recent findings on the involvement of the orexin system in the pathophysiology of psychiatric disorders, including sleep disorders, depression, anxiety, and drug addiction. We discuss the actions of orexin receptor antagonists, including selective OX1R antagonists (SORA1s), selective OX2R antagonists (SORA2s), and dual OX1/2R antagonists (DORAs), in the treatment of these disorders based on both preclinical and clinical evidence. SORA2s and DORAs have more pronounced efficacy in the treatment of sleep disorders, whereas SORA1s may be promising for the treatment of anxiety and drug addiction. We also discuss potential challenges and opportunities for the application of orexin receptor antagonists to clinical interventions.

Keywords Orexin · Insomnia · Depression · Anxiety · Drug addiction

Introduction

Orexins and hypocretins were almost simultaneously discovered by Sakurai and de Lecea, respectively, in 1998 and were later shown to be the same neuropeptide [1, 2]. There are two types of orexins: orexin-A (hypocretin-1) and orexin-B (hypocretin-2). Both are produced from the same precursor peptide, prepro-orexin, by neuronal cleavage in the lateral and posterior hypothalamus, and orexin projections are found throughout the brain [1–3]. Orexin peptides are ligands for G protein-coupled orexin type 1 receptors (OX1Rs) and OX2Rs. Orexin-A activates both OX1Rs and OX2Rs with approximately equal potency, while orexin-B preferentially activates OX2Rs [4, 5]. The anatomical distribution of OX1Rs and OX2Rs in the brain shows partially overlapping and partially distinct patterns [4, 6–8] (Fig. 1A). Both receptors are expressed in the lateral hypothalamus (LH), medial prefrontal cortex (mPFC), hippocampus (Hip), central nucleus of the amygdala (CeA), bed nucleus of the stria terminalis (BNST), dorsal raphe (DR), ventral tegmental area (VTA), laterodorsal tegmental nucleus (LDT)/pedunculopontine nucleus (PPT), and nucleus of the solitary tract (NTS). OX1Rs are selectively expressed in the locus coeruleus (LC) and cingulate cortex, while OX2Rs are selectively

Ying Han and Kai Yuan have contributed equally to this work.

✉ Lin Lu
linlu@bjmu.edu.cn

1 National Institute of Drug Dependence and Beijing Key Laboratory of Drug Dependence, Peking University, Beijing 100191, China

2 Peking University Sixth Hospital, Peking University Institute of Mental Health, NHC Key Laboratory of Mental Health (Peking University), National Clinical Research Center for Mental Disorders (Peking University Sixth Hospital), Beijing 100191, China

3 Peking-Tsinghua Center for Life Sciences and PKU-IDG/McGovern Institute for Brain Research, Peking University, Beijing 100871, China

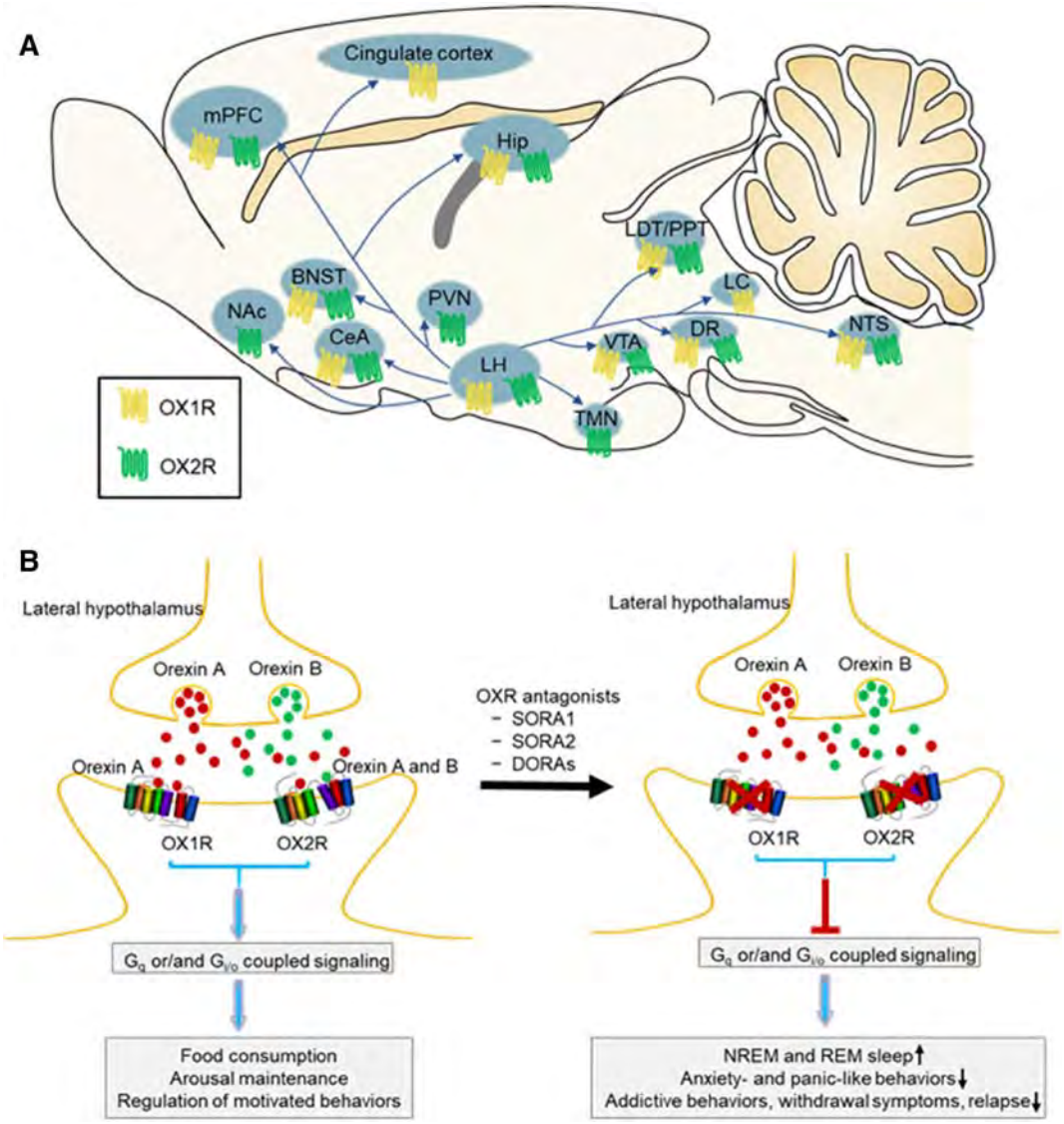

Fig. 1 Orexin receptor distribution and potential application of orexin receptor antagonists for the treatment of psychiatric disorders. **A** Orexin neurons in the lateral hypothalamus send extensive projections to brain areas associated with feeding, sleep-wake regulation, and motivated and emotional behaviors. The anatomical distribution of OX1Rs and OX2Rs in these regions is shown. **B** Orexin A and orexin B are hypothalamic neuropeptides. Their actions are mediated by G_q- and/or $G_{i/o}$-coupled OX1Rs and OX2Rs, playing important roles in many physiological processes, such as feeding, the sleep-to-wakefulness transition, and motivation. Antagonism of the orexin system increases NREM and REM sleep, decreases anxiety- and panic-like behaviors, and inhibits the reinforcing and motivational properties of addictive drugs. Orexin receptor antagonists may be promising for the treatment of psychiatric disorders, such as insomnia, anxiety, and drug addiction. BNST, bed nucleus of the stria terminalis; CeA, central nucleus of the amygdala; DORA, dual OX1/2R antagonist; DR, dorsal raphe; Hip, hippocampus; LC, locus coeruleus; LDT/PPT, laterodorsal tegmental nucleus/pedunculopontine nucleus; LH, lateral hypothalamus; mPFC, medial prefrontal cortex; NAc, nucleus accumbens; NREM, non-rapid-eye-movement; NTS, nucleus of the solitary tract; OX1R, orexin type 1 receptor; OX2R, orexin type 2 receptor; PVN, hypothalamic paraventricular nucleus; REM, rapid-eye-movement; SORA1, selective OX1R antagonist; SORA2, selective OX2R antagonist; TMN, tuberomammillary nucleus; VTA, ventral tegmental area.

expressed in the tuberomammillary nucleus (TMN), hypothalamic paraventricular nucleus (PVN), and nucleus accumbens (NAc). These brain regions are major effector sites of orexin neurons in the LH, which is involved in feeding, sleep, and motivated behaviors [9–11].

Fasting has been shown to increase prepro-orexin mRNA levels, and the central administration of orexin-A and orexin-B stimulates food consumption, suggesting that they play important physiological roles in regulating feeding behavior [2]. Satiety activates anorexigenic pro-

opiomelanocortin (POMC)-containing neurons and inhibites orexin-producing neurons in the hypothalamus, thus suppressing feeding and/or stimulating energy expenditure [12, 13]. However, orexin-A and OX1R stimulation have been shown to inhibit satiety-inducing POMC neurons and increase the motivation for food [14, 15]. The exogenous administration of orexin-A into the LH increases wakefulness in rats [16]. The selective optogenetic activation of orexin neurons in the LH increases the probability of the sleep-to-wakefulness transition, and OX1Rs and OX2Rs play differential roles in the regulation of rapid-eye-movement (REM) sleep and non-REM (NREM) sleep [17]. NREM sleep is mainly regulated by OX2Rs, but there are important synergistic effects of OX1R and OX2R signaling in this regulation [18, 19]. Many reviews have indicated that the orexin system is involved in the regulation of reward, motivated behaviors, and stress-related psychiatric disorders [6, 9, 20, 21].

Given the critical role of orexin in multiple physiological processes and the wide distribution of orexin receptors throughout the brain, compounds that target orexin receptors may be beneficial for the treatment of various disorders. A growing number of patents for orexin receptor antagonists has emerged for use in the areas of sleep disorders, anxiety, panic, and addictive disorders[22]. Orexin receptor antagonists are classified into selective OX1R antagonists (SORA1s), selective OX2R antagonists (SORA2s), and dual OX1/2R antagonists (DORAs), based on their binding affinities. Several DORAs and SORA2s have been translated from basic research to clinical interventions. They have been shown to have sustained clinical efficacy and are well-tolerated for the management of primary insomnia [23, 24]. The DORA suvorexant was the first orexin receptor antagonist approved by United States Food and Drug Administration (FDA) for the treatment of primary insomnia [25]. Another DORA, lemobrexant, has been shown to be effective for the treatment of insomnia disorder in randomized controlled clinical trials [23, 26]. In addition, orexin receptor antagonists have been extensively investigated for use in psychiatric disorders associated with the dysregulation of orexin function [10, 20, 21, 27] (Fig. 1B). In this review, we discuss the potential involvement of the orexin system in the pathophysiology of several psychiatric disorders, including sleep disorders, anxiety, and drug addiction, and summarize the progress of recent research on orexin receptor antagonists for the treatment of these disorders, from basic research to clinical studies.

From the Laboratory to the Clinic: Orexin Receptor Antagonists for the Treatment of Psychiatric Disorders

Although orexin neurons are concentrated only in the LH and adjacent areas, their nerve fibers project widely to much of the central nervous system, from the brainstem to the cortex. These widespread connections are involved in the regulation of feeding, sleep/wake states, stress, and reward processing [6, 9, 28, 29]. Specific hypothalamic nuclei, such as the LH and PVN, are often referred to as "centers" for hunger and satiety, and the activation of orexin projections to the NTS and NAc has been shown to increase food intake [9, 12, 30]. The effects of orexin neuropeptides on sleep-wake regulation may be reflected by their innervation of noradrenergic neurons in the LC, histaminergic neurons in the TMN, serotonergic neurons in the DR, and cholinergic neurons in the LDT/PPT [11, 31]. Orexin terminals are also expressed in the CeA, BNST, mPFC, and Hip, which are critical for the regulation of stress and anxiety-related responses [10, 32]. Orexin neurons also send projections to dopamine neurons in the VTA and NAc, which are well known to modulate reward processing [9, 21]. Accumulating evidence indicates that the orexin system contributes to the etiology of several psychiatric disorders. Orexin receptor antagonists have shown promise for the treatment of these disorders.

Sleep Disorders, Especially Primary Insomnia

The discovery of selective orexin neuron loss in narcolepsy sparked great research interest in the sleep field and raised the possibility of an alternative approach of treating the symptoms of insomnia with orexin receptor antagonists [11]. The number of orexin neurons is selectively reduced in human narcolepsy, and canine narcolepsy is caused by a mutation of the OX2R gene [33, 34]. Intranasal administration of orexin peptide, orexin neuron transplants, and orexin gene therapy are promising approaches to the treatment of narcolepsy [35, 36]. The selective OX2R agonist YNT-185 has been shown to ameliorate cataplexy-like episodes in a mouse model of narcolepsy [37]. OX2R agonists (a modified orexin-B peptide) have also been reported to promote resilience to stress and have anxiolytic and anti-depressive effects [38, 39]. Inactivation of each orexin receptor subtype is required to induce narcoleptic effects, but OX1Rs and OX2Rs play distinct roles in gating NREM and REM sleep. OX2Rs are the pivotal receptors that regulate wakefulness and NREM sleep, whereas REM sleep is controlled by both receptor subtypes [19]. The selective inhibition of OX2Rs results in an increase in NREM sleep and a decrease in the latency to NREM sleep,

but no effect on REM or NREM sleep occurs when OX1Rs are selectively inhibited [40–42]. Although OXR1s do not have a direct action on regulating sleep, almorexant has been shown to enhance the total REM sleep time in OX1R-knockout mice compared with wild-type mice, thus indicating that OX1Rs play additional roles in REM sleep [43]. Knockdown of OX1Rs in the LC selectively increases the time spent in REM sleep during the dark period [44]. The SORA1 JNJ-54717793 has minimal effects on spontaneous sleep in rats and wild-type mice, but JNJ-54717793 administration in OX2R-knockout mice selectively reduces REM sleep latency and increases REM sleep duration [45]. Pharmacological experiments have also shown that co-administration of an OX1R antagonist and an OX2R antagonist reduces REM sleep latency and increases REM sleep duration [18]. However, another study have showed that the inhibition of OX1Rs attenuates the increase in REM sleep time that is induced by selective OX2R antagonism, which appeared to be correlated with dopaminergic neurotransmission [46]. These reports suggest that OX2Rs play a dominant role in regulating sleep, while OX1Rs alone only make a minimal contribution to sleep induction but exert synergistic effects with OX2Rs to regulate REM sleep.

DORAs block the activity of both OX1Rs and OX2Rs and result in a rapid transition to sleep. Administered orally, the DORA suvorexant significantly and dose-dependently reduces locomotor activity and promotes both NREM and REM sleep in rats, dogs, and rhesus monkeys [47]. Suvorexant promotes sleep primarily by increasing REM sleep duration and reducing the latency to REM sleep [48]. It also increases NREM sleep and improves the impairment in glucose tolerance in an animal model of diabetes mellitus [49]. These studies suggest that DORAs effectively improve sleep without significantly disrupting its architecture. Treatment with the DORA MK6096 and the SORA2 MK1064 but not a SORA1 stabilizes sleep and improves sleep-dependent memory function [50]. Fos immunohistochemistry showed that the DORA almorexant does not block the sleep deprivation-induced activation of wake-promoting cell groups in the LH, TMN, or basal forebrain, which suggests a mechanism by which almorexant causes less cognitive impairment than the benzodiazepine receptor agonist zolpidem [51].

Consistent cross-species evidence for the sleep-promoting effects of orexin receptor antagonists spurred the pharmaceutical development of new orexin-targeted treatments for insomnia. Almorexant was the first-in-class compound that targeted the orexin system and the first DORA to proceed to Phase II sleep disorder studies in 2007, but investigations of almorexant were halted during Phase III trials for undisclosed reasons. Currently, the most advanced DORA is suvorexant, which was approved by the FDA in 2014 for the treatment of insomnia [25]. Several meta-analyses and reviews of clinical trials support the efficacy of suvorexant for the treatment of insomnia [52–55]. Randomized controlled clinical trials have reported that suvorexant generally improves sleep maintenance and onset over 3 months of nightly treatment and is well-tolerated in both adult and elderly patients with primary insomnia [56–59]. DORA treatment results in significant and dose-related improvements in both subjective and objective sleep [26, 60, 61]. A meta-analysis and several clinical trials found that suvorexant is associated with significant improvements in subjective time to sleep onset, subjective total sleep time, and subjective sleep quality [24, 62–64]. Statistically significant sleep-promoting effects on both REM and NREM sleep have been reported, and sleep architecture and the power spectral profile are not disrupted in patients with primary insomnia or healthy people who are treated with suvorexant [23, 60, 65, 66]. The DORA SB-649868 has been shown to increase total sleep time and REM sleep duration and reduce waking after sleep onset, the latency to persistent sleep, and the latency to REM sleep in healthy men in a model of situational insomnia and men with primary insomnia [67, 68]. Another DORA, lemborexant, improves sleep efficiency, decreases the latency to persistent sleep, decreases the latency to subjective sleep onset, and decreases waking after sleep onset in adults and elderly individuals with insomnia disorder [26].

In addition to treating primary insomnia, the DORA suvorexant has been evaluated for the treatment of insomnia symptoms in patients with psychosis and physical disease. Suvorexant is effective for the treatment of insomnia in patients with Alzheimer's disease, but whether it influences Alzheimer's disease itself remains unclear [69]. Suvorexant significantly increases sleep efficiency and decreases glucose levels in individuals with insomnia symptoms and type 2 diabetes mellitus, and these effects are consistent with the effects of suvorexant in an animal model [49, 70]. Combination therapy with suvorexant and ramelteon improves subjective sleep quality without inducing delirium in acute stroke patients [71]. Some case reports have also suggested that suvorexant treatment is useful in patients with schizophrenia [72] and Parkinson's disease [73], but its efficacy in these patients remains unclear and needs further validation. Overall, DORAs have shown efficacy for the treatment of primary insomnia and insomnia symptoms. Several studies have focused on suvorexant for the treatment of patients with sleep apnea, but it lacks clinically important respiratory effects during sleep [74–76]. The SORA2 seltorexant has also been found to decrease the latency to persistent sleep and increase total sleep time and sleep efficiency in patients with major depressive disorder (MDD) and persistent insomnia who

are being treated with antidepressants and individuals with insomnia disorder without psychiatric comorbidity [77, 78].

Data from a Japanese post-marketing survey suggested that adverse effects of suvorexant are rare, with an incidence of 8.8%. Next-day somnolence is the most commonly reported side-effect, which may be an inevitable consequence of pharmacological interventions that promote sleep in some patients [79]. Suvorexant is generally effective and well tolerated. However, compared with traditional sleep agents (e.g., benzodiazepines), the efficacy of suvorexant requires further validation [80, 81]. Some studies have reported infrequent but notable side-effects of suvorexant in the treatment of insomnia disorder, such as abnormal dreams, sleep paralysis, over-sedation, the acute worsening of depressive symptoms, and suicidal thoughts [82–84].

Overall, several SORA2s and DORAs that are clinically used for patients with primary insomnia have been shown to be safe and effective (Table 1). Additional orexin-targeted drugs are expected to be approved by the FDA for clinical use. Further studies are needed to evaluate the action of orexin receptor antagonists in the treatment of other sleep disorders and mental illnesses.

Mood Disorders

Orexin receptor antagonists have been implicated in the treatment of depression and anxiety (Table 2). Acute restraint stress activates orexin neurons in the LH and increases orexin-A levels in the VTA [85]. OX1R gene variants are associated with the development of MDD and depressive symptom severity [86]. Systemic administration of the SORA2 LSN2424100 has dose-dependent antidepressant-like effects in a delayed-reinforcement of low-rate assay in rodents, and the SORA2 seltorexant has a tendency to improve mood in antidepressant-treated MDD patients with persistent insomnia [77, 87]. The DORA almorexant prevents chronic unpredictable mild stress-induced depressive-like behavior in mice but does not affect hippocampal cell proliferation or neurogenesis [88]. Suvorexant has also been shown to improve sleep quality and mood in psychiatric inpatients with insomnia symptoms [89]. Another Phase 2 clinical trial reported inconsistent results, in which 6 weeks of treatment with the DORA filorexant did not have significant effects in patients with MDD, but this study had limitations with regard to enrollment challenges and insufficient statistical power, the results of which should be interpreted with caution [90].

Orexin modulates neuronal circuitry that is implicated in the expression and extinction of conditioned fear, suggesting that it may be a promising target for the treatment of anxiety disorders [10, 91]. Panic disorder is a common disabling anxiety disorder characterized by recurrent panic attacks. The orexin system in the medial hypothalamus and orexin-related molecular mechanisms in the amygdala–hippocampus–prefrontal cortex pathway are involved in the behavioral expression of panic disorder [92, 93]. Orexin-related pharmacological targets may be promising for the treatment of panic attacks. Orexin neurons are activated in a rat model of panic disorder, and the orexin levels in cerebrospinal fluid (CSF) increase in humans with panic-related anxiety [94]. OX1R gene variations are associated with the development of panic disorder and the treatment response to cognitive behavioral therapy [95]. Systemic administration of the SORA1 SB-334867 and silencing the orexin gene in the hypothalamus block panic responses and anxiety-like behavior in a rat model of CO_2- and sodium lactate-induced panic [94, 96]. Intracerebroventricular injection of SB-334867 decreases seizures and anxiety in pentylenetetrazol-kindled rats [97]. Systemic SB-334867 administration has no effect on anxiety-like behavior in the open field, whereas microinjection of SB-334867 into the trigeminal nucleus caudalis reduces orofacial pain-induced anxiety-like behavior in rats [98, 99]. SB-334867 treatment also attenuates FG-7142-induced anxiety-like behavior, increases heart rate, and increases neuronal activation in anxiety- and stress-related brain regions, such as the CeA and BNST [100].

The novel brain-penetrant SORA1 JNJ-54717793 attenuates CO_2- and sodium lactate-induced panic-like behavior and cardiovascular responses [45]. The SORA1 compound 56 also attenuates this behavior and cardiovascular responses without altering baseline locomotor or autonomic activity, while the SORA2 JNJ10397049 has no effects on panic-like responses [101, 102]. The antagonism of OX1Rs in the hypothalamus has been shown to treat panic disorder. However, a previous study showed that OX1R transcript levels increase and OX2R transcripts decrease in the basolateral amygdala in chronic social defeat-susceptible mice. Knockdown of either orexin receptor in the BLA has no effects on depressive-like behavior, whereas OX2R knockdown in the BLA increases anxiety-like behavior [103]. Therefore, the roles of the two orexin receptor subtypes in depressive- and anxiety-like behaviors may be brain region-specific.

Drug Addiction

Some addictive drugs act both locally on orexin neurons in the LH and at orexin terminals in the VTA. Orexin system activation promotes drug-seeking by stimulating postsynaptic OX1Rs and modulating the drug-induced glutamatergic synaptic plasticity in dopamine neurons in the VTA [21]. Hypothalamic orexin neurons co-release orexin and dynorphin in the VTA, and the SORA1 SB334867 has

Table 1 Summary of recent findings on orexin receptor antagonists for the treatment of sleep disorders.

Manipulation and target	Subjects	Findings	References
Filorexant (MK-6096) DORA	Rats and dogs	Dose-dependently reduced locomotor activity and increased sleep in rats and dogs.	Winrow *et al.* [151]
	Mice	Stabilized sleep and improved sleep-dependent memory function.	Li *et al.* [50]
	Patients (18–65 years old) with primary insomnia	Increased SE, decreased WASO, and decreased the latency to persistent sleep onset.	Connor *et al.* [61]
Suvorexant (MK-4305) DORA	Rats, dogs, and rhesus monkeys	Reduced locomotor activity and promoted sleep in rats, dogs, and rhesus monkeys.	Winrow *et al.* [47]
	Mice	Disturbed sleep architecture by selectively increasing REM sleep and decreasing wake time.	Hoyer *et al.* [48]
	Type 2 diabetic db/db mice	Increased NREM sleep and improved impairment in glucose tolerance in db/db mice.	Tsuneki *et al.* [49]
	Non-elderly patients with primary insomnia	Increased SE, decreased LPS, and decreased WASO	Herring *et al.* [152]
	Patients with primary insomnia	Showed greater efficacy than placebo in improving subjective TST and subjective TSO; was generally safe and well tolerated over 1 year of nightly treatment.	Michelson *et al.* [64]
	Nonelderly and elderly patients with insomnia.	Improved sleep onset and maintenance over 3 months of nightly treatment and was generally safe and well tolerated.	Herring *et al.* [57]
	Patients with insomnia	Increased TST (average increase $\leq$ 3.9% in REM sleep) and reduced REM sleep latency.	Snyder *et al.* [66]
	Elderly patients with insomnia	Generally improved sleep maintenance and onset over 3 months of nightly treatment and was well-tolerated.	Herring *et al.* [56]
	Elderly and nonelderly insomnia patients	Generally effective and well tolerated in both women and men with insomnia.	Herring *et al.* [59]
	Psychiatric inpatients with insomnia	Overall improvement in the quality of sleep and the severity of anxiety and depression.	Nakamura *et al.* [89]
	Adolescent patients with insomnia	Improved sleep quality in adolescent insomnia.	Kawabe *et al.* [62]
	Japanese elderly patients with chronic insomnia	Appeared to be more cost-effective than the alternative zolpidem in a virtual cohort.	Nishimura and Nakao [153]
	Elderly and non-elderly insomnia patients	Improved sleep to a greater extent than placebo as assessed by the ISI.	Herring *et al.* [63]
	Insomnia patients	Reduced WASO by reducing the number and time spent in long wake bouts.	Svetnik *et al.* [154]
	Healthy young men (18–45 years old)	Decreased LPS and wake after sleep onset time and increased SE; did not affect EEG frequency bands.	Sun *et al.* [60]
	Patients with primary insomnia	Limited effects on EEG power spectral density compared with placebo.	Ma *et al.* [65]
	Alzheimer's disease patients with insomnia	Adequate efficacy for the treatment of insomnia in patients with Alzheimer's disease.	Hamuro *et al.* [69]
	Patients with type 2 diabetes mellitus and insomnia	Increased TST and SE and decreased glucose levels.	Toi *et al.* [70]
	COPD patients	Did not have an overt respiratory depressant effect.	Sun *et al.* [76]
	Healthy adult men and women	Lacked clinically important respiratory effects during sleep.	Uemura *et al.* [74]
	Patients (18–65 years old) with OSA	Did not appear to have clinically important respiratory effects during sleep.	Sun *et al.* [75]

Table 1 continued

Manipulation and target	Subjects	Findings	References
Almorexant (ACT-078573) DORA	Healthy male participants	Equivalent to zolpidem with regard to subjectively assessed alertness.	Hoever *et al.* [155]
	Mice	Increased REM and NREM sleep in wild-type mice but not in OX2R-knockout mice.	Mang *et al.* [43]
	Mice	Promoted sleep and exacerbated cataplexy in a mouse model of narcolepsy.	Black *et al.* [156]
	Rats	Promoted sleep without impairing memory performance.	Morairty *et al.* [157]
	Rats	Promoted sleep but was permissive for the activation of wake-promoting systems.	Parks *et al.* [51]
	Male and female adult patients with primary insomnia	Decreased subjective WASO, decreased objective and subjective LPS, decreased the latency to sleep onset, and increased objective and subjective TST.	Black *et al.* [158]
	Elderly patients with primary insomnia	Increased TST, decreased WASO, and decreased LPS.	Roth *et al.* [159]
SB-649868 DORA	Healthy male volunteers	Increased TST and REM sleep duration, decreased WASO and LPS, and decreased the latency to REM sleep; did not affect SWS or EEG power spectra in NREM sleep.	Bettica *et al.* [67]
	Male patients with primary insomnia	Decreased LPS, decreased WASO, increased TST, increased REM sleep, and decreased REM sleep latency.	Bettica *et al.* [68]
Lemborexant (E2006) DORA	Mice	Efficacy demonstrated in an *in vivo* study that used objective sleep parameter measurements.	Yoshida *et al.* [160]
	Adults and elderly subjects with insomnia	Improved SE and subjective SE, decreased LPS and subjective sleep onset latency, and decreased WASO and subjective WASO.	Murphy *et al.* [26]
Seltorexant (JNJ-42847922 and MIN 202) SORA2	Rats, mice, and healthy humans	Reduced latency to NREM sleep and prolonged NREM sleep duration in rats but not in OX2R-knockout mice; increased somnolence in healthy humans.	Bonaventure *et al.* [102]
	Individuals with insomnia	Increased TST, decreased LPS, and decreased WASO in individuals with insomnia without psychiatric comorbidity.	De Boer *et al.* [78]
	MDD patients with persistent insomnia	Decreased LPS and increased TST and SE, accompanied by a tendency to subjectively improved mood in antidepressant-treated MDD patients with persistent insomnia.	Brooks *et al.* [77]
MK-1064 SORA2	Rats, dogs, and healthy humans	Increased NREM and REM sleep.	Gotter *et al.* [42]
JNJ-54717793 SORA1	Rats and mice	Minimal effects on spontaneous sleep in rats and wild-type mice; selectively promoted REM sleep in OX2R-knockout mice.	Bonaventure *et al.* [45]
IPSU SORA2	Mice	Influenced sleep only during the active phase and induced sleep by increasing NREM sleep.	Hoyer *et al.* [48]
Compound 5 DORA	Rats	Decreased locomotor activity and the time awake and increased REM sleep and delta sleep.	Whitman *et al.* [161]
3,9-diazabicyclo[4.2.1]nonanes DORA	Rats	Better oral bioavailability and exerted sleep-promoting activity in a rat EEG model.	Coleman *et al.* [162]

COPD, chronic obstructive pulmonary disease; DORA, dual orexin receptor 1/2 antagonist; E2006, (1*R*,2*S*)-2-{[(2,4-dimethylpyrimidin-5-yl)oxy]methyl}-2(3-fluorophenyl)-*N*-(5-fluoropyridin-2-yl)cyclopropanecarboxamide; EEG, electroencephalogram; IPSU, 2-([1H-Indol-3-yl]methyl)9-(4-methoxypyrimidin-2-yl)-2,9-diazaspiro[5.5]undecan-1-one; ISI, Insomnia Severity Index; LPS, latency to persistent sleep; MDD, major depressive disorder; NREM, non-rapid-eye-movement; OSA, obstructive sleep apnea; OX1R, orexin type 1 receptor; OX2R, orexin type 2 receptor; REM, rapid-eye-movement; SE, sleep efficiency; SORA1, selective orexin receptor 1 antagonist; SORA2, selective orexin receptor 2 antagonist; TSO, time to sleep onset; TST, total sleep time; WASO, wake after sleep onset.

been shown to decrease reward thresholds, impulsive-like behavior, and cocaine self-administration, and these effects are reversed by dynorphin blockade with nor-binaltorphimine [21, 104]. Cocaine has been shown to modulate the σ1 receptor–corticotropin-releasing factor-1 receptor–OX1R complex. The SORA1 SB-334867 blocks the reinstatement of cocaine-induced conditioned place preference (CPP) that is induced by an intra-VTA microinjection of orexin-A [85, 105]. A recent study showed that intermittent access to cocaine produces a multi-endophenotype addiction-like state and persistently increases the number of orexin neurons and orexin neuron activity in the LH. The pharmacological blockade of OX1Rs with SB-334867 and the selective knockdown of orexin neurons in the LH reduce the motivation for cocaine and attenuate the addiction-like phenotype [106]. SB-334867 decreases cocaine self-administration in both rats and female rhesus monkeys. It also reduces the motivation for cocaine-associated cues and blocks the cue-induced reinstatement of cocaine-seeking behavior [107–109]. SB-334867 and almorexant, but not the SORA2 4PT, attenuate the cocaine-induced inhibition of dopamine uptake and reduce cocaine self-administration [110]. Prolonged access to cocaine self-administration enhances γ-aminobutyric acid neurotransmission in the medial CeA, and intra-CeA microinjections of SB-334867 reduce cocaine intake and attenuate the yohimbine-induced reinstatement of cocaine-seeking [111]. Systemic administration of the SORA2 RTIOX-276 decreases responding for cocaine under high-effort conditions and attenuates the cocaine-induced inhibition of dopamine uptake [112]. The DORA suvorexant attenuates the motivational and hedonic properties of cocaine and impulsive cocaine-seeking [113, 114]. The overall abuse liability of suvorexant has been shown to be low in both rodents and healthy recreational polydrug users with a history of sedative and psychedelic drug use [115, 116].

The orexinergic system has been implicated in the motivational effects of alcohol and opioids as well as other addictions [21, 117]. The SORA1s SB-334867 and GSK1059865 decrease alcohol intake and preference and reduce relapse to alcohol drinking but have no effects on sucrose intake [118–120]. SB-334867 selectively reduces alcohol self-administration and cue-induced reinstatement in highly-motivated rats [121]. SB-334867 inhibits the acquisition and expression of locomotor sensitization induced by morphine and amphetamine [122, 123]. SB-334867 also significantly attenuates morphine-induced CPP but does not affect morphine-induced hyperactivity [124]. SB-334867 reduces the motivation for the opioid remifentanil and reduces the cue-induced reinstatement of remifentanil-seeking in low takers [125]. Systemic SB-334867 administration significantly attenuates naloxone-induced morphine withdrawal symptoms and blocks activation of the NAc shell [126]. Intra-LC microinjections of SB-334867 significantly attenuate the somatic signs of morphine withdrawal, and this is blocked by the $GABA_A$ receptor antagonist bicuculline [127, 128]. Intra-VTA microinjections of SB-334867 and the DORA2 TCS-OX2-29 significantly attenuate the acquisition and expression of morphine-induced CPP [129]. Intra-dentate gyrus administration of SB-334867 and TCS-OX2-29 attenuates morphine priming-induced reinstatement and the acquisition and expression of LH stimulation-induced CPP in rats [130, 131].

Alcohol intake increases the mRNA levels of OX2Rs but not OX1Rs in the anterior paraventricular thalamus, and microinjections of TCS-OX2-29 but not SB-334867 into this nucleus decrease intermittent-access alcohol drinking [132]. Extended access to intravenous heroin self-administration increases OX2R mRNA levels in the CeA, and systemic administration of the SORA2 NBI-80713 dose-dependently decreases heroin self-administration in prolonged-access rats [133]. The DORA almorexant interferes with the expression of morphine-induced locomotor sensitization, attenuates the expression of cocaine- and amphetamine-induced CPP, and decreases alcohol self-administration [134, 135]. Almorexant does not potentiate the cognitive-impairing effects of alcohol in humans and does not affect motor performance in rats [136, 137]. Sleep disturbances occur during both alcohol exposure and withdrawal. Suvorexant decreases the latency to sleep onset but also exacerbates sleep fragmentation in rats exposed to chronic intermittent alcohol vapor and protracted withdrawal, which may help prevent relapse to alcohol use [138, 139].

Nicotine withdrawal increases the activation of orexin neurons in the LH and activates the PVN. Intra-PVN microinjections of the SORA1 SB334867 attenuate the somatic signs of nicotine withdrawal, but the SORA2 TCS-OX2-29 has no effect [140]. A genome-wide association study showed that the OX2R gene polymorphism Val308Ile is associated with nicotine dependence [141]. The DORA TCS1102 has no significant effects on palatable food self-administration or reinstatement in either hungry or sated rats and does not affect the reinstatement of nicotine-seeking [142, 143]. Administration of the SORA1 SB-334867 and knockdown of the orexin gene in the LH decrease responding for food under both variable-ratio and progressive-ratio schedules of reinforcement (i.e., impair the reinforcing and motivational properties of food) [144]. Contingent self-administration of the synthetic cannabinoid agonist WIN55,212-2 increases the activation of orexin neurons in the LH, and systemic administration of the SORA1 SB334867 but not SORA2 TCS-OX2-29 reduces the reinforcing and motivational properties of WIN55,212-2 [145].

Table 2 Summary of recent findings on orexin receptor antagonists for the treatment of depression and panic/anxiety.

Disorder	Manipulation	Target	Subjects	Findings	References
Depression	LSN2424100	OX2R	Rats	Systemic administration dose-dependently produced antidepressant-like activity.	Fitch *et al.* [87]
	Seltorexant	OX2R	MDD patients with persistent insomnia	Induced a tendency toward subjective improvements in mood in antidepressant-treated MDD patients with insomnia.	Brooks *et al.* [77]
	Almorexant	dual OX1/2R	Mice	Induced a robust antidepressant-like effect in the CUMS model of depression, and this effect was neurogenesis-independent.	Nollet *et al.* [88]
	Filorexant (MK-6096)	dual OX1/2R	Patients with MDD	No significant difference was found in the primary endpoint of change after 6 weeks of treatment.	Connor *et al.* [61]
	Suvorexant	dual OX1/2R	Psychiatric patients with insomnia	Overall improvement in the quality of sleep and the severity of anxiety and depression.	Nakamura *et al.* [89]
Panic/ anxiety	JNJ-54717793	OX1R	Rats	Attenuated CO_2- and sodium lactate-induced panic-like behaviors and cardiovascular responses.	Bonaventure *et al.* [45]
	Compound 56	OX1R	Rats	With a DORA, attenuated CO_2-induced anxiety-like behaviors; Compound 56 attenuated CO_2-induced cardiovascular responses; the SORA2 JnJ10397049 had no effect on panic-like responses.	Johnson *et al.* [101]
	SB-334867	OX1R	Rats	Intracerebroventricular injections decreased seizures and anxiety in pentylenetetrazol-kindled rats.	Kordi Jaz *et al.* [97]
	Compound 56	OX1R	Rats and mice	Attenuated sodium lactate-induced panic-like behaviors and cardiovascular responses.	Bonaventure *et al.* [102]
	SB-334867	OX1R	Rats	Systemic administration blocked panic-like responses.	Johnson *et al.* [94]
	SB-334867	OX1R	Rats	Systemic administration attenuated CO_2-induced pressor and anxiety-like responses.	Johnson *et al.* [96]
	SB-334867	OX1R	Rats	Attenuated FG-7142-induced anxiety-like behaviors and increased heart rate.	Johnson *et al.* [100]
	SB-334867	OX1R	Rats	Microinjection into the trigeminal nucleus caudalis inhibited orofacial pain-induced anxiety-like behavior in rats.	Bahaaddini *et al.* [99]
	SB-334867	OX1R	Rats	Systemic administration had opposite effects on arousal in adolescent and adult males and had no effect on anxiety-like behavior.	Blume *et al.* [98]

OX1R, orexin type 1 receptor; OX2R, orexin type 2 receptor; MDD, major depressive disorder; CUMS, chronic unpredictable mild stress; CO_2, carbon dioxide; SORA2, selective orexin receptor 2 antagonist; DORA, dual orexin receptor 1/2 antagonist.

Overall, OX1R antagonists may be useful for the treatment of cocaine and other drug addictions [146, 147] (Table 3).

Further Challenges and Unique Opportunities for the Application of Orexin Receptor Antagonists to Treating Psychiatric Disorders

Significant progress has been made in understanding the role of the orexin system in physiological processes and pathological behaviors. Hypothalamic orexin neurons have extensive projections throughout the central nervous system and act as regulators of sleep-to-wake transitions, emotion, and motivation [6]. Technical advances have allowed more precise manipulation of orexin neurons and their target brain regions, revealing the dysregulation of orexin function in various psychiatric disorders. Targeting the orexin system may be a promising strategy for the treatment of such disorders. Suvorexant has been found to promote sleep and was the first orexin receptor antagonist to be approved by the FDA in 2014 for the treatment of primary insomnia [25, 148]. The approval of suvorexant for the treatment for insomnia has helped pave the way for the development of more orexin receptor antagonists for the treatment of other disorders, such as anxiety and addiction.

Table 3 Summary of recent findings on orexin receptor antagonists for the treatment of drug addiction.

Addictive drug	Manipulation	Target	Subjects	Findings	References
Cocaine	Suvorexant	dual OX1/2R	Rats	Attenuated acute cocaine-induced impulsivity when administered systemically or directly into the ventral tegmental area.	Gentile *et al.* [113]
	Suvorexant	dual OX1/2R	Rats	Attenuated motivational and hedonic properties of cocaine.	Gentile *et al.* [114]
	SB-334867	OX1R	Rats	Reduced the acquisition and expression of cocaine self-administration and expression of amphetamine-induced conditioned place preference.	Hutcheson *et al.* [108]
	SB-334867	OX1R	Rats	Systemic administration decreased cocaine intake specifically in prolonged-access rats; microinjections into the central nucleus of the amygdala reduced cocaine intake in prolonged-access rats and attenuated yohimbine-induced reinstatement of cocaine seeking.	Schmeichel *et al.* [111]
	SB-334867	OX1R	Mice	Intra-ventral tegmental area microinjections of orexin-A reinstated extinguished cocaine-induced conditioned place preference in wildtype mice, which was blocked by SORA1 SB-334867.	Tung *et al.* [85]
	SB-334867	OX1R	Mice	Intra-ventral tegmental area injections decreased cocaine self-administration, lateral hypothalamus self-stimulation, and impulsive-like behavior, which were reversed by dynorphin antagonism.	Muschamp *et al.* [104]
	SB-334867	OX1R	Rats	Reduced the motivation for cocaine and attenuated the addiction phenotype.	James *et al.* [106]
	SB-334867	OX1R	Female rhesus monkeys	Decreased cocaine self-administration.	Foltin *et al.* [107]
	SB-334867	OX1R	Rats	Reduced cocaine demand in the presence of cocaine-associated cues and blocked cue-induced reinstatement.	Bentzley *et al.* [109]
	SB-334867	OX1R	Rats	SB-334867 but not the SORA2 4PT attenuated the cocaine-induced inhibition of dopamine uptake and reduced cocaine self-administration.	Prince *et al.* [110]
	Almorexant	dual OX1/2R	Rats	Attenuated the cocaine-induced inhibition of dopamine uptake and reduced cocaine self-administration.	Prince *et al.* [110]
	RTIOX-276	OX1R	Rats	Systemic administration decreased high-effort responding for cocaine and reduced the inhibition of cocaine-induced dopamine uptake.	Levy *et al.* [112]
Alcohol	Suvorexant	dual OX1/2R	Rats	Dose-dependently decreased the latency to REM sleep and SWS onset and produced REM sleep and SWS fragmentation in rats exposed to chronic intermittent alcohol and protracted withdrawal.	Sanchez-Alavez *et al.* [138]
	Almorexant	dual OX1/2R	Healthy humans	Did not potentiate impairing effects of alcohol.	Hoch *et al.* [137]
	Almorexant	dual OX1/2R	Rats	Systemic or intra-ventral tegmental area administration decreased alcohol self-administration.	Srinivasan *et al.* [135]
	Almorexant	dual OX1/2R	Rats	Did not interfere with forced motor performance or grip strength in rats and did not further increase the sedative effects of alcohol.	Steiner *et al.* [136]
	SB-334867	OX1R	Rats	Intra-nucleus accumbens infusions decreased alcohol intake and preference.	Mayannavar *et al.* [118]
	SB-334867	OX1R	Rats	Reduced alcohol relapse drinking.	Dhaher *et al.* [120]
	SB-334867	OX1R	Rats	Attenuated alcohol self-administration and the cue-induced reinstatement of alcohol-seeking in highly motivated rats.	Moorman *et al.* [121]

Table 3 continued

Addictive drug	Manipulation	Target	Subjects	Findings	References
	GSK1059865	OX1R	Mice	Reduced alcohol drinking in alcohol-dependent mice but had no effect on sucrose intake.	Lopez *et al.* [119]
	TCS-OX2-29	OX2R	Rats	Microinjections of TCS-OX2-29 but not SB-334867 into the anterior paraventricular nucleus of the thalamus decreased intermittent-access alcohol drinking.	Barson *et al.* [132]
Opioids	SB-334867	OX1R	Mice	Inhibited the acquisition of morphine-induced locomotor sensitization.	Łupina *et al.* [123]
	SB-334867	OX1R	Rats	Intra-locus coeruleus microinjections significantly attenuated somatic signs of naloxone-induced morphine withdrawal, which was blocked by the $GABA_A$ receptor antagonist bicuculline.	Davoudi *et al.* [127]
	SB-334867	OX1R	Rats	Intra-locus coeruleus microinjections attenuated the expression of glutamate-induced morphine withdrawal during the active phase.	Hooshmand *et al.* [128]
	SB-334867	OX1R	Mice	Systemic administration significantly attenuated naloxone-induced morphine withdrawal symptoms.	Sharf *et al.* [126]
	SB-334867	OX1R	Mice	Significantly attenuated morphine-induced conditioned place preference but not morphine-induced hyperactivity or sensitization.	Sharf [144]
	SB-334867	OX1R	Rats	Intra-ventral tegmental area microinjections significantly attenuated the acquisition and expression of morphine-induced conditioned place preference.	Farahimanesh *et al.* [129]
	SB-334867	OX1R	Rats	Intra-dentate gyrus administration dose-dependently attenuated morphine priming-induced reinstatement.	Ebrahimian *et al.* [130]
	SB-334867	OX1R	Rats	Reduced motivation and the cue-induced reinstatement of remifentanil-seeking in low takers.	Porter-Stransky *et al.* [125]
	NBI-80713	OX2R	Rats	Systemic administration dose-dependently decreased heroin self-administration in prolonged-access rats and had no effect on food pellet self-administration.	Schmeichel *et al.* [133]
	TCS-OX2-29	OX2R	Rats	Intra-ventral tegmental area microinjections significantly attenuated the acquisition and expression of morphine-induced conditioned place preference.	Farahimanesh *et al.* [129]
	TCS-OX2-29	OX2R	Rats	Intra-dentate gyrus administration dose-dependently attenuated morphine priming-induced reinstatement.	Ebrahimian *et al.* [130]
Amphetamine	Almorexant	dual OX1/2R	Rats	Attenuated the expression of cocaine- and amphetamine-induced conditioned place preference but not morphine-induced conditioned place preference; interfered with the expression of morphine-induced locomotor sensitization but not cocaine- or amphetamine-induced locomotor sensitization.	Steiner *et al.* [134]
	SB-334867	OX1R	Rats	Reduced amphetamine-induced dopamine outflow in the nucleus accumbens shell and decreased the expression of amphetamine sensitization.	Quarta *et al.* [122]
Cannabis	SB334867	OX1R	Mice	Systemic SB334867 administration but not the SORA2 TCSOX229 reduced the reinforcing and motivational properties of the synthetic cannabinoid agonist WIN55,212-2.	Flores *et al.* [145]
Nicotine	TCS 1102	dual OX1/2R	Rats	No effect on the reinstatement of nicotine seeking.	Khoo *et al.* [143]
	SB334867	OX1R	Mice	SB334867 but not the SORA2 TCS-OX2-29 attenuated somatic signs of nicotine withdrawal.	Plaza-Zabala *et al.* [140]

OX1R, orexin type 1 receptor; OX2R, orexin type 2 receptor; REM, rapid-eye-movement; SWS, slow-wave sleep; SORA1, selective orexin receptor 1 antagonist; SORA2, selective orexin receptor 2 antagonist; DORA, dual orexin receptor 1/2 antagonist.

Further research is needed to optimize orexin receptor antagonists across diverse structural classes with better physicochemical properties (e.g., better solubility, higher functional and binding potencies at orexin receptors), and better pharmacokinetics (e.g., slower blood clearance, faster distribution, higher oral bioavailability, a plasma half-life that is appropriate for rapid sleep onset and maintenance, brain penetration, and *in vivo* activity) [149].

Hypothalamic orexin neurons have extensive projections to stress-sensitive brain regions, including the amygdala, BNST, and mPFC. The orexin system plays a critical role in the pathophysiology of stress-related psychiatric disorders [20, 32]. Patients with panic-related anxiety exhibit elevated orexin-A levels in the CSF, and patients with depression have low CSF orexin-A levels [20]. Given the role of the orexin system in the modulation of stress reactivity and fear responses, orexin-related pharmacological targets may represent promising opportunities for the treatment of depression and anxiety. However, clinical trials have reported inconsistent effects in the case of depression. Suvorexant attenuates anxiety and depressive symptoms in psychiatric patients with insomnia, and seltorexant has a tendency to subjectively improve depressive symptoms in antidepressant-treated MDD patients with persistent insomnia, whereas filorexant is not effective in patients with MDD [77, 89, 90]. Orexin system function is downregulated under conditions of chronic stress [20, 150], which may limit the application of orexin receptor antagonists for depression treatment. Nonetheless, SORA1s have been reported to consistently reduce panic- and anxiety-like behaviors in rodents. Further clinical trials are warranted to evaluate their efficacy in patients with anxiety and panic disorders.

Accumulating evidence indicates that the orexin system plays an important role in cocaine, opioid, alcohol, and other addictions. Orexin receptor antagonists, especially SORA1s, reduce drug-induced CPP and decrease the reinforcing and motivational properties of addictive drugs and relapse. Exposure to addictive drugs activates orexin neurons in the LH and regulates glutamatergic or GABAergic neurotransmission within orexin neuron-projecting brain regions, such as the VTA and CeA [104, 106, 111]. Orexin receptor antagonism in these regions also attenuates drug-seeking behavior and relapse. However, most of the currently available data have been derived from preclinical studies, and future work is needed to evaluate the efficacy of orexin receptor antagonists for the clinical treatment of addiction.

In conclusion, orexin receptor antagonism appears to be a very promising therapeutic avenue for the treatment of insomnia and other psychiatric disorders. Targeting the orexin system represents a breakthrough in our understanding of sleep disorders and the treatment of anxiety and drug addiction, although more preclinical and clinical studies are clearly needed.

Acknowledgements This review was supported by the National Natural Science Foundation of China (81701312 and 81521063) and the Interdisciplinary Medicine Seed Fund of Peking University (BMU2018MX024).

Conflict of interest The authors declare that they do not have any conflict of interest.

References

1. de Lecea L, Kilduff TS, Peyron C, Gao X, Foye PE, Danielson PE, *et al.* The hypocretins: hypothalamus-specific peptides with neuroexcitatory activity. Proc Natl Acad Sci U S A 1998, 95: 322–327.
2. Sakurai T, Amemiya A, Ishii M, Matsuzaki I, Chemelli RM, Tanaka H, *et al.* Orexins and orexin receptors: a family of hypothalamic neuropeptides and G protein-coupled receptors that regulate feeding behavior. Cell 1998, 92: 573–585.
3. Lee MG, Hassani OK, Jones BE. Discharge of identified orexin/hypocretin neurons across the sleep-waking cycle. J Neurosci 2005, 25: 6716–6720.
4. Matsuki T, Sakurai T. Orexins and orexin receptors: from molecules to integrative physiology. Results Probl Cell Differ 2008, 46: 27–55.
5. Boss C, Roch C. Recent trends in orexin research–2010 to 2015. Bioorg Med Chem Lett 2015, 25: 2875–2887.
6. Nevarez N, de Lecea L. Recent advances in understanding the roles of hypocretin/orexin in arousal, affect, and motivation. F1000Res 2018, 7: F1000 Faculty Rev-1421.
7. Marcus JN, Aschkenasi CJ, Lee CE, Chemelli RM, Saper CB, Yanagisawa M, *et al.* Differential expression of orexin receptors 1 and 2 in the rat brain. J Comp Neurol 2001, 435: 6–25.
8. Bisetti A, Cvetkovic V, Serafin M, Bayer L, Machard D, Jones BE, *et al.* Excitatory action of hypocretin/orexin on neurons of the central medial amygdala. Neuroscience 2006, 142: 999–1004.
9. Sakurai T. The role of orexin in motivated behaviours. Nat Rev Neurosci 2014, 15: 719–731.
10. Flores A, Saravia R, Maldonado R, Berrendero F. Orexins and fear: implications for the treatment of anxiety disorders. Trends Neurosci 2015, 38: 550–559.
11. Mahoney CE, Cogswell A, Koralnik IJ, Scammell TE. The neurobiological basis of narcolepsy. Nat Rev Neurosci 2019, 20: 83–93.
12. Klockars A, Levine AS, Olszewski PK. Hypothalamic integration of the endocrine signaling related to food intake. Curr Top Behav Neurosci 2018. https://doi.org/10.1007/7854_2018_54.
13. Hirasawa M, Parsons MP, Alberto CO. Interaction between orexins and the mesolimbic system for overriding satiety. Rev Neurosci 2007, 18: 383–393.
14. Morello G, Imperatore R, Palomba L, Finelli C, Labruna G, Pasanisi F, *et al.* Orexin-A represses satiety-inducing POMC neurons and contributes to obesity via stimulation of endocannabinoid signaling. Proc Natl Acad Sci U S A 2016, 113: 4759–4764.
15. Williams DL. Neural integration of satiation and food reward: role of GLP-1 and orexin pathways. Physiol Behav 2014, 136: 194–199.

16. Cun Y, Tang L, Yan J, He C, Li Y, Hu Z, *et al.* Orexin A attenuates the sleep-promoting effect of adenosine in the lateral hypothalamus of rats. Neurosci Bull 2014, 30: 877–886.
17. Adamantidis AR, Zhang F, Aravanis AM, Deisseroth K, de Lecea L. Neural substrates of awakening probed with optogenetic control of hypocretin neurons. Nature 2007, 450: 420–424.
18. Dugovic C, Shelton JE, Yun S, Bonaventure P, Shireman BT, Lovenberg TW. Orexin-1 receptor blockade dysregulates REM sleep in the presence of orexin-2 receptor antagonism. Front Neurosci 2014, 8: 28.
19. Mieda M, Hasegawa E, Kisanuki YY, Sinton CM, Yanagisawa M, Sakurai T. Differential roles of orexin receptor-1 and -2 in the regulation of non-REM and REM sleep. J Neurosci 2011, 31: 6518–6526.
20. James MH, Campbell EJ, Dayas CV. Role of the orexin/hypocretin system in stress-related psychiatric disorders. Curr Top Behav Neurosci 2017, 33: 197–219.
21. Baimel C, Bartlett SE, Chiou LC, Lawrence AJ, Muschamp JW, Patkar O, *et al.* Orexin/hypocretin role in reward: implications for opioid and other addictions. Br J Pharmacol 2015, 172: 334–348.
22. Boss C, Roch C. Orexin research: patent news from 2016. Expert Opin Ther Pat 2017, 27: 1123–1133.
23. Coleman PJ, Gotter AL, Herring WJ, Winrow CJ, Renger JJ. The discovery of suvorexant, the first orexin receptor drug for insomnia. Annu Rev Pharmacol Toxicol 2017, 57: 509–533.
24. Kuriyama A, Tabata H. Suvorexant for the treatment of primary insomnia: a systematic review and meta-analysis. Sleep Med Rev 2017, 35: 1–7.
25. Sheridan C. Insomniacs get new mechanism sleep drug Belsomra. Nat Biotechnol 2014, 32: 968.
26. Murphy P, Moline M, Mayleben D, Rosenberg R, Zammit G, Pinner K, *et al.* Lemborexant, a dual orexin receptor antagonist (DORA) for the treatment of insomnia disorder: results from a bayesian, adaptive, randomized, double-blind, placebo-controlled study. J Clin Sleep Med 2017, 13: 1289–1299.
27. Yeoh JW, Campbell EJ, James MH, Graham BA, Dayas CV. Orexin antagonists for neuropsychiatric disease: progress and potential pitfalls. Front Neurosci 2014, 8: 36.
28. Scammell TE, Arrigoni E, Lipton JO. Neural circuitry of wakefulness and sleep. Neuron 2017, 93: 747–765.
29. Zhang XY, Yu L, Zhuang QX, Zhu JN, Wang JJ. Central functions of the orexinergic system. Neurosci Bull 2013, 29: 355–365.
30. Flores A, Maldonado R, Berrendero F. Cannabinoid-hypocretin cross-talk in the central nervous system: what we know so far. Front Neurosci 2013, 7: 256.
31. Sakurai T, Mieda M. Connectomics of orexin-producing neurons: interface of systems of emotion, energy homeostasis and arousal. Trends Pharmacol Sci 2011, 32: 451–462.
32. Sargin D. The role of the orexin system in stress response. Neuropharmacology 2019, 154: 68–78.
33. Lin L, Faraco J, Li R, Kadotani H, Rogers W, Lin X, *et al.* The sleep disorder canine narcolepsy is caused by a mutation in the hypocretin (orexin) receptor 2 gene. Cell 1999, 98: 365–376.
34. Thannickal TC, Moore RY, Nienhuis R, Ramanathan L, Gulyani S, Aldrich M, *et al.* Reduced number of hypocretin neurons in human narcolepsy. Neuron 2000, 27: 469–474.
35. Takenoshita S, Sakai N, Chiba Y, Matsumura M, Yamaguchi M, Nishino S. An overview of hypocretin based therapy in narcolepsy. Expert Opin Investig Drugs 2018, 27: 389–406.
36. Nepovimova E, Janockova J, Misik J, Kubik S, Stuchlik A, Vales K, *et al.* Orexin supplementation in narcolepsy treatment: a review. Med Res Rev 2019, 39: 961–975.
37. Irukayama-Tomobe Y, Ogawa Y, Tominaga H, Ishikawa Y, Hosokawa N, Ambai S, *et al.* Nonpeptide orexin type-2 receptor agonist ameliorates narcolepsy-cataplexy symptoms in mouse models. Proc Natl Acad Sci U S A 2017, 114: 5731–5736.
38. Summers CH, Yaeger JDW, Staton CD, Arendt DH, Summers TR. Orexin/hypocretin receptor modulation of anxiolytic and antidepressive responses during social stress and decision-making: potential for therapy. Brain Res 2018; e-pub ahead of print 24 December 2018; https://doi.org/10.1016/j.brainres.2018.12.036.
39. Staton CD, Yaeger JDW, Khalid D, Haroun F, Fernandez BS, Fernandez JS, *et al.* Orexin 2 receptor stimulation enhances resilience, while orexin 2 inhibition promotes susceptibility, to social stress, anxiety and depression. Neuropharmacology 2018, 143: 79–94.
40. Betschart C, Hintermann S, Behnke D, Cotesta S, Fendt M, Gee CE, *et al.* Identification of a novel series of orexin receptor antagonists with a distinct effect on sleep architecture for the treatment of insomnia. J Med Chem 2013, 56: 7590–7607.
41. Etori K, Saito YC, Tsujino N, Sakurai T. Effects of a newly developed potent orexin-2 receptor-selective antagonist, compound 1 m, on sleep/wakefulness states in mice. Front Neurosci 2014, 8: 8.
42. Gotter AL, Forman MS, Harrell CM, Stevens J, Svetnik V, Yee KL, *et al.* Orexin 2 receptor antagonism is sufficient to promote NREM and REM sleep from mouse to man. Sci Rep 2016, 6: 27147.
43. Mang GM, Durst T, Burki H, Imobersteg S, Abramowski D, Schuepbach E, *et al.* The dual orexin receptor antagonist almorexant induces sleep and decreases orexin-induced locomotion by blocking orexin 2 receptors. Sleep 2012, 35: 1625–1635.
44. Chen L, McKenna JT, Bolortuya Y, Winston S, Thakkar MM, Basheer R, *et al.* Knockdown of orexin type 1 receptor in rat locus coeruleus increases REM sleep during the dark period. Eur J Neurosci 2010, 32: 1528–1536.
45. Bonaventure P, Dugovic C, Shireman B, Preville C, Yun S, Lord B, *et al.* Evaluation of JNJ-54717793 a novel brain penetrant selective orexin 1 receptor antagonist in two rat models of panic attack provocation. Front Pharmacol 2017, 8: 357.
46. Dugovic C, Shelton JE, Aluisio LE, Fraser IC, Jiang X, Sutton SW, *et al.* Blockade of orexin-1 receptors attenuates orexin-2 receptor antagonism-induced sleep promotion in the rat. J Pharmacol Exp Ther 2009, 330: 142–151.
47. Winrow CJ, Gotter AL, Cox CD, Doran SM, Tannenbaum PL, Breslin MJ, *et al.* Promotion of sleep by suvorexant-a novel dual orexin receptor antagonist. J Neurogenet 2011, 25: 52–61.
48. Hoyer D, Durst T, Fendt M, Jacobson LH, Betschart C, Hintermann S, *et al.* Distinct effects of IPSU and suvorexant on mouse sleep architecture. Front Neurosci 2013, 7: 235.
49. Tsuneki H, Kon K, Ito H, Yamazaki M, Takahara S, Toyooka N, *et al.* Timed inhibition of orexin system by suvorexant improved sleep and glucose metabolism in type 2 diabetic db/db mice. Endocrinology 2016, 157: 4146–4157.
50. Li SB, Nevarez N, Giardino WJ, de Lecea L. Optical probing of orexin/hypocretin receptor antagonists. Sleep 2018. https://doi.org/10.1093/sleep/zsy141.
51. Parks GS, Warrier DR, Dittrich L, Schwartz MD, Palmerston JB, Neylan TC, *et al.* The dual hypocretin receptor antagonist almorexant is permissive for activation of wake-promoting systems. Neuropsychopharmacology 2016, 41: 1144–1155.
52. Citrome L. Suvorexant for insomnia: a systematic review of the efficacy and safety profile for this newly approved hypnotic - what is the number needed to treat, number needed to harm and likelihood to be helped or harmed? Int J Clin Pract 2014, 68: 1429–1441.

53. Kishi T, Matsunaga S, Iwata N. Suvorexant for primary insomnia: a systematic review and meta-analysis of randomized placebo-controlled trials. PLoS One 2015, 10: e0136910.
54. Lee-Iannotti JK, Parish JM. Suvorexant: a promising, novel treatment for insomnia. Neuropsychiatr Dis Treat 2016, 12: 491–495.
55. Norman JL, Anderson SL. Novel class of medications, orexin receptor antagonists, in the treatment of insomnia – critical appraisal of suvorexant. Nat Sci Sleep 2016, 8: 239–247.
56. Herring WJ, Connor KM, Snyder E, Snavely DB, Zhang Y, Hutzelmann J*, et al.* Suvorexant in elderly patients with insomnia: pooled analyses of data from phase III randomized controlled clinical trials. Am J Geriatr Psychiatry 2017, 25: 791–802.
57. Herring WJ, Connor KM, Ivgy-May N, Snyder E, Liu K, Snavely DB*, et al.* Suvorexant in patients with insomnia: results from two 3-month randomized controlled clinical trials. Biol Psychiatry 2016, 79: 136–148.
58. Herring WJ, Connor KM, Snyder E, Snavely DB, Zhang Y, Hutzelmann J*, et al.* Suvorexant in patients with insomnia: pooled analyses of three-month data from phase-3 randomized controlled clinical trials. J Clin Sleep Med 2016, 12: 1215–1225.
59. Herring WJ, Connor KM, Snyder E, Snavely DB, Zhang Y, Hutzelmann J*, et al.* Clinical profile of suvorexant for the treatment of insomnia over 3 months in women and men: subgroup analysis of pooled phase-3 data. Psychopharmacology (Berl) 2017, 234: 1703–1711.
60. Sun H, Kennedy WP, Wilbraham D, Lewis N, Calder N, Li X*, et al.* Effects of suvorexant, an orexin receptor antagonist, on sleep parameters as measured by polysomnography in healthy men. Sleep 2013, 36: 259–267.
61. Connor KM, Mahoney E, Jackson S, Hutzelmann J, Zhao X, Jia N*, et al.* A phase II dose-ranging study evaluating the efficacy and safety of the orexin receptor antagonist filorexant (MK-6096) in patients with primary insomnia. Int J Neuropsychopharmacol 2016, 19: pyw022.
62. Kawabe K, Horiuchi F, Ochi M, Nishimoto K, Ueno SI, Oka Y. Suvorexant for the treatment of insomnia in adolescents. J Child Adolesc Psychopharmacol 2017, 27: 792–795.
63. Herring WJ, Connor KM, Snyder E, Snavely DB, Morin CM, Lines C*, et al.* Effects of suvorexant on the Insomnia Severity Index in patients with insomnia: analysis of pooled phase 3 data. Sleep Med 2019, 56: 219–223.
64. Michelson D, Snyder E, Paradis E, Chengan-Liu M, Snavely DB, Hutzelmann J*, et al.* Safety and efficacy of suvorexant during 1-year treatment of insomnia with subsequent abrupt treatment discontinuation: a phase 3 randomised, double-blind, placebo-controlled trial. Lancet Neurol 2014, 13: 461–471.
65. Ma J, Svetnik V, Snyder E, Lines C, Roth T, Herring WJ. Electroencephalographic power spectral density profile of the orexin receptor antagonist suvorexant in patients with primary insomnia and healthy subjects. Sleep 2014, 37: 1609–1619.
66. Snyder E, Ma J, Svetnik V, Connor KM, Lines C, Michelson D*, et al.* Effects of suvorexant on sleep architecture and power spectral profile in patients with insomnia: analysis of pooled phase 3 data. Sleep Med 2016, 19: 93–100.
67. Bettica P, Squassante L, Groeger JA, Gennery B, Winsky-Sommerer R, Dijk DJ. Differential effects of a dual orexin receptor antagonist (SB-649868) and zolpidem on sleep initiation and consolidation, SWS, REM sleep, and EEG power spectra in a model of situational insomnia. Neuropsychopharmacology 2012, 37: 1224–1233.
68. Bettica P, Squassante L, Zamuner S, Nucci G, Danker-Hopfe H, Ratti E. The orexin antagonist SB-649868 promotes and maintains sleep in men with primary insomnia. Sleep 2012, 35: 1097–1104.
69. Hamuro A, Honda M, Wakaura Y. Suvorexant for the treatment of insomnia in patients with Alzheimer's disease. Aust N Z J Psychiatry 2018, 52: 207–208.
70. Toi N, Inaba M, Kurajoh M, Morioka T, Hayashi N, Hirota T*, et al.* Improvement of glycemic control by treatment for insomnia with suvorexant in type 2 diabetes mellitus. J Clin Transl Endocrinol 2019, 15: 37–44.
71. Kawada K, Ohta T, Tanaka K, Miyamura M, Tanaka S. Addition of suvorexant to ramelteon therapy for improved sleep quality with reduced delirium risk in acute stroke patients. J Stroke Cerebrovasc Dis 2019, 28: 142–148.
72. Suzuki H, Hibino H, Inoue Y, Mikami A, Matsumoto H, Mikami K. Reduced insomnia following short-term administration of suvorexant during aripiprazole once-monthly treatment in a patient with schizophrenia. Asian J Psychiatr 2017, 28: 165–166.
73. Tabata H, Kuriyama A, Yamao F, Kitaguchi H, Shindo K. Suvorexant-induced dream enactment behavior in parkinson disease: a case report. J Clin Sleep Med 2017, 13: 759–760.
74. Uemura N, McCrea J, Sun H, Donikyan M, Zammit G, Liu R*, et al.* Effects of the orexin receptor antagonist suvorexant on respiration during sleep in healthy subjects. J Clin Pharmacol 2015, 55: 1093–1100.
75. Sun H, Palcza J, Card D, Gipson A, Rosenberg R, Kryger M*, et al.* Effects of suvorexant, an orexin receptor antagonist, on respiration during sleep in patients with obstructive sleep apnea. J Clin Sleep Med 2016, 12: 9–17.
76. Sun H, Palcza J, Rosenberg R, Kryger M, Siringhaus T, Rowe J*, et al.* Effects of suvorexant, an orexin receptor antagonist, on breathing during sleep in patients with chronic obstructive pulmonary disease. Respir Med 2015, 109: 416–426.
77. Brooks S, Jacobs GE, de Boer P, Kent JM, Van Nueten L, van Amerongen G*, et al.* The selective orexin-2 receptor antagonist seltorexant improves sleep: An exploratory double-blind, placebo controlled, crossover study in antidepressant-treated major depressive disorder patients with persistent insomnia. J Psychopharmacol 2019, 33: 202–209.
78. De Boer P, Drevets WC, Rofael H, van der Ark P, Kent JM, Kezic I*, et al.* A randomized Phase 2 study to evaluate the orexin-2 receptor antagonist seltorexant in individuals with insomnia without psychiatric comorbidity. J Psychopharmacol 2018, 32: 668–677.
79. Asai Y, Sano H, Miyazaki M, Iwakura M, Maeda Y, Hara M. Suvorexant (Belsomra((R)) tablets 10, 15, and 20 mg): Japanese drug-use results survey. Drugs R D 2019, 19: 27–46.
80. Rhyne DN, Anderson SL. Suvorexant in insomnia: efficacy, safety and place in therapy. Ther Adv Drug Saf 2015, 6: 189–195.
81. Schroeck JL, Ford J, Conway EL, Kurtzhalts KE, Gee ME, Vollmer KA*, et al.* Review of safety and efficacy of sleep medicines in older adults. Clin Ther 2016, 38: 2340–2372.
82. Hatano M, Kamei H, Inagaki R, Matsuzaki H, Hanya M, Yamada S*, et al.* Assessment of switching to suvorexant versus the use of add-on suvorexant in combination with benzodiazepine receptor agonists in insomnia patients: a retrospective study. Clin Psychopharmacol Neurosci 2018, 16: 184–189.
83. Sutton EL. Profile of suvorexant in the management of insomnia. Drug Des Devel Ther 2015, 9: 6035–6042.
84. Petrous J, Furmaga K. Adverse reaction with suvorexant for insomnia: acute worsening of depression with emergence of suicidal thoughts. BMJ Case Rep 2017, 2017: bcr-2017-222037.
85. Tung LW, Lu GL, Lee YH, Yu L, Lee HJ, Leishman E*, et al.* Orexins contribute to restraint stress-induced cocaine relapse by endocannabinoid-mediated disinhibition of dopaminergic neurons. Nat Commun 2016, 7: 12199.

86. Cengiz M, Karaj V, Kocabasoglu N, Gozubatik-Celik G, Dirican A, Bayoglu B. Orexin/hypocretin receptor, Orx1, gene variants are associated with major depressive disorder. Int J Psychiatry Clin Pract 2019, 23: 114–121.
87. Fitch TE, Benvenga MJ, Jesudason CD, Zink C, Vandergriff AB, Menezes MM, *et al.* LSN2424100: a novel, potent orexin-2 receptor antagonist with selectivity over orexin-1 receptors and activity in an animal model predictive of antidepressant-like efficacy. Front Neurosci 2014, 8: 5.
88. Nollet M, Gaillard P, Tanti A, Girault V, Belzung C, Leman S. Neurogenesis-independent antidepressant-like effects on behavior and stress axis response of a dual orexin receptor antagonist in a rodent model of depression. Neuropsychopharmacology 2012, 37: 2210–2221.
89. Nakamura M, Nagamine T. Neuroendocrine, autonomic, and metabolic responses to an orexin antagonist, suvorexant, in psychiatric patients with insomnia. Innov Clin Neurosci 2017, 14: 30–37.
90. Connor KM, Ceesay P, Hutzelmann J, Snavely D, Krystal AD, Trivedi MH, *et al.* Phase II proof-of-concept trial of the orexin receptor antagonist filorexant (MK-6096) in patients with major depressive disorder. Int J Neuropsychopharmacol 2017, 20: 613–618.
91. Dustrude ET, Caliman IF, Bernabe CS, Fitz SD, Grafe LA, Bhatnagar S, *et al.* Orexin depolarizes central amygdala neurons via orexin receptor 1, phospholipase c and sodium-calcium exchanger and modulates conditioned fear. Front Neurosci 2018, 12: 934.
92. Park SC, Kim YK. A novel bio-psychosocial-behavioral treatment model of panic disorder. Psychiatry Investig 2019, 16: 4–15.
93. Abreu AR, Molosh AI, Johnson PL, Shekhar A. Role of medial hypothalamic orexin system in panic, phobia and hypertension. Brain Res 2018. https://doi.org/10.1016/j.brainres.2018.09.010.
94. Johnson PL, Truitt W, Fitz SD, Minick PE, Dietrich A, Sanghani S, *et al.* A key role for orexin in panic anxiety. Nat Med 2010, 16: 111–115.
95. Gottschalk MG, Richter J, Ziegler C, Schiele MA, Mann J, Geiger MJ, *et al.* Orexin in the anxiety spectrum: association of a HCRTR1 polymorphism with panic disorder/agoraphobia, CBT treatment response and fear-related intermediate phenotypes. Transl Psychiatry 2019, 9: 75.
96. Johnson PL, Samuels BC, Fitz SD, Lightman SL, Lowry CA, Shekhar A. Activation of the orexin 1 receptor is a critical component of CO2-mediated anxiety and hypertension but not bradycardia. Neuropsychopharmacology 2012, 37: 1911–1922.
97. Kordi Jaz E, Moghimi A, Fereidoni M, Asadi S, Shamsizadeh A, Roohbakhsh A. SB-334867, an orexin receptor 1 antagonist, decreased seizure and anxiety in pentylenetetrazol-kindled rats. Fundam Clin Pharmacol 2017, 31: 201–207.
98. Blume SR, Nam H, Luz S, Bangasser DA, Bhatnagar S. Sex- and age-dependent effects of orexin 1 receptor blockade on open-field behavior and neuronal activity. Neuroscience 2018, 381: 11–21.
99. Bahaaddini M, Khatamsaz S, Esmaeili-Mahani S, Abbasnejad M, Raoof M. The role of trigeminal nucleus caudalis orexin 1 receptor in orofacial pain-induced anxiety in rat. Neuroreport 2016, 27: 1107–1113.
100. Johnson PL, Samuels BC, Fitz SD, Federici LM, Hammes N, Early MC, *et al.* Orexin 1 receptors are a novel target to modulate panic responses and the panic brain network. Physiol Behav 2012, 107: 733–742.
101. Johnson PL, Federici LM, Fitz SD, Renger JJ, Shireman B, Winrow CJ, *et al.* Orexin 1 and 2 receptor involvement in CO2 -induced panic–associated behavior and autonomic responses. Depress Anxiety 2015, 32: 671–683.
102. Bonaventure P, Yun S, Johnson PL, Shekhar A, Fitz SD, Shireman BT, *et al.* A selective orexin-1 receptor antagonist attenuates stress-induced hyperarousal without hypnotic effects. J Pharmacol Exp Ther 2015, 352: 590–601.
103. Arendt DH, Hassell J, Li H, Achua JK, Guarnieri DJ, Dileone RJ, *et al.* Anxiolytic function of the orexin 2/hypocretin A receptor in the basolateral amygdala. Psychoneuroendocrinology 2014, 40: 17–26.
104. Muschamp JW, Hollander JA, Thompson JL, Voren G, Hassinger LC, Onvani S, *et al.* Hypocretin (orexin) facilitates reward by attenuating the antireward effects of its cotransmitter dynorphin in ventral tegmental area. Proc Natl Acad Sci U S A 2014, 111: E1648–E1655.
105. Navarro G, Quiroz C, Moreno-Delgado D, Sierakowiak A, McDowell K, Moreno E, *et al.* Orexin-corticotropin-releasing factor receptor heteromers in the ventral tegmental area as targets for cocaine. J Neurosci 2015, 35: 6639–6653.
106. James MH, Stopper CM, Zimmer BA, Koll NE, Bowrey HE, Aston-Jones G. Increased number and activity of a lateral subpopulation of hypothalamic orexin/hypocretin neurons underlies the expression of an addicted state in rats. Biol Psychiatry 2019, 85: 925–935.
107. Foltin RW, Evans SM. Hypocretin/orexin antagonists decrease cocaine self-administration by female rhesus monkeys. Drug Alcohol Depend 2018, 188: 318–327.
108. Hutcheson DM, Quarta D, Halbout B, Rigal A, Valerio E, Heidbreder C. Orexin-1 receptor antagonist SB-334867 reduces the acquisition and expression of cocaine-conditioned reinforcement and the expression of amphetamine-conditioned reward. Behav Pharmacol 2011, 22: 173–181.
109. Bentzley BS, Aston-Jones G. Orexin-1 receptor signaling increases motivation for cocaine–associated cues. Eur J Neurosci 2015, 41: 1149–1156.
110. Prince CD, Rau AR, Yorgason JT, Espana RA. Hypocretin/orexin regulation of dopamine signaling and cocaine self-administration is mediated predominantly by hypocretin receptor 1. ACS Chem Neurosci 2015, 6: 138–146.
111. Schmeichel BE, Herman MA, Roberto M, Koob GF. Hypocretin neurotransmission within the central amygdala mediates escalated cocaine self-administration and stress-induced reinstatement in rats. Biol Psychiatry 2017, 81: 606–615.
112. Levy KA, Brodnik ZD, Shaw JK, Perrey DA, Zhang Y, Espana RA. Hypocretin receptor 1 blockade produces bimodal modulation of cocaine-associated mesolimbic dopamine signaling. Psychopharmacology (Berl) 2017, 234: 2761–2776.
113. Gentile TA, Simmons SJ, Watson MN, Connelly KL, Brailoiu E, Zhang Y, *et al.* Effects of suvorexant, a dual orexin/hypocretin receptor antagonist, on impulsive behavior associated with cocaine. Neuropsychopharmacology 2018, 43: 1001–1009.
114. Gentile TA, Simmons SJ, Barker DJ, Shaw JK, Espana RA, Muschamp JW. Suvorexant, an orexin/hypocretin receptor antagonist, attenuates motivational and hedonic properties of cocaine. Addict Biol 2018, 23: 247–255.
115. Schoedel KA, Sun H, Sellers EM, Faulknor J, Levy-Cooperman N, Li X, *et al.* Assessment of the abuse potential of the orexin receptor antagonist, suvorexant, compared with zolpidem in a randomized crossover study. J Clin Psychopharmacol 2016, 36: 314–323.
116. Born S, Gauvin DV, Mukherjee S, Briscoe R. Preclinical assessment of the abuse potential of the orexin receptor antagonist, suvorexant. Regul Toxicol Pharmacol 2017, 86: 181–192.
117. Anderson RI, Moorman DE, Becker HC. Contribution of dynorphin and orexin neuropeptide systems to the motivational effects of alcohol. Handb Exp Pharmacol 2018, 248: 473–503.

118. Mayannavar S, Rashmi KS, Rao YD, Yadav S, Ganaraja B. Effect of Orexin A antagonist (SB-334867) infusion into the nucleus accumbens on consummatory behavior and alcohol preference in Wistar rats. Indian J Pharmacol 2016, 48: 53–58.
119. Lopez MF, Moorman DE, Aston-Jones G, Becker HC. The highly selective orexin/hypocretin 1 receptor antagonist GSK1059865 potently reduces ethanol drinking in ethanol dependent mice. Brain Res 2016, 1636: 74–80.
120. Dhaher R, Hauser SR, Getachew B, Bell RL, McBride WJ, McKinzie DL, *et al.* The Orexin-1 receptor antagonist SB-334867 reduces alcohol relapse drinking, but not alcohol-seeking, in alcohol-preferring (P) rats. J Addict Med 2010, 4: 153–159.
121. Moorman DE, James MH, Kilroy EA, Aston-Jones G. Orexin/hypocretin-1 receptor antagonism reduces ethanol self-administration and reinstatement selectively in highly-motivated rats. Brain Res 2017, 1654: 34–42.
122. Quarta D, Valerio E, Hutcheson DM, Hedou G, Heidbreder C. The orexin-1 receptor antagonist SB-334867 reduces amphetamine-evoked dopamine outflow in the shell of the nucleus accumbens and decreases the expression of amphetamine sensitization. Neurochem Int 2010, 56: 11–15.
123. Lupina M, Tarnowski M, Baranowska-Bosiacka I, Talarek S, Listos P, Kotlinska J, *et al.* SB-334867 (an Orexin-1 Receptor Antagonist) effects on morphine-induced sensitization in mice-a view on receptor mechanisms. Mol Neurobiol 2018, 55: 8473–8485.
124. Sharf R, Guarnieri DJ, Taylor JR, DiLeone RJ. Orexin mediates morphine place preference, but not morphine-induced hyperactivity or sensitization. Brain Res 2010, 1317: 24–32.
125. Porter-Stransky KA, Bentzley BS, Aston-Jones G. Individual differences in orexin-I receptor modulation of motivation for the opioid remifentanil. Addict Biol 2017, 22: 303–317.
126. Sharf R, Sarhan M, Dileone RJ. Orexin mediates the expression of precipitated morphine withdrawal and concurrent activation of the nucleus accumbens shell. Biol Psychiatry 2008, 64: 175–183.
127. Davoudi M, Azizi H, Mirnajafi-Zadeh J, Semnanian S. The blockade of GABAA receptors attenuates the inhibitory effect of orexin type 1 receptors antagonist on morphine withdrawal syndrome in rats. Neurosci Lett 2016, 617: 201–206.
128. Hooshmand B, Azizi H, Javan M, Semnanian S. Intra-LC microinjection of orexin type-1 receptor antagonist SB-334867 attenuates the expression of glutamate-induced opiate withdrawal like signs during the active phase in rats. Neurosci Lett 2017, 636: 276–281.
129. Farahimanesh S, Zarrabian S, Haghparast A. Role of orexin receptors in the ventral tegmental area on acquisition and expression of morphine-induced conditioned place preference in the rats. Neuropeptides 2017, 66: 45–51.
130. Ebrahimian F, Naghavi FS, Yazdi F, Sadeghzadeh F, Taslimi Z, Haghparast A. Differential roles of orexin receptors within the dentate gyrus in stress- and drug priming-induced reinstatement of conditioned place preference in rats. Behav Neurosci 2016, 130: 91–102.
131. Parsania S, Moradi M, Fatahi Z, Haghparast A. Involvement of orexin-1 and orexin-2 receptors within the dentate gyrus of the hippocampus in the acquisition, expression and extinction of lateral hypothalamic-induced conditioned place preference in the rats. Brain Res 2016, 1639: 149–160.
132. Barson JR, Ho HT, Leibowitz SF. Anterior thalamic paraventricular nucleus is involved in intermittent access ethanol drinking: role of orexin receptor 2. Addict Biol 2015, 20: 469–481.
133. Schmeichel BE, Barbier E, Misra KK, Contet C, Schlosburg JE, Grigoriadis D, *et al.* Hypocretin receptor 2 antagonism dose-dependently reduces escalated heroin self-administration in rats. Neuropsychopharmacology 2015, 40: 1123–1129.
134. Steiner MA, Lecourt H, Jenck F. The dual orexin receptor antagonist almorexant, alone and in combination with morphine, cocaine and amphetamine, on conditioned place preference and locomotor sensitization in the rat. Int J Neuropsychopharmacol 2013, 16: 417–432.
135. Srinivasan S, Simms JA, Nielsen CK, Lieske SP, Bito-Onon JJ, Yi H, *et al.* The dual orexin/hypocretin receptor antagonist, almorexant, in the ventral tegmental area attenuates ethanol self-administration. PLoS One 2012, 7: e44726.
136. Steiner MA, Lecourt H, Strasser DS, Brisbare-Roch C, Jenck F. Differential effects of the dual orexin receptor antagonist almorexant and the GABA(A)-alpha1 receptor modulator zolpidem, alone or combined with ethanol, on motor performance in the rat. Neuropsychopharmacology 2011, 36: 848–856.
137. Hoch M, Hay JL, Hoever P, de Kam ML, te Beek ET, van Gerven JM, *et al.* Dual orexin receptor antagonism by almorexant does not potentiate impairing effects of alcohol in humans. Eur Neuropsychopharmacol 2013, 23: 107–117.
138. Sanchez-Alavez M, Benedict J, Wills DN, Ehlers CL. Effect of suvorexant on event-related oscillations and EEG sleep in rats exposed to chronic intermittent ethanol vapor and protracted withdrawal. Sleep 2019, 42: zsz020.
139. Campbell EJ, Marchant NJ, Lawrence AJ. A sleeping giant: suvorexant for the treatment of alcohol use disorder? Brain Res 2018; e-pub ahead of print 3 August 2018; https://doi.org/10.1016/j.brainres.2018.08.005.
140. Plaza-Zabala A, Flores A, Maldonado R, Berrendero F. Hypocretin/orexin signaling in the hypothalamic paraventricular nucleus is essential for the expression of nicotine withdrawal. Biol Psychiatry 2012, 71: 214–223.
141. Nishizawa D, Kasai S, Hasegawa J, Sato N, Yamada H, Tanioka F, *et al.* Associations between the orexin (hypocretin) receptor 2 gene polymorphism Val308Ile and nicotine dependence in genome-wide and subsequent association studies. Mol Brain 2015, 8: 50.
142. Khoo SY, Clemens KJ, McNally GP. Palatable food self-administration and reinstatement are not affected by dual orexin receptor antagonism. Prog Neuropsychopharmacol Biol Psychiatry 2018, 87: 147–157.
143. Khoo SY, McNally GP, Clemens KJ. The dual orexin receptor antagonist TCS1102 does not affect reinstatement of nicotine-seeking. PLoS One 2017, 12: e0173967.
144. Sharf R, Sarhan M, Brayton CE, Guarnieri DJ, Taylor JR, DiLeone RJ. Orexin signaling via the orexin 1 receptor mediates operant responding for food reinforcement. Biol Psychiatry 2010, 67: 753–760.
145. Flores A, Maldonado R, Berrendero F. The hypocretin/orexin receptor-1 as a novel target to modulate cannabinoid reward. Biol Psychiatry 2014, 75: 499–507.
146. Brodnik ZD, Alonso IP, Xu W, Zhang Y, Kortagere S, Espana RA. Hypocretin receptor 1 involvement in cocaine-associated behavior: Therapeutic potential and novel mechanistic insights. Brain Res 2018. https://doi.org/10.1016/j.brainres.2018.07.027.
147. Perrey DA, Zhang Y. Therapeutics development for addiction: orexin-1 receptor antagonists. Brain Res 2018. https://doi.org/10.1016/j.brainres.2018.08.025.
148. Dubey AK, Handu SS, Mediratta PK. Suvorexant: The first orexin receptor antagonist to treat insomnia. J Pharmacol Pharmacother 2015, 6: 118–121.
149. Coleman PJ, Cox CD, Roecker AJ. Discovery of dual orexin receptor antagonists (DORAs) for the treatment of insomnia. Curr Top Med Chem 2011, 11: 696–725.
150. Nocjar C, Zhang J, Feng P, Panksepp J. The social defeat animal model of depression shows diminished levels of orexin in

mesocortical regions of the dopamine system, and of dynorphin and orexin in the hypothalamus. Neuroscience 2012, 218: 138–153.
151. Winrow CJ, Gotter AL, Cox CD, Tannenbaum PL, Garson SL, Doran SM, *et al*. Pharmacological characterization of MK-6096 - a dual orexin receptor antagonist for insomnia. Neuropharmacology 2012, 62: 978–987.
152. Herring WJ, Snyder E, Budd K, Hutzelmann J, Snavely D, Liu K, *et al*. Orexin receptor antagonism for treatment of insomnia: a randomized clinical trial of suvorexant. Neurology 2012, 79: 2265–2274.
153. Nishimura S, Nakao M. Cost-effectiveness analysis of suvorexant for the treatment of Japanese elderly patients with chronic insomnia in a virtual cohort. J Med Econ 2018, 21: 698–703.
154. Svetnik V, Snyder ES, Tao P, Scammell TE, Roth T, Lines C, *et al*. Insight Into reduction of wakefulness by suvorexant in patients with insomnia: analysis of wake bouts. Sleep 2018. https://doi.org/10.1093/sleep/zsx178.
155. Hoever P, de Haas S, Winkler J, Schoemaker RC, Chiossi E, van Gerven J, *et al*. Orexin receptor antagonism, a new sleep-promoting paradigm: an ascending single-dose study with almorexant. Clin Pharmacol Ther 2010, 87: 593–600.
156. Black SW, Morairty SR, Fisher SP, Chen TM, Warrier DR, Kilduff TS. Almorexant promotes sleep and exacerbates cataplexy in a murine model of narcolepsy. Sleep 2013, 36: 325–336.
157. Morairty SR, Wilk AJ, Lincoln WU, Neylan TC, Kilduff TS. The hypocretin/orexin antagonist almorexant promotes sleep without impairment of performance in rats. Front Neurosci 2014, 8: 3.
158. Black J, Pillar G, Hedner J, Polo O, Berkani O, Mangialaio S, *et al*. Efficacy and safety of almorexant in adult chronic insomnia: a randomized placebo-controlled trial with an active reference. Sleep Med 2017, 36: 86–94.
159. Roth T, Black J, Cluydts R, Charef P, Cavallaro M, Kramer F, *et al*. Dual orexin receptor antagonist, almorexant, in elderly patients with primary insomnia: a randomized, controlled study. Sleep 2017. https://doi.org/10.1093/sleep/zsw034.
160. Yoshida Y, Naoe Y, Terauchi T, Ozaki F, Doko T, Takemura A, *et al*. Discovery of (1R,2S)-2-{[(2,4-Dimethylpyrimidin-5-yl)oxy]methyl}-2-(3-fluorophenyl)-N-(5-fluor opyridin-2-yl)cyclopropanecarboxamide (E2006): a potent and efficacious oral orexin receptor antagonist. J Med Chem 2015, 58: 4648–4664.
161. Whitman DB, Cox CD, Breslin MJ, Brashear KM, Schreier JD, Bogusky MJ, *et al*. Discovery of a potent, CNS-penetrant orexin receptor antagonist based on an n,n-disubstituted-1,4-diazepane scaffold that promotes sleep in rats. ChemMedChem 2009, 4: 1069–1074.
162. Coleman PJ, Schreier JD, Roecker AJ, Mercer SP, McGaughey GB, Cox CD, *et al*. Discovery of 3,9-diazabicyclo[4.2.1]nonanes as potent dual orexin receptor antagonists with sleep-promoting activity in the rat. Bioorg Med Chem Lett 2010, 20: 4201–4205.

Neurosci. Bull. April, 2020, 36(4):449–451
https://doi.org/10.1007/s12264-019-00453-x

www.neurosci.cn
www.springer.com/12264

RESEARCH HIGHLIGHT

Sleep Disturbance: An Early Sign of Alzheimer's Disease

Chao He[1] · Zhian Hu[1] · Chenggang Jiang[2,3]

Received: 21 July 2019 / Accepted: 15 August 2019 / Published online: 5 December 2019

Alzheimer's disease (AD) is a progressive neurodegenerative disorder associated with cognitive impairment in older adults. The accumulation of insoluble forms of amyloid-β (Aβ) in plaques in extracellular spaces and the aggregation of hyperphosphorylated microtubule-associated protein tau in neurofibrillary tangles in neurons are considered to be central pathological features of AD [1, 2]. Before the cognitive symptoms and pathological signs are present, preclinical synaptic and neuronal injury begins to occur, and this continues for 10–20 years. Currently, one focus of AD research is to discern the preclinical stage of AD, when Aβ deposition has begun to occur but before clear cognitive impairment, as well as to develop therapeutic interventions at this stage to prevent AD progression [3].

Sleep disturbance is recognized as a common and often highly disruptive behavioral symptom associated with AD. It has been reported that Aβ deposition pathology itself can alter sleep architecture [4]. Moreover, recent evidence supports a role of sleep disturbance in the occurrence of AD. Sleep promotes the clearance of Aβ and tau to maintain homeostasis. Sleep disturbance significantly increases the levels of Aβ and tau and promotes senile plaque formation in AD mice [5, 6]. Based on this initial evidence, it has been proposed that the relationship between sleep and Aβ deposition is bidirectional: sleep disturbance leads to Aβ deposition and Aβ deposition in turn leads to sleep disruption. To thoroughly test this hypothesis, it is necessary to know how sleep is disrupted across the different stages of AD pathogenesis. Now, Zhang *et al.* report new findings that systematically address this issue: they found that sleep disturbance occurs before the cognitive decline and even precedes the pre-pathological stage of AD [7].

Using a battery of behavioral tests including the Morris water maze and novel object recognition tests, Zhang *et al.* initially investigated cognitive functions in $APP^{swe}/PS1^{\Delta E9}$ AD mice at 3, 4, and 6 months of age. The authors found that AD mice at 6 months but not 3 and 4 months display a reduction in learning and memory. Moreover, Aβ plaque deposition and tau hyperphosphorylation appeared at 6 months but not at 3 and 4 months in these mice, suggesting that transgenic AD mice at 3 and 4 months of age are in a pre-pathological stage.

Next, Zhang *et al.*, monitored the sleep-wake cycle in $APP^{swe}/PS1^{\Delta E9}$ AD mice at 3, 4, and 6 months of age. The AD mice already spend more time in wakefulness and less time in slow-wave sleep during the dark period at 3 months. The AD mice at 4 and 6 months spend less time in slow-wave sleep during the light period, but these animals spend more time in slow-wave sleep during the dark period. Interestingly, the electroencephalogram (EEG) of AD mice exhibit lower delta rhythm power during sleep than WT mice. Altogether, these results demonstrate that

✉ Chao He
hechaochongqing@163.com

✉ Zhian Hu
zhianhu@aliyun.com

✉ Chenggang Jiang
jcgaqq@126.com

[1] Department of Physiology, Institute of Brain and Intelligence, Third Military Medical University, Chongqing 400038, China

[2] Department of Medical Psychology, Chongqing Health Center for Women and Children, Chongqing 400021, China

[3] Department of Sleep and Psychology, Daping Hospital, Third Military Medical University, Chongqing 400042, China

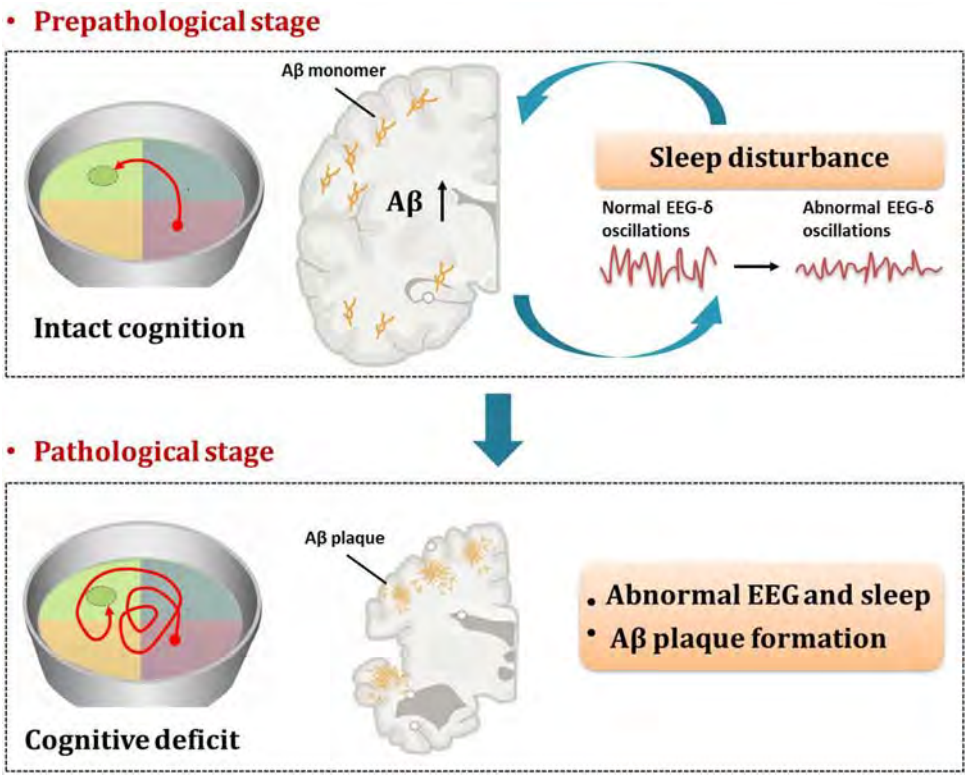

Fig. 1 Decreases in slow-wave sleep time and EEG δ-power occur before the cognitive decline and pathological stage of AD, indicating that sleep disturbance serves as a valuable early sign of AD.

disturbed sleep quality and architecture precede cognitive deficits and AD-like pathology (Fig. 1).

Several studies from animals have reported that sleep architecture and the EEG are disrupted at the pathological stage of AD [8, 9]. Consistent with these animal findings, monitoring has revealed changes in sleep EEG in patients with mild cognitive impairment (MCI) or mild-to-moderate AD [10, 11]. Patients with mild-to-moderate AD present abnormal theta oscillations in both rapid eye-movement (REM) and slow-wave sleep [11]. Another study quantified the EEG during REM sleep in patients with MCI, and found that the MCI subgroup shows EEG slowing in fronto-lateral regions compared to controls [10]. Zhang *et al.* provide evidence that sleep disturbance already occurs before the cognitive decline and even precedes the pre-pathological stage of AD [7]. These findings strongly suggest that sleep EEG changes may serve as a valuable early sign of AD in the preclinical stage, which would be beneficial for preclinical evaluation and therapeutic intervention to prevent progression to symptomatic AD.

The report by Zhang *et al.* further demonstrated a bidirectional relationship between deep sleep disorders and AD pathology. On one hand, a slight increase in Aβ in the AD animal model at the early stage disrupts sleep. On the other hand, the sleep-wake cycle influences Aβ and tau levels. High neural activity during wakefulness produces high levels of Aβ and tau, while sleep promotes the clearance of these waste products [5, 6]. The lower delta rhythm power during sleep in AD mice reported by Zhang *et al.* indicates high cortical neural activity, which could cause more Aβ and tau production. Furthermore, less sleep might also disrupt the clearance of these waste products. Through these dual mechanisms, sleep disorders trigger a vicious cycle to AD pathogenesis. Epidemiological studies have shown that up to 45% of patients with AD have various kinds of sleep disturbance. Consistent with this idea, sleep disturbance is positively correlated with the severity of cognitive and pathological impairment. AD patients with poor sleep quality have a greater Aβ burden and exhibit more severe cognitive impairment [12, 13].

Overall, the study by Zhang *et al.* provides crucial new insights into the changes in sleep in preclinical AD, as well as offering the possibility of preventing or delaying the occurrence of AD through interventions in sleep. Future studies will be helpful to test the causal role of sleep disturbance in the pathogenesis of AD by monitoring the sleep changes in patients. Moreover, it is also important to clarify how sleep-wakefulness is disrupted during the progression of AD. Multiple slow wave sleep-controlling nuclei, including the preoptic area, zona incerta, parafacial zone, and perioculomotor nucleus, and wakefulness-promoting nuclei, such as the paraventricular thalamus, basal forebrain, hypothalamus, and locus coeruleus, have been identified [14, 15]. Overexpressing Aβ protein in an AD animal model causes sleep-wakefulness disturbance preceding the cognitive deficit, indicating that the sleep-

wakefulness-controlling systems are more vulnerable to Aβ than the cognition-related systems. Indeed, it has been reported that Aβ plaques develop in the basal forebrain before they appear in the hippocampus, and the locus coeruleus is affected by abnormal tau pathology during pre-pathological stages [16]. Despite these contributions, however, the field still lacks a comprehensive understanding of the cellular and molecular injuries underlying the sleep-wakefulness disturbance in AD and further studies are needed.

References

1. Gao Y, Liu Q, Xu L, Zheng N, He X, Xu F. Imaging and spectral characteristics of amyloid plaque autofluorescence in brain slices from the APP/PS1 mouse model of Alzheimer's disease. Neurosci Bull 2019, 35: 1126–1137.
2. Wei YP, Ye JW, Wang X, Zhu LP, Hu QH, Wang Q, *et al.* Tau-induced Ca(2+)/calmodulin-dependent protein kinase-IV activation aggravates nuclear Tau hyperphosphorylation. Neurosci Bull 2018, 34: 261–269.
3. Sperling RA, Aisen PS, Beckett LA, Bennett DA, Craft S, Fagan AM, *et al.* Toward defining the preclinical stages of Alzheimer's disease: recommendations from the National Institute on Aging-Alzheimer's Association workgroups on diagnostic guidelines for Alzheimer's disease. Alzheimers Dement 2011, 7: 280–292.
4. Roh JH, Huang Y, Bero AW, Kasten T, Stewart FR, Bateman RJ, *et al.* Disruption of the sleep-wake cycle and diurnal fluctuation of beta-amyloid in mice with Alzheimer's disease pathology. Sci Transl Med 2012, 4: 150ra122.
5. Holth JK, Fritschi SK, Wang C, Pedersen NP, Cirrito JR, Mahan TE, *et al.* The sleep-wake cycle regulates brain interstitial fluid tau in mice and CSF tau in humans. Science 2019, 363: 880–884.
6. Xie L, Kang H, Xu Q, Chen MJ, Liao Y, Thiyagarajan M, *et al.* Sleep drives metabolite clearance from the adult brain. Science 2013, 342: 373–377.
7. Zhang F, Zhong R, Li S, Fu Z, Wang R, Wang T, *et al.* Alteration in sleep architecture and electroencephalogram as an early sign of Alzheimer's disease preceding the disease pathology and cognitive decline. Alzheimers Dement 2019, 15: 590–597.
8. Jyoti A, Plano A, Riedel G, Platt B. EEG, activity, and sleep architecture in a transgenic AbetaPPswe/PSEN1A246E Alzheimer's disease mouse. J Alzheimers Dis 2010, 22: 873–887.
9. Schneider F, Baldauf K, Wetzel W, Reymann KG. Behavioral and EEG changes in male 5xFAD mice. Physiol Behav 2014, 135: 25–33.
10. Brayet P, Petit D, Frauscher B, Gagnon JF, Gosselin N, Gagnon K, *et al.* Quantitative EEG of rapid-eye-movement sleep: a marker of amnestic mild cognitive impairment. Clin EEG Neurosci 2016, 47: 134–141.
11. Hot P, Rauchs G, Bertran F, Denise P, Desgranges B, Clochon P, *et al.* Changes in sleep theta rhythm are related to episodic memory impairment in early Alzheimer's disease. Biol Psychol 2011, 87: 334–339.
12. Spira AP, Gamaldo AA, An Y, Wu MN, Simonsick EM, Bilgel M, *et al.* Self-reported sleep and beta-amyloid deposition in community-dwelling older adults. JAMA Neurol 2013, 70: 1537–1543.
13. Vitiello MV, Prinz PN, Williams DE, Frommlet MS, Ries RK. Sleep disturbances in patients with mild-stage Alzheimer's disease. J Gerontol 1990, 45: M131–138.
14. Zhang Z, Zhong P, Hu F, Barger Z, Ren Y, Ding X, *et al.* An excitatory circuit in the perioculomotor midbrain for non-REM sleep control. Cell 2019, 177: 1293–1307.
15. Ren S, Wang Y, Yue F, Cheng X, Dang R, Qiao Q, *et al.* The paraventricular thalamus is a critical thalamic area for wakefulness. Science 2018, 362: 429–434.
16. Goedert M. Neurodegeneration. Alzheimer's and Parkinson's diseases: The prion concept in relation to assembled Abeta, tau, and alpha-synuclein. Science 2015, 349: 1255555.

NEUROSCIENCE BULLETIN

Impact Factor

4.246

Q2

2018 Journal Citation Report
(Clarivate Analytics, 2019)

NEUROSCIENCE BULLETIN 神经科学通报 (Monthly)

Vol. 36 No. 4 April 15, 2020

Sponsored by: Shanghai Institutes for Biological Sciences, Chinese Academy of Sciences
Chinese Neuroscience Society
Second Military Medical University

Editors-in-Chief: Shumin Duan, Ru-Rong Ji

Edited by: Editorial Board of *Neuroscience Bulletin*
319 Yueyang Road, Building 31 B, Room 405, Shanghai 200031, China
Phone: +86-21-54922863; Fax: +86-21-54922833
E-mail:nsb@sibs.ac.cn; http://www.neurosci.cn

Editors: Bin Wei, Xu Jiang, Zhi-Rui Liu

Published by: Shanghai Institutes for Biological Sciences, Chinese Academy of Sciences (320 Yueyang Road, Shanghai)

Printed by: Shanghai Shengtong Times Printing Co., Ltd (A6, No. 2888, Caolang Highway, Jinshan District, Shanghai)

Overseas Distributed by: Springer Nature

Home Distributed by: Local Post Offices

ISSN 1673-7067
CN 31-1975/R

Post Office Code Number: 4-608
Permit of Ad. Number: 3100420130051
Price: ¥ 100.00

ISSN 1673-7067
9 771673 706209 04

OLYMPUS

转盘共聚焦超分辨显微镜

SpinSR10

IXplore

兼顾分辨率和速度的
转盘共聚焦活细胞超分辨系统 SpinSR10

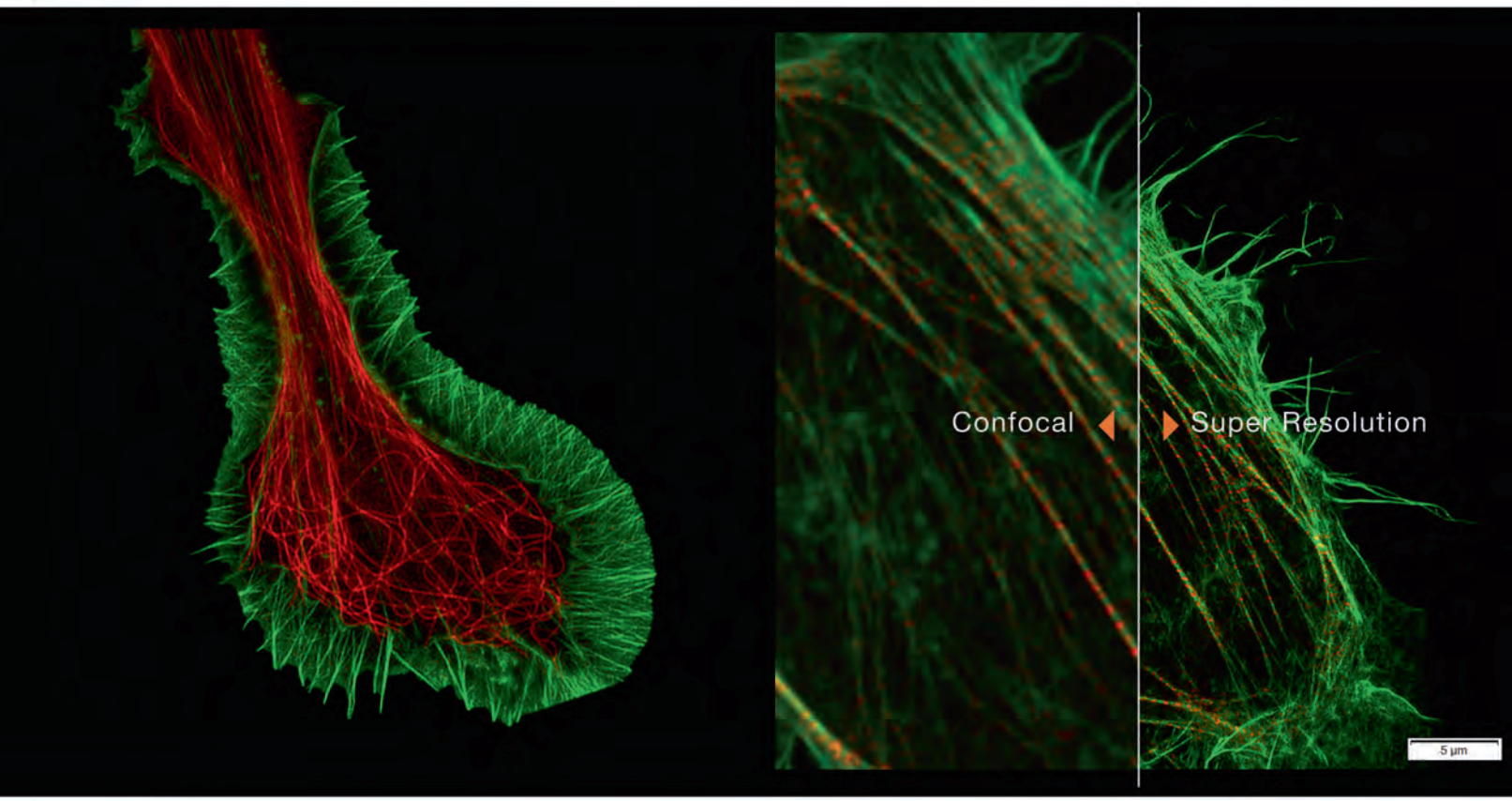

- 分辨率高达110 nm的实时超分辨率成像
- 专有反卷积算法进一步提升图像质量
- 宽视野成像，速度高达 200fps
- 特色硅油物镜可以实现活细胞深层成像
- 宽场、共聚焦、超分辨率模式自由切换
- 功能强大的智能cellSens软件平台

奥林巴斯（北京）销售服务有限公司

北京朝阳区酒仙桥路10号恒通商务园B12C座2F （北京） 010-59756006
上海市徐汇区淮海中路1010号嘉华中心11楼 （上海） 021-51582084
广州市环市东路403号广州电子大厦16楼 （广州） 020-61227171
陕西省西安市新城区尚德路85号太平洋保险大厦8F （西安） 029-87206108
湖北省武汉市江岸区中山大道1628号武汉天地企业中心5号7楼701单元 （武汉） 027-82718838
四川省成都市人民南路四段三号来福士广场T1-11楼 （成都） 028-86703700
辽宁省沈阳市沈河区友好街10号新地中心1号楼3501室 （沈阳） 024-23342084

http://www.olympus-lifescience.com.cn/zh/